
ASTROPHYSICAL NEUTRINOS

Signal and background in searches for
fundamental physics

Edoardo Vitagliano



München 2019

ASTROPHYSICAL NEUTRINOS

Signal and background in searches for fundamental physics

Dissertation
an der Fakultät für Physik
der Ludwig-Maximilians-Universität
München

vorgelegt von
Edoardo Vitagliano
aus Neapel

München, den 5. Juni 2019



Dissertation

an der Fakultät für Physik
der Ludwig-Maximilians-Universität München
vorgelegt von Edoardo Vitagliano
am 5. Juni 2019.

Erstgutachter: PD Dr. Georg Raffelt
Zweitgutachter: Prof. Dr. Achim Weiss

Tag der mündlichen Prüfung: 12. Juli 2019

Max-Planck-Institut für Physik,
München, den 5. Juni 2019.

Zusammenfassung

Während die experimentellen Grenzen von Energie und Intensität stetig hinausgeschoben werden, entwickelt sich die Astroteilchenphysik immer stärker als Schlüssel zum Verständnis der mikroskopischen und makroskopischen Mechanismen, die unser Universum bestimmen. In dieser Dissertation wird die Teilchenphysik jenseits des Standardmodells untersucht, insbesondere dunkle Materie und Neutrinoeigenschaften, durch die Benützung astrophysikalischer Neutrinos und anderer Botenteilchen. Die gleichzeitige Betrachtung von Neutrinos und Photonen, zusammen mit kosmischer Strahlung und Gravitationswellen, bildet den Kern der Multi-Messenger Astronomie, einem jungen und sich rasch entwickelnden Gebiet, das verspricht, unser Verständnis des Universums auf völlig verschiedenen Energieskalen neu zu formen. Gerade Neutrinos sind besonders interessant, da sie sowohl Hintergrund als auch Signal sein können.

In dem ersten Teil der Arbeit präsentiere ich eine neue Analyse des “großen vereinheitlichten Neutrinospektrums” (*Grand Unified Neutrino Spectrum*), womit der irdische Neutrinofluss gemeint ist, der aus unterschiedlichen Quellen ein breites Energiespektrum umfasst. Nach einer kurzen Übersicht über die Beiträge zu diesem vereinheitlichten Neutrinospektrum wenden wir uns einem zuvor nicht beachteten Fluss zu, den niederenergetischen Neutrinos aus thermischen Prozessen in der Sonne. Dieser Fluss schließt die Lücke zwischen dem kosmischen Neutrinohintergrund und dem solaren Neutrinofluss aus Kernfusionen.

Der zweite Teil widmet sich der Suche nach Physik jenseits des Standardmodells. Zunächst zeigen wir, wie sich aus Sonnenneutrino-Messungen eine obere Schranke an den Neutrinozerfall in leichte Pseudoskalare herleiten lässt, wobei die Suche nach solaren Antineutrinos durch KamLAND, SNO und Borexino besonders nützlich ist. Schließlich untersuche ich Andeutungen eines Signals der dunklen Materie im Kontext der Multi-Messenger Astronomie bei unterschiedlichen Wellenlängen. Diese Anzeichen stammen von einer erhöhten kosmischen Hintergrundstrahlung im Infrarotspektrum (gemessen von der Sonde CIBER), die mittels des Zerfalls axionartiger Teilchen mit einer eV-Masse erklärt werden kann. Gleichzeitig würde damit eine Diskrepanz zwischen Fermi und IceCube Messungen erklärt, nämlich dass weniger Gammastrahlung beobachtet wird, als man aus dem gemessenen Neutrinofluss erwarten würde.

Abstract

As the experimental boundaries of the energy and intensity frontiers are pushed forwards, astroparticle physics increasingly becomes a key tool to understand the microscopic and macroscopic mechanisms governing our universe. In this thesis particle physics beyond the Standard Model is explored, especially dark matter and neutrino properties, through the use of astrophysical neutrinos and other messengers. The combined use of neutrinos and photons, as well as cosmic rays and gravitational waves, is at the core of multi-messenger astronomy, a young and rapidly developing field which promises to reshape our understanding of the universe at hugely different energy scales. Neutrinos are of particular interest as they play the double role of possible signal and background.

In the first part of the thesis, I present a new analysis of what we will call the “grand unified neutrino spectrum” (GUNS) at Earth, the flux of neutrinos coming from many different sources, both at low and high energies. After a short review of the contributions to the grand unified neutrino spectrum, we will turn to a previously overlooked flux, the low-energy component of neutrinos produced in the Sun by thermal processes, which fills the gap between the cosmic neutrino background and the solar neutrino flux from nuclear reactions.

The second part of the thesis is dedicated to the search for physics beyond the Standard Model. First, I will show how solar neutrino observations can be used to constrain neutrino decay to light pseudoscalars, particularly taking advantage of antineutrino searches from the Sun tackled by KamLAND, SNO and Borexino. Finally, I will scrutinize hints for a dark matter signal in the context of multi-messenger, multi-wavelength astronomy, as the decay of axionlike particles with eV mass enhances the infrared cosmic background radiation (as detected by the sounding rocket CIBER), explaining at the same time an existing tension between the observations of Fermi and IceCube, namely that we observe less gamma rays than expected from the measured high-energy neutrino flux.

Projects and publications

This thesis is based on completed and ongoing projects to which I contributed during my research conducted at the Ludwig–Maximilians–Universität München and the Max-Planck-Institut für Physik from January 2016 to June 2019.

A substantial part of this thesis was originally published in papers listed below. The presentation in this thesis, including figures and tables, often closely follows these papers:

1. E. Vitagliano, I. Tamborra and G. Raffelt, “Grand Unified Neutrino Spectrum at Earth,” work in progress.
2. L. Funcke, G. Raffelt and E. Vitagliano, “Distinguishing Dirac and Majorana neutrinos by their gravi-majoron decays,” [arXiv:1905.01264](#), submitted to *Phys. Rev. D*.
3. O. Kalashev, A. Kusenko and E. Vitagliano, “Cosmic infrared background excess from axionlike particles and implications for multimessenger observations of blazars,” *Phys. Rev. D* **99** (2019) 023002, [arXiv:1808.05613](#).
4. E. Vitagliano, J. Redondo and G. Raffelt, “Solar neutrino flux at keV energies,” *JCAP* **12** (2017) 010, [arXiv:1708.02248](#).

There are further projects carried out during the period 2016–2019. They are not discussed or are only quoted as ordinary references in the main text where appropriate:

7. S. Appel, L. Oberauer, G. Raffelt and E. Vitagliano (for the Borexino collaboration), “Solar antineutrino fluxes with Borexino at LNGS and neutrino decay,” work in progress.
8. M. Lawson, A. Millar, M. Pancaldi, E. Vitagliano and F. Wilczek, “Tunable axion plasma haloscopes,” [arXiv:1904.11872](#), submitted to *Phys. Rev. Lett.*
9. A. Millar, G. Raffelt, L. Stodolsky and E. Vitagliano, “Neutrino mass from bremsstrahlung endpoint in coherent scattering on nuclei,” *Phys. Rev. D* **98** (2018) 123006, [arXiv:1810.06584](#).
10. M. Chianese, G. Miele, S. Morisi and E. Vitagliano, “Low energy IceCube data and a possible Dark Matter related excess,” *Phys. Lett. B* **757** (2016) 251–256, [arXiv:1601.02934](#).

Acknowledgements

I am greatly indebted to many people for their help and support in writing this thesis. Foremost I thank my supervisor Georg Raffelt for his support during the last years. He has been a fantastic mentor, with advices going from thinking about new possible research topics and reanalyzing old ones to managing projects, though I will probably never acquire his pace; his attention to both the grand scheme and the smallest (even typographical) details has been inspirational. Besides, his kindness and willingness to discuss every time I stepped in his office has been outstanding, and I will always be thankful to him for teaching me how a great physicist works. I am also grateful to the Elusives network, which allowed me to work in Barcelona, Madrid, and Tokyo, and gave me incredible opportunities.

My work would have been impossible without the help of amazing collaborators; therefore I thank Simon Appel, Lena Funcke, Oleg Kalashev, Alexander Kusenko, Alexander Millar, Lothar Oberauer, Javier Redondo and Leo Stodolsky, hoping we will keep on writing together. I especially thank Irene Tamborra, who has been an unofficial supervisor to me.

During the daily life, the Max Planck Institute has been a great environment. I thank the Theoretical Astroparticle Group for the physics discussions as well as the (slightly...) less physics related ones during lunch. Above all I would like to thank again Lena, Francesco, Alex and Tobias, particularly for allowing me to occupy essentially every single desk in our office. I am also very grateful to the administration for helping me with bureaucracy, my apartment, and everything which made my life in Munich comfortable. Finally, thanks to the Italian connection friends; without breaks we would have produced more papers, but our foosball skills would be much worse — and life in Munich much more boring. Identically, thanks to my flatmates, who included Marco and Stephan (who took care of me together with Julia); I will miss you.

Writing this thesis would have been much more difficult without the support of my oldest friends and my family; we grew up together. I am grateful to my friends at the physics department in Naples, especially Alessandro, Maria and Caterina, as well as to the guys from Pomigliano, especially Carmela. Finally and foremost, thanks to both my parents Michelangelo and Rosaria, and to my siblings Vincenzo, Giovanni, Paola and Elena, and to Roberto (the fifth sibling). I love you all.

This list should be much longer, since I am grateful to the wonderful people who have been, are and/or will be in my life. Sarete sempre casa.

Contents

Zusammenfassung	v
Abstract	vi
Projects and publications	vii
Acknowledgements	viii
List of abbreviations	xii
1 Introduction: grand unified neutrino spectrum at Earth	1
2 Cosmological neutrinos	5
2.1 Cosmic neutrino background	5
2.1.1 Standard properties of the CNB	6
2.1.2 Neutrinos as hot dark matter	7
2.1.3 Spectrum at Earth	7
2.1.4 Detection perspectives	9
2.2 Neutrinos from big-bang nucleosynthesis	10
2.2.1 Primordial nucleosynthesis	10
2.2.2 Neutrinos from decaying light isotopes	11
2.2.3 Neutrinos with mass	13
3 Astrophysical and terrestrial neutrinos	15
3.1 Neutrinos from nuclear reactions in the Sun	16
3.1.1 The Sun as a neutrino source	16
3.1.2 Production processes and spectra	16
3.1.3 Standard solar models	21
3.1.4 Antineutrinos	23
3.1.5 Flavor conversion	23
3.1.6 Observations and detection perspectives	25
3.2 Geoneutrinos	27
3.2.1 Production mechanisms	27
3.2.2 Earth modeling	29
3.2.3 Detection opportunities	32
3.3 Reactor neutrinos	33
3.3.1 Production and detection of reactor neutrinos	33
3.3.2 Measurements	35
3.4 Neutrinos from exploding stars: supernova neutrinos	36

3.4.1	Generic features of supernova neutrinos	37
3.4.2	Generic features of the neutrino signal	38
3.4.3	Failed explosions	39
3.4.4	Flavor conversion	40
3.4.5	Detection perspectives	40
3.5	Diffuse supernova neutrinos	41
3.5.1	Basic estimate	41
3.5.2	Redshift integral	42
3.5.3	Cosmic core-collapse rate	43
3.5.4	Average emission spectrum	44
3.5.5	Detection perspectives	45
4	High-energy neutrinos	47
4.1	Atmospheric neutrinos	47
4.1.1	Cosmic rays	48
4.1.2	Conventional atmospheric neutrinos	49
4.1.3	Prompt atmospheric neutrinos	50
4.1.4	Atmospheric neutrinos: predictions and observations	51
4.1.5	Solar atmospheric neutrinos	52
4.2	High-energy astrophysical neutrinos	53
4.2.1	Introduction	53
4.2.2	Detection and multi-messenger constraints	55
4.3	Astrophysical sources of high-energy neutrinos	56
4.3.1	Star-forming galaxies	57
4.3.2	Gamma-ray bursts	58
4.3.3	Blazars	59
4.3.4	Cosmogenic neutrinos	62
5	Filling a gap in the GUNS: solar keV neutrino emission	65
5.1	General features of the thermal flux from the Sun	65
5.2	Plasmon decay	68
5.2.1	Matrix element	68
5.2.2	Nonrelativistic limit	69
5.2.3	Decay rate and spectrum	70
5.2.4	Thermal emission spectrum	71
5.2.5	Compton pole process?	73
5.2.6	Solar neutrino flux	74
5.3	Photo production	76
5.3.1	Matrix element and decay rate	76
5.3.2	Correlation effects	77
5.3.3	Solar neutrino flux	79
5.4	Bremsstrahlung	80
5.4.1	Matrix element	80
5.4.2	Emission rate	82
5.4.3	Photon and axion emission	83

5.4.4	Medium response function and screening effects	84
5.4.5	Electron-electron bremsstrahlung	86
5.4.6	Solar neutrino flux	87
5.4.7	Beyond the Born approximation	87
5.5	Free-bound and bound-bound transitions	89
5.6	Solar neutrino flux at Earth	91
5.6.1	Flavor-dependent fluxes	91
5.6.2	Including flavor mixing	92
6	Distinguishing Dirac and Majorana neutrinos by their gravi-majoron decays	95
6.1	Differences to previous majoron-like models	96
6.1.1	Dirac or Majorana neutrino nature	96
6.1.2	Late neutrinoless Universe	97
6.1.3	Stellar and laboratory bounds	98
6.2	Neutrino decay rate	99
6.2.1	Matrix element for the neutrino decay	99
6.2.2	Differential rate	101
6.3	Constraints and detection opportunities	104
6.3.1	Solar, atmospheric, and long-baseline neutrinos	104
6.3.2	IceCube and supernova neutrinos	106
7	Axionlike particle detection with multi-messenger astronomy	107
7.1	Introduction	107
7.2	Flux from axionlike particle decay	108
7.2.1	ALP cold dark matter	111
7.2.2	ALP warm dark matter	111
7.3	Anisotropy constraints	114
7.4	Star cooling constraints	117
7.5	Gamma-ray attenuation	118
7.6	A check: consistency with blazar observations	119
8	Conclusions	121
A	Neutrino Mass Matrix	125
B	Neutrino Mixing in Matter	129
C	Standard solar model	135
	Bibliography	139

List of abbreviations

AGN	Active galactic nuclei
ALP	Axionlike particle
BBN	Big Bang nucleosynthesis
BH	Black hole
BSE	Bulk silicate Earth
BSM	Beyond the Standard Model
CDM	Cold dark matter
CIB	Cosmic infrared background
CL	Confidence level
CMB	Cosmic microwave background
CNB	Cosmic neutrino background
DM	Dark matter
DSNB	Diffuse supernova neutrino background
EBL	Extragalactic background light
EC	Electron capture
EHE	Extremely high energy
FSRQ	Flat spectrum radio quasar
GRB	Gamma-ray burst
GUNS	Grand unified neutrino spectrum
HPE	Heat producing elements
IGRB	Isotropic gamma-ray background
ND	Non-degenerate
NS	Neutron star
PNS	Proto-neutron star
PREM	Preliminary reference Earth model
SM	Standard Model
SN	Supernova
SN _u	Supernova unit
SSM	Standard (or simplified) solar model
TNU	Terrestrial neutrino unit
UHECR	Ultra-high-energy cosmic rays
WDM	Warm dark matter
WIMP	Weakly interactive massive particle

Chapter 1

Introduction: grand unified neutrino spectrum at Earth

Ever since the unification of phenomena ranging from falling apples to the motion of planets by Isaac Newton, the sky has been a fundamental tool to investigate fundamental physics. To put it in the words of Arthur Eddington, we hit “the road to a knowledge of the stars [...] through the atom; and important knowledge of the atom has been reached through the stars.” Moreover, many centuries have passed from Galileo Galilei’s invention of the telescope, and a huge advancement in observations has taken place. In our epoch of multi-messenger astronomy, the Universe is no longer explored with electromagnetic radiation alone, but in addition to cosmic rays, neutrinos and gravitational waves are becoming crucial astrophysical probes. While the age of gravitational-wave detection has only begun, neutrino astronomy has evolved from modest beginnings in the late 1960s with first detections of atmospheric and solar neutrinos to a main-stream effort. Today, a vast array of experiments observes the neutrino sky over a large range of energies.

Neutrinos are special in this regard because questions about their internal properties were on the table almost immediately after the first observation of solar neutrinos. The daring interpretation of the observed deficit in terms of flavor oscillations eventually proved correct. Today this effect is a standard ingredient to interpret neutrino measurements from practically any source. While some parameters of the neutrino mixing matrix remain to be settled (the mass ordering and the CP-violating phase), it is probably fair to say that in neutrino astronomy today the focus is on the sources and less on properties of the radiation. Of course, there is always room for surprises and new discoveries. The goal of this thesis is to search for such surprises.

The thesis is roughly divided into two parts. In the first part, I will present a summary of neutrino astronomy for different energy ranges. The different contributions can be thought as part of what one could call the *grand unified neutrino spectrum* (GUNS), borrowing the terminology from Ted Ressel and Michael Turner’s seminal *grand unified photon spectrum* [1]. This is the neutrino and antineutrino background at Earth from the cosmic neutrino background in the meV range to the highest-energy cosmic neutrinos at PeV (10^{15} eV) energies. While Chapters 2,

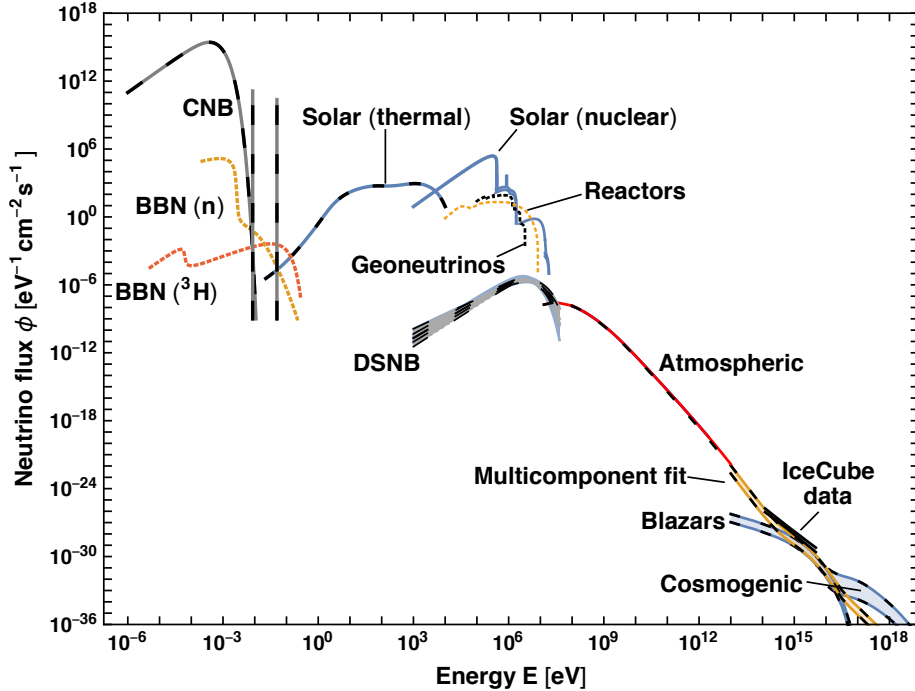


Figure 1.1: Grand Unified Neutrino Spectrum at Earth. Each flux is the sum of all the flavors. Neutrinos are represented with solid lines, antineutrinos with dashed lines; dashed lines are superimposed on solid lines for sources of both neutrinos and antineutrinos. Line sources are in units of $\text{cm}^{-2}\text{s}^{-1}$.

3 and 4 can be minimally thought of as an updated and annotated version of the traditional GUNS plot, ideally they serve as a compact resource to get a first sense in particular of different parts of the spectrum. The large range of energies and the very different types of sources and detectors makes it difficult to stay abreast of the developments in the entire field of neutrino astronomy; this is why these Chapters will be collected in a review to be published soon [2].

I will show the dominant sources of neutrinos in the low-energy range, namely the cosmic neutrino background and the decay of elements during big bang nucleosynthesis in Chapter 2. Though produced via different physical mechanism (neutrino decoupling and nuclear decays) their energy is comparable and small, and they can both be considered a signal for early-universe phenomena.

Chapter 3 is a *résumé* for the higher energy range, where neutrinos are dominantly produced by MeV processes. Sources include the Earth, the Sun, reactors and stellar collapses, which could be exploding or failed supernovae, and could be observed either in a single nearby event or through diffuse events (the so called diffuse supernova neutrino background).

Other sources of neutrinos in the high-energy range include atmospheric processes, in which neutrinos are produced by cosmic ray interactions in the atmosphere, and other unidentified astrophysical sources which produce the flux detected by neutrino telescopes. Some of these high-energy astrophysical phenomena are described, including star-forming galaxies, gamma-ray burst, and blazars. These will be the topics of Chapter 4.

Of course, there can always be some additional sources contributing to the GUNS; in Chapter 5 we turn to an analysis of the previously overlooked flux of solar neutrinos produced by thermal processes, which fills a gap in the literature. I will calculate the solar neutrino and antineutrino flux in the keV energy range. The dominant thermal source processes are photo production, bremsstrahlung, plasmon decay, and neutrino emission in free-bound and bound-bound transitions of partially ionized elements heavier than hydrogen and helium. These latter processes dominate in the energy range of a few keV and thus carry information about the solar metallicity. To calculate their rate one can use libraries of monochromatic photon radiative opacities in analogy to a previous calculation of solar axion emission. Our overall flux spectrum and many details differ significantly from previous works. While this low-energy flux is not measurable with present-day technology, it could become a significant background for future direct searches for keV-mass sterile neutrino dark matter. Chapter 5 is a paradigmatic example of how neutrinos can be at the same time a signal (for solar physics studies) and a background (for sterile neutrino searches). Moreover, we will see how the Sun, and more generally other stars, can be laboratories for particle physics: this is another *fil rouge* of this thesis.

Astrophysical and terrestrial neutrino fluxes can be modified by any number of nonstandard effects, including mixing with hypothetical sterile neutrinos, large nonstandard interactions, spin-flavor oscillations by large nonstandard magnetic dipole moments, decays and annihilation into majoron-like bosons, for the CNB large primordial asymmetries and other novel early-universe phenomena, or entirely new sources such as dark-matter annihilation in the Sun or Earth. In the second part of the thesis I will show specific examples of how neutrino astronomy can be a tool to explore fundamental particle physics. Chapter 6 is devoted to the exploration of a model in which neutrinos may acquire small Dirac or Majorana masses by new low-energy physics in terms of the chiral gravitational anomaly. This model predicts fast neutrino decays to neutrinos or antineutrinos accompanied by gravi-majorons, pseudoscalar Nambu-Goldstone bosons. The final-state neutrino and antineutrino distributions differ depending on the Dirac or Majorana mass of the initial state. This opens a channel for distinguishing these cases. I will show how to put strong bounds on the decay of the heaviest neutrino to a light pseudoscalar using data from experiments searching for antineutrino appearance from the Sun.

Blazars, discussed in Chapter 4, are one of the main ingredients of Chapter 7, where I carry out a multi-messenger, multi-wavelength study with the help of the infrared background radiation, the observation of the gamma-ray flux and neutrinos. Here, I identify possible tensions between the expected fluxes of photons and neutrinos and propose as an explanation for these astrophysical observations the existence of

an axionlike particle. The first measurement of the diffuse background spectrum in the infrared range from the CIBER experiment has indeed revealed a significant excess of the cosmic infrared background radiation compared to the theoretically expected spectrum. We will see that such an axionlike particle scenario is not excluded by anisotropy measurements nor by stellar cooling arguments. Furthermore, the increased EBL attenuates the diffuse TeV gamma-ray flux and alleviates the tension between the detected neutrino and gamma ray fluxes, connected through multi-messenger arguments. Once more, neutrinos are shown to be an interesting tool to explore models beyond the Standard Model.

Finally, Chapter 8 is a summary of what we can learn with neutrinos from cosmological and astrophysical observations, both in the realm of macroscopic physics as well as in the one of fundamental particle physics.

Cosmological neutrinos¹

Low-energy neutrino astronomy has long been a great tool to investigate particle physics. As an example, the observation of solar neutrinos, which will be discussed in the next Chapter, allowed us to infer the existence of a neutrino mass term. Though the non-zero mass of neutrinos is usually relevant only because of their oscillation, there is an important exception, namely, the cosmic neutrino background (CNB). This component of the GUNS is very peculiar in this regard, since massive neutrinos are detected as a cold relic rather than like a radiation component. In Sec. 2.1 we begin with the CNB, discussing primarily the impact of neutrino masses. CNB is a fundamental feature of the early universe evolution, and its future detection will help us to better understand a plethora of cosmological phenomena, from the primordial synthesis of elements to the anisotropies of the cosmic microwave background (CMB). At the moment, however, we still lack a direct signature of the CNB, that only a laboratory detection experiment could provide.

At slightly larger energies other components dominate the neutrino flux. In Sec. 2.2 we turn to BBN neutrinos, which form a small but dominant contribution at energies just above the CNB. This very recently recognized flux derives from neutron and triton decays, $n \rightarrow p + e^- + \bar{\nu}_e$ and ${}^3\text{H} \rightarrow {}^3\text{He} + e^- + \bar{\nu}_e$, that are left over from big-bang nucleosynthesis (BBN). Analogously to the CNB, the observations of these antineutrinos would open a new window on the early Universe processes.

2.1 Cosmic neutrino background

The cosmic neutrino background is a relic from the early universe when it was about 1 sec old. It consists today of about 112 cm^{-3} neutrinos plus antineutrinos per flavor and is the largest neutrino density at Earth, yet it has never been measured. If neutrinos were massless, the CNB would be blackbody radiation at $T_\nu = 1.945 \text{ K} = 0.168 \text{ meV}$. However, the mass differences implied by flavor oscillation data show that at least two mass eigenstates must be nonrelativistic today, providing a dark-matter

¹This Chapter closely follows the discussion of E. Vitagliano, I. Tamborra and G. Raffelt, “Grand unified neutrino spectrum at Earth,” work in progress [2].

component instead of radiation. The CNB and its possible detection is a topic tightly interwoven with the question of the absolute scale of neutrino masses and their Dirac vs. Majorana nature.

2.1.1 Standard properties of the CNB

Cosmic neutrinos [3–6] are a thermal relic from the hot early universe, in analogy to the cosmic microwave background (CMB). At cosmic temperature T above a few MeV, photons, leptons and nucleons are in thermal equilibrium so that neutrinos follow a Fermi-Dirac distribution. If the lepton-number asymmetry in neutrinos is comparable to that in charged leptons or to the primordial baryon asymmetry, i.e., of the order of 10^{-9} , their chemical potential is negligibly small.

The true origin of primordial particle asymmetries remains unknown, but one particularly attractive scenario is leptogenesis, which can be directly connected to the origin of neutrino masses [7–9]. There exist many variations of leptogenesis, but its generic structure suggests sub-eV neutrino Majorana masses. In this sense, everything that exists in the universe today may trace its fundamental origin to neutrino Majorana masses.

Much later in the cosmic evolution, at $T \sim 1$ MeV, neutrinos freeze out in that their interaction rates become slow compared to the Hubble expansion, but they continue to follow a Fermi-Dirac distribution at a common T because, for essentially massless neutrinos, the distribution is kinematically cooled by cosmic expansion. Around $T \sim 0.1$ MeV, electrons and positrons disappear, heating photons relative to neutrinos. In the adiabatic limit, one finds that afterwards $T_\nu = (4/11)^{1/3} T_\gamma$. Based on the present-day value $T_{\text{CMB}} = 2.725$ K one finds $T_\nu = 1.945$ K today.

The radiation density after e^+e^- disappearance is provided by photons and neutrinos and is usually expressed as

$$\rho_{\text{rad}} = \left[1 + N_{\text{eff}} \frac{7}{8} \left(\frac{4}{11} \right)^{4/3} \right] \rho_\gamma, \quad (2.1.1)$$

where N_{eff} , the effective number of thermally excited neutrino degrees of freedom, is a way to parameterize ρ_{rad} . The standard value is $N_{\text{eff}} = 3.045$ [10], where the deviation from 3 arises from residual neutrino heating by e^+e^- annihilation and other small corrections. (Other authors find $N_{\text{eff}} = 3.044$ [11] and 3.052 [12].) Both big-bang nucleosynthesis and cosmological data, notably of the CMB angular power spectrum measured by Planck, confirm N_{eff} within $\sim 10\%$ errors [6, 13–15].

While leptogenesis in the early universe is directly connected to the origin of neutrino masses, they play no role in the subsequent cosmic evolution. In particular, sub-eV masses are so small that helicity-changing scattering rates have no practical effect. If neutrino masses are of Majorana type and thus violate lepton number, any primordial asymmetry would remain conserved, i.e., helicity plays the role of lepton number and allows for a chemical potential. In the Dirac case, the same reasoning implies that the sterile partners will not be thermally excited. Therefore, the standard CNB will be the same for both types of neutrino masses.

Leptogenesis is not proven and one may speculate about large primordial neutrino-antineutrino asymmetries in one or all flavors. In this case flavor oscillations would essentially equilibrate the neutrino distributions before or around thermal freeze-out at $T \sim 1$ MeV so that, in particular, the ν_e chemical potential would be representative of that for any flavor [16, 17]. It is strongly constrained by big-bang nucleosynthesis and its impact on β equilibrium through reactions of the type $p + e^- \leftrightarrow n + \nu_e$. Moreover, a large neutrino asymmetry would enhance N_{eff} . Overall, a possible neutrino chemical potential, common to all flavors, is constrained by $|\mu_\nu/T| \lesssim 0.1$ [17, 18], allowing at most for a modest modification of the radiation density in the CNB.

2.1.2 Neutrinos as hot dark matter

Flavor oscillation data reveal the squared-mass differences discussed in Appendix A. They imply a minimal neutrino mass spectrum

$$m_1 = 0, \quad m_2 = 8.6 \text{ meV}, \quad m_3 = 50 \text{ meV}. \quad (2.1.2)$$

While normal mass ordering is favored by global fits, it could also be inverted ($m_3 < m_1 < m_2$) and there could be a common offset from zero. The value of the smallest neutrino mass remains a key open question.

In view of $T_\nu = 0.168$ meV for massless neutrinos, at least two mass eigenstates are dark matter today. Indeed, cosmological data provide restrictive limits on the hot dark matter fraction, implying 95% C.L. limits on $\sum m_\nu$ in the range 0.11–0.68 eV, depending on the used data sets and assumed cosmological model [6, 14, 15]. Near-future surveys should be sensitive enough to actually provide a lower limit [6, 19], i.e., a neutrino-mass detection perhaps even on the level of the minimal mass spectrum of Eq. (2.1.2).

Ongoing laboratory searches for neutrino masses include, in particular, the KATRIN experiment [20] to measure the detailed electron endpoint spectrum in tritium β decay. The neutrino-mass sensitivity reaches about 0.2 eV for the common mass scale, i.e., a detection would imply a significant tension with cosmological limits and thus point to a nonstandard CNB or to other issues with standard cosmology.

2.1.3 Spectrum at Earth

Which neutrino spectrum would be expected at Earth and should be shown on the GUNS plot? For neutrinos with mass, not the energy but the momentum is redshifted by cosmic expansion, so the phase-space occupation at redshift z for free-streaming neutrinos is

$$f_\nu(p) = \frac{1}{e^{p/T_z} + 1}, \quad (2.1.3)$$

where $T_z = T_\nu(1+z)$ and $T_\nu = 1.945$ K is today's temperature of hypothetical massless neutrinos. The present-day number density for one species of ν or $\bar{\nu}$, differential relative to momentum, is therefore

$$\frac{dn_\nu}{dp} = \frac{1}{2\pi^2} \frac{p^2}{e^{p/T_\nu} + 1}. \quad (2.1.4)$$

Integration provides $n_\nu = 56 \text{ cm}^{-3}$ as mentioned earlier.

However, expressed as an isotropic flux, perhaps for a detection experiment, one needs to include the velocity p/E with $E = \sqrt{p^2 + m_i^2}$, where m_i is one of the mass eigenstates $i = 1, 2$ or 3 . Therefore, the isotropic differential flux today is

$$\frac{d\Phi_\nu}{dp} = \frac{p}{E} \frac{dn_\nu}{dp} = \frac{1}{2\pi^2} \frac{p^3}{\sqrt{p^2 + m_i^2}} \frac{1}{e^{p/T_\nu} + 1}. \quad (2.1.5)$$

In Fig. 2.1 I show this flux for our reference mass spectrum given in Eq. (2.1.2).

On the other hand, for plotting the GUNS, the spectrum in terms of energy is more useful. In this case we need to include a Jacobian $dp/dE = E/p$ that cancels the velocity factor so that

$$\frac{d\Phi_\nu}{dE} = \frac{p}{E} \frac{dn_\nu}{dE} = \frac{1}{2\pi^2} \frac{E^2 - m_i^2}{e^{\sqrt{E^2 - m_i^2}/T_\nu} + 1}. \quad (2.1.6)$$

The maximum of this function does not depend on m_i and is

$$2.70 \times 10^{12} \text{ cm}^{-2} \text{ s}^{-1} \text{ meV}^{-1}.$$

The energy spectrum for our reference neutrino masses is shown in Fig. 2.2, where one can see that for larger masses it is tightly concentrated at $E \gtrsim m_i$. Traditional GUNS plots [21, 22] apply only to massless neutrinos.

These results ignore that the Earth is located in the gravitational potential of the Milky Way. Beginning with the momentum distribution of Eq. (2.1.4) we find for the average of the velocity $v = p/E$

$$\langle v \rangle = \frac{2700 \zeta_5}{7\pi^4} \frac{T}{m} + \mathcal{O}\left(\frac{T}{m}\right)^3 \approx 4.106 \frac{T}{m}. \quad (2.1.7)$$

For $T = 0.168 \text{ meV}$ and $m = 50 \text{ meV}$ this is $\langle v \rangle = 1.38 \times 10^{-2}$, significantly larger than the galactic virial velocity of about 10^{-3} . Therefore, gravitational clustering is a

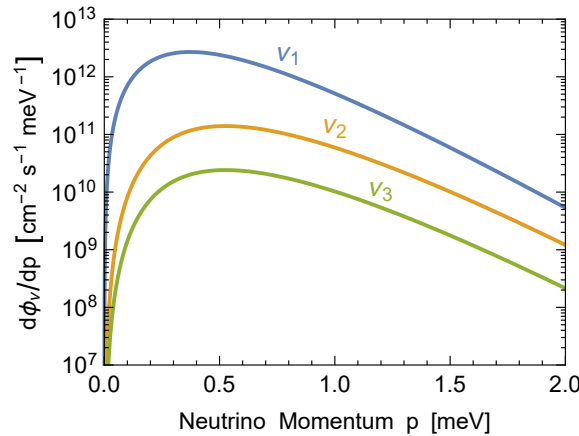


Figure 2.1: Isotropic ν or $\bar{\nu}$ differential flux today, $d\Phi_\nu/dp$, for neutrinos with mass as given in Eq. (2.1.5). The different curves correspond to our reference mass spectrum of Eq. (2.1.2).

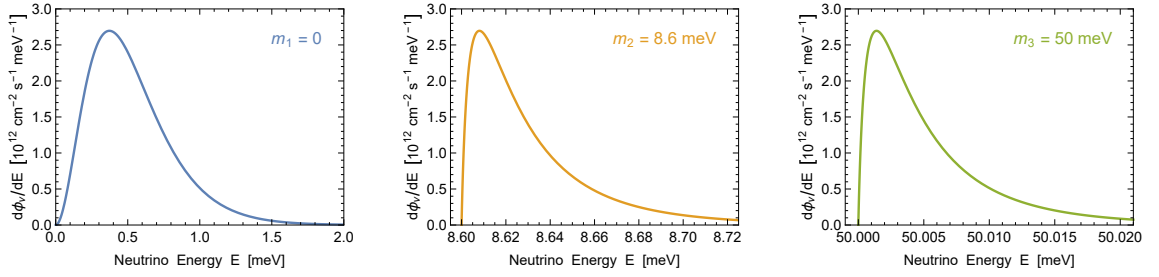


Figure 2.2: Neutrino differential flux $d\Phi_\nu/dE$ according to Eq. (2.1.6) for our reference mass spectrum of Eq. (2.1.2). The maximum flux does not depend on m_ν and is $2.70 \times 10^{12} \text{ cm}^{-2} \text{ s}^{-1} \text{ meV}^{-1}$.

small effect [23,24] and our momentum and energy distributions remain approximately valid if neutrino masses are as small as we have assumed.

In summary, the local number and energy density of one CNB mass eigenstate of neutrinos plus antineutrinos are

$$n_{\nu\bar{\nu}} = 112 \text{ cm}^{-3}, \quad (2.1.8a)$$

$$\rho_{\nu\bar{\nu}} = 59.2 \text{ meV cm}^{-3} \quad \text{for } m_\nu \ll T_\nu, \quad (2.1.8b)$$

$$\rho_{\nu\bar{\nu}} = 112 \text{ meV cm}^{-3} \frac{m_\nu}{\text{meV}} \quad \text{for } m_\nu \gg T_\nu, \quad (2.1.8c)$$

ignoring small clustering effects in the galaxy.

2.1.4 Detection perspectives

Directly measuring the CNB remains extremely challenging [25–27]. Those ideas based on the electroweak potential on electrons caused by the cosmic neutrino sea [28], an $\mathcal{O}(G_F)$ effect, depend on the net lepton number in neutrinos which today we know cannot be large as explained earlier and would also be washed out in the limit of nonrelativistic neutrinos.

At $\mathcal{O}(G_F^2)$ one can also consider mechanical forces on macroscopic bodies by neutrino scattering and the annual modulation caused by the Earth’s motion in the neutrino wind [29,30], but the experimental realization seems implausible with the available Cavendish-like balances technology. The results are not encouraging also for similar concepts based on interferometers [31].

Another idea for the distant future proposes radiative atomic emission of a neutrino pair [32]. The CNB would affect this process by Pauli phase-space blocking.

Extremely high-energy (EHE) neutrinos, produced as cosmic-ray secondaries or from ultra-heavy particle decay or cosmic strings, would be absorbed by the CNB, the process being resonant if the CM energy matches the Z^0 mass [33]. For now there is no evidence for EHE neutrinos in the required energy range beyond 10^{20} eV so that absorption dips cannot yet be looked for [25].

Perhaps the most realistic approach uses inverse β decay [34–38], notably on tritium, $\nu_e + \text{H}^3 \rightarrow \text{He}^3 + e^-$, which is currently pursued by the PTOLEMY project [39,40]. However, our reference scenario with the mass spectrum given in Eq. (2.1.2) is particularly difficult because ν_3 has the smallest ν_e admixture of all mass eigenstates.

On the other hand, if the mass spectrum is inverted and/or quasi degenerate, the detection opportunities may be more realistic. Such an experiment may also be able to distinguish Dirac from Majorana neutrinos [36] and place constraints on nonstandard neutrino couplings [37]. Moreover, the polarization of the target might achieve directionality [38].

The properties of the CNB, the search for the neutrino mass scale, and the Dirac vs. Majorana question, remain at the frontier of particle cosmology and neutrino physics. Moreover, while neutrinos are but a small dark-matter component, detecting the CNB would be a first step in the future field of dark-matter astronomy.

2.2 Neutrinos from big-bang nucleosynthesis

During its first few minutes, the universe produces the observed light elements. Subsequent decays of neutrons ($n \rightarrow p + e + \bar{\nu}_e$) and tritons (${}^3\text{H} \rightarrow {}^3\text{He} + e + \bar{\nu}_e$) produce a very small $\bar{\nu}_e$ flux, which however dominates the GUNS in the gap between the CNB and thermal solar neutrinos roughly for $E_\nu = 10\text{--}100$ meV. While a detection is currently out of the question, it would provide a direct observational window to primordial nucleosynthesis.

2.2.1 Primordial nucleosynthesis

Big-bang nucleosynthesis of the light elements is one of the pillars of cosmology [13, 41–44] and historically has led to a prediction of the CMB long before it was actually detected [45, 46]. In the early universe, protons and neutrons are in β equilibrium, so their relative abundance is $n/p = \exp(-\Delta m/T)$ with $\Delta m = 1.293$ MeV their mass difference. Weak interactions freeze out about 1 s after the big bang when $T \approx 1$ MeV, leaving $n/p \approx 1/6$. Nuclei form only 5 min later when T falls below 60 keV and the large number of thermal photons no longer keeps nuclei dissociated. Neutrons decay, but their lifetime of 880 s leaves about $n/p \approx 1/7$ at that point. Subsequently most neutrons end up in ${}^4\text{He}$, leaving the famous primordial helium mass fraction of 25%.

In detail, one has to solve a nuclear reaction network in the expanding universe and finds the evolution of light isotopes as shown in Fig. 2.3, where the unstable isotopes are shown in color. Besides the nuclear-physics input, the result depends on the cosmic baryon fraction $\eta = n_B/n_\gamma$. Assuming $\eta = 6.23 \times 10^{-10}$, chosen for the example of Fig. 2.3 and the density $n_\gamma = 411 \text{ cm}^{-3}$ of CMB photons, the baryon density is $n_B = 2.56 \times 10^{-7} \text{ cm}^{-3}$. (The 95% C.L. range for n_B is 2.4–2.7 in these units [47].) Of particular interest will be the unstable but long-lived isotopes tritium and ${}^7\text{Be}$ for which Fig. 2.3 shows final mass fractions 1.4×10^{-7} and 3.1×10^{-9} , corresponding to

$$n_{\text{T}} = 1.2 \times 10^{-14} \text{ cm}^{-3}, \quad (2.2.1a)$$

$$n_{\text{Be}7} = 1.1 \times 10^{-16} \text{ cm}^{-3} \quad (2.2.1b)$$

in terms of a present-day number density.

2.2.2 Neutrinos from decaying light isotopes

The isotopes shown in color in Fig. 2.3 are β unstable and thus produce a small cosmic $\bar{\nu}_e$ or ν_e density which is very much smaller than the CNB density given in Eq. (2.1.8), but shows up at larger energies because of less redshifting due to late decays [48, 49]. Ignoring for now the issues of neutrino masses and flavor conversion, the resulting present-day number densities are shown in Fig. 2.4 in comparison with the CNB (Sec. 2.1) and the low-energy tail of thermal solar neutrinos (Chapter 5). These two sources produce $\nu\bar{\nu}$ pairs of all flavors, so their number density is equal for

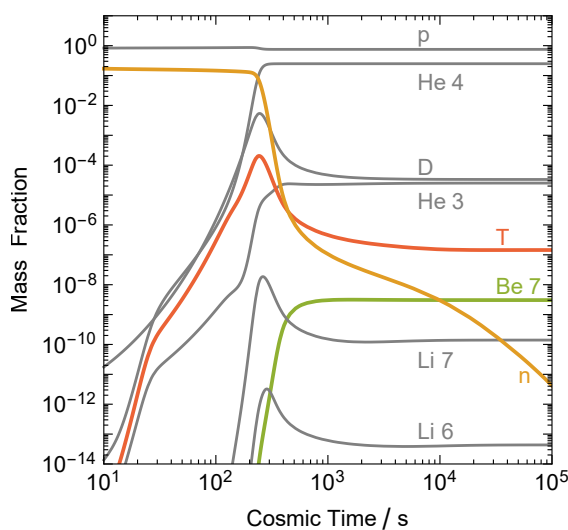


Figure 2.3: Evolution of light-element abundances in the early universe. (Plot was adapted from http://cococubed.asu.edu/code_pages/net_bigbang.shtml, where $\eta = 6.23 \times 10^{-10}$ and $H_0 = 70.5 \text{ km s}^{-1} \text{ Mpc}^{-1}$ was used.)

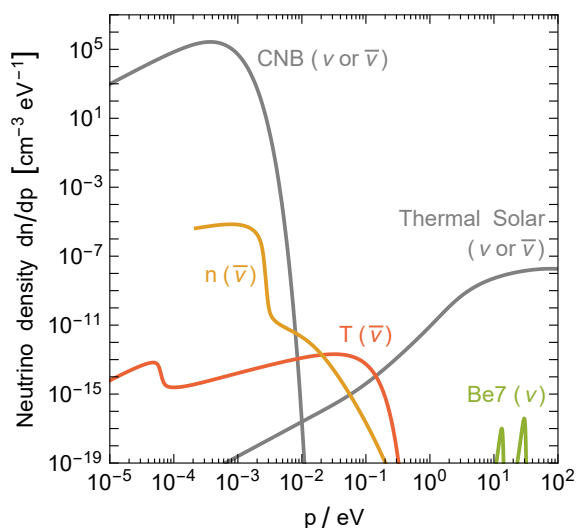


Figure 2.4: Density of low-energy neutrinos, taken to be massless ($p = E$). The CNB and thermal solar neutrinos include all flavors, but only ν or $\bar{\nu}$. Colored lines are BBN neutrinos: $\bar{\nu}_e$ from n and T decay and ν_e from ${}^7\text{Be}$ electron capture.

ν and $\bar{\nu}$. In Fig. 2.4 the all-flavor ν density of these sources is shown, equal to that for $\bar{\nu}$, to compare with either the ν or $\bar{\nu}$ density of BBN neutrinos. The low-energy tail of traditional solar ν_e from nuclear reactions (Sec. 3.1) and of the $\bar{\nu}_e$ geoneutrino (Sec. 3.2) and reactor fluxes (Sec. 3.3) are all very much smaller than the solar thermal ν or $\bar{\nu}$ flux. One concludes that the BBN neutrinos ($\bar{\nu}_e$) from later neutron (n) and tritium (T) decays produce the dominant density in the valley between the CNB and thermal solar neutrinos around neutrino energies of 10–200 meV. Of course, a detection of this flux is out of the reach with present-day technology.

Beryllium recombination

Considering the individual sources in more detail, we begin with ${}^7\text{Be}$ which is produced with a much larger abundance than ${}^7\text{Li}$. Eventually it decays to ${}^7\text{Li}$ by electron capture, producing ν_e of 861.8 keV (89.6%) or 384.2 keV (10.4%), analogous to the solar ${}^7\text{Be}$ flux (Sec. 3.1). However, in the Sun free electrons are captured, so the average ν_e energy increases by a thermal amount of a few keV (Table 3.1). In the dilute plasma of the early universe, electrons are captured from bound states, which happens only at around 900 years (cosmic redshift $z_{\text{rec}} \approx 29,200$) when ${}^7\text{Be}$ atoms form. The kinetics of ${}^7\text{Be}$ recombination and decay was solved by Khatri and Sunyaev [48] who found z_{rec} to be larger by about 5000 than implied by the Saha equation. The present-day energies of the lines are 13.1 eV = 384.2 keV/($z_{\text{rec}} + 1$) and 29.5 eV = 861.8 keV/($z_{\text{rec}} + 1$), each with a full width at half maximum of 7.8%, given by the redshift profile of ${}^7\text{Be}$ recombination, i.e., 1.0 and 2.3 eV.

The ${}^7\text{Be}$ lines shown in Fig. 2.4 were extracted from Fig. 5 of Ref. [48] with two modifications. The integrated number densities in the lines should be 10.4 : 89.6 according to the branching ratio of the ${}^7\text{Be}$ decay, whereas in Ref. [48] the strength of the lower-energy line is reduced by an additional factor $(384.2/861.8)^2$ which has been undone.² Moreover, we have multiplied both lines with a factor 5.6 to arrive at the number density $n_{\text{Be}7}$ of Eq. (2.2.1). Notice that Ref. [48] cites a relative ${}^7\text{Be}$ number density at the end of BBN of around 10^{-10} , whereas their cited literature and also our Fig. 2.3 shows about 5–6 times more.

Tritium decay

BBN produces a tritium (T or ${}^3\text{H}$) abundance given in Eq. (2.2.1) which later decays with a lifetime of 17.8 years by ${}^3\text{H} \rightarrow {}^3\text{He} + e + \bar{\nu}_e$, producing the same number density of $\bar{\nu}_e$ with a spectral shape given by Eq. (3.1.2) with $E_{\text{max}} = 18.6$ keV. During radiation domination, a cosmic age of 17.8 years corresponds to a redshift of 2×10^5 , so an energy of 18.6 keV is today 90 meV, explaining the approximate $\bar{\nu}_e$ range shown in Fig. 2.4.

This spectrum was taken from Fig. 2 of Ref. [49], where pre-asymptotic tritium was also included, producing the low-energy step-like feature. The isotropic flux

²Thanks to Rishi Khatri for confirming this issue which was caused at the level of plotting by a multiplication with 384.2/861.8 instead of 861.8/384.2 to convert the high-energy line to the low-energy one. The formula for the redshifted lines given in their Sec. 4 is correct.

shown in Ref. [49] was multiplied with a factor $2/c$ to obtain our number density.³ Our integrated $\bar{\nu}_e$ density then corresponds well to the tritium density in Eq. (2.2.1).

Neutron decay

After weak-interaction freeze-out at around 1 sec, neutrons decay with a lifetime of 880 s, producing $\bar{\nu}_e$ with a spectrum given by Eq. (3.1.2) with $E_{\max} = 782$ keV. The short lifetime implies that there is no asymptotic value around the end of BBN. Notice also that the late n evolution shown in Fig. 2.4 is not explained by decay alone that would imply a much faster decline, i.e., residual nuclear reactions provide a late source of neutrons. The $\bar{\nu}_e$ number density shown in Fig. 2.4 was obtained from Ref. [49] with the same prescription that we used for tritium.

2.2.3 Neutrinos with mass

Neutrinos have sub-eV masses, so the spectrum for energies roughly below the cross-over between thermal solar and BBN neutrinos needs to be modified. For the purpose of illustration we will use the minimal masses in normal ordering of Eq. (2.1.2) with 0, 8.6, and 50 meV. Neutrinos reaching Earth will have decohered into mass eigenstates, so one needs to determine the three corresponding spectra.

The CNB consists essentially of an equal mixture of all flavors, so the probability for finding a random CNB neutrino or antineutrino in any of the mass eigenstates is

$$P_i^{\text{CNB}} = \frac{1}{3} \quad \text{for } i = 1, 2, 3. \quad (2.2.2)$$

The BBN neutrinos are produced in the e flavor, so here we use the best-fit probabilities P_{ei} given by the top row of Eq. (A.2), forcing them to add up to unity,

$$P_1^{\text{BBN}} = 0.681, \quad P_2^{\text{BBN}} = 0.297, \quad P_3^{\text{BBN}} = 0.022. \quad (2.2.3)$$

The CNB and BBN neutrinos are produced with high energies and later their momenta are redshifted by cosmic expansion. Therefore, their comoving differential number spectrum dn/dp as a function of p remains unchanged. If we interpret the horizontal axis of Fig. 2.4 as p instead of E and the vertical axis as dn/dp instead of dn/dE , the CNB and BBN curves actually do not change, except that we get three curves, one for each mass eigenstate, with the relative amplitudes of Eqs. (2.2.2) and (2.2.3).

For thermal solar neutrinos, the same argument applies to bremsstrahlung, which dominates at low energies, because the spectrum is essentially determined by phase space alone (Chapter 5). At higher energies, where our assumed small masses are not important, the mass would also enter in the matrix element and one would need an appropriate evaluation of plasmon decay.

³I thank the authors of Ref. [49] for providing a data file for this curve and for explaining the required factor. They define the flux of an isotropic gas by the number of particles passing through a 1 cm^2 disk per sec according to their Eq. (7) and following text, providing a factor $c/4$. Then they apply a factor of 2 to account for neutrinos passing from both sides.

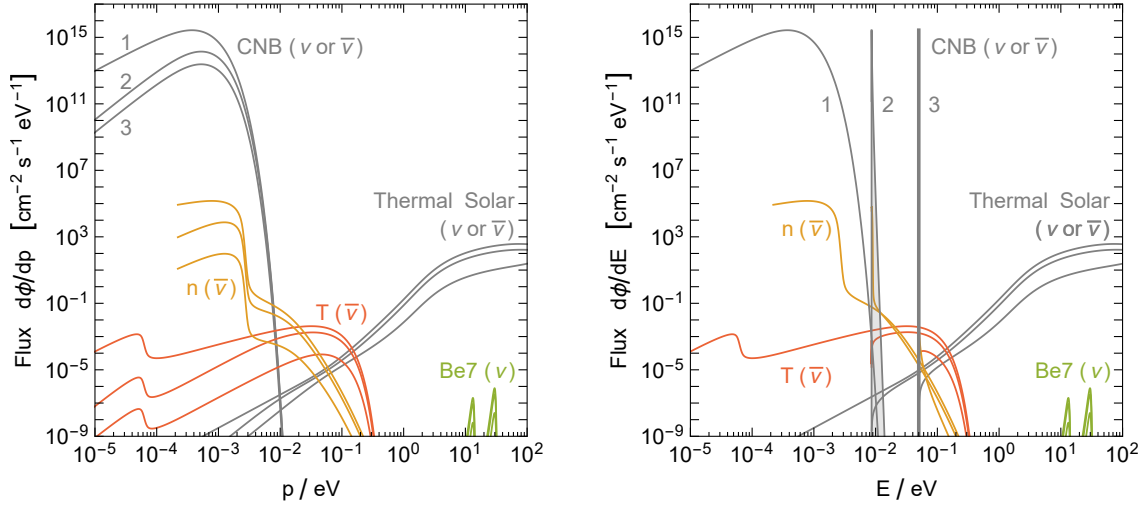


Figure 2.5: *Left*: Flux densities $d\Phi/dp$ of mass-eigenstate neutrinos for $m_i = 0, 8.6$ and 50 meV, using the probabilities of Eqs. (2.2.2). The spectra correspond to Fig. 2.4, now including a velocity factor $v_i = p/E_i$ for each mass state. *Right*: $d\Phi/dE$ as a function of E .

For experimental searches, the flux may be a more appropriate quantity. Multiplying the number density spectra of Fig. 2.4 for each p with the velocity $v_i = p/\sqrt{p^2 + m_i^2}$ provides the mass-eigenstate flux spectra $d\Phi/dp$ shown in Fig. 2.5 (left), in analogy to Fig. 2.1.

For experiments considering the absorption of neutrinos, e.g. inverse β decay on tritium, the energy E is a more appropriate variable instead of the momentum p , so I show $d\Phi/dE$ as a function of E in Fig. 2.5 (right). Notice that the velocity factor v_i is undone by a Jacobian E/p , so for example the maxima of the mass-eigenstate curves are the same for every m_i as discussed in Sec. 2.1.3 and illustrated in Fig. 2.2. Relative to the massless case of Fig. 2.4, the vertical axis is simply scaled with a factor c , whereas the curves are compressed in the horizontal direction by $p \rightarrow E = \sqrt{p^2 + m_i^2}$. Effectively one obtains narrow lines at the non-vanishing neutrino masses that are vastly dominated by the CNB. The integrated fluxes of the three mass eigenstates in either ν or $\bar{\nu}$ are

$$\Phi_1 = 1.68 \times 10^{12} \text{ cm}^{-2} \text{ s}^{-1}, \quad (2.2.4a)$$

$$\Phi_2 = 1.35 \times 10^{11} \text{ cm}^{-2} \text{ s}^{-1}, \quad (2.2.4b)$$

$$\Phi_3 = 2.32 \times 10^{10} \text{ cm}^{-2} \text{ s}^{-1}, \quad (2.2.4c)$$

where we have used Eqs. (2.1.7) and (2.1.8) of Sec. 2.1.

Astrophysical and terrestrial neutrinos⁴

We address MeV energies in this Chapter, reviewing several contributions to the GUNS which are both theoretically and experimentally well known. In Sec. 3.1 we turn to the Sun, which is especially bright in neutrinos because of its proximity, beginning with the traditional MeV-range neutrinos from nuclear reactions which produce only ν_e . In Chapter 5 we will study a new contribution in the keV range of thermally produced fluxes that are equal for ν and $\bar{\nu}$. In both cases, what exactly arrives at Earth depends on flavor conversion, and for MeV energies also whether the Sun is observed through the Earth or directly (day-night effect).

Nuclear fusion in the Sun produces only ν_e , implying that in the MeV range $\bar{\nu}_e$ fluxes, also modified by oscillations, are mostly of terrestrial origin from nuclear fission. In Sec. 3.2 I will consider geoneutrinos that predominantly come from natural radioactive decays of potassium, uranium and thorium, while in Sec. 3.3 we turn to nuclear power reactors. Both fluxes strongly depend on location so that their contributions to the GUNS are not universal.

In Sec. 3.4 we turn to the 1–100 MeV range where neutrinos from a next nearby stellar collapse, which could be an exploding or failed supernova, is one of the most exciting though rare targets. On the one hand, such sources fit poorly on the diffuse GUNS, since the most interesting information is in the detailed time profile of these few-second bursts, the range of expected distances is large and the signal depends on the viewing angle of these very asymmetric events. On the other hand, the diffuse supernova neutrino background (DSNB) from all past collapsing stellar cores in the Universe dominates in the 10–25 MeV range (Sec. 3.5). If the CNB is all hot dark matter, the DSNB is actually the largest neutrino radiation component in the Universe. It may soon be detected by the upcoming JUNO and gadolinium-enhanced Super-Kamiokande experiments, opening a completely new frontier.

⁴This Chapter closely follows the discussion of E. Vitagliano, I. Tamborra and G. Raffelt, “Grand unified neutrino spectrum at Earth,” work in progress [2].

3.1 Neutrinos from nuclear reactions in the Sun

The Sun emits 2.3% of its nuclear energy production in the form of MeV-range neutrinos. They arise from the effective fusion reaction $4p + 2e^- \rightarrow {}^4\text{He} + 2\nu_e + 26.73 \text{ MeV}$ that proceeds through several reaction chains and cycles. The history of solar neutrino measurements is tightly connected with the discovery of flavor conversion and the matter effect on neutrino dispersion. There is also a close connection to precision modeling of the Sun, leading to a new problem in the form of discrepant sound-speed profiles relative to helioseismology. This issue may well be related to the photon opacities and thus to the detailed chemical abundances in the solar core, a prime target of future neutrino precision experiments. Meanwhile, solar neutrinos are becoming a background to WIMP dark-matter searches, which in future may thus double as solar neutrino observatories.

3.1.1 The Sun as a neutrino source

The Sun produces nuclear energy by hydrogen fusion to helium that proceeds through the PP chains (exceeding 99% for solar conditions) and the rest through the CNO cycle [50–55]. For every produced ${}^4\text{He}$ nucleus, two protons need to convert to neutrons by what amounts to $p + e^- \rightarrow n + \nu_e$, i.e., two electrons disappear in the Sun and emerge as ν_e . The individual ν_e -producing reactions are listed in Table 3.1 (for more details see below) and the expected flux spectra at Earth are shown in Fig. 3.1.

The PP chains all begin with $p + p \rightarrow d + e^+ + \nu_e$, the pp reaction, which on average releases 0.267 MeV as ν_e . Including the other processes (GS98 predictions of Table 3.1) implies $\langle E_{\nu_e} \rangle = 0.312 \text{ MeV}$. The solar luminosity without neutrinos is $L_\odot = 3.828 \times 10^{33} \text{ erg s}^{-1} = 2.39 \times 10^{39} \text{ MeV s}^{-1}$, implying a solar ν_e production of $1.83 \times 10^{38} \text{ s}^{-1}$. The average distance of $1.496 \times 10^{13} \text{ cm}$ thus implies a flux, number density, and energy density at Earth of

$$\Phi_\nu = 6.51 \times 10^{10} \text{ cm}^{-2} \text{ s}^{-1}, \quad (3.1.1a)$$

$$n_\nu = 2.17 \text{ cm}^{-3}, \quad (3.1.1b)$$

$$\rho_\nu = 0.685 \text{ MeV cm}^{-3}. \quad (3.1.1c)$$

These numbers change by $\pm 3.4\%$ in the course of the year due to the ellipticity of the Earth's orbit, a variation confirmed by the Super-Kamiokande detector [56].

While this overall picture is robust, the flux spectra of those reactions with larger E_{ν_e} are particularly important for detection and flavor-oscillation physics, but are side issues for overall solar physics. Therefore, details of the production processes and of solar modeling are crucial for predicting the solar neutrino spectrum.

3.1.2 Production processes and spectra

The proton-neutron conversion required for hydrogen burning proceeds either as β^+ decay of the effective form $p \rightarrow n + e^+ + \nu_e$, producing a continuous spectrum, or as

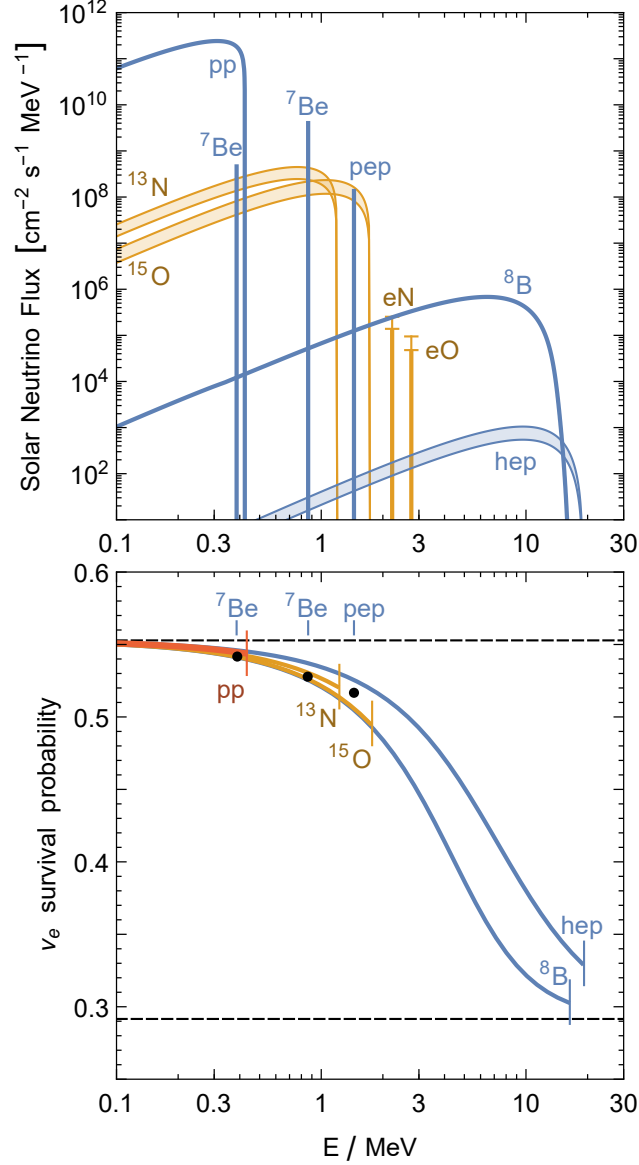


Figure 3.1: *Top panel:* Solar neutrino flux from PP chains (blue) and CNO cycle (orange). Line sources in units of $\text{cm}^{-2} \text{s}^{-1} \text{MeV}^{-1}$. PP-chain fluxes (except for hep) according to the measurements shown in Table 3.1 where the uncertainties are too small to show. For the CNO and hep fluxes the range is bracketed by the lowest AGSS09 and highest GS98 predictions. ¹⁷F is a minimal correction to the ¹⁵O flux and thus not shown. *Bottom panel:* Adiabatic ν_e survival probability due to flavor conversion (see Sec. 3.1.5) which depends on the radial distributions of the different production processes. For the eN and eO lines, these distributions have not been published. The horizontal dashed lines show the survival probability for vanishing and infinite neutrino energy.

electron capture (EC) $e^- + p \rightarrow n + \nu_e$, producing a line spectrum. The nuclear MeV energies imply a much larger final-state β^+ phase space than the initial-state phase space occupied by electrons with keV thermal energies, so the continuum fluxes tend to dominate [57].

However, line energies are larger ($+2m_e$ relative to the end point of the continuum) and lines produce a distinct detection signature [58, 59]. One particularly important case is the ${}^7\text{Be}$ line where the nuclear energy is too small for β^+ decay. Actually in 10% of all the cases this reaction proceeds through an excited state of ${}^7\text{Li}$, so there are two lines, together forming the ${}^7\text{Be}$ flux.

I neglect ${}^3\text{He} + e^- + p \rightarrow {}^4\text{He} + \nu_e$, the hep flux [57]. On the other hand, I am including the often neglected lines from EC in CNO reactions, also called ecCNO processes [60, 61]. These flux predictions were obtained by scaling the continuum fluxes [62] with the ratios provided by Stonehill et al. [60], although these are based on a different solar model. This inconsistency is very small compared with the overall uncertainty of the CNO fluxes.

The endpoint E_{max} of a continuum spectrum is given, in vacuum, by the nuclear transition energy. However, for the reactions taking place in the Sun one needs to include thermal kinetic energy of a few keV. The endpoint and average energies listed in Table 3.1 include this effect according to Bahcall [63]. For the same reason the EC lines are slightly shifted and have a thermal width of a few keV [64], which is irrelevant in practice for present-day experiments. The energies of the ecCNO lines were obtained from the listed continuum endpoints by adding $2m_e$, which agrees with Stonehill et al. [60] except for ${}^{17}\text{F}$, where they show 2.761 instead of 2.758 MeV.

Except for ${}^8\text{B}$, the continuum spectra follow from an allowed nuclear β decay, being dominated by the phase space of the final-state e^+ and ν_e . In vacuum and

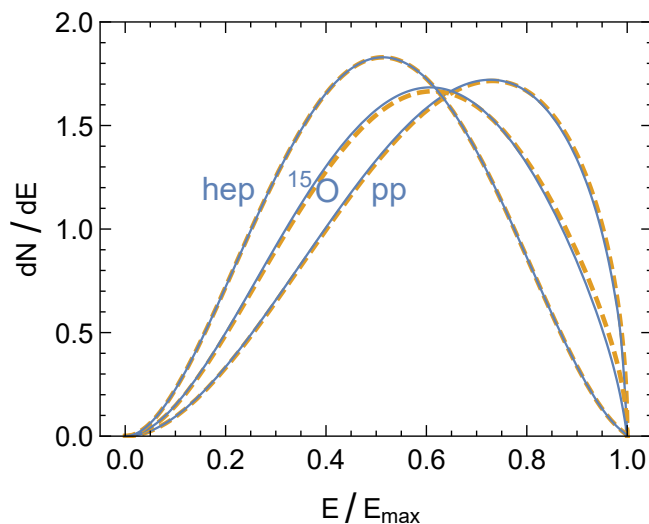


Figure 3.2: Spectra of pp, ${}^{15}\text{O}$ and hep neutrinos. The other CNO spectra are similar to ${}^{15}\text{O}$. *Solid*: Tabulated spectra according to Bahcall [63]. *Dashed*: According to Eq. (3.1.2).

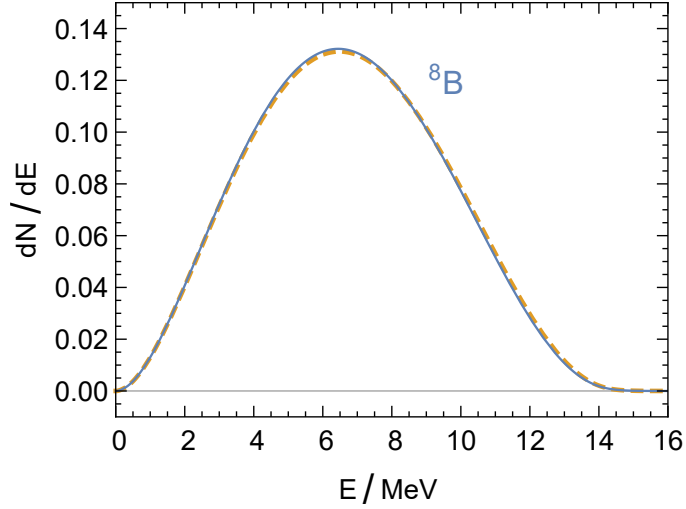


Figure 3.3: Spectrum of ${}^8\text{B}$ neutrinos. *Solid*: According to the analysis of Bahcall et al. [65]. *Dashed*: According to the analysis of Winter et al. [66].

ignoring e^+ final-state interactions it is

$$\frac{dN}{dE} \propto E^2(Q - E)\sqrt{(Q - E)^2 - m_e^2}, \quad (3.1.2)$$

where $Q = E_{\text{max}} + m_e$. In Fig. 3.2 (dashed lines) I show these spectra in normalized form for the pp and hep fluxes as well as ${}^{15}\text{O}$, which is representative of the CNO fluxes. I also show the spectra (solid lines), where final-state corrections and thermal initial-state distributions are included according to Ref. [63]. (Notice that the spectra provided on the late [John Bahcall's homepage](#) are not always exactly identical with those in Ref. [63].)

The ${}^8\text{B}$ flux is the dominant contribution in many solar neutrino experiments because it reaches to large energies and the detection cross section typically scales with E^2 , yet it is the one with the least simple spectrum. The decay ${}^8\text{B} \rightarrow {}^8\text{Be} + e^+ + \nu_e$ has no sharp cutoff because the final-state ${}^8\text{Be}$ is unstable against 2α decay. The ν_e spectrum can be inferred from the measured α and β^+ spectra. The ν_e spectrum provided by Bahcall et al. [65] is shown in Fig. 3.3 as a solid line. As a dashed line it is shown the determination of Winter et al. [66], based on a new measurement of the α spectrum.

For comparison with keV thermal neutrinos (which we will explore in Chapter 5) it is useful to consider an explicit expression for the solar flux at low energies where the pp flux strongly dominates. Using the observed total pp flux from Table 3.1, we find that an excellent approximation for the flux at Earth is

$$\frac{d\Phi_{\text{pp}}}{dE} = \frac{832.7 \times 10^{10}}{\text{cm}^2 \text{ s MeV}} \left(\frac{E}{\text{MeV}} \right)^2 \left(1 - 2.5 \frac{E}{\text{MeV}} \right). \quad (3.1.3)$$

To achieve sub-percent precision, the purely quadratic term can be used for E up to a few keV. With the next correction, the expression can be used up to 100 keV.

Table 3.1: Neutrino fluxes at Earth from different nuclear reactions in the Sun. Theoretical predictions from Vinyoles et al. [62] for models with GS98 [67] and AGSS09 [68] abundances. The predicted electron capture (EC) fluxes from the CNO cycle were obtained by scaling the β^+ -decay fluxes [60]. The neutrino endpoint energy E_{\max} and average E_{av} includes thermal energy of a few keV [63] except for the CNO-EC lines, where the given E_{av} is $E_{\max} + 2m_e$ of the corresponding β^+ process. Observed fluxes with 1σ errors from the global analysis of Bergström et al. [69].

Channel	Flux	Reaction	E_{av} MeV	E_{\max} MeV	Flux at Earth			Units
					GS98	AGSS09	Observed	
PP Chains (β^+)	Φ_{pp}	$p + p \rightarrow d + e^+ + \nu_e$	0.267	0.423	5.98 \pm 0.6%	6.03 \pm 0.5%	5.971 ^{+0.62%} _{-0.55%}	$10^{10} \text{ cm}^{-2} \text{ s}^{-1}$
	Φ_{B}	${}^8\text{B} \rightarrow {}^8\text{Be}^* + e^+ + \nu_e$	6.735 ± 0.036	~ 15	5.46 \pm 12%	4.50 \pm 12%	$5.16_{-1.7\%}^{+2.5\%}$	$10^6 \text{ cm}^{-2} \text{ s}^{-1}$
	Φ_{hep}	${}^3\text{He} + p \rightarrow {}^4\text{He} + e^+ + \nu_e$	9.628	18.778	0.80 \pm 30%	0.83 \pm 30%	$1.9_{-47\%}^{+63\%}$	$10^4 \text{ cm}^{-2} \text{ s}^{-1}$
PP Chains (EC)	Φ_{Be}	$e^- + {}^7\text{Be} \rightarrow {}^7\text{Li} + \nu_e$	0.863 (89.7%)		4.93 \pm 6%	4.50 \pm 6%	$4.80_{-4.6\%}^{+5.9\%}$	$10^9 \text{ cm}^{-2} \text{ s}^{-1}$
	Φ_{pep}	$e^- + {}^7\text{Be} \rightarrow {}^7\text{Li}^* + \nu_e$	0.386 (10.3%)		1.44 \pm 1%	1.46 \pm 0.9%	$1.448_{-0.90\%}^{+0.90\%}$	$10^8 \text{ cm}^{-2} \text{ s}^{-1}$
		$p + e^- + p \rightarrow d + \nu_e$	1.445					
CNO Cycle (β^+)	Φ_{N}	${}^{13}\text{N} \rightarrow {}^{13}\text{C} + e^+ + \nu_e$	0.706	1.198	2.78 \pm 15%	2.04 \pm 14%	< 13.7	$10^8 \text{ cm}^{-2} \text{ s}^{-1}$
	Φ_{O}	${}^{15}\text{O} \rightarrow {}^{15}\text{N} + e^+ + \nu_e$	0.996	1.732	2.05 \pm 17%	1.44 \pm 16%	< 2.8	$10^8 \text{ cm}^{-2} \text{ s}^{-1}$
	Φ_{F}	${}^{17}\text{F} \rightarrow {}^{17}\text{O} + e^+ + \nu_e$	0.998	1.736	5.29 \pm 20%	3.26 \pm 18%	< 8.5	$10^6 \text{ cm}^{-2} \text{ s}^{-1}$
CNO Cycle (EC)	Φ_{eN}	${}^{13}\text{N} + e^- \rightarrow {}^{13}\text{C} + \nu_e$	2.220		2.20 \pm 15%	1.61 \pm 14%	—	$10^5 \text{ cm}^{-2} \text{ s}^{-1}$
	Φ_{eO}	${}^{15}\text{O} + e^- \rightarrow {}^{15}\text{N} + \nu_e$	2.754		0.81 \pm 17%	0.57 \pm 16%	—	$10^5 \text{ cm}^{-2} \text{ s}^{-1}$
	Φ_{eF}	${}^{17}\text{F} + e^- \rightarrow {}^{17}\text{O} + \nu_e$	2.758		3.11 \pm 20%	1.91 \pm 18%	—	$10^3 \text{ cm}^{-2} \text{ s}^{-1}$

3.1.3 Standard solar models

The neutrino flux predictions, such as those shown in Table 3.1, depend on a detailed solar model that provides the variation of temperature, density, and chemical composition with radius. While the neutrino flux from the dominant pp reaction is largely determined by the overall luminosity, the small but experimentally dominant higher-energy fluxes depend on the branching between different terminations of the PP chains and the relative importance of the CNO cycle, all of which depends sensitively on chemical composition and temperature. For example, the ${}^8\text{B}$ flux scales approximately as T_c^{24} with solar core temperature [70] — the neutrino fluxes are sensitive solar thermometers.

The flux predictions are usually based on a Standard Solar Model (SSM) [55], although the acronym might be more appropriately interpreted as Simplified Solar Model. One assumes spherical symmetry and hydrostatic equilibrium, neglecting dynamical effects, rotation, and magnetic fields. The zero-age model is taken to be chemically homogeneous without further mass loss or gain. Energy is transported by radiation (photons) and convection. The latter is relevant only in the outer region (2% by mass or 30% by radius) and is treated phenomenologically with the

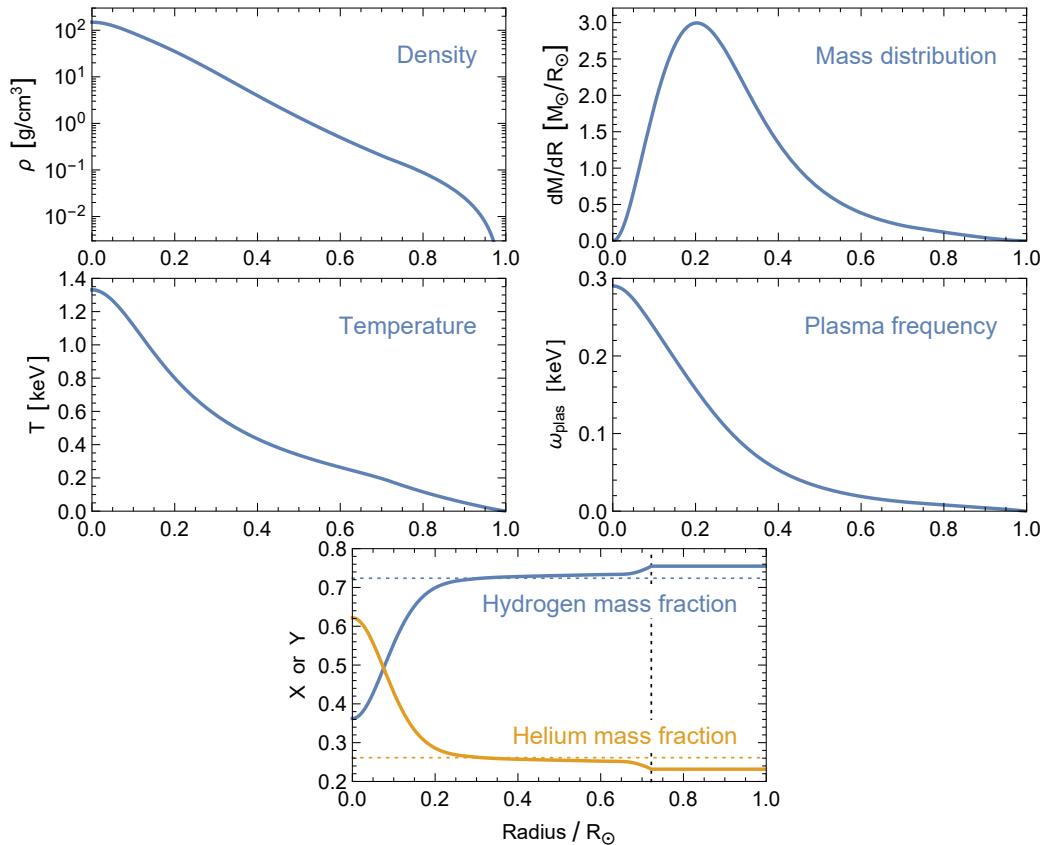


Figure 3.4: Standard Solar Model of the Barcelona group [62] with AGSS09 composition. *Bottom panel:* The vertical dotted line shows R_{CZ} , the depth of the convection zone, whereas the horizontal lines show the initial H and He mass fractions.

adjustable parameter α_{MLT} to express the mixing length in terms of the pressure scale height. Further adjustable parameters are the initial mass fractions of hydrogen, X_{ini} , helium, Y_{ini} , and “metals” (anything heavier than helium), Z_{ini} , with the constraint $X_{\text{ini}} + Y_{\text{ini}} + Z_{\text{ini}} = 1$. These parameters must be adjusted such that the evolution to the present age of $\tau_{\odot} = 4.57 \times 10^9$ years reproduces the measured luminosity $L_{\odot} = 3.8418 \times 10^{33}$ erg s⁻¹, the radius $R_{\odot} = 6.9598 \times 10^{10}$ cm, and the spectroscopically observed metal abundance at the surface, Z_{S} , relative to that of hydrogen, X_{S} . These surface abundances differ from the initial ones because of gravitational settling of heavier elements relative to lighter ones. As an example I show in Fig. 3.4 the radial variation of several solar parameters for a SMM of the Barcelona group [62].

The relative surface abundances of different elements are determined by spectroscopic measurements which agree well, for non-volatile elements, with those found in meteorites. The older standard abundances (GS98) of Grevesse and Sauval [67] were superseded in 2009 by the AGSS09 composition of Asplund, Grevesse, Sauval and Scott and updated in 2015 [68, 71–73]. The AGSS09 composition shows significantly smaller abundances of volatile elements. According to Ref. [62], the surface abundances are $Z_{\text{S}} = 0.0187 \pm 0.0013$ (GS98) and 0.0149 ± 0.0009 (AGSS09), the difference being almost entirely due to CNO elements.

The CNO abundances not only affect CNO neutrino fluxes directly, but determine the solar model through the photon opacities that regulate radiative energy transfer. Theoretical opacity calculations include OPAL [74], the Opacity Project (OP) [75], OPAS [76, 77], STAR [78], and OPLIB [79], which for solar conditions agree within 5%, but strongly depend on input abundances.

A given SSM can be tested with helioseismology that determines the sound-speed profile, the depth of the convective zone, R_{CZ} , and the surface helium abundance, Y_{S} . Ever since the first appearance of the new spectroscopic surface abundances, a problem has appeared in that these parameters deviate significantly from the solar values, whereas the old GS98 abundances had provided much better agreement. (See Table 3.2 for a comparison based on recent Barcelona models.) So while SSMs with the old GS98 abundances provide good agreement with helioseismological measurements, they disagree with the modern measured surface abundances, whereas for the AGSS09 class of models it is the other way around. There is no satisfactory solution to this conundrum, which is labelled as the “solar abundance problem,” although it is not clear if something is wrong with the abundances, the opacity calculations, other input physics, or any of the assumptions entering the SSM framework.

The PP-chains neutrino fluxes predicted by these two classes of models bracket the measurements (Table 3.1), which however do not clearly distinguish between them. A future measurement of the CNO fluxes might determine the solar-core CNO abundances and thus help to solve the “abundance problem.” While it is not assured that the two classes of models actually bracket the true case, one may speculate that the CNO fluxes might lie between the lowest AGSS09 and the largest GS98 predictions. Therefore, this range is taken to define the flux prediction shown in Fig. 3.1.

Table 3.2: Main characteristics of two Barcelona SSMs [62] with GS98 and AGSS09 abundances. R_{CZ} is the depth of the convection zone and $\langle \delta c/c \rangle$ the average deviation of the sound-speed profile relative to helioseismic measurements.

Quantity	B16-GS98	B16-AGSS09	Solar [80, 81]
Y_{S}	0.2426 ± 0.0059	0.2317 ± 0.0059	0.2485 ± 0.0035
R_{CZ}/R_{\odot}	0.7116 ± 0.0048	0.7223 ± 0.0053	0.713 ± 0.001
$\langle \delta c/c \rangle$	$0.0005^{+0.0006}_{-0.0002}$	0.0021 ± 0.001	—
α_{MLT}	2.18 ± 0.05	2.11 ± 0.05	—
Y_{ini}	0.2718 ± 0.0056	0.2613 ± 0.0055	—
Z_{ini}	0.0187 ± 0.0013	0.0149 ± 0.0009	—
Z_{S}	0.0170 ± 0.0012	0.0134 ± 0.0008	—

3.1.4 Antineutrinos

The Borexino scintillator detector has set the latest limit on the flux of solar $\bar{\nu}_e$ at Earth of $760 \text{ cm}^{-2} \text{ s}^{-1}$, assuming a spectral shape of the undistorted ^8B ν_e flux and using a threshold of 1.8 MeV [82]. This corresponds to a 90% C.L. limit on a putative $\nu_e \rightarrow \bar{\nu}_e$ transition probability of 1.3×10^{-4} for $E_{\nu} > 1.8 \text{ MeV}$.

However, in analogy to the geoneutrinos of Sec. 3.2, the Sun contains a small fraction of the long-lived isotopes ^{40}K , ^{232}Th , and ^{238}U that produce a $\bar{\nu}_e$ flux [83]. However, it is immediately obvious that at the Earth's surface, this solar flux must be much smaller than that of geoneutrinos. If the mass fraction of these isotopes were the same in the Sun and Earth and if their distributions in the Earth were spherically symmetric, the fluxes would have the proportions of M_{\odot}/D_{\odot}^2 vs. M_{\oplus}/R_{\oplus}^2 , with the solar mass M_{\odot} , its distance D_{\odot} , the Earth mass M_{\oplus} , and its radius R_{\oplus} . So the solar flux would be smaller in the same proportion as the solar gravitational field is smaller at Earth, i.e., about 6×10^{-4} times smaller.

The largest $\bar{\nu}_e$ flux comes from ^{40}K decay. The solar potassium mass fraction is around 3.5×10^{-6} [68], the relative abundance of the isotope ^{40}K is 0.012%, so the ^{40}K solar mass fraction is 4×10^{-10} , corresponding to $8 \times 10^{23} \text{ g}$ of ^{40}K in the Sun or 1.3×10^{46} atoms. With a lifetime of 1.84×10^9 years, the $\bar{\nu}_e$ luminosity is $2 \times 10^{29} \text{ s}^{-1}$ or a flux at Earth of around $100 \text{ cm}^{-2} \text{ s}^{-1}$. With a geo- $\bar{\nu}_e$ luminosity of around $2 \times 10^{25} \text{ s}^{-1}$ from potassium decay (Sec. 3.2), the average geoneutrino flux is $5 \times 10^6 \text{ cm}^{-2} \text{ s}^{-1}$ at the Earth's surface, although with large local variations.

An additional flux of higher-energy solar $\bar{\nu}_e$ comes from photo fission of heavy elements such as uranium by the 5.5 MeV photon from the solar fusion reaction $p + d \rightarrow ^3\text{He} + \gamma$ [83]. One expects a $\bar{\nu}_e$ spectrum similar to a power reactor, where the fission is caused by neutrons. However, this tiny flux of around $10^{-3} \text{ cm}^{-2} \text{ s}^{-1}$ is vastly overshadowed by reactor neutrinos.

3.1.5 Flavor conversion

While solar neutrinos are produced in the ν_e flavor, the flux at Earth shown in Fig. 3.1 (top) has a different flavor composition because of flavor conversion on the

way out of the Sun. The long distance of travel between Sun and Earth relative to the vacuum oscillation length implies that the different propagation eigenstates effectively decohere, so we can picture the neutrinos arriving at Earth to be mass eigenstates. These can be re-projected on interaction eigenstates, notably on ν_e , if the detector is flavor sensitive.

Flavor conversion of solar neutrinos is almost perfectly adiabatic and, because of the hierarchy of neutrino mass differences, well approximated by an effective two-flavor treatment. The probability of a produced ν_e to emerge at Earth in any of the three mass eigenstates is given by Eq. (B.12) and the probability to be measured as a ν_e , the survival probability, by Eq. (B.13). For the limiting case of very small E_ν , the matter effect is irrelevant and

$$P_{ee}^{\text{vac}} = \frac{1 + \cos^2 2\theta_{12}}{2} \cos^4 \theta_{13} + \sin^4 \theta_{13} = 0.533, \quad (3.1.4)$$

corresponding to the best-fit mixing parameters in normal ordering. In the other extreme of very large energy or a very large matter density, one finds

$$P_{ee}^\infty = \frac{1 - \cos 2\theta_{12}}{2} \cos^4 \theta_{13} + \sin^4 \theta_{13} = 0.292. \quad (3.1.5)$$

These extreme cases are shown as horizontal dashed lines in the lower panel of Fig. 3.1. Otherwise, P_{ee} depends on the weak potential at the point of production, so P_{ee} for a given E_ν depends on the radial source distributions in the Sun. These are shown in Fig. 3.5 according to an AGSS09 model of the Barcelona group, using the best-fit mixing parameters in normal ordering. Notice that these distributions for the EC-CNO reactions have not been provided, but would be different from the continuum processes. The survival probabilities for the different source processes are shown in the lower panel of Fig. 3.1. As we can see from the radial distributions of the ${}^8\text{B}$ and hep processes, the corresponding curves in Fig. 3.1 essentially bracket the range of survival probabilities for all processes.

While neutrinos arriving at Earth have decohered into mass eigenstates, propagation through the Earth causes flavor oscillations, producing coherent superpositions at the far end. So if the solar flux is observed through the Earth (“at night”), this small effect needs to be included. This day-night asymmetry for the ${}^8\text{B}$ flux was measured by the Super-Kamiokande detector to be [84, 85]

$$A_{\text{DN}} = \frac{\Phi_{\text{day}} - \Phi_{\text{night}}}{(\Phi_{\text{day}} + \Phi_{\text{night}})/2} = (-3.3 \pm 1.0_{\text{stat}} \pm 0.5_{\text{syst}})\%, \quad (3.1.6)$$

corresponding to a 2.9σ significance. As measured in ν_e , the Sun shines brighter at night!

The energy-dependent ν_e survival probability for ${}^8\text{B}$ neutrinos shown in the lower panel of Fig. 3.1 implies a spectral deformation of the measured flux relative to the ${}^8\text{B}$ source spectrum. The latest Super-Kamiokande analysis [85] is consistent with this effect, but also consistent with no distortion at all.

3.1.6 Observations and detection perspectives

Solar neutrino observations have a 50-year history, beginning in 1968 with the Homestake experiment [86,87], a pioneering achievement that earned Raymond Davis the Physics Nobel Prize (2002). Homestake was based on the radiochemical technique of $^{37}\text{Cl}(\nu_e, e^-)^{37}\text{Ar}$ and subsequent argon detection, registering approximately 800 solar ν_e in its roughly 25 years of data taking that ended in 1994. Since those early days, many experiments have measured solar neutrinos [88], and in particular Super-Kamiokande [85], based on elastic scattering on electrons measured by Cherenkov radiation in water, has registered around 80,000 events since 1996 and has thus become sensitive to percent-level effects. The chlorine experiment was mainly sensitive to ^8B and ^7Be neutrinos, whereas the lowest threshold achieved for the water Cherenkov technique is around 4 MeV and thus registers only ^8B neutrinos.

Historically, the second experiment to measure solar neutrinos (1987–1995) was Kamiokande II and III in Japan [89,90], a 2140 ton water Cherenkov detector, which at first however registered the neutrino burst from SN 1987A on 23 February 1987, feats which earned Masatoshi Koshiba the Physics Nobel Prize (2002).

The lower-energy fluxes, and notably the dominant pp neutrinos, became accessible with gallium radiochemical detectors using $^{71}\text{Ga}(\nu_e, e^-)^{71}\text{Ge}$. GALLEX

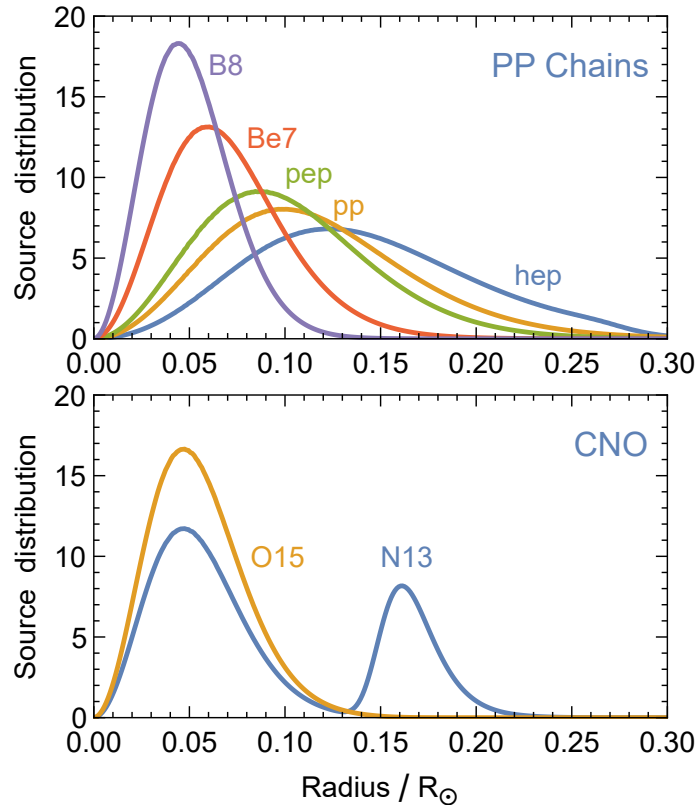


Figure 3.5: Normalised distribution of neutrino production for the indicated source reactions according to the SSM of the Barcelona group [62] with AGSS09 composition. In the CNO cycle, the ^{17}F distribution is very similar to that of ^{15}O .

(1991–1997) and subsequently GNO (1998–2003), using 30 tons of gallium, were installed in the Italian Gran Sasso National Laboratory [91–93]. The SAGE experiment in the Russian Baksan laboratory, using 50 tons of metallic gallium, has taken data since 1989 with published results until 2007 [94]. However, the experiment keeps running [95], mainly to investigate the Gallium Anomaly, a deficit of registered ν_e using laboratory sources [96], with a new source experiment BEST [97].

A breakthrough was achieved by the Sudbury Neutrino Observatory (SNO) in Canada [98, 99] that took data in two phases over the period 1999–2006. It used 1000 tons of heavy water (D_2O) and was sensitive to three detection channels: (i) Electron scattering $\nu + e \rightarrow e + \nu$, which is dominated by ν_e , but has a small contribution from all flavors and is analogous to normal water Cherenkov detectors. (ii) Neutral-current dissociation of deuterons $\nu + d \rightarrow p + n + \nu$, which is sensitive to the total flux. (iii) Charged-current dissociation $\nu_e + d \rightarrow p + p + e$, which is sensitive to ν_e . Thus one could directly compare the total ν flux with the ν_e one, confirming flavor conversion, an achievement honored with the Physics Nobel Prize (2015) for Arthur MacDonal.

Another class of experiments uses mineral oil to detect the scintillation light emitted by recoiling electrons in $\nu + e \rightarrow e + \nu$. One instrument is KamLAND, using 1000 tons of liquid scintillator, that has taken data since 2002. It was installed in the cave of the decommissioned Kamiokande water Cherenkov detector. Its main achievement was to measure the $\bar{\nu}_e$ flux from distant power reactors to establish flavor oscillations, it has also measured the geoneutrino flux, and today searches for neutrinoless double beta decay. In the solar neutrino context, it has measured the 7Be and 8B fluxes [100, 101].

After flavor conversion has been largely settled, the focus in solar neutrino research is precision spectroscopy, where the 300 ton liquid scintillator detector Borexino in the Gran Sasso Laboratory, which has taken data since 2007, plays a leading role because of its extreme radiopurity. It has spectroscopically measured the pp, 7Be , pep and 8B fluxes and has set the most restrictive constraints on the hep and CNO fluxes [102]. The detection of the latter remains one of the main challenges in the field and might help to solve the solar opacity problem.

Future scintillator detectors with significant solar neutrino capabilities include the 1000 ton SNO+ [103], using the vessel and the infrastructure of the decommissioned SNO detector, JUNO in China [104], a shallow 20 kton medium-baseline precision reactor neutrino experiment that is under construction, and the proposed 4 kton Jinping neutrino experiment [105] that would be located deep underground in the China JinPing Laboratory (CJPL). Very recently, the SNO+ experiment has measured the 8B flux during its water commissioning phase [106].

The largest neutrino observatory yet will be the approved Hyper-Kamiokande experiment [107], a 258 kton water Cherenkov detector (187 kton fiducial volume) that would register 8B neutrinos, with a threshold of 4.5 MeV visible energy and with a rate of 130 neutrinos per day.

Other proposed experiments include THEIA, which would be the realization of the Advanced Scintillator Detector Concept (ASDC) [108]. The latter would

take advantage of recent developments in water based liquid scintillators and other technological advancements, with the physics case ranging from neutrinoless double beta decay and supernova neutrinos, to beyond Standard Model physics [109]. The liquid argon scintillator project DUNE, to be built for long-baseline neutrino oscillations, could also have solar neutrino capabilities [110].

Remarkably, the idea of using Dark Matter experiments to detect solar neutrinos has been proposed, taking advantage of coherent neutrino scattering on large nuclei [111]. For example, liquid argon based WIMP direct detection experiments could be competitive in the detection of CNO neutrinos [112].

3.2 Geoneutrinos

Our knowledge of the Earth's structure and composition is very poor yet. The deepest hole dug into our planet is around 10 km. Seismic wave studies and geo-chemical rock analysis give a broad picture, but only geoneutrinos (the neutrinos emitted by the radioactive decay of Earth elements) can be employed as direct probes to explore the Earth structure. The detection of geoneutrinos would allow us to assess the energy budget of the Earth and estimate the amount of the radiogenic heat eventually driving plate tectonics. The detection of geoneutrinos became possible only about a decade ago thanks to the development of neutrino detectors with an extremely low background.

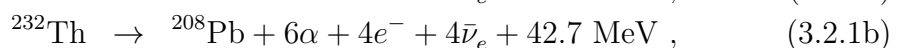
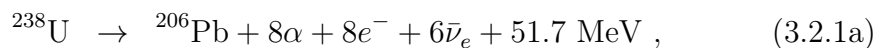
In the following, I will review the production mechanisms and the detection opportunities of geoneutrinos. I refer the reader to dedicated review papers for more details [113–116].

3.2.1 Production mechanisms

Geoneutrinos are the electron neutrinos and antineutrinos produced in the decay of radioactive elements with lifetime comparable to the age of the Earth, the so-called heat producing elements (HPE). The HPE have a non trivial distribution over the Earth interior. Geoneutrinos carry information on the HPE abundance and possibly their distribution.

Geoneutrinos provide constraints on the determination of the fraction of radiogenic heat contributing to the total surface heat flux and provide indirect information on plate tectonics, mantle convection, generation of the Earth magnetic field, as well as the processes that led to the Earth formation.

In the Earth, 99% of the radiogenic heat is produced in the decay chains of ^{232}Th , ^{238}U and ^{40}K . The main reactions are:



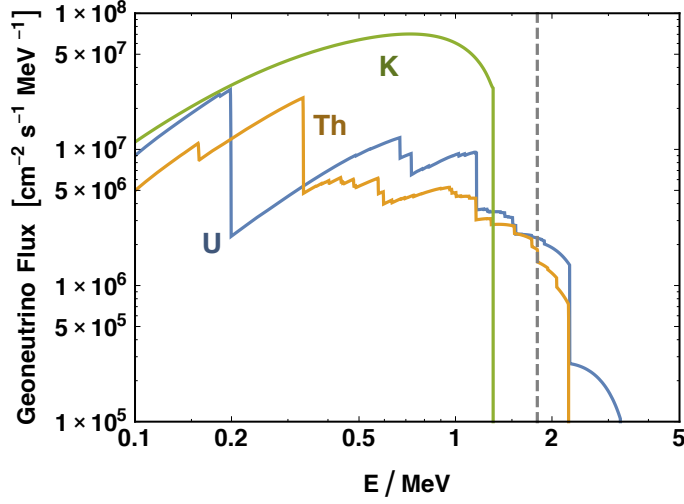


Figure 3.6: Electron geoneutrino flux at production, before flavor oscillations, with various contributions from different reactions. The grey dashed line corresponds to the threshold for inverse beta decay reactions.

A contribution from ^{235}U is also present, however, its isotopic abundance is small. In addition, 1% of the radiogenic heat is coming from the decay of ^{87}Rb , ^{138}La and ^{176}Lu . Note that antineutrinos are mostly produced, while neutrinos are only coming from ^{40}K and have very low energy. Hence, in contrast to the Sun, the Earth shines in antineutrinos.

The differential geoneutrino flux at the position \mathbf{r} on Earth is given by the isotope abundances $a_i(\mathbf{r}')$ for any isotope i at the position \mathbf{r}' and integrating over the entire Earth; neglecting matter effects one has

$$\Phi_{\bar{\nu}_e}(E, \mathbf{r}) = \sum_i A_i \frac{dn_i}{dE} \int_{\oplus} d^3\mathbf{r}' \frac{a_i(\mathbf{r}')\rho(\mathbf{r}')P_{ee}(E, |\mathbf{r} - \mathbf{r}'|)}{4\pi|\mathbf{r} - \mathbf{r}'|^2}, \quad (3.2.2)$$

where $\frac{dn_i}{dE}$ is the $\bar{\nu}_e$ energy spectrum for each decay mode, A_i is the decay rate per unit mass, $\rho(\mathbf{r})$ is the rock density, and P_{ee} the $\bar{\nu}_e$ survival probability.

The geoneutrinos produced by each of these reactions (and before flavor oscillations) have different spectra which depend on the possible decay branches, as shown in Fig. 3.6. The resulting geoneutrino spectrum extends up to 3.26 MeV. However, the contribution to this spectrum coming from ^{40}K is not detectable because only geoneutrinos with energies above 1.8 MeV (the kinematic threshold for inverse-beta decay reaction off protons) are detectable. One can see that a large fraction of the heat arises from the decay chains of uranium and thorium. The resulting flux at Earth is $\Phi_{\bar{\nu}_e} \simeq 2 \times 10^6 \text{ cm}^{-2} \text{ s}^{-1}$. This flux is comparable with the electron neutrino from ^8B decay from solar neutrinos. On the other hand, as we will see in the following,

Table 3.3: Neutrino fluxes, radiogenic heat production in TW, and the mantle signal in terrestrial neutrino unit (number of interactions detected on a target of 10^{32} protons in one year with maximum efficiency) [114] produced by ^{238}U and ^{232}Th and observed in KamLAND [117] and Borexino [118] .

Production channel	Experiment	$\bar{\nu}_e$ Flux ($10^6 \text{ cm}^{-2} \text{ s}^{-1}$)	Radiogenic heat production (TW)	Mantle signal (TNU)
$^{238}\text{U} + ^{232}\text{Th}$	KamLAND	$3.4_{-0.8}^{+0.8}$	$11.2_{-5.1}^{+7.9}$	5.0 ± 7.3
^{238}U (^{232}Th)	Borexino	$2.7_{-0.7}^{+0.7}$ ($2.3_{-0.6}^{+0.6}$)	26-36	15.4 ± 12.3

detecting geoneutrinos is more challenging than detecting ^8B solar neutrinos because of their typical energies.

As will be discussed in the next section and shown in Eq. (3.2.2), to estimate the geoneutrino signal at a certain location, one needs to know the absolute amount and distribution of HPE. Although the crust composition is relatively well known, the mantle composition is quite uncertain. Usually, the signal from HPE in the crust is computed on the basis of the total amount of HPE coming from the bulk silicate Earth (BSE) model, i.e., the model describing the Earth region outside its metallic core; then the corresponding amount of elements in the mantle is extrapolated. The content of elements in the Earth mantle can be estimated on the basis of cosmochemical arguments, implying that abundances in the deep layers are expected to be larger than the ones expected in the upper samples. Given their chemical affinity, the majority of HPE are in the continental crust; this is useful as most of the detectors sensitive to geoneutrinos are in the continental crust and the corresponding event is dominated by the Earth contribution. Usually the continental crust is further divided in upper, lower and middle continental crust. Among existing detectors, Borexino is placed on a continental crust in Italy, while KamLAND is in a complex geological structure around the subduction zone.

3.2.2 Earth modeling

The Earth was created by the accretion from undifferentiated material. Chondritic meteorites seem to resemble this picture as for composition and structure. The Earth can be divided in five regions according to seismic data: core, mantle, crust (continental and oceanic), and sediment. The mantle is solid but it is affected by convection that is responsible for plate tectonics and earthquakes.

Seismology has shown that the Earth is divided into several layers that can be distinguished by discontinuities in the sound speed. Although seismology allows the reconstruction of the density profile of the Earth, it cannot determine the Earth composition. The basic structure of the Earth's interior is defined by the 1D

seismological profile dubbed preliminary reference Earth model (PREM). The PREM model is the basis for the estimation of the geoneutrino production in the mantle. Meanwhile, thanks to seismic tomography, a 3D view of the mantle structure became available. Differences with respect to the 1D PREM model are, however, negligible for what concerns the geoneutrino estimation.

As discussed in the previous section, uranium and thorium are the main HPE producing geoneutrinos. After the metallic core of the Earth separated, the rest of the Earth was made by a homogeneous primitive mantle mainly composed of silicate rocks that then led to the formation of the present mantle and crust.

The Earth outer layer is a thin crust which accounts for 70% of the geoneutrino production. The crust is supposed to host about one half of the total uranium content. The lithophile elements (uranium and thorium) tend to cluster in liquid phase and therefore concentrate in the crust. The Earth crust is either oceanic or continental. The oceanic crust is young and less than 10 km thick. The continental crust is thicker, more heterogeneous and older than the oceanic counterpart. The crust is vertically stratified in terms of its chemical composition and is heterogeneous. The HPE are distributed both in the crust and in the mantle. The expected geoneutrino flux is very different for different portions of the crust; in particular, the continental crust is about one order of magnitude richer in HPE than the oceanic crust. The continental crust is 0.34% of the Earth's mass, but it contains 40% of U and Th budget.

The mantle can be divided in upper and lower mantle. The mantle is a layer of pressurized rocks at high temperature. However, seismic discontinuities between the two parts do not divide the mantle into layers. We do not know whether the mantle moves as single or multiple layers, its convection dynamics and whether it is homogeneous or heterogeneous in composition. The available observational data for the mantle are scarce and are restricted to the uppermost part. The inner part is the core, which accounts for 32% of the Earth's mass. The core is made by iron with small amounts of nickel. Because of their chemical affinity, U and Th are believed to do not be present in the Earth core. Two models have been proposed to describe the mantle. One is a two-layer model with a demarcation surface and a complete insulation between the upper mantle (poor of HPE) and the lower layer. Another one is a fully mixed model, which is favored by seismic tomography. Concerning the estimation of the related geoneutrino flux, both models foresee the same amount of HPE; however, their geometrical distribution changes. In the following, I assume a homogeneous distribution of U and Th in the mantle. Geophysicists proposed models of mantle convection predicting that 70% of the total surface heat flux comes from radioactive isotopes. Geochemists estimate this figure is 25%. So there is a large spread.

The BSE models adopted to estimate the geoneutrino flux have been divided in three classes: geochemical, geodynamical and cosmochemical models. Geochemical BSE models are based on the fact that the composition of carbonaceous chondrites matches the solar photospheric abundances in the refractory lithophile and siderophile elements. A typical value of the bulk mass Th/U ratio is 3.9. Geodynamical

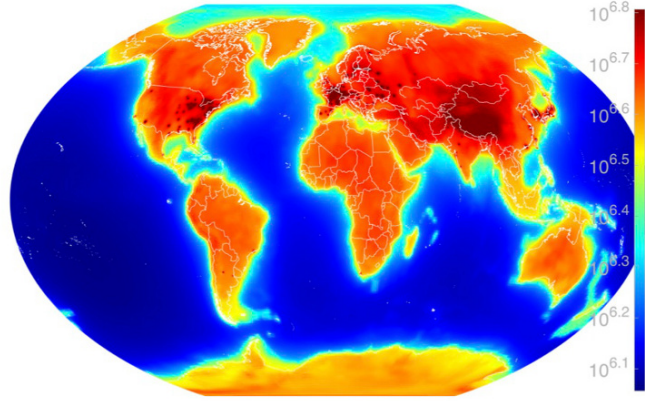


Figure 3.7: Earth map of the expected geoneutrino and reactor neutrino flux ($\bar{\nu}_e/\text{cm}^2/\text{s}$); figure from Ref. [119], which provides an erratum to the original figure [120].

BSE models look at the amount of HPE needed to sustain the mantle convection. Cosmochemical models are similar to the geochemical models, but assume a mantle composition based on enstatite chondrites, and yield a lower radiogenic abundance.

A reference BSE model to estimate the geoneutrino production is the starting point for studying the expectations and potential of various neutrino detectors. It should incorporate the best available geochemical and geophysical information. Note that the geoneutrino flux is strongly dependent on the Earth location (\mathbf{r}) at which this is measured. Hence, the one shown here is only representative. In Fig. 3.7 I show a contour map of the flux of geoneutrinos and reactor neutrinos (Sec. 3.3) expected from the U and Th decay chains.

The geoneutrino flux is used to estimate our planet's radiogenic heat production and to constrain the composition of the BSE model. A leading BSE model [121] predicts a radiogenic heat production of 8 TW from ^{238}U , 8 TW from ^{232}Th and 4 TW from ^{40}K . This would be about half of the heat dissipation rate from the Earth's surface (which is about 50 TW). According to the measurements of the concentrations of Th and U in the chondritic meteorites, the concentration mass ratio of Th to U in the Earth is 3.9. Currently, the uncertainties on the neutrino fluxes are as large as the predicted values.

The neutrino event rate is usually expressed in the literature in the so-called terrestrial neutrino unit (TNU), which stands for the number of interactions detected on a target of 10^{32} protons (roughly correspondent to 1 kton of liquid scintillator) in one year with maximum efficiency. The neutrino event rates S due to Th and U decay can be expressed as

$$S[\text{TNU}](^{232}\text{Th}) = 4.07 \Phi_{\bar{\nu}_e} \quad (3.2.3a)$$

$$S[\text{TNU}](^{238}\text{U}) = 12.8 \Phi_{\bar{\nu}_e} \quad (3.2.3b)$$

where $\Phi_{\bar{\nu}_e}$ is the electron antineutrino flux in units of $10^6 \text{ cm}^{-2} \text{ s}^{-1}$.

3.2.3 Detection opportunities

Geoneutrinos were considered in the first attempts of detecting neutrinos, at the Hanford nuclear reactor by Reines and Cowan. The first estimate of the geoneutrino flux was from Reines, but at that time unavoidable backgrounds made the detection very hard. In the 1960s, geoneutrinos were for the first time reported in the literature by Eder [122] and then Marx a few years later [123].

The first experiment that observed geoneutrinos was KamLAND, a liquid scintillator detector located in the Kamioka mine. In 2005, KamLAND found evidence for 28 neutrino events from Th and U decay with a two years exposure [124]. The detector employs a delayed coincidence method, since inverse beta decay on protons (the main interaction channel) produces two correlated signals: a prompt signal given by the slowing down positron and a delayed γ -ray event due to neutron capture. This strategy allowed for an excellent signal discrimination. This was an extremely challenging measurement, because it required the detection of about one geoneutrino per month to be distinguished from a background that is five times larger. Muon tagging efficiency decreased over time due to a gradual increase of failures of the photomultipliers. Recently, KamLAND replaced the damaged photomultipliers and improved the light collection efficiency [125].

Recent results from KamLAND [117,126] are reported in Table 3.3. The observed event rate agrees with predictions from the BSE models within 2σ . The estimated radiogenic heat is found to be smaller than the heat flow from the Earth surface (47 ± 2 TW), hence indicating secular cooling of the Earth. KamLAND data tend to disfavor the geodynamical model with the homogeneous hypothesis at 89% C.L., but it is still consistent at 2σ . Cosmochemical and geochemical models are still consistent with the data within 1σ .

Another experiment that has been able to detect geoneutrinos is Borexino, a liquid scintillator detector located in the Gran Sasso National Laboratory in Italy. Borexino measured geoneutrinos in 2010 for the first time [118]. I report the results in Table 3.3. By exploiting the different endpoints of the U and Th geoneutrino energy spectra, Borexino measures the bulk of uranium to thorium in the Earth and can provide an estimation of the overall Earth's radiogenic heat power. With a larger exposure, Borexino will also be able to separate the U and Th contributions. Studies of the layers of the crust up to the mantle in the Gran Sasso area allow us to estimate the fraction of neutrinos produced in the crust and in the mantle. According to Borexino, 70% of the emitted heat is due to radiogenic power.

KamLAND and Borexino tried to extract the individual U and Th contributions by removing the chondritic constraint from the spectral fits. Borexino observed $S(\text{U})/S(\text{Th}) \simeq 2.5$ and KamLAND 14.5. Both results are not in contradiction and compatible at 1σ with the chondritic values. Estimated values for the mantle signal are shown in Table 3.3. KamLAND seems to find a smaller mantle signal than Borexino. This points towards an interesting difference in the mantle structure between the two locations. However, current uncertainties are still too large to extrapolate conclusions.

Antineutrinos from nuclear power plants are the main background for geoneutrino

detection. Negligible backgrounds come from atmospheric neutrinos and the diffuse supernova neutrino background. Other spurious signals may also come from intrinsic detector contamination, from cosmogenic sources and from random coincidences of non-correlated events. Because there are no nuclear power plants in Italy, the reactor flux in Borexino is 4–5 lower than in KamLAND. An event rate of 5 and 21 geoneutrino events/year is then expected in Borexino and KamLAND with 100% efficiency [114].

Several experiments, at different development stages, will improve our knowledge on geoneutrinos. For example, SNO+ [127] in Canada expects a rate of 20 geoneutrinos/year. The site is in the old continental crust containing felsic rocks which are rich in U and Th. The crust at the SNO+ location is especially thick, about 40% more than the Gran Sasso and Kamioka ones. JUNO in China also plans to be sensitive to geoneutrinos. Finally, there is Hanohano [128], which is proposed to be built in Hawaii. The latter would be a 5 kton detector on the ocean crust. Since the oceanic crust is thin, most of the neutrinos that Hanohano will measure will come from the mantle (75% of the signal).

3.3 Reactor neutrinos

Neutrinos produced by nuclear power plants have been fundamental to the study of neutrino properties. The very first direct detection of the neutrino was performed using reactors in the previously mentioned experiment conducted by Cowan and Reines in the 1950s. More recently, reactor neutrinos have been exploited to measure some of the neutrino mass and mixing parameters. Nowadays, they are still used to explore other issues, ranging from mass ordering to the search for sterile neutrinos. This section is devoted to a brief introduction to this topic; see also Refs. [47, 129, 130]. Let me stress that reactor neutrinos are the main contribution to man-made neutrino fluxes, and do not discuss several other possible sources like accelerators, where neutrinos can be produced by pion decay in flight, muon decay at rest and beam dump.

3.3.1 Production and detection of reactor neutrinos

Reactor neutrinos are produced in nuclear power plants through β -decay of neutron-rich nuclei. The main contributions come from ^{235}U (55%), ^{239}Pu (32%), ^{238}U (7%) and ^{241}Pu (6%), where the percentages vary over time and I reported typical average values of fission fractions during operation. In addition, below the threshold of inverse beta decay $E_{\text{min}} = 1.8$ MeV there is another neutrino source due to neutron captures; the most important is the decay of ^{239}U produced by the neutron capture of ^{238}U , which is usually written as $^{238}\text{U}(n, \gamma)^{239}\text{U}$. A basic estimate of the flux from a reactor is obtained as follows. On average the energy produced in a fission event is about 200 MeV, and the number of $\bar{\nu}_e$ emitted in the subsequent chain is about 6. A nuclear power plant producing 1 GW of thermal power will then produce a flux of $2 \times 10^{20} \text{ s}^{-1}$ electron antineutrinos.

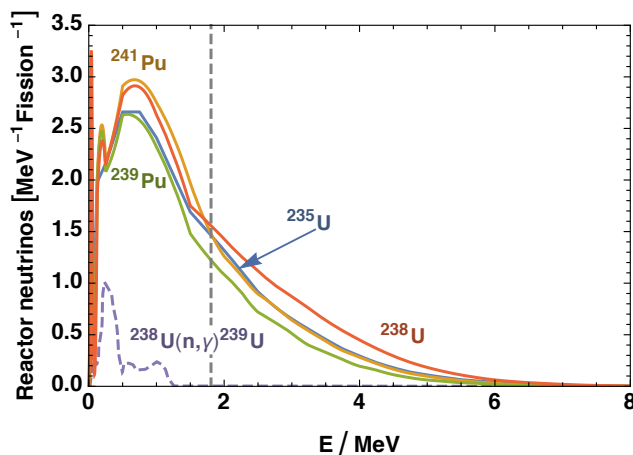


Figure 3.8: The $\bar{\nu}_e$ energy spectra for ^{235}U , ^{238}U , ^{239}Pu , and ^{241}Pu fissions. The inverse beta decay threshold is marked by the vertical dashed line. At low energies, the dominant contribution is due to neutron capture processes $^{238}\text{U}(n, \gamma)^{239}\text{U}$ (here rescaled by a factor 1/20).

Obtaining the differential energy spectrum of reactor neutrinos is a much more complicated task, as many different decay branches must be taken into account. In the last 50 years two main approaches have been used. One method predicts the time dependent total flux by summing over all the possible beta decay branches. The problem with this approach is in the large uncertainties plaguing the calculated spectrum: the fission yields and the endpoint energies are often not well known, one needs a good model for the Coulomb corrections entering the Fermi function, and so forth. The alternative is to use the measured electron spectrum for different decay chains, which can be inverted taking advantage of the relation

$$E_\nu = E_e + T_n + m_n - m_p \simeq E_e + 1.293 \text{ MeV} \quad (3.3.1)$$

where T_n is the small recoil kinetic energy of the neutron and E_e is the energy of the outgoing positron.

Until 2011, the standard results were the ones obtained by Vogel and Engel [131]. In the same year, two papers with different approaches recalculated the spectrum at energies larger than 2 MeV, one by Huber [132] and one Mueller et al. [133]. In Fig. 3.8 I show the spectrum due to the dominant processes as reported in Table II of Ref. [131] for energies smaller than 2 MeV, while for larger energies I use Tables VII to IX from Ref. [132] for ^{235}U , ^{239}Pu and ^{241}Pu and Table III of Ref. [133] for ^{238}U ; finally, the low-energy spectrum of neutron capture $^{238}\text{U}(n, \gamma)^{239}\text{U}$ are directly extracted from Ref. [130]. Notice that best fits to these tables are reported in the above-mentioned references.

The detection of reactor neutrinos typically relies on the inverse beta decay on proton, $\bar{\nu}_e + p \rightarrow n + e^+$. The cross section is usually expressed in terms of well

measured quantities such as the neutron lifetime τ_n and the electron mass m_e [134],

$$\sigma_{\text{CC}}^{\bar{\nu}_e p} = \frac{2\pi^2}{\tau_n m_e^5 f} E_e \sqrt{E_e^2 - m_e^2} \quad (3.3.2)$$

where f is the dimensionless phase-space integral

$$f = \int_{m_e}^{m_n - m_p} dE_e \frac{(m_n - m_p - E_e)^2 E_e \sqrt{E_e^2 - m_e^2}}{m_e^5} \quad (3.3.3)$$

where I neglected the small recoil kinetic energy of the neutron. The detection will feature a prompt signal due to the positron, followed by the recoil neutron capture. Alternatives to this process are given by charged and neutral current deuteron break-up using heavy water, antineutrino-electron elastic scattering, and coherent antineutrino-nucleus interactions [129].

The left panel of Fig. 3.9 shows the typical flux for a reactor like the Japanese JOYO [135], which has a thermal power of 140 MW and a detector located at 24.3 m. The convolution of the flux with the cross section (right panel of Fig. 3.9) shows that the interactions in the detector peak for $\bar{\nu}_e$ with energy around 4 MeV. While the quantitative details strongly depend on the reactors and on the detector, several general features can be pointed out [129]. First, the large threshold implies that only reactions with large Q-value can be observed, so that only one fourth of the total antineutrinos produced can be detected. Another important point is that reactors shutdowns can be used to better measure the background, and the intensity of the flux is proportional to the thermal power, which is accurately measured. Moreover, the flux is very large, so that reactor neutrino experiments do not need large shielding against cosmic ray background, which will be discussed in Chapter 4. All these advantages make reactor neutrinos a fundamental tool for the measurement of neutrinos properties such as mixing angles and mass differences. The flavor conversion will follow the same logic as the solar neutrino oscillations described in Sec. 3.1.5, App. A and App. B, the main difference being that matter effects play a smaller role.

3.3.2 Measurements

As already mentioned, reactor experiments were the first successful attempt to detect the elusive neutrinos. The proposal of using inverse beta decay to observe neutrinos dates back to Bethe and Peierls, but it was only in 1953 that Reines and Cowan started their experiments at Hanford and Savannah River which directly detected neutrinos for the first time. Nuclear power plants have been employed in the following decades to measure neutrino properties many times. Reactor neutrinos helped to confirm the existence of a non-zero mass for neutrinos, which was established by solar neutrino measurements as described in Sec. 3.1.6.

The measurements of θ_{12} and δm^2 by KamLAND and solar neutrino experiments, as well as measurements with atmospheric neutrinos of θ_{23} and Δm^2 by experiments

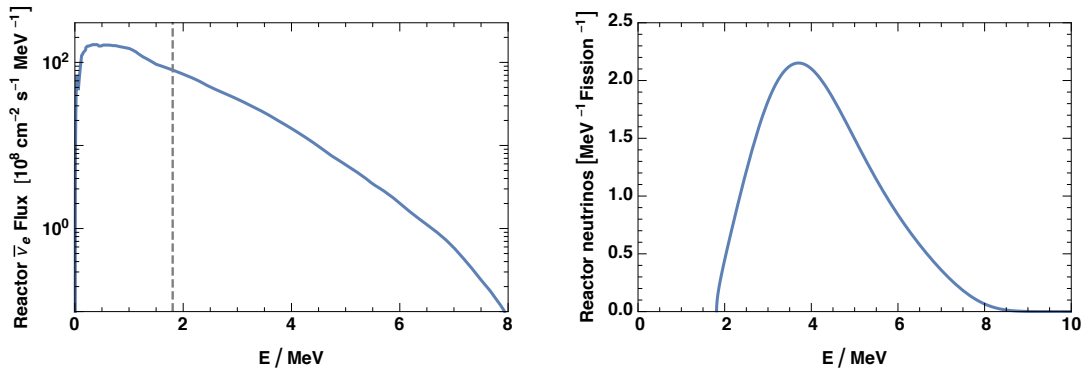


Figure 3.9: *Left panel:* typical reactor neutrino flux (here the Japanese JOYO reactor [135] is used as an example). *Right panel:* energy distribution of the neutrinos interacting in the detector, in arbitrary units; neutrinos are measured about the inverse beta decay threshold and their interaction peaks around 4 MeV.

such as Super-Kamiokande [136], motivated the search for the third mixing angle, θ_{13} . It looked natural for it to be large as the other two parameters. Nevertheless, both the CHOOZ [137] and Palo Verde [138] experiments, searching for electron antineutrino disappearance, found measurements compatible to zero in the late 1990s to early 2000s. It has been only recently with a new generation of reactor experiments (Double Chooz [139], Daya Bay [140], and RENO [141]) that a non-zero value for θ_{13} has been measured with large significance.

In the near future, reactor neutrinos such as JUNO will set out to measure the mass ordering and to access to neutrino mixing parameters with high precision. Moreover, physics beyond the Standard Model could potentially be discovered. As an example, recent reactor antineutrino observations suggested $\bar{\nu}_e$ disappearance from a deficit in the measured antineutrino events compared to the theoretical prediction based on the the reactor antineutrino flux calculations [142]. The latter has also been interpreted in terms of the existence of an additional eV mass sterile neutrino [143, 144].

3.4 Neutrinos from exploding stars: supernova neutrinos

The core collapse of a massive star within a few seconds releases the gravitational binding energy of a neutron star $E_b \sim 3 \times 10^{53}$ erg in the form of neutrinos and this is known as supernova (SN) explosion. The energy released is roughly comparable to the energy of all stars in the Universe within the same period. While the neutrino burst from the next nearby SN would be a milestone for neutrino astronomy, it is a transient signal and thus not part of the GUNS. The topic of supernova neutrinos

is rather technical; I here summarize the main features of core-collapse neutrino emission (see Refs. [145–148] for reviews) primarily as an ingredient for the diffuse SN neutrino background (DSNB) presented in Sec. 3.5.

3.4.1 Generic features of supernova neutrinos

At the end of its life, the compact core of an evolved star becomes unstable and collapses to nuclear density, where the equation of state stiffens. At this core bounce, a shock wave forms, moves outward, and ejects most of the mass in the form of a SN explosion, leaving behind a compact remnant that cools to become a neutron star (NS). Typical NS masses are around $1.5 M_{\odot}$, with $2 M_{\odot}$ the largest observed case. The radius is 12–14 km, the exact value and NS structure depending on the nuclear equation of state. Within these uncertainties one expects the release of around $E_b = 3 \times 10^{53}$ erg or 2×10^{59} MeV of gravitational binding energy [149].

This huge amount of energy must appear in the form of neutrinos because the interaction rate of γ and e^{\pm} is so large that they contribute little to energy transfer in dense matter, whereas gravitons interact far too weakly to be effective. Moreover, in hot nuclear matter the neutrino mean free path is short compared to the geometric dimension of the collapsed object, so ν and $\bar{\nu}$ of all flavors thermalize, for example by nucleon-nucleon bremsstrahlung and other processes. So, very approximately we may think of the collapsed SN core as a blackbody source for ν and $\bar{\nu}$ of all flavors.

The diffusion character of neutrino transport leads to an estimated time of a few seconds for most of the energy trapped in the NS to escape. The emission temperature depends on radiative transfer in the decoupling region (“neutrino sphere”) and one finds 3–5 MeV, which means that neutrino energies are 10–15 MeV after their decoupling [149]. This scale is similar to that of solar and geoneutrinos, where however it is set by nuclear physics. So one expects the emission of around 3×10^{57} particles for each of the six ν and $\bar{\nu}$ species.

Besides energy, the SN core must also radiate lepton number (deleptonization). The final NS contains only a small proton (or electron) fraction, while the collapsing material, consisting of chemical elements between O and Fe, initially has an electron fraction $Y_e = 0.46$ – 0.5 . A baryonic mass of $1.5 M_{\odot}$ corresponds to 2×10^{57} nucleons, implying that 1×10^{57} units of electron lepton number must escape in the form of ν_e , ignoring for now flavor conversion. Comparison with the estimated 6×10^{57} of ν_e plus $\bar{\nu}_e$ to be radiated by the required energy loss reveals a significant excess of ν_e over $\bar{\nu}_e$ emission.

The basic picture of neutrino energies and time scale of emission was confirmed on 23 February 1987 by the neutrino burst from SN 1987A in the Large Magellanic Cloud with a total of about two dozen events in three small detectors [150–152]. However, the data was too poor for detailed quantitative tests. The next nearby SN would provide high statistics, especially in Super-Kamiokande, in IceCube, or in other upcoming large detectors such as Hyper-Kamiokande or DUNE. The expected large number of neutrino events in these detectors may show detailed imprints of SN physics.

3.4.2 Generic features of the neutrino signal

The standard paradigm of core-collapse SNe has evolved over decades of numerical modeling [145, 148], originally in spherical symmetry (1D) and over the past years with 3D models. After the collapse has begun and when the density exceeds some $10^{12} \text{ g cm}^{-3}$, neutrinos are entrained by the infalling matter because of coherent scattering on large nuclei. When nuclear density of $3 \times 10^{14} \text{ g cm}^{-3}$ is reached, the core bounces and a shock wave forms within the core at an enclosed mass of around $0.5 M_{\odot}$. As the shock propagates outward, it loses energy by dissociating iron and eventually stalls at a radius of some 150 km, while matter keeps falling in. Meanwhile the neutrino flux streaming through this region deposits some of its energy, rejuvenating the shock wave, which finally moves on and ejects the outer layers. It leaves behind a hot and dense proto neutron star (PNS), which cools and deleptonizes within a few seconds. This is the essence of the neutrino-driven explosion mechanism, also called delayed explosion mechanism or Bethe-Wilson mechanism [153].

The corresponding neutrino signal falls into three main phases: a prompt burst, an accretion phase, and an explosion, followed by cooling.

Prompt Burst.—Soon after bounce, the shock wave breaks through the edge of the iron core, liberating a prompt ν_e burst that corresponds to a significant fraction of the total lepton number and is therefore also called the deleptonization burst or neutronization burst. During the post-bounce time window -20 ms to 60 ms , the SN core radiates about 5% of the total energy that corresponds to the period shown in the rightmost panels, whereas it radiates 0.4×10^{57} units of lepton number, i.e., around 50% of what is emitted over the full period. The features of the prompt-burst phase are thought to be essentially universal [154, 155].

Accretion Phase.—As the shock wave stalls, neutrino emission is due to the accretion flow of matter onto the SN core, emitting ν_e and $\bar{\nu}_e$ with almost equal luminosities, but somewhat different average energies, so the ν_e particle flux is about 20% larger than the $\bar{\nu}_e$ one. The production and interaction is mostly by β processes on protons and neutrons. Heavy-flavor ν and $\bar{\nu}$, on the other hand, are produced in pairs from deeper layers, with a smaller radiating region and therefore smaller fluxes. Their average energies, however, are very similar to that of $\bar{\nu}_e$.

Explosion.—Spherically symmetric numerical models do not explode except for the smallest-mass progenitors, so the duration of the accretion phase, and if an explosion occurs at all, can not be inferred from these models. The quenching of accretion strongly reduces the $\nu_e \bar{\nu}_e$ luminosity which drops to the component provided by core emission.

Cooling.—The remaining evolution consists of cooling and deleptonization of the PNS. The luminosity is essentially equipartitioned among the six species, whereas $\langle E_{\nu_e} \rangle$ is smaller than the others, i.e., there is a net lepton number flux. The quantitative details depend strongly on the PNS mass and the nuclear equation of state.

The instantaneous neutrino spectra are quasi thermal, but do not follow exactly a Fermi-Dirac distribution. Rather they are “pinched,” which means that the spread of energies around the mean is less than in the thermal case. Phenomenologically, the numerical spectra are well described by a Gamma distribution of the form [156, 157]

$$f(E) \propto \left(\frac{E}{E_{av}}\right)^\alpha \exp\left[-\frac{(\alpha+1)E}{E_{av}}\right], \quad (3.4.1)$$

where α is the “pinching parameter” with $\alpha = 2$ corresponding to a Maxwell-Boltzmann distribution. For any α , the parameter E_{av} matches $\langle E \rangle$, whereas α is fixed to match, for example, $\langle E^2 \rangle$ of the numerical spectrum by

$$\alpha = (2\langle E \rangle^2 - \langle E^2 \rangle) / (\langle E^2 \rangle - \langle E \rangle^2). \quad (3.4.2)$$

In addition, the overall normalization is fixed to match the numerical case. The pinching is largest for ν_e , especially during the prompt burst, and smallest for ν_x .

Assuming this scenario to capture the main features of a SN neutrino signal, one still expects large case-by-case variations depending on progenitor properties. The lowest-mass SN progenitors (about 8–10 M_\odot) become unstable due to electron capture before nuclear burning of their O-Ne-Mg core can be ignited, so they never reach an iron core. These “electron capture SNe” or “O-Ne-Mg-core SNe” could represent 30% of all cases because the initial mass function decreases rapidly with increasing mass.

3.4.3 Failed explosions

For higher-mass progenitors, numerical models do not explode. It remains open if this question depends, for example, on quantitative details of neutrino energy transfer and 3D effects, on details of the progenitor models, or if a crucial piece of input physics is missing. Moreover, probably not all collapsing stellar cores lead to successful explosions — the class of failed SNe, leaving a black hole (BH) instead of a NS as a compact remnant. Using the “compactness parameter” as a criterion, recent theoretical work hints that up to 40% of all collapsing cores may lead to BH formation [158–160].

The cosmic star-formation rate predicts perhaps twice the observed SN rate at high redshifts, suggesting a significant fraction of failed explosions [161, 162]. Likewise, the “red supergiant problem” suggests a cutoff of around 18 M_\odot in the mass range of identified SN progenitors [163, 164]. A significant fraction of failed SNe would also naturally explain the compact-object mass distribution [165]. Motivated by these hints, a survey looks for disappearing red supergiants in 27 galaxies within 10 Mpc with the Large Binocular Telescope [166]. Over the first seven years, ending in early 2016, this survey found six core-collapse SNe and one candidate for a failed SN, providing $0.14_{-0.10}^{+0.33}$ for the fraction of failed SNe.

In the neutrino signal of a failed SN, the cooling phase would be missing, whereas the accretion phase would abruptly end. The average neutrino energies would increase until this point and the $\nu_e \bar{\nu}_e$ fluxes dominate. The overall emitted neutrino energy

could exceed that of an exploding SN. The crucial point is that BH formation is delayed, not prompt, so the core bounce and shock scenario is crucial for the expected neutrino burst of both exploding and failed cases.

An intermediate class between exploding and failed progenitors are fallback SNe, where BH formation is delayed, if the explosion energy is not sufficient to unbind the star. Hence, a fraction of the stellar mantle may fall back and push the NS beyond the BH limit.

3.4.4 Flavor conversion

Numerical SN models treat neutrino transport usually in a three-species formalism consisting of ν_e , $\bar{\nu}_e$ and ν_x , representing any of ν_μ , $\bar{\nu}_\mu$, ν_τ , or $\bar{\nu}_\tau$, and completely ignore flavor conversion. From a numerical perspective, including flavor conversion is completely out of the question. From a theoretical perspective, many questions remain open because the matter effect of neutrinos on each other leads to collective flavor conversion phenomena that are not yet fully understood [147, 167].

The flavor evolution of the prompt ν_e burst is probably similar to MSW conversion of solar neutrinos, except that the starting point is at far larger densities, requiring a three-flavor treatment. Moreover, neutrino-neutrino refraction would cause synchronized oscillations and, depending on the matter profile, cause a spectral split, i.e., a discontinuity in the conversion probability.

During the accretion phase, the $\nu_e\bar{\nu}_e$ flux is larger than the $\nu_\mu\bar{\nu}_\mu$ or $\nu_\tau\bar{\nu}_\tau$ one. Collective effects can lead to pair conversion of the type $\nu_e\bar{\nu}_e \leftrightarrow \nu_\mu\bar{\nu}_\mu$ or $\nu_e\bar{\nu}_e \leftrightarrow \nu_\tau\bar{\nu}_\tau$, i.e., pair annihilation on the level of forward scattering with a rate much faster than the usual non-forward scattering process. Conceivably it could lead to flavor equilibration not far from the neutrino decoupling region [168, 169]. In addition to collective effects, one expects MSW conversion by the ordinary matter profile [170], although the matter effect could be modified by density variations caused, e.g., by turbulence in the convective regions. Far away from the SN, neutrinos would decohere into mass eigenstates; however, unlike for solar neutrinos, one cannot easily predict the energy-dependent probability for the various ν_i and $\bar{\nu}_i$ components.

3.4.5 Detection perspectives

The neutrino signal of SN 1987A (whose remnant is shown in Fig. 3.10) on 23 February 1987 in three small detectors was a historical achievement, but the event statistics was sparse. The next nearby (probably galactic) SN would be observed in a large number of detectors of different size, ranging from a few expected events to thousands (Super-Kamiokande) or even millions (IceCube), although in the latter case without event-by-event recognition [146, 147, 171]. The various detectors would provide complementary information. What exactly one would learn depends, of course, on the exact type of core-collapse event that could range from an electron-capture SN to a failed explosion with BH formation. It would also depend on concomitant electromagnetic and possibly gravitational-wave observations.

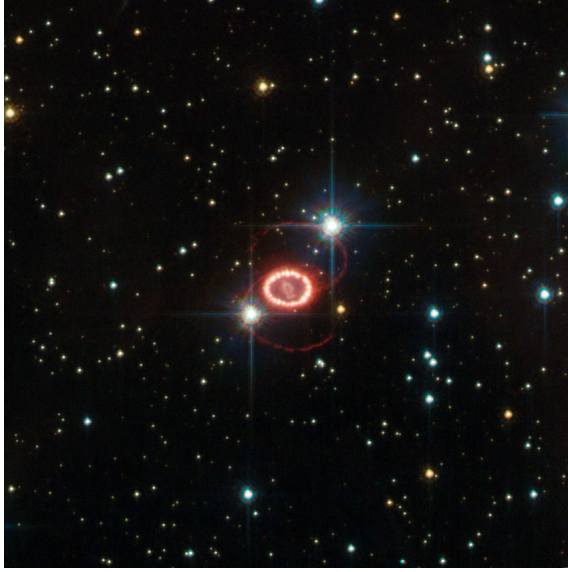


Figure 3.10: Remnant of the supernova SN 1987A as seen by the NASA/ESA Hubble Space Telescope. Credit: [ESA/Hubble & NASA](#).

While the next nearby SN is perhaps the most cherished target of low-energy neutrino astronomy and would provide a bonanza of astrophysical and particle-physics information, its fast transient nature sets it apart from the general neutrino background at Earth. A more detailed discussion of the detection is given in the literature [147, 171].

3.5 Diffuse supernova neutrinos

All collapsing stars in the visible universe, a few per second, provide the diffuse supernova neutrino background (DSNB). It dominates at Earth for 10–25 MeV and in future could be measured by the JUNO and Gd-enriched Super-Kamiokande detectors, providing hints on the SN redshift distribution, the fraction of electromagnetically dim progenitors, and average SN energetics.

3.5.1 Basic estimate

The idea that the accumulated neutrinos from all collapsed stars in the universe form an interesting cosmic background goes back to the early 1980s [172–174], while modern reviews are Refs. [147, 175–177]. The DSNB flux and spectrum depend on the overall core-collapse rate that is uncertain within perhaps a factor of two and on the average neutrino emission spectrum. The baseline case of the forthcoming paper predicts for the sum of all species

$$\Phi_{\Sigma\nu\bar{\nu}} = 126 \text{ cm}^{-2} \text{ s}^{-1}, \quad (3.5.1a)$$

$$n_{\Sigma\nu\bar{\nu}} = 4.2 \times 10^{-9} \text{ cm}^{-3}, \quad (3.5.1b)$$

$$\rho_{\Sigma\nu\bar{\nu}} = 25 \text{ meV cm}^{-3}, \quad (3.5.1c)$$

with an average energy of 6.0 MeV, corresponding to an emission energy, averaged over all species, of 12.8 MeV. The DSNB energy density is almost the same as the CNB energy density of massless neutrinos. If the lightest neutrino mass is so large that all CNB neutrinos are dark matter today, the DSNB is the dominant neutrino radiation density in the present-day universe.

We can compare the DSNB with the accumulated photons from all stars, the extra-galactic background light (EBL), that provides a radiation density of around $50 \text{ nW m}^{-2} \text{ sr}^{-1}$ [178]. Integrating over directions yields an isotropic flux of $400 \text{ MeV cm}^{-2} \text{ s}^{-1}$ and thus an energy density of 13 meV cm^{-3} . Photons and neutrinos are redshifted in the same way, so the stars of the universe have emitted about twice as much energy in the form of core-collapse neutrinos as in the form of light.

We can express the time-averaged neutrino luminosity L_ν of a given stellar population in units of the number of core-collapse events per unit time, assuming one event releases 2.5×10^{53} erg. Moreover, we can express the photon luminosity L_γ in units of the solar luminosity of $L_\odot = 4 \times 10^{33}$ erg/s, so a ratio $L_\nu/L_\gamma = 2$ corresponds to $1/100$ years/ $10^{10} L_\odot$ core-collapse events. This rate corresponds approximately to the usual SN unit that is defined as $1 \text{ SNU} = 1 \text{ SN}/10^{10} L_{\odot\text{B}}/100 \text{ yr}$ with $L_{\odot\text{B}}$ the solar luminosity in the blue spectral band. While the SN rate depends strongly on galaxy type, e.g. no core-collapse SNe in elliptical galaxies where no star formation takes place, averaged over all galaxies it is around 1 SNU [179, 180]. Very roughly, 1 SNU corresponds to one SN per century per galaxy. In other words, $L_\nu/L_\gamma \sim 2$ of an average stellar population corresponds to the usual astronomical measure of the SN rate. Within uncertainties, the DSNB density of Eq. (3.5.1c) follows from expressing 1 SNU as a neutrino-to-photon luminosity ratio.

For DSNB detection, the $\bar{\nu}_e$ component is of particular interest. For energies below 10 MeV it is hidden under the reactor $\bar{\nu}_e$ background, so the higher-energy part of the DSNB spectrum is particularly important. It requires a more detailed discussion than a simple prediction of the overall DSNB density.

3.5.2 Redshift integral

The DSNB depends on the core-collapse rate $R_{\text{cc}}(z)$ at cosmic redshift z and the average spectrum $F_\nu(E) = dN_\nu/dE$ emitted per such event, where ν can be any of the six species of neutrinos or antineutrinos. The long propagation distance implies loss of flavor coherence, so each ν represents a mass eigenstate. Each neutrino burst lasts for a few seconds, but this time structure plays no practical role because one will need to integrate for several years to detect even a small number of DSNB neutrinos. Moreover, the bursts sweeping through the detector somewhat overlap. Therefore, $F_\nu(E)$ is the average time-integrated number of neutrinos per energy interval emitted by a collapsing star.

The neutrino density spectrum accumulated from all cosmic epochs is given by

the redshift integral

$$\frac{dn_\nu}{dE} = \int_0^\infty dz (z+1) F_\nu(E_z) n'_{\text{cc}}(z), \quad (3.5.2)$$

to be multiplied with the speed of light to obtain the diffuse flux. Here $E_z = (1+z)E$ is the blue-shifted energy at emission of the detected energy E . The first factor $(1+z)$ arises as a Jacobian $dE_z/dE = (1+z)$ between emitted and detected energy interval. It is assumed that the average neutrino flux spectrum $F_\nu(E)$ is the same at all cosmic epochs.

Finally $n'_{\text{cc}}(z) = dn_{\text{cc}}/dz$ is the core-collapse number per comoving volume per redshift interval. It is usually expressed in the form

$$n'_{\text{cc}}(z) = \frac{R_{\text{cc}}(z)}{H_0 (1+z) \sqrt{\Omega_{\text{M}}(1+z)^3 + \Omega_{\Lambda}}}, \quad (3.5.3)$$

where H_0 is the Hubble expansion parameter, while Ω_{M} and Ω_{Λ} are the present-day cosmic matter and dark-energy fractions. In the literature one usually finds $R_{\text{cc}}(z)$, the number of core-collapse events per comoving volume per unit time (units $\text{Mpc}^{-3} \text{yr}^{-1}$). However, $R_{\text{cc}}(z)$ is derived in terms of an assumed cosmological model because observations for a given redshift interval need to be translated to intervals of cosmic time, i.e., only $n'_{\text{cc}}(z)$ has direct meaning. So a given $R_{\text{cc}}(z)$ makes sense only in conjunction with the assumed underlying cosmological model.

We may further express $n'_{\text{cc}}(z) = n_{\text{cc}} f_{\text{cc}}(z)$ in terms of the comoving density n_{cc} of all past core-collapse events, times its normalised redshift distribution with $\int_0^\infty dz f_{\text{cc}}(z) = 1$. Likewise, the neutrino emission spectrum is expressed as $F_\nu(E) = N_\nu f_\nu(E)$ with N_ν the total number of species ν emitted by an average core collapse times its normalised spectrum with $\int_0^\infty dE f_\nu(E) = 1$. With these definitions, Eq. (3.5.2) is

$$\frac{dn_\nu}{dE} = N_\nu n_{\text{cc}} g_\nu(E) \quad (3.5.4)$$

with the energy spectrum of the accumulated neutrinos

$$g_\nu(E) = \int_0^\infty dz (z+1) f_\nu[(z+1)E] f_{\text{cc}}(z). \quad (3.5.5)$$

It fulfills the normalisation $\int_0^\infty dE g_\nu(E) = 1$ if $f_\nu(E)$ and $f_{\text{cc}}(z)$ are normalised.

3.5.3 Cosmic core-collapse rate

The core-collapse rate as a function of redshift can be determined by direct SN observations. However, this approach may be significantly incomplete because core-collapse SNe can be electromagnetically dim or, for non-exploding cases, completely invisible. Therefore, usually one estimates the rate from the star-formation activity, essentially translating ultraviolet and infrared astronomical observations into a

neutrino emission rate. To convert the star-formation rate into a core-collapse rate $R_{\text{cc}} = k_{\text{cc}} \dot{\rho}_*$ we need the factor

$$k_{\text{cc}} = \frac{\int_{M_{\text{min}}}^{M_{\text{max}}} dM \psi(M)}{\int_{M_1}^{M_u} dM M \psi(M)} = (135 M_{\odot})^{-1}, \quad (3.5.6)$$

where $\psi(M) \propto M^{-2.35}$ is the Salpeter initial mass function [181] and $(M_1, M_u) = (0.1, 125) M_{\odot}$ the overall stellar mass range. Uncertainties in $\psi(M)$ largely cancel as it is used to convert astronomical observations into $\dot{\rho}_*$ in the first place. For stars that develop collapsing cores I use $(M_{\text{min}}, M_{\text{max}}) = (8, 125) M_{\odot}$, including those cases that do not explode as a SN but rather form a black hole (BH) because these non-exploding cases are also powerful neutrino sources.

With this conversion factor we find for the integrated core-collapse density of the past cosmic history for the best-fit star-formation rates of the mentioned authors

$$n_{\text{cc}} = \begin{cases} 1.05 \times 10^7 \text{ Mpc}^{-3} & \text{Yüksel et al. [182],} \\ 0.84 \times 10^7 \text{ Mpc}^{-3} & \text{Mathews et al. [183],} \\ 0.69 \times 10^7 \text{ Mpc}^{-3} & \text{Robertson et al. [184],} \\ 0.58 \times 10^7 \text{ Mpc}^{-3} & \text{Madau et al. [185].} \end{cases} \quad (3.5.7)$$

If every core collapse emits on average $N_{\nu} \sim 2 \times 10^{57}$ neutrinos of each species, $n_{\text{cc}} \sim 10^7 \text{ Mpc}^{-3}$ yields a DSNB density in one species of $n_{\nu} \sim 2 \times 10^{64} \text{ Mpc}^{-3} = 0.7 \times 10^{-9} \text{ cm}^{-3}$ or, after multiplying with the speed of light, an isotropic flux of $20 \text{ cm}^{-2} \text{ s}^{-1}$ in one species. The DSNB spectrum is fairly insensitive to the exact redshift distribution $f_{\text{cc}}(z)$.

The DSNB derived from a Maxwell-Boltzmann source spectrum is strongly anti-pinchd (average energy for our fiducial case $\langle E \rangle = 1.41 T$ and pinching parameter 0.84) and not well represented by a Gamma distribution of the form of Eq. (3.4.1). However, one finds that the decreasing part of the spectrum is very close to an exponential $e^{-E/T}$ and a good overall fit to a fiducial case is

$$g_{\nu}(E/T) = 1.15 \arctan[3 (E/T)^{3/2}] e^{-1.03 E/T}. \quad (3.5.8)$$

The main uncertainty of the DSNB prediction is the total number of core-collapse events shown in Eq. (3.5.7). Moreover, these predictions involve an overall uncertainty in converting the star-formation rate into a core-collapse rate (the factor k_{cc}). A mismatch of about a factor of 2 between direct SN observations and the core-collapse rate estimated from star formation was found, the so-called SN-rate problem [162]. The most likely explanation is dust extinction, especially at higher redshift, or a relatively large fraction of dim SNe, and in particular of non-exploding, BH forming cases.

3.5.4 Average emission spectrum

The sparse data of SN 1987A are not detailed enough to give a good estimate of the neutrino spectrum and also need not be representative of the average case. Therefore,

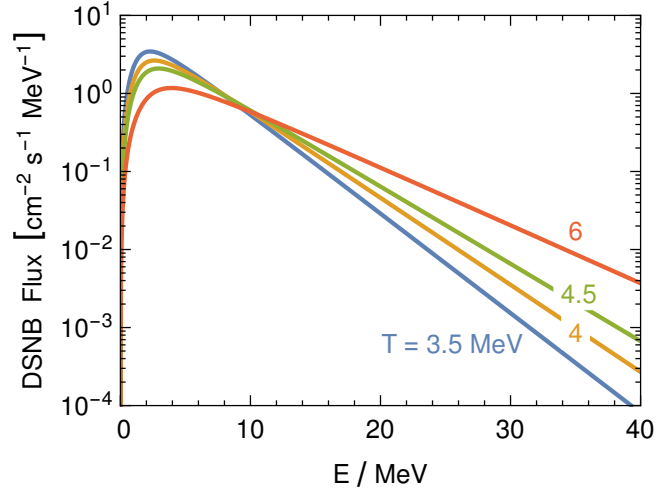


Figure 3.11: DSNB flux in one species according to Eq. (3.5.9). The emission spectrum is taken to be Maxwell-Boltzmann with the indicated temperatures.

DSNB predictions depend on numerical SN models. To get a first impression we can assume that the time-integrated spectrum is of Maxwell-Boltzmann type. With Eq. (3.5.4) the DSNB flux for a given species ν is

$$\begin{aligned} \frac{d\Phi_\nu}{dE} &= 4.45 \text{ cm}^{-2} \text{ s}^{-1} \text{ MeV}^{-1} \frac{n_{\text{cc}}}{10^7 \text{ Mpc}^{-3}} \\ &\times \frac{6 E_\nu^{\text{tot}}}{2 \times 10^{53} \text{ erg}} \left(\frac{4 \text{ MeV}}{T} \right)^2 g_\nu(E/T), \end{aligned} \quad (3.5.9)$$

where E_ν^{tot} is the total emitted energy in the considered species ν , and $g_\nu(E/T)$ is the normalised spectrum of Eq. (3.5.8) that includes our fiducial redshift distribution. I show this spectrum for $T = 3.5, 4, 4.5$ and 6 MeV in Fig. 3.11, where values around 4 MeV would be typical for a core-collapse SN, whereas 6 MeV could represent a BH forming event with larger spectral energies.

We conclude that around the detection threshold of 10 MeV, the flux predictions are very similar and depend primarily on the overall normalisation, i.e., the cosmic core-collapse rate and the average energy release. For larger E , the spectra scale essentially as $e^{-E/T}$ and thus depend strongly on the effective emission temperature. Therefore, the flux at the upper end of the detection window (~ 30 MeV) is particularly sensitive to the fraction of BH forming events.

3.5.5 Detection perspectives

The DSNB has not yet been detected, but the experimental limits have been obtained by the Super-Kamiokande (sometimes abbreviated to SK) I/II/III water Cherenkov detector [186], SK IV with neutron tagging [187], and the KamLAND liquid scintillator detector [188]. All of these limits are based on the inverse-beta decay reaction $\bar{\nu}_e + p \rightarrow n + e^+$. These limits do not yet reach predictions, but keeping in mind that

the cosmic core-collapse rate and its BH forming component could be larger than assumed here means that any significant experimental improvement can lead to a detection.

DSNB detection is not only a question of event rate, but of identification and rejection of several backgrounds that can mimic DSNB events. A first detection should become possible over the next decade with the upcoming Gd-enhanced Super-Kamiokande water Cherenkov detector [189, 190] and later with a possible Gd-enhanced version of the upcoming Hyper-Kamiokande [107]. Another promising contender is the upcoming JUNO 20 kt scintillator detector [104]. A complementary detection channel, using the ν_e flux, may be offered by the upcoming liquid argon detector DUNE at the LBNF facility in the US [191, 192]. A detailed forecast of these opportunities is beyond the scope of our discussion.

Chapter 4

High-energy neutrinos⁵

High-energy neutrinos have emerged to be outstanding astrophysical messengers for many different reasons. First of all, neutrinos offer a better understanding of astrophysical objects, because they can escape from the source as they interact only with matter, even at high energies. As a second reason, the universe is not transparent to high-energy photons, which can scatter both on CMB photons as well as on other background radiation, while neutrinos can travel large distances undisturbed; moreover, differently from cosmic rays, which are diffused by magnetic fields, neutrinos point back to the source. Finally, the observation of astrophysical neutrinos can help us to discriminate the mechanism of production of cosmic rays because, while photons can be produced both from hadronic (pp and $p\gamma$) and leptonic interactions, neutrinos can only be created by hadronic interactions such as pion decay. This means that neutrinos can be used to observe distance sources, probe the core of cosmic accelerators, and help us to understand which fundamental processes play a role [193–195].

4.1 Atmospheric neutrinos⁶

The lower energy background (from 30 MeV to 10 TeV) to astrophysical neutrinos is due to atmospheric neutrinos. The latter are produced through different chains, starting from cosmic-ray particles interacting with the particles of the Earth or Sun atmosphere [195, 197]. Atmospheric neutrinos have played a fundamental role in establishing the existence of neutrino masses, as the existence of oscillations has been proved at experiments such as Super-Kamiokande [136], while nowadays they mostly play the role of background to astrophysical neutrinos, although surprises are always possible.

Certain astrophysical environments are known to accelerate charged particles

⁵This Chapter closely follows the discussion of E. Vitagliano, I. Tamborra and G. Raffelt, “Grand unified neutrino spectrum at Earth,” work in progress [2].

⁶This Section is partly based on the discussion in the Master’s Degree thesis: E. Vitagliano, “High energy events in IceCube: models and theory” [196].

like electrons, protons and heavier nuclei, which constitute the cosmic-ray flux. The latter then enter Earth atmosphere and produce the so-called secondary flux, which includes neutrinos.

4.1.1 Cosmic rays

To predict the neutrino flux, one needs to know the composition of cosmic rays, their scattering cross section with the atmosphere (as well as the possible energy losses), and the decay rate and branching ratios of the by-products. The relative abundances of cosmic rays can be compared to the chemical composition of the solar system, and one finds some interesting differences [195]. First, heavy nuclei are more abundant than hydrogen in the cosmic-ray flux; this could be due to the relative greater ionization energy of hydrogen compared to heavy elements, because atoms have to be ionized before being accelerated in cosmic-ray reservoirs [198]. Of course, an additional, straightforward reason for this feature could be a difference in the source composition itself. As a second striking difference, there are two groups of elements (Li, Be and B is one of them, the other one Sc, Ti, V, Cr and Mn) which are more abundant in cosmic rays than in the solar system. This is because they are not products of stellar nucleosynthesis, but are rather produced in spallation processes (scattering of cosmic rays in the interstellar medium) ([47] and references therein).

Besides the composition, another important ingredient of the primary flux is the energy spectrum. Above 10 GeV, a good approximation to the differential spectra per nucleon is given by an inverse power law:

$$\frac{dN_N}{dE} \propto E^{-(\gamma+1)}, \quad (4.1.1)$$

where $\gamma \approx 1.7$ up to around 3×10^6 GeV (for example, $\gamma_{\text{proton}} = 1.71 \pm 0.05$ [195]), and $\gamma \approx 2.0$ at larger energies. This break in the spectrum is known as the knee of the cosmic-ray flux. At very high energies (around 10^9 GeV) there is another break known as ankle. Including the normalization given in Ref. [47],

$$\frac{dN_N}{dE} = 1.8 \times 10^4 \left(\frac{E}{\text{GeV/nucleon}} \right)^{-(\gamma+1)} [(\text{GeV/nucleon}) \text{ m}^2 \text{ s sr}]^{-1}. \quad (4.1.2)$$

Below 10 GeV, all cosmic-ray spectra show time dependence, called solar modulation, due to the effects of the solar wind, a low-energy plasma of electrons and protons ejected by the Sun with 11 years cycle; the shield-like effect of the solar activity translates to an anti-correlation between the latter and cosmic-ray spectra. Moreover, low-energy particles entering the atmosphere are also subject to geomagnetic effects. Therefore, low-energy secondary particles, including neutrinos, will depend on location and time.

4.1.2 Conventional atmospheric neutrinos

Cosmic rays entering the atmosphere scatter and produce secondary particles as charged or neutral pions and kaons. At lower energies, the main contribution to atmospheric neutrinos comes from the so-called conventional neutrinos [193]. They are produced via two chains. The first one is

$$\begin{aligned} \pi^\pm &\rightarrow \mu^\pm + \nu_\mu(\bar{\nu}_\mu) \\ &\downarrow \\ e^\pm + \nu_e(\bar{\nu}_e) &+ \bar{\nu}_\mu(\nu_\mu) . \end{aligned} \quad (4.1.3)$$

The second chain starts from kaons, which can decay through e.g.

$$K^\pm \rightarrow \mu^\pm + \nu_\mu(\bar{\nu}_\mu) ; \quad (4.1.4)$$

kaons can also decay through three body decays,

$$K^\pm \rightarrow \pi^0 + e^\pm + \nu_e(\bar{\nu}_e) . \quad (4.1.5)$$

Note, however, that part of the kaons decay also in π^\pm without producing neutrinos, for example in processes such as

$$K^\pm \rightarrow \pi^\pm + \pi^0 . \quad (4.1.6)$$

Notice that cosmic rays also produce π^0 that decay to photons, which will be later important to establish the connection between high-energy astrophysical photons and neutrinos,

$$\pi^0 \rightarrow \gamma + \gamma . \quad (4.1.7)$$

Up to energies of 1 GeV all muons decay before reaching the ground level, implying the flavor ratio between muon and electron neutrinos

$$\frac{\nu_\mu + \bar{\nu}_\mu}{\nu_e + \bar{\nu}_e} \simeq 2 \quad (4.1.8)$$

At higher energies, where μ decay is negligible, both π and K decays are important. The flux is approximately given by [193]

$$\frac{dN_\nu}{dE_\nu} \simeq 0.0096 E_\nu^{-2.7} \left[\frac{1}{1 + \frac{3.7 E_\nu \cos \theta}{\epsilon_\pi}} + \frac{0.38}{1 + \frac{1.7 E_\nu \cos \theta}{\epsilon_K}} \right] \quad (4.1.9)$$

where ϵ is the energy scale which sets the most probable process in propagation (decay vs interaction); for pions and kaons, it is $\epsilon_\pi \simeq 115$ GeV and $\epsilon_K \simeq 850$ GeV. Note that asymptotically the neutrino production from π and K is one to three. The flavor is mainly muonic, with electron neutrinos becoming more negligible at high energies. This feature can be understood observing that at high enough energy the differential flux of muon neutrinos scales as $E^{-3.7}$, while electron neutrinos originating from muons have a flux which scales as $E^{-4.7}$, one of the power coming from the Lorentz

factor. When muons are too fast to decay, the electron neutrino flux is due to the decay of kaons, and it scales as $E^{-3.7}$ (just like the muon neutrino flux); anyway, its contribution at lower energies is disfavoured by the small branching ratio.

Let us conclude our discussion with some observations about the angular distribution of atmospheric neutrinos [193]. Consider neutrinos up to 1 TeV. At these energies, the Earth is transparent to neutrinos and the flux seen at the detector is totally isotropic. To understand this feature, imagine the atmosphere as made up of many sources; each source will produce a flux that scales as $1/r^2$, being r the distance from the source itself. A detector sees more sources from below the horizon than from above, but this is compensated by the bigger distance of sources below. At higher energies, the Earth is no more transparent to neutrinos. At energies up to $E_\nu \simeq 1$ PeV, neutrinos are more efficiently absorbed than antineutrinos (independently of the flavor) because they scatter on nuclei, while scattering on electrons is negligible. Nuclei in the Earth interior are heavy, and contain more neutrons (quark content udd) than protons (quark content uud); taking into account that neutrinos (respectively antineutrinos) can exchange a W boson with d (respectively u),

$$\nu + A \rightarrow l + B \quad (4.1.10)$$

is more probable than

$$\bar{\nu} + A \rightarrow l + B . \quad (4.1.11)$$

When the energy gets higher, valence quarks are negligible with respect to the sea quarks, so the u to d ratio is negligible and the cross sections of neutrinos and antineutrinos on nuclei become asymptotically equal. One needs to include, however, the Glashow resonance

$$e^- + \bar{\nu}_e \rightarrow W^- \rightarrow X \quad (4.1.12)$$

at $E_\nu \simeq m_W^2/2m_e \simeq 6$ PeV, so that there is a region in which $\bar{\nu}_e$ are more absorbed than ν_e . Moreover, at high energy there is anisotropy because horizontal kaons have more time to decay than vertical ones.

4.1.3 Prompt atmospheric neutrinos

Neutrinos produced by charmed mesons (in turn created via hadronic interactions) are called prompt neutrinos [199]. Their contribution to the total flux of atmospheric neutrinos was expected to be large in the TeV to PeV range ($\epsilon_{\text{charm}} \simeq \text{PeV}$), where the only other contribution is given by kaon decay. The latter is distinguishable from the prompt component thanks to its angular distribution; in fact, horizontal conventional atmospheric neutrinos are more abundant than vertical ones, because at higher energy kaons arrive before decaying, and obviously horizontal kaons have more time to decay than vertical ones.

Prompt neutrinos, instead, are isotropic up to high energies; this fact is related to the short life time of charmed mesons ($\tau \simeq 10^{-12}$ – 10^{-13} s), which decay before propagating for an appreciable length. Moreover, the prompt neutrino flux is harder than the conventional one, so that it will dominate over the conventional one beyond

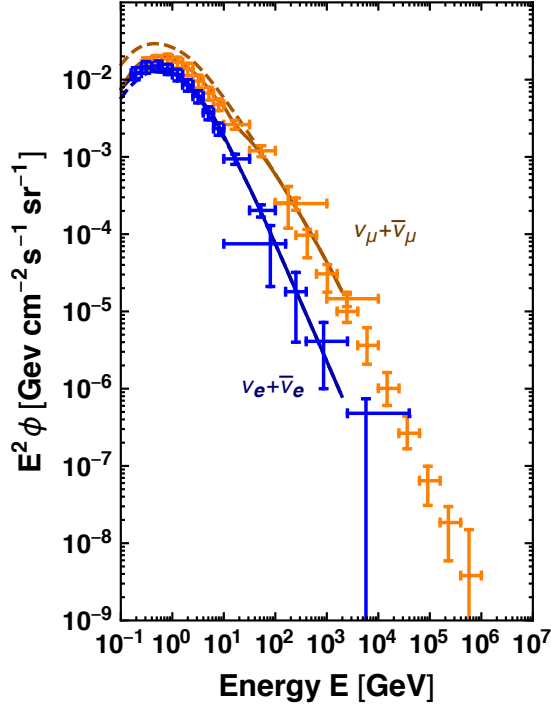


Figure 4.1: The atmospheric neutrino flux as a function of the neutrino energy, in orange $\nu_\mu + \bar{\nu}_\mu$, in blue $\nu_e + \bar{\nu}_e$. The data points reproduce the observations by Super-Kamiokande (low energy and medium energies) [203] and IceCube (high energies) [204, 205]. The dashed lines are the theoretical predictions at the Kamioka site of Ref. [206] when assuming maximal solar activity; the solid lines are the expected flux including flavor oscillations. I thank F. Capozzi for providing the Tables used to include oscillations.

a certain energy. Finally, charmed particles produce an equal number of electron and muon neutrinos in decay.

It should be stressed, however, that the IceCube collaboration has not found a significant contribution from prompt neutrinos to the atmospheric flux [200, 201]. Moreover, recent calculations (such as the one in Ref. [202]), accounting for the latest measurements of the hadronic cross sections, predict a prompt neutrino flux that is in general lower than its previous benchmark estimation.

4.1.4 Atmospheric neutrinos: predictions and observations

The production of atmospheric neutrinos due to cosmic rays is obtained by solving a set of transport equations, which are coupled integro-differential equations. While semi-analytical approximations are possible, a more reliable prediction of the flux can be obtained only numerically. In Fig. 4.1, I plot the data points of Super-Kamiokande (at low and medium energies, 10^{-1} – 10^3 GeV) [203] and IceCube (at high energies, 10^2 – 10^6 GeV) [204, 205]. We have already discussed Super-Kamiokande in Sec. 3.1.6; its contribution has been fundamental to test the hypothesis of neutrino oscillations by observing depletion in the atmospheric muon neutrino flux, which is dependent

on the zenith angle.

The IceCube Neutrino Observatory [207] is located at the National Science Foundation's Amundsen-Scott South-Pole Station. The experiment, successor of the Antarctic Muon And Neutrino Detection Array (AMANDA), is a Cherenkov detector in the clear Antarctica ice.

Let us turn to some features of the plot shown in Fig. 4.1. To reproduce the theoretically expected flux, I used the Tables publicly available on [Mitsuhito Honda's homepage](#) [206], which allow for a better comparison to data with respect to a semi-analytical approximation. As a location I chose Kamioka, because the spatial dependence is more important for low-energy neutrinos. Because we are not aiming for a high-precision fit, I considered the flux under the mountain in Kamioka and the Sun at its average magnetic activity, but a different choice would have not affected the broad features of the plot. The dashed lines show the flux before oscillations, whereas the solid lines include oscillations. As previously mentioned, the ν_μ to ν_e ratio is approximately 2 at low energies. The oscillation is especially important for muon neutrinos, as they can be converted to tau neutrinos en route to the Earth surface. At high energy, we see that the muon to electron neutrino ratio gets larger, as previously discussed.

A final remark concerns the uncertainties in the predicted neutrino flux. The authors of Ref. [208] have quantified the systematic uncertainties of atmospheric neutrino fluxes due to the choice of the primary cosmic-ray flux models and the interaction models employed. The average errors on the flux of muon and electron neutrinos at high were found to be $^{+32\%}_{-22\%}$ and $^{+25\%}_{-19\%}$ respectively.

4.1.5 Solar atmospheric neutrinos

An additional contribution to the GUNS comes from the Sun and is analogous to the atmospheric neutrinos previously described, the so-called solar atmospheric neutrino flux [197, 209, 210] (see Ref. [211] for a previous estimate). This flux is due to the interactions of cosmic rays in the solar atmosphere. The processes producing neutrinos are the same as in the Earth atmosphere, with the production of pions and kaons via hadronic interactions (and photohadronic interactions at energies larger than 1 PeV). However, the Sun atmosphere is thinner than the Earth one. While pions and kaons undergo many scatterings when produced in the terrestrial atmosphere, thus losing energy, these particles can propagate large distances in the solar atmosphere. This results in a solar atmospheric neutrino flux which is both larger and harder at high energies. While the detection of these neutrinos is not possible with on-going experiments, it would probe the magnetic field of the solar atmosphere, which has an effect on the low-energy part of the flux [197], as can be seen by the blue band in Fig. 4.2.

The fluxes represented in this figure are the ones from Fig. 1 of Ref. 4.2, where the authors assumed for the magnetic field the model [212] up to 300 GeV and the model [211] at larger energies. The terrestrial atmospheric flux is integrated over the solar angular cone, to show the amount of neutrinos we expect from that

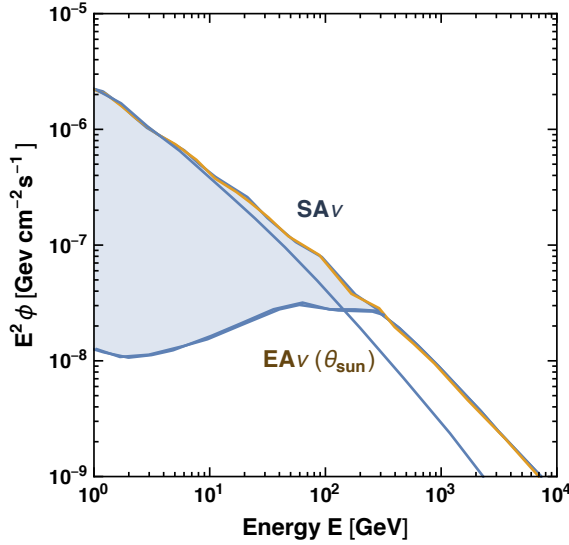


Figure 4.2: The solar atmospheric neutrino flux ($SA\nu$, blue) compared to the terrestrial one ($EA\nu$, orange), with the latter integrated over the solar angular cone (Ref. [197] and references therein). The uncertainty at low energies is due to the modelling of the magnetic fields at the solar surface and the ones carried by solar winds. Thanks to Kenny C.Y. Ng for providing the fluxes.

portion of sky. We should note however that the Sun atmospheric flux dominates only at around 4 TeV. One has to take into account the fact that muons coming from different directions can decay producing a neutrino whose direction lies in the solar angular cone; so, the muon-neutrino separation angle after the decay of the first is the angular cone to be considered when comparing the two fluxes [197]. For what concerns the flavor, oscillations decrease the muon flux by a factor of 2, within the uncertainty of predictions [197].

4.2 High-energy astrophysical neutrinos

4.2.1 Introduction

Associated to the acceleration of cosmic-ray particles, whose flux is given by Eq. (4.1.2), there is a flux of neutrinos of astrophysical origin. They are produced by the interactions of cosmic-rays in the source or in the environment surrounding the source, or while cosmic rays are propagating en route to Earth, just like atmospheric neutrinos are produced in the atmosphere. Neutrinos can be produced through proton-proton (“ pp ”) or proton-photon (“ $p\gamma$ ”) interactions. They are also known as hadronuclear and photohadronic interactions respectively, and both produce neutrinos and photons via the processes described in Sec. 4.1.2. The relative ratio between the neutrino and gamma-ray fluxes is approximately regulated by the ratio of π^0 and π^\pm produced in these sources. Notice however that photons can be also produced in processes not involving hadrons (inverse Compton scattering, bremsstrahlung).

Moreover, these fluxes are related to the cosmic-ray flux: this connection is at the

core of high-energy multi-messenger astronomy, which allows us to predict different messengers by knowing the flux of one of them. As perhaps expected, the dominating processes are the same ones which source the atmospheric neutrino flux, with some striking difference in the energy flux. The cosmic-ray flux is indeed softened by propagation in galactic and extra-galactic magnetic fields, as can be shown even by a simple propagation model as the leaky-box assumption. A more precise treatment, based on the Ginzburg-Syrovatskii equations, confirms that the flux of cosmic rays at the source is much harder [195]. Nowadays, propagation of cosmic rays is studied numerically with codes such as `GALPROP`. By comparing the secondary to primary ratio (using “cosmic clocks” like ^{10}Be) one finds that the effect of magnetic diffusion softens the cosmic-ray spectrum to

$$\frac{dN_N}{dE} \propto E^{-(\gamma+1)+\delta} \simeq E^{-2} , \quad (4.2.1)$$

where $\delta \simeq 0.6$ includes the effect of diffusion; intriguingly, the result is what we expected from pp sources, where acceleration is due to the first-order Fermi mechanism, a stochastic process in which cosmic rays get accelerated through a shock wave [195, 213]. Notice however that many approximations enter the expected flux of Eq. (4.2.1): the most important sources must be galactic, the precise softening could be different, and so forth. Moreover, the Fermi mechanism itself shall be modified when considering e.g. relativistic acceleration of particles [214], so that expressions more complicated than a single power-law should be used [215]. Given that neutrinos do not interact electromagnetically, they are not diffused by galactic and extra-galactic magnetic fields, so that the simplest prediction of their flux at Earth should be reminiscent of the cosmic-ray spectrum at the source,

$$\phi_\nu(E_\nu) \propto E_\nu^{-2} . \quad (4.2.2)$$

The diffuse neutrino intensity from extragalactic sources is more precisely given by the integral of the neutrino spectral distribution obtained for each sources, F_{ν_α} , convolved with the source distribution (a function of redshift and luminosity) over the co-moving volume $\dot{\rho}(z, L)$

$$\phi(E_\nu) = \frac{1}{4\pi} \int_0^\infty dz \int_{L_{\min}}^{L_{\max}} dL \frac{1}{H(z)} \dot{\rho}(z, L) \sum_\alpha F_{\nu_\alpha} [(1+z)E_\nu] , \quad (4.2.3)$$

with $H(z)$ being the Hubble factor at redshift z . The existence of the knee in the cosmic-ray spectrum suggests that an educated guess for the neutrino flux should be

$$F_{\nu_\alpha}(E_\nu) \propto \begin{cases} E_\nu^{-s} & (E_\nu \leq E_\nu^b) \\ E_\nu^{-s'} & (E_\nu^b < E_\nu) \end{cases} \quad (4.2.4)$$

where E_ν^b is the energy at the break of the neutrino spectrum, and s and s' are power-law exponents that depend on the specific production mechanism. For example, $p\gamma$ scenarios can predict $s \simeq 0$, which is due to the increasing optical depth to

photomeson production with increasing energy of cosmic rays; on the other hand, in pp scenarios $s \simeq 2$ [216]. I should stress that this is a very simple approximation, because many different breaks can be present in the neutrino spectrum. Moreover, the neutrino flux produced by a class of sources should have a cut-off corresponding to the maximum possible energy, which is typically modelled as an exponential.

The final ingredient for a theoretical prediction of the astrophysical neutrino flux is the flavor content. According to the standard production scenario described above, the following flavor ratio is obtained at the production site: $\nu_e : \nu_\mu : \nu_\tau \simeq 1 : 2 : 0$. After flavor conversions, the oscillation-averaged composition reaching the detector is expected to be $\nu_e : \nu_\mu : \nu_\tau \simeq 1 : 1 : 1$ [217].

4.2.2 Detection and multi-messenger constraints

Despite such simple predictions, observations have proven once more that Nature can be more complicated than our expectations. As previously discussed, direct correlation between the TeV–PeV neutrinos and the ultra-high-energy cosmic rays is supposed to exist, but no clear evidence has been found yet. The production of cosmic rays is thought to be of extragalactic origin above the knee, while it is expected to be mainly of galactic origin below those energies. As already mentioned, cosmic rays could be trapped within the sources because of strong magnetic fields and hence produce neutrinos through collisions with the gas. The efficiency of this process is related to the total energy stored in the source under the assumption that the source is calorimetric. The observation of cosmic rays allows one to establish an upper bound on the flux of neutrinos of astrophysical origin produced by cosmic accelerators under the assumption that they behave as calorimeters, the so-called Waxman-Bahcall bound [218, 219],

$$E_\nu^2 \phi_\nu \lesssim 2 \times 10^{-8} \text{ GeV}/(\text{cm}^2 \text{ s sr}) . \quad (4.2.5)$$

The Waxman-Bahcall bound should be considered as an upper limit on the neutrino production from the sources of ultra-high-energy cosmic rays under the assumption that the spectrum scales as E^{-2} . Notice that the Waxman-Bahcall bound was derived under the assumption that sources are optically thin to photo-meson and proton-nucleon interactions such that protons are free to escape from the source. If optically thick sources exist, then this bound does not hold anymore.

The era of high-energy neutrino astronomy was born with the first detection of neutrinos of astrophysical origin by the IceCube Neutrino Observatory [201, 220, 221]. The IceCube events have energies in the range between few TeV to few PeV [201, 220, 221]; these neutrino events are isotropically distributed. This suggests that only up to $\sim 1\%$ of the observed flux may come from our Galaxy [222]. A more copious amount of neutrinos is instead expected from sources distributed on cosmological scales, such as dim or choked astrophysical jets, starburst galaxies, gamma-ray bursts, and active galactic nuclei. Therefore there are many possible sources to high-energy neutrinos, and many puzzles remain to be solved. We will discuss some of these possibility in Sec. 4.3.

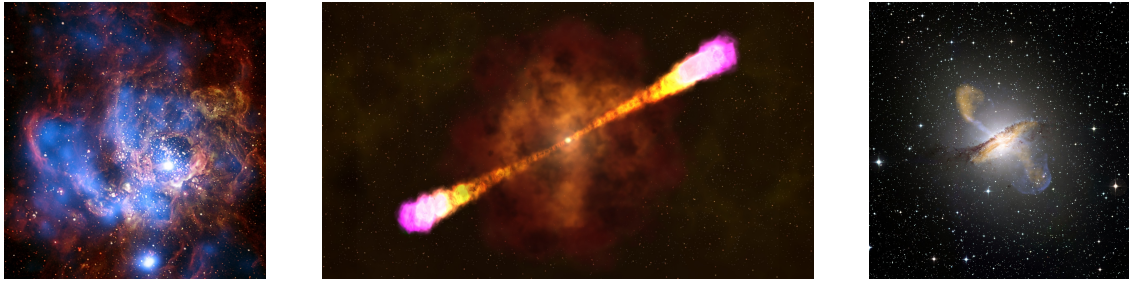


Figure 4.3: Examples of neutrino sources include star-forming galaxies, gamma-ray bursts and blazars. *Left panel:* star-forming galaxy NGC 694, credit: X-ray: NASA/CXC/CfA/R. Tuellmann et al., optical: NASA/AURA/STScI. *Central panel:* illustration of a gamma-ray burst, credit: NASA/GSFC. *Right panel:* active galactic nuclei Centaurus A; blazars are AGNs with the jet pointing towards the Earth; credit: visible: ESO/WFI, microwave: MPIfR/ESO/APEX/A.Weiss et al., X-ray: NASA/CXC/CfA/R.Kraft et al.

Assuming that all particles populating the high-energy sky originate from the same source classes, the cosmic energy density of high-energy neutrinos should be directly comparable to the one of gamma rays observed by the Fermi telescope [223] and to the one of ultra-high-energy cosmic rays seen by the Auger observatory [224]. The extra-galactic gamma-ray background observed by Fermi consists of point-like sources and an isotropic gamma-ray background. The IceCube data set cannot be consistently interpreted by employing the same composition of sources currently estimated for the Fermi extra-galactic background. This is especially true for the region between 10 and 100 TeV in the neutrino spectrum that cannot be fitted by invoking a common origin for neutrinos and gamma rays, see e.g. [225] and references therein.

Considering further experimental efforts in the field of high-energy neutrino astronomy, IceCube-Gen2 [226] is currently under planning. Another upcoming detector is KM3NeT [227] which will have better sensitivity to Galactic sources. Concerning neutrino energies above the PeV range, GRAND [228] is currently being designed and developed. ARIANNA [229], an hexagonal radio array, has already delivered the first constraints on cosmogenic neutrinos. ARA, the Askaryan Radio Array, is currently being developed [230]. POEMMA [231] is currently being designed for the detection of cosmogenic tau neutrinos.

4.3 Astrophysical sources of high-energy neutrinos

Although high-energy neutrinos are emitted by a plethora of astrophysical sources, in the following I will focus on star-forming galaxies (pp sources), gamma-ray bursts and active galactic nuclei ($p\gamma$ sources). Those are the most efficient neutrino emitters either because they are very abundant or because they are especially bright in neutrinos. In particular, for what concerns active galactic nuclei, I will focus on a sub-class, blazars, currently estimated to compose the bulk of the extra-galactic gamma-ray diffuse emission [232]. Notably, a dozen of IceCube neutrino events is likely to be emitted by TXS 0506+056, a very high-energy blazar [233, 234]. The

non-detection of point sources generating multiple neutrino events from astrophysical sources provides a lower limit on the local density of these sources and an upper limit on their effective neutrino luminosity [235, 236]. Finally, I will discuss the predicted flux of very high-energy cosmogenic neutrinos, produced by cosmic-ray interactions en route to Earth. I refer the interested reader to Refs. [225, 237–240] for recent dedicated reviews on the topic.

4.3.1 Star-forming galaxies

Star-forming galaxies are stationary sources compared to gamma-ray bursts and active galactic nuclei that will be discussed in the following subsections. Star-forming galaxies are perfect examples of calorimetric sources and have been proposed as neutrino reservoirs [239, 241]. Beyond normal galaxies, such as our Milky Way, another class of star-forming galaxies consists of starburst galaxies. These are individually more luminous as they undergo a phase of enhanced star-formation activity (up to 100 times higher than normal galaxies).

Our understanding of star formation has dramatically improved in the last decade. In particular, the Herschel Space Observatory [242] provided an unprecedented estimation of the infrared luminosity function of star-forming galaxies up to redshift 4 and made possible the distinction among different sub-classes of star-forming galaxies. In fact, beyond normal galaxies and starburst galaxies, Herschel provided for the first time information on star-forming galaxies containing low-luminosity active galactic nuclei (AGNs) or AGNs obscured by dust. All these classes contribute to the star-formation activity.

Among the known galaxies, about 38% are normal galaxies, 7% are starburst galaxies, and the remaining ones are star-forming galaxies containing AGNs. The abundance of each of these classes varies as a function of the redshift, with the normal galaxies being more abundant at low redshifts ($z < 1.5$). The gamma-ray energy spectral distribution of normal galaxies is observed to be softer ($F_\gamma \propto E_\gamma^{-2.7}$) on average than the one of starburst galaxies ($F_\gamma \propto E_\gamma^{-2.2}$). Finally, star-forming galaxies containing AGNs can have an energy spectral distribution resembling normal galaxies or starburst galaxies according to the redshift [243].

Neutrinos are thought to be produced in star-forming galaxies through pp interactions under the assumption that 100 PeV cosmic rays are produced and confined in these sources. As a consequence, a direct connection between the estimated neutrino and gamma-ray emission can be established.

The Fermi Telescope has recently provided tight constraints on the composition of the diffuse extra-galactic gamma-ray sky [232, 244]. By relying on the electromagnetic emission of these sources, one can estimate the correspondent neutrino diffuse emission following the modeling proposed in [243, 244] and by applying the following relation

$$\sum_{\nu_\alpha} \phi_{\nu_\alpha}(E_{\nu_\alpha}) \simeq 6\phi_\gamma(E_\gamma) , \quad (4.3.1)$$

with $E_\gamma \simeq 2E_\nu$, and ϕ_γ the gamma-ray diffuse intensity.

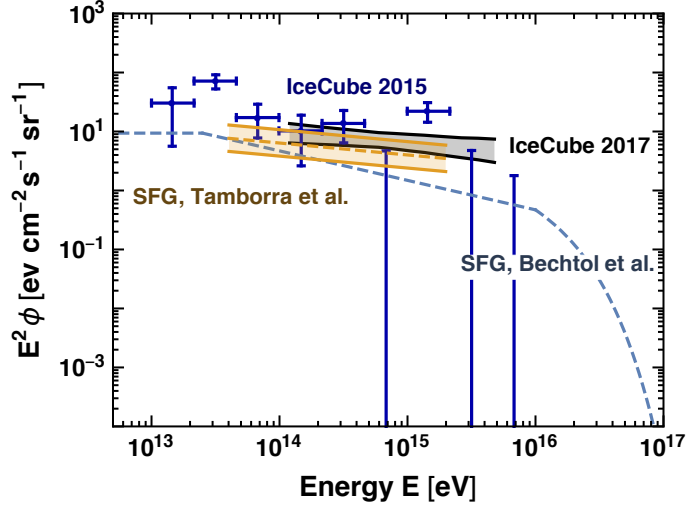


Figure 4.4: The neutrino flux per flavor $\nu_\alpha + \bar{\nu}_\alpha$ from star-forming galaxies. The dashed purple line reproduces the results from [244], where an upper limit to the blazars contribution was calculated by analyzing the gamma-ray flux. The orange band reproduce the results of Ref. [243]. Notice that the spectrum shape is slightly different as there is some uncertainty in the injection spectral shape. Also shown is the per-flavor IceCube neutrino flux according to [245] (blue data points) and a more recent estimate [246] (black band).

The expected ϕ_{ν_α} from star-forming galaxies as a function of the neutrino energy is shown in Fig. 4.4. These results are in agreement with current tomographic constraints [247]. Notably, the detection of neutrinos from stacked searches of star-forming galaxies is currently statistically disfavored [235, 236, 248].

4.3.2 Gamma-ray bursts

Gamma-ray bursts (GRB) are among the most energetic transients in our Universe. GRBs are usually divided in long (> 2 s) and short (< 2 s) duration bursts according to the electromagnetic observation by BATSE [249]. Long-duration GRBs are thought to originate from the death of massive stars and they are usually distinguished in low-luminosity and high-luminosity GRBs according to their isotropic luminosity.

High-luminosity GRBs are routinely observed by Swift and the Fermi-GBM, they are characterized by a Lorentz boost factor of $\Gamma \simeq 500$ and isotropic luminosity of about 10^{52} erg/s. While we know less of the low-luminosity GRBs mostly because these sources are dimmer, with a typical isotropic luminosity of about 10^{48} erg/s, and therefore more difficult to observe. Low-luminosity GRBs are observed to have a Lorentz factor one order of magnitude lower than high-luminosity GRBs.

GRBs produce high-energy neutrinos mostly through $p\gamma$ interactions. In particu-

lar, the main reactions leading to the neutrino production are

$$p + \gamma \rightarrow \Delta \rightarrow n + \pi^+ \text{ or } p + \pi^0 \quad (4.3.2a)$$

$$p + \gamma \rightarrow K^+ + \Lambda/\Sigma ; \quad (4.3.2b)$$

in turn, the pions, muons, kaons and neutrons decay to neutrinos of muon and electron flavor [250]. Usually the injected gamma-ray spectrum is parametrized through a band-spectrum (broken power law) with a break energy defined as a function of the isotropic energy. Because the interactions are $p\gamma$ and the proton spectrum is proportional to E_p^{-2} (without breaks), the resultant neutrino spectrum will have a break in correspondence with the break energy of the photon spectrum. Above the first break, the neutrino spectrum should be the same as the proton spectrum. However processes such as radiative, hadronic and adiabatic cooling affect the observable neutrino spectrum via other breaks at higher energies [251].

Neutrinos from GRBs could in principle show up at IceCube, however neutrino events are not in spatial and time correlation with known GRBs, constraining the proposed theoretical models. High-luminosity GRBs are also excluded as main sources of the diffuse high-energy neutrino flux observed by IceCube [238]. However, low-luminosity or choked GRBs could produce high-energy neutrinos abundantly and partially explain the IceCube neutrino events. A choked GRB is characterized by a jet successful in accelerating particles but such that the electromagnetic radiation is not able to escape from the envelope. Moreover, choked jets have been invoked to explain the neutrino data in the low-energy tail of the spectrum but this seems not to be the case [216, 252].

Figure 4.5 shows the neutrino emission in flavor and mass eigenstates from long-duration GRBs. It has been obtained according to the advanced model presented in Fig. 5 of [253]. The astrophysical uncertainty is based on the error in the measurement of the local star-formation rate [254].

Short GRBs have typical luminosities similar to the ones of long high-luminosity GRBs but originate from compact binary mergers. They do not copiously produce neutrinos because of the merger distribution on cosmic scales [251]. However, a sizable neutrino flux could be foreseen if e.g. one invokes a large fraction of magnetars connected to these bursts [255].

4.3.3 Blazars

Active galactic nuclei are mainly powered by the mass accretion onto supermassive black holes at the center of their host galaxy [256]. AGNs are among the most luminous sources of electromagnetic radiation. They have been considered as powerful high-energy cosmic accelerators [240].

AGNs have been divided in radio quiet and radio loud objects. The radio-loud objects are characterized by an emission from the jet and the lobes that is especially prominent at radio wavelengths, while in the radio-quiet objects the continuum emission comes from the core regions and the jet-related emission is weak. Radio-loud AGNs are promising cosmic accelerators and neutrino reservoirs.

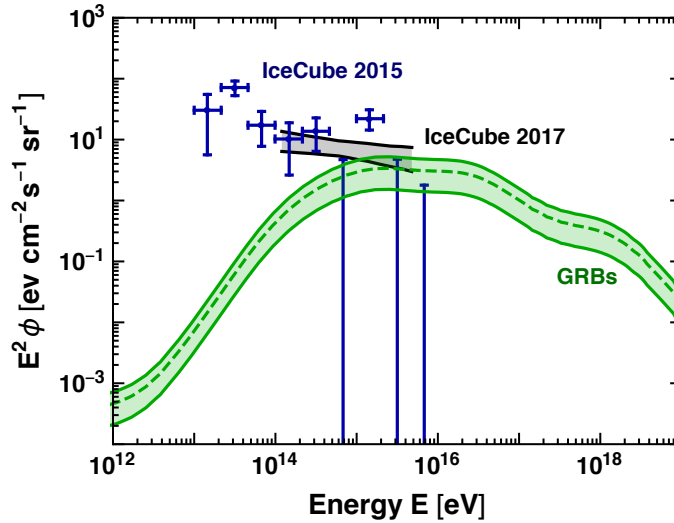


Figure 4.5: The neutrino flux per flavor $\nu_\alpha + \bar{\nu}_\alpha$ from gamma-ray bursts [253]. The bands reproduce the uncertainty of the measured local star-formation rate [254]. Also shown is the per-flavor IceCube neutrino flux according to [245] (blue data points) and a more recent estimate [246] (black band).

Blazars are a special kind of loud AGNs with the jet pointing towards us. Blazars are characterized by extreme variability and strong emission over the entire electromagnetic spectrum. Blazars are divided into BL Lacertae objects (BL-Lacs) and flat spectrum radio quasars (FSRQs). Those two categories have different optical spectra, the latter showing strong and broad emission lines and the former characterized by optical spectra with weak emission lines.

In the following, I will focus on the neutrino production from blazars as they are expected to be rich neutrino factories. However, note that also radio-quiet AGNs may contribute to the diffuse neutrino background [240], although the neutrino production is affected by large uncertainties.

The photon spectrum of blazars is characterized by two broad bumps [256]. The low-energy peak can occur at frequencies ranging from 0.01 to 13 keV while the high-energy peak can be in the range between 0.4 and 400 MeV. The low-energy emission of blazars comes from electron synchrotron radiation with the peak frequency being related to the maximum energy at which electrons can be accelerated. On the other hand, the origin of the high-energy emission is still under debate, it might originate from inverse Compton radiation or may be coming from proton synchrotron radiation.

The neutrino emission depends on the blazar luminosity function. In fact the electromagnetic spectrum evolves with the blazar luminosity, the so-called blazar sequence. Neutrino production becomes more efficient through $p\gamma$ interactions when the photon luminosity is larger. Given their abundance and brightness, the detection

of neutrinos from stacked searches of blazars is statistically favored [235, 236, 248].

BL-Lacs produce up to 40–70% of the gamma-ray diffuse radiation in the 0.1–10 GeV range. Assuming that neutrinos are produced in these environments through $p\gamma$ interactions, the gamma-ray and the neutrino luminosity from blazars may be connected through an efficiency factor $Y_{\nu\gamma}$ varying between 0.1 and 2, so that $L_\nu = Y_{\nu\gamma} L_\gamma$ [257].

The main paradigm is that the gamma-ray emission from these sources has a photo-hadronic origin. In fact, high-energy protons are accelerated through diffusive shock acceleration or stochastic acceleration in the jet. Protons then interact with synchrotron photons coming by the non-thermal electrons that are co-accelerated in the jets.

In order to estimate the neutrino production from the blazar population, it is useful to rely on the so-called blazar sequence, i.e. an empirical relation between the blazar luminosity and the photon spectral energy distribution. Although one can assume a distribution in the Lorentz factor of the jet, $\Gamma = 10$ is here assumed as a representative value during a typical flaring period of 10^6 s. Cosmic rays undergo Fermi acceleration and assume a power-law energy distribution $F_p(E) = E_p^{-2} \exp(-E/E_{\max})$ with E_{\max} the maximum energy that cosmic rays have in the source. In $p\gamma$ interactions, neutrinos carry about 5% of the energy of the primary proton.

The target photon field is determined according to the blazar sequence [258]. Beyond synchrotron and inverse Compton peaks present in the BL-Lac spectral energy distribution, FSRQs typically exhibit broad lines from atomic emission of the gas surrounding the accretion disk. By deriving the neutrino spectral energy distribution from the gamma-ray one and by relying on the blazar distribution at cosmological distances as from Fermi [259, 260], Ref. [261] estimated the neutrino diffuse emission from blazars by imposing bounds on the non-observation of neutrino events from dedicated stacking searches and by assuming that the baryonic loading varies with the luminosity as a power law. The neutrino production from FSRQs is estimated to be about 30% of the BL-Lac one [262].

Figure 4.6 shows the neutrino emission per flavor eigenstate from blazars. It has been obtained from scenario 3 presented in Ref. [261].⁷ I also show a possible multi-component fit [263], which includes also residual atmospheric background and galactic contributions. Notice however that there is no consensus regarding the latter contributions, implying hints of tension between the measurements of the diffuse gamma-ray flux detected by Fermi-LAT and the neutrino flux detected by IceCube. The reason is simple: we observe more neutrinos than expected from measurements of gamma rays. As already mentioned, possible solutions invoking cosmic accelerators that are optically thicker than expected, such as in the case of choked GRBs [216], do not seem to be viable [252]. It is tempting to speculate if this could be a signal of physics beyond the Standard Model; this will be the topic of Sec. 7.

⁷Thanks to A. Palladino for providing the data used in Fig. 4.6.

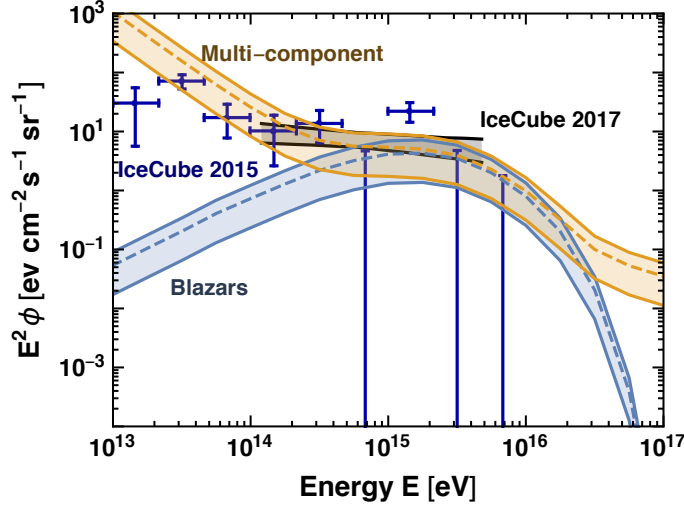


Figure 4.6: The neutrino flux per flavor $\nu_\alpha + \bar{\nu}_\alpha$ [261]. The bands reproduce the possible variations (1σ) due to the uncertainties on the modeling of the neutrino emission. Also shown is the per-flavor IceCube neutrino flux according to [245] (blue data points) and a more recent estimate [246] (black band). The orange band reproduce a possible multi-component fit [263], which includes also residual atmospheric background and galactic contributions.

4.3.4 Cosmogenic neutrinos

Ultra-high-energy cosmic rays (UHECR) have energies up to 10^{20} eV; these are the particles with the highest energy observed in Nature [264]. The sources producing such particles and the mechanisms behind their acceleration are unknown. Possible acceleration sites may be young pulsars, active galactic nuclei, gamma-ray bursts, magnetars and tidal disruption events. Results from the Auger experiment suggest a light composition at 1 EeV which tends to become heavier as the energy increases [265]. Telescope Array (TA) seem to confirm this trend excluding a purely proton dominated composition [266].

On their way to Earth, UHECR interact with radiation, specifically with the cosmic microwave background (CMB) and the extragalactic background light (EBL), which is the cosmic population of photons e.g. in the infrared wavelength range. The energy spectrum of nucleons is mostly affected by the CMB because of pair production and photo-pion production, whereas the energy spectrum of heavier nuclei is affected by the EBL through pair production and photo-disintegration. The photo-pion process occurs when nucleons (N) with Lorentz factor $\Gamma \geq 10^{10}$ interact with the CMB and pions are produced ($N + \gamma \rightarrow N + \pi^{0,\pm}$). For lower Γ , the same process can take place with the EBL. The strong flux suppression at high energies coming from the photo-pion production is responsible for the so-called Greisen-Zatsepin-Kuzmin (GZK) cutoff. Photodisintegration takes place when UHE

nuclei are stripped by one or more nucleons by interacting with the CMB or EBL,

$$(A, Z) + \gamma \rightarrow (A - n, Z - n') + nN \quad (4.3.3)$$

with $n(n')$ being the number of stripped nucleons. Mesons produced during these interactions quickly decay and produce a flux of cosmogenic neutrinos. The beta-decay of nucleons and nuclei from the photo-disintegration can also lead to the production of neutrinos. However, while the neutrinos produced from pion decay have energies that are few percent of the parent nucleus, the neutrinos produced from beta decay carry less than one part per thousand of the energy of the parent nucleon.

The cosmogenic neutrino spectrum is also sensitive to the maximum energy of UHECR and heavy composition at the source (or a weaker evolution of cosmic-ray sources) tends to produce a significantly lower cosmogenic neutrino flux [267]. The largest contribution is instead obtained if one assumes a proton source. This is however currently disfavored by Fermi data [268].

Interestingly, while the cosmic-ray spectrum is dominated by nearby sources, the neutrino flux will receive contributions up to cosmological scales. Moreover, the cosmogenic neutrino flux will also change according to the assumed source composition [267, 269].

Cosmogenic neutrinos have not been detected yet. The IceCube Neutrino Observatory recently placed upper limits on the non-detection of the cosmogenic neutrino flux [270]. Notably, the non-observation of those neutrinos also disfavors sources with a cosmological evolution that is stronger than the one predicted from the star-formation rate, such as active galactic nuclei [270], if one assumes a proton composition at the source. I show the predicted flux in Fig. 4.7, where I reproduce the results reported in [271]. The exclusion measurements obtained by ANITA and Auger are respectively shown in green and orange [272]. The next generation of radio facilities, such as the Giant Radio Array for Neutrino Detection (GRAND), and the Antarctic Ross Ice-Shelf ANTenna Neutrino Array (ARIANNA), will be able to detect this flux, the contribution to the highest energy range in the GUNS.

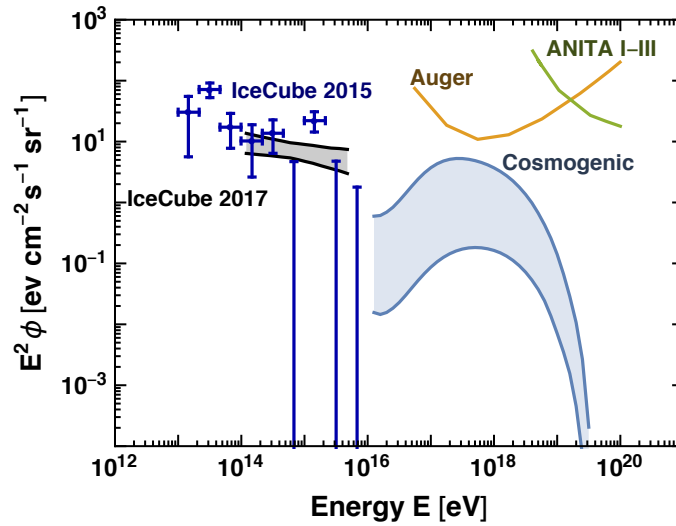


Figure 4.7: The cosmogenic neutrino flux per flavor $\nu_\alpha + \bar{\nu}_\alpha$ from [271]. The bands reproduce the largest possible variations due to the uncertainties on the ultra-high-energy cosmic ray composition and source redshift evolution. The exclusion measurements obtained by ANITA and Auger are respectively shown in green and orange [272]. Also shown is the per-flavor IceCube neutrino flux according to [245] (blue data points) and a more recent estimate [246] (black band).

Filling a gap in the GUNS: Solar keV neutrino emission⁸

The nuclear reactions in the Sun produce the usual solar neutrino flux of about $6.6 \times 10^{10} \text{ cm}^{-2} \text{ s}^{-1}$ with MeV energies. At Earth this is the largest neutrino flux, except perhaps in the immediate vicinity of a nuclear power reactor. However, besides the flux due to nuclear reactions, the Sun produces neutrino-antineutrino pairs by thermal processes triggered by electromagnetic interactions of the particles making up the plasma: electrons, ions and photons.

Thermal neutrino emission from stars is an old topic, central to the physics of stellar evolution, and detailed studies exist as well as Computer routines to be coupled with stellar evolution codes [274]. However, in this context neutrinos play the role of a local energy sink for the stellar plasma and so the emission spectrum is not provided. Moreover, for a low-mass main-sequence star like our Sun, energy loss by thermal neutrinos is negligible. Therefore, standard energy-loss rates, which cover a large range of temperatures, densities and chemical compositions, may not be optimized for solar conditions. This is a standard neutrino flux, yet it is conspicuously absent from previous plots of the GUNS at Earth [22]. The only detailed previous study of the keV range solar flux [275] ignores bremsstrahlung production and overestimates photo production by a spurious plasmon resonance. This situation provided motivation for a fresh look, which takes advantage of recent progress in calculating the keV-range solar flux of other low-mass particles such as axions and hidden photons [276–281].

5.1 General features of the thermal flux from the Sun

Low-energy neutrinos are produced in the solar plasma by the pair-production processes shown in Fig. 5.1. The various neutrino flux contributions can be listed in a mnemonically helpful way as ABCD processes: atomic deexcitation, including free-bound (fb, also known as electron capture or recombination) and bound-bound

⁸This Chapter closely follows the discussion of E. Vitagliano, J. Redondo and G. Raffelt, “Solar neutrino flux at keV energies,” *JCAP* **12** (2017) 010, [arXiv:1708.02248](https://arxiv.org/abs/1708.02248) [273].

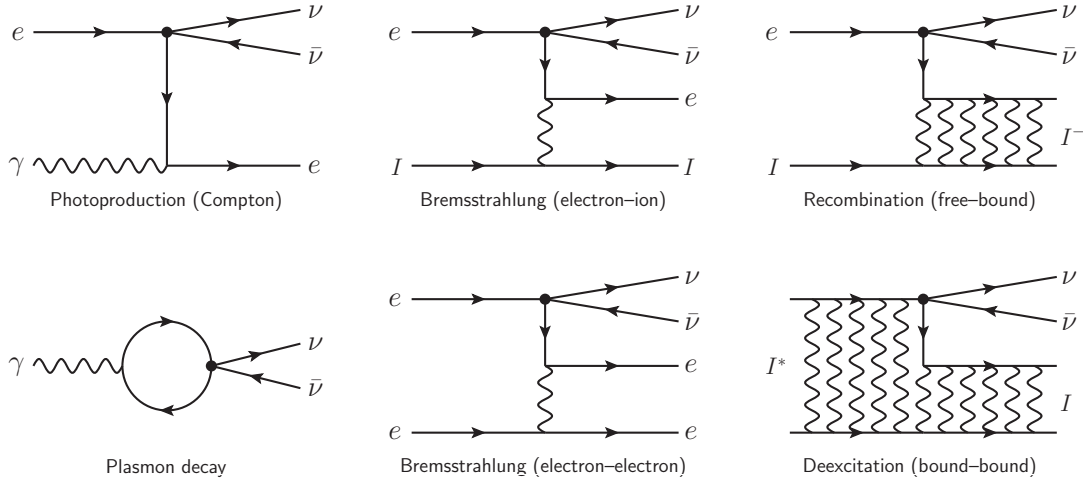


Figure 5.1: Processes for thermal neutrino pair production in the Sun.

(bb) processes; bremsstrahlung, including free-free (ff, atomic bremsstrahlung) and electron-electron (ee) interactions; Compton scattering; and plasmon decay, i.e., the decay of a photon, which is kinematically allowed thanks to its dispersion relation in a medium. In all these processes, nonrelativistic electrons are the sources. Electron velocities and spins are “kicked” by the ambient electromagnetic fields, leading to the emission of neutrino pairs. At low energies, the weak interaction is sufficiently well described by an effective four-fermion local interaction proportional to the Fermi constant G_F . The effective coupling constants for the vector and axial-vector interaction, C_V and C_A , are different for ν_e and the other flavors, leading to a nontrivial flavor dependence of the emitted fluxes. The vector-current interaction leads essentially to electric dipole radiation caused by the time variation of the electron velocity, whereas the axial-vector current leads to magnetic dipole radiation caused by fluctuations of the electron spin. Yet in the nonrelativistic limit, the rates for both mechanisms are related by simple numerical factors and there is no interference between them, so all processes provide rates proportional to $(a C_V^2 + b C_A^2) G_F^2$ with coefficients a and b that depend on the specific emission process. One consequence of this simple structure is that the emission rates are closely related to those for axions (axial current interaction) or hidden photons (vector current interaction) and also closely related to photon absorption rates. We will take full advantage of these similarities, i.e., the relation between these different processes by simple phase-space factors.

In Fig. 5.2 I show the overall low-energy solar neutrino and antineutrino flux at Earth from our calculation, obtained using the solar model described in App. C. All thermal processes shown in Fig. 5.1 produce $\nu\bar{\nu}$ pairs and thus equal fluxes of neutrinos and antineutrinos. This equipartition is another consequence of the nonrelativistic approximation, where weak magnetism effects disappear along with $C_V C_A$ cross terms in the emission rate [282]. In addition, the low-energy tail of the neutrino spectrum produced in the nuclear pp reaction contributes significantly to the keV flux. At the source, this reaction produces ν_e which, like the other channels,

have decohered into their mass components long before they reach Earth. The pp flux causes an overall asymmetry between the keV-range ν and $\bar{\nu}$ spectra. The fractional contribution of the 1, 2 and 3 mass eigenstates arriving at Earth are shown in the lower panels of Fig. 5.2. Different emission processes have different energy dependences and there are different coefficients ($aC_V^2 + bC_A^2$) for ν_e and the other flavors, thus explaining the fractional flux variation.

Besides being an interesting signal *per se*, we shall study solar neutrinos as background to dark matter searches. It is indeed a remarkable shift of paradigm that solar neutrinos today, fifty years after their first detection, are part of the “neutrino floor,” the dominant background for direct searches of dark matter in the form of weakly interacting massive particles (WIMPs). Another well-motivated dark matter candidate is a sterile neutrino in the keV mass range [283]. One idea for a direct search is the sterile-neutrino capture on a stable isotope of dysprosium if $m_s > 2.83$ keV [284]. Other searches for slightly heavier sterile neutrinos include unstable isotopes [285, 286], coherent inelastic scattering on atoms [287] and electron

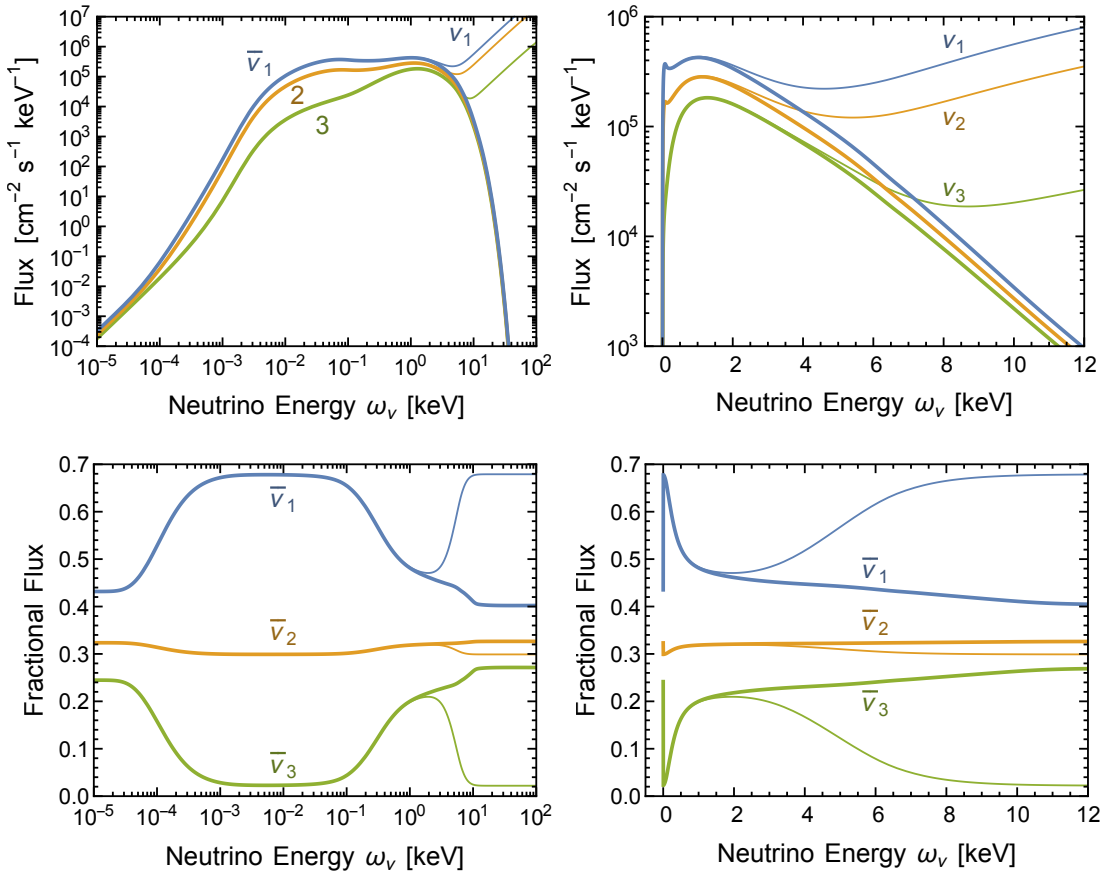


Figure 5.2: Solar neutrino flux at Earth in the keV range. The flavor dependence is given in the mass basis for the 1, 2 and 3 mass eigenstates (blue, orange and green). Thick lines are for $\bar{\nu}$, thin lines for ν which includes a contribution from the nuclear pp reaction which produces only ν_e at the source. The other source channels are thermal reactions which produce ν and $\bar{\nu}$ in equal measure. The bottom panels show the fractions of the total flux provided by the individual mass eigenstates.

scattering [288]. Once again, solar neutrinos could be a limiting background, now those with keV energies that emerge from various thermal processes in the solar plasma which has a typical temperature of 1 keV. While this idea is futuristic with present-day technology, it gives us another motivation to consider keV-range solar neutrinos.

5.2 Plasmon decay

5.2.1 Matrix element

We begin our calculation of neutrino pair emission from the solar interior with plasmon decay, $\gamma \rightarrow \nu\bar{\nu}$, the process of Fig. 5.1 involving the smallest number of participating particles. This process is also special in that it has no counterpart for axion emission. In any medium, electromagnetic excitations with wave vector $k = (\omega, \mathbf{k})$ acquire a nontrivial dispersion relation that can be written in the form $\omega^2 - \mathbf{k}^2 = \Pi(\mathbf{k})$, where $\Pi_{\mathbf{k}} = \Pi(\mathbf{k})$ is the on-shell polarization function. I will always consider an unmagnetized and isotropic plasma. It supports both transverse (T) modes, corresponding to the usual photons, and longitudinal (L) modes, corresponding to collective oscillations of electrons against ions. Whenever $\Pi_{\mathbf{k}} > 0$ (time like dispersion), the decay into a neutrino pair, taken to be massless, is kinematically allowed. For both T and L modes, neutrino pairs are actually emitted by electrons which oscillate coherently as a manifestation of the plasma wave.

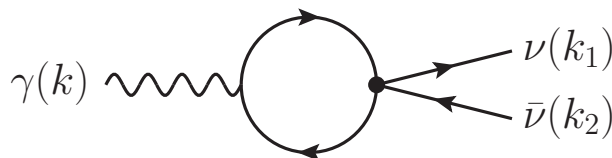


Figure 5.3: Plasmon decay mediated by electrons of the medium.

Therefore, plasmon decay and actually all other processes significant for thermal pair emission in the Sun depend on the neutrino-electron interaction. At low energies, it is given by the effective neutral-current interaction

$$\mathcal{L}_{\text{int}} = \frac{G_{\text{F}}}{\sqrt{2}} \bar{\psi}_e \gamma^\mu (C_{\text{V}} - C_{\text{A}} \gamma_5) \psi_e \bar{\psi}_\nu \gamma_\mu (1 - \gamma_5) \psi_\nu, \quad (5.2.1)$$

where G_{F} is Fermi's constant. The effective vector (V) and axial-vector (A) coupling constants include a neutral-current contribution and for ν_e also a charged-current piece from W^\pm exchange. Altogether one finds

$$C_{\text{V}} = \frac{1}{2}(4 \sin \Theta_{\text{W}} + 1) \quad \text{and} \quad C_{\text{A}} = +\frac{1}{2} \quad \text{for } \nu_e, \quad (5.2.2a)$$

$$C_{\text{V}} = \frac{1}{2}(4 \sin \Theta_{\text{W}} - 1) \quad \text{and} \quad C_{\text{A}} = -\frac{1}{2} \quad \text{for } \nu_\mu \text{ and } \nu_\tau, \quad (5.2.2b)$$

where $4\sin^2\Theta_W = 0.92488$ in terms of the weak mixing angle. In particular, this implies that the rates of A processes, proportional to $C_A^2 = 1/4$, are the same for all flavors. On the other hand, the rates for V processes are proportional to

$$C_V^2 = 0.9263 \text{ for } \nu_e\bar{\nu}_e \quad \text{and} \quad C_V^2 = 0.0014 \text{ for } \nu_{\mu,\tau}\bar{\nu}_{\mu,\tau}. \quad (5.2.3)$$

Thus for heavy-lepton neutrinos we may safely ignore the vector-current interaction, i.e., such processes produce an almost pure $\nu_e\bar{\nu}_e$ flux.

Plasmon decay has been extensively studied in the literature [289–293]. The squared matrix element for the transition $\gamma \rightarrow \nu\bar{\nu}$ with photon four-momentum $k = (\omega, \mathbf{k})$ and ν and $\bar{\nu}$ four momenta $k_1 = (\omega_1, \mathbf{k}_1)$ and $k_2 = (\omega_2, \mathbf{k}_2)$ is found to be (see Fig. 5.3),

$$|\mathcal{M}_{\gamma \rightarrow \nu\bar{\nu}}|^2 = \frac{C_V^2 G_F^2}{8\pi\alpha} Z_{\mathbf{k}} \Pi_{\mathbf{k}}^2 \epsilon_{\mu} \epsilon_{\nu}^* N^{\mu\nu}, \quad (5.2.4)$$

where $\alpha = e^2/4\pi$ is the fine-structure constant. $Z_{\mathbf{k}}$ is the on-shell wave-function renormalization factor and $\Pi_{\mathbf{k}}$ the polarization factor appropriate for the T or L excitation. The photon polarization vector is ϵ^{μ} with $\epsilon^{\mu}\epsilon_{\mu}^* = -1$. The neutrino tensor, appearing in all pair emission processes, is

$$N^{\mu\nu} = 8(k_1^{\mu}k_2^{\nu} + k_1^{\nu}k_2^{\mu} - k_1 \cdot k_2 g^{\mu\nu} + i\varepsilon^{\alpha\mu\beta\nu} k_{1\alpha}k_{2\beta}). \quad (5.2.5)$$

Inserting this expression in the squared matrix element yields

$$|\mathcal{M}_{\gamma \rightarrow \nu\bar{\nu}}|^2 = \frac{C_V^2 G_F^2}{\pi\alpha} Z_{\mathbf{k}} \Pi_{\mathbf{k}}^2 (\epsilon^* \cdot k_1 \epsilon \cdot k_2 + \epsilon \cdot k_1 \epsilon^* \cdot k_2 + k_1 \cdot k_2). \quad (5.2.6)$$

Notice that the axial-vector interaction does not induce plasmon decay under the approximations described. This is particularly obvious in the nonrelativistic limit where we can think of the emission process as dipole radiation from coherently oscillating electrons, whereas the electron spins, responsible for non-relativistic axial-current processes, do not oscillate coherently. The absence of a sizeable axial-current rate implies that plasmon decay produces with high accuracy only $\nu_e\bar{\nu}_e$ pairs.

5.2.2 Nonrelativistic limit

In a classical plasma (nonrelativistic and nondegenerate), the electromagnetic dispersion relations for transverse (T) and longitudinal (L) plasmons are found to be

$$\omega^2|_T = \omega_p^2 \left(1 + \frac{\mathbf{k}^2}{\omega_p^2 + \mathbf{k}^2} \frac{T}{m_e} \right) + \mathbf{k}^2 \quad \text{and} \quad \omega^2|_L = \omega_p^2 \left(1 + 3 \frac{\mathbf{k}^2}{\omega_p^2} \frac{T}{m_e} \right). \quad (5.2.7)$$

The plasma frequency is given in terms of the electron density n_e by

$$\omega_p^2 = \frac{4\pi\alpha n_e}{m_e}. \quad (5.2.8)$$

In the Sun, $T \lesssim 1.3$ keV so that $T/m_e \lesssim 0.0025$ and with excellent approximation we may limit our discussion to the lowest-order term. Moreover, the lowest-order expression pertains to any level of degeneracy as long as the electrons remain nonrelativistic. In this case, T modes propagate in the same way as particles with mass ω_p , i.e., $\omega^2 = \mathbf{k}^2 + \omega_p^2$, whereas L modes oscillate with a fixed frequency $\omega = \omega_p$, independently of \mathbf{k} . Therefore, the L-plasmon dispersion relation is time-like only for $|\mathbf{k}| < \omega_p$, so only these soft quanta can decay into neutrino pairs.

In the nonrelativistic limit and using Lorentz gauge one finds $Z_T = 1$, $\Pi_T = \omega_p^2$, $Z_L = \omega_p^2/(\omega_p^2 - \mathbf{k}^2)$ and $\Pi_L = \omega_p^2 - \mathbf{k}^2$. Without loss of generality, we may assume the photon to move in the z direction. The T polarization vectors are in this case $\epsilon^\mu = (0, 1, 0, 0)$ and $\epsilon^\mu = (0, 0, 1, 0)$, respectively, whereas the L case with $|\mathbf{k}| < \omega_p$ has $\epsilon^\mu = (|\mathbf{k}|, 0, 0, \omega_p)/(\omega_p^2 - \mathbf{k}^2)^{1/2}$. In Coulomb gauge one finds different expressions for the L quantities.

5.2.3 Decay rate and spectrum

Next we consider the decay rate of a transverse or longitudinal on-shell plasmon with wave vector \mathbf{k} and ask for its decay rate

$$\Gamma_{\gamma \rightarrow \nu \bar{\nu}} = \int \frac{d^3 \mathbf{k}_1}{(2\pi)^3} \frac{d^3 \mathbf{k}_2}{(2\pi)^3} \frac{|\mathcal{M}_{\gamma \rightarrow \nu \bar{\nu}}|^2}{2\omega 2\omega_1 2\omega_2} (2\pi)^4 \delta^4(k - k_1 - k_2). \quad (5.2.9)$$

In a nonrelativistic plasma one easily finds the usual result

$$\Gamma_T = \Gamma_p \frac{\omega_p}{\omega_{\mathbf{k}}} \quad \text{and} \quad \Gamma_L = \Gamma_p \frac{(\omega_p^2 - \mathbf{k}^2)^2}{\omega_p^4} \quad \text{with} \quad \Gamma_p = \frac{C_V^2 G_F^2 \omega_p^5}{48 \pi^2 \alpha}. \quad (5.2.10)$$

For T plasmons $\omega_{\mathbf{k}} = (\omega_p^2 + \mathbf{k}^2)^{1/2}$ with $0 \leq |\mathbf{k}| < \infty$, whereas for L plasmons the decay is allowed for $0 \leq |\mathbf{k}| < \omega_p$. The T case is reminiscent of a decaying particle with mass ω_p where the laboratory decay rate is time-dilated by the factor $\omega_p/\omega_{\mathbf{k}}$. In the limit $\mathbf{k} \rightarrow 0$ both rates are the same. Indeed, in the limit of vanishing wave number one cannot distinguish a transverse from a longitudinal excitation.

We are primarily interested in the neutrino energy spectrum. The symmetry of the squared matrix element under the exchange $k_1 \leftrightarrow k_2$ implies that it is enough to find the ν spectrum which is identical to the one for $\bar{\nu}$. Therefore, in Eq. (5.2.9) we integrate over $d^3 \mathbf{k}_2$ to remove the momentum delta function, and over $d\Omega_1$ to remove the one for energy conservation. Overall, with $\omega_\nu = \omega_1$ we can write the result in the form

$$\frac{d\Gamma}{d\omega_\nu} = \Gamma g(\omega_\nu), \quad (5.2.11)$$

where $g(\omega_\nu)$ is a normalized function. For T plasmons, averaged over the two polarization states, I find

$$g_T(\omega_\nu) = \frac{3}{4} \frac{\mathbf{k}^2 + (\omega_{\mathbf{k}} - 2\omega_\nu)^2}{|\mathbf{k}|^3} \quad \text{for} \quad \frac{\omega_{\mathbf{k}} - |\mathbf{k}|}{2} < \omega_\nu < \frac{\omega_{\mathbf{k}} + |\mathbf{k}|}{2} \quad (5.2.12)$$

and zero otherwise. If the T plasmon were an unpolarized massive spin-1 particle, this would be a top-hat spectrum on the shown interval, corresponding to isotropic emission boosted to the laboratory frame. However, the T plasmon misses the third polarization state so that even unpolarized T plasmons do not show this behavior. For L plasmons I find

$$g_L(\omega_\nu) = \frac{3}{2} \frac{\mathbf{k}^2 - (\omega_p - 2\omega_\nu)^2}{|\mathbf{k}|^3} \quad \text{for} \quad \frac{\omega_p - |\mathbf{k}|}{2} < \omega_\nu < \frac{\omega_p + |\mathbf{k}|}{2} \quad (5.2.13)$$

and zero otherwise, with the additional constraint $0 \leq |\mathbf{k}| < \omega_p$.

I show these distributions in Fig. 5.4. Assuming equal ω for both types of excitations and also equal \mathbf{k} , the distributions add to a top-hat spectrum of the form $\frac{2}{3}g_T(\omega_\nu) + \frac{1}{3}g_L(\omega_\nu) = 1/|\mathbf{k}|$ on the interval $(\omega - |\mathbf{k}|)/2 < \omega_\nu < (\omega + |\mathbf{k}|)/2$, i.e., this average resembles the decay spectrum of an unpolarized spin-1 particle. However, the dispersion relations are different for T and L plasmons so that, for equal \mathbf{k} , they have different ω and these distributions are not on the same ω_ν interval. The only exception is the $\mathbf{k} \rightarrow 0$ limit when $\omega \rightarrow \omega_p$ for both types.

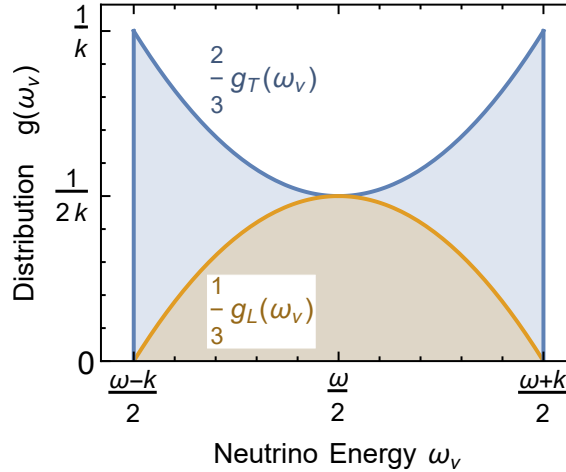


Figure 5.4: Normalized ν spectrum from transverse and longitudinal plasmon decay $\gamma \rightarrow \nu\bar{\nu}$. For T plasmons $\omega = (\omega_p^2 + \mathbf{k}^2)^{1/2}$, whereas for L plasmons $\omega = \omega_p$.

5.2.4 Thermal emission spectrum

As our final result we determine the spectral emission density from a nonrelativistic plasma with temperature T . The number of neutrinos emitted per unit volume per

unit time per unit energy interval from T plasmon decay is

$$\begin{aligned} \left. \frac{dn_\nu}{d\omega_\nu} \right|_T &= \int_{V_{\mathbf{k}}} \frac{d^3\mathbf{k}}{(2\pi)^3} \frac{2\Gamma_T g_T(\omega_\nu)}{e^{\omega_{\mathbf{k}}/T} - 1} \\ &= \frac{3\Gamma_p \omega_p T}{4\pi^2} \int_{\omega_\nu + \frac{\omega_p^2}{4\omega_\nu}}^{\infty} \frac{d\omega}{T} \frac{1}{e^{\omega/T} - 1} \left[1 + \frac{(\omega - 2\omega_\nu)^2}{\omega^2 - \omega_p^2} \right]. \end{aligned} \quad (5.2.14)$$

The integration is over the volume in \mathbf{k} -space allowed by the decay kinematics given in Eq. (5.2.12) and the factor of 2 accounts for two transverse degrees of freedom. For $\omega_\nu \ll \omega_p$ the required plasmon energy is large so that we may approximate $e^{\omega/T} - 1 \rightarrow e^{\omega/T}$ and $(\omega - 2\omega_\nu)^2 / (\omega^2 - \omega_p^2) \rightarrow 1$. In this case the dimensionless integral is $2e^{-\omega_p^2/4\omega_\nu T}$, i.e., this neutrino flux is exponentially suppressed at low energies due to the exponential suppression of the density of T-plasmons with sufficient energy. In Fig. 5.5 I show the dimensionless integral as a function of ω_ν/T for $\omega_p/T = 0.25$ and 1. Notice that in the central solar region $T = 1.3$ keV and $\omega_p = 0.3$ keV so that $\omega_p/T = 0.25$ corresponds approximately to conditions of the central Sun. The external shells of the Sun, where ω_p^2/T is smaller, turn out to be relevant for the lowest energy neutrinos from T-plasmon decay. However, I will show later that this contribution is subdominant.

For L plasmons, the integral over the initial photon distribution yields the

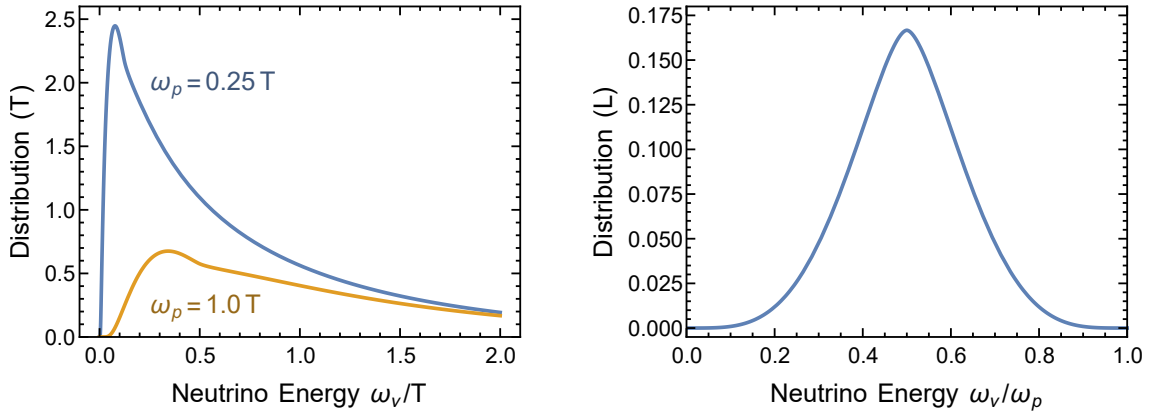


Figure 5.5: Neutrino spectrum from thermal plasmon decay. *Left panel:* Transverse plasmons. The curves represent the dimensionless integral in Eq. (5.2.14) and correspond to $\omega_p/T = 0.25$ and 1 as indicated. *Right panel:* Longitudinal plasmons. The curve is the dimensionless integral in Eq. (5.2.15). To make the vertical scale comparable to T plasmons, a factor $(\omega_p/T)/(e^{\omega_p/T} - 1) = 1 + \mathcal{O}(\omega_p/T)$ must be included.

spectrum of the number emission rate

$$\begin{aligned}
\left. \frac{d\dot{n}_\nu}{d\omega_\nu} \right|_L &= \int_{V_{\mathbf{k}}} \frac{d^3\mathbf{k}}{(2\pi)^3} \frac{\Gamma_L g_L(\omega_\nu)}{e^{\omega_p/T} - 1} \\
&= \frac{3\Gamma_p \omega_p^2}{4\pi^2 (e^{\omega_p/T} - 1)} \int_{|\omega_p - 2\omega_\nu|}^{\omega_p} d|\mathbf{k}| \frac{|\mathbf{k}| (\omega_p^2 - \mathbf{k}^2)^2}{\omega_p^6} \left[1 - \frac{(\omega_p - 2\omega_\nu)^2}{\mathbf{k}^2} \right] \\
&= \frac{3\Gamma_p \omega_p T}{4\pi^2} \frac{\omega_p/T}{e^{\omega_p/T} - 1} \left(\frac{2 + 3y^2 - 6y^4 + y^6}{12} + y^2 \log|y| \right), \quad (5.2.15)
\end{aligned}$$

where $y = (2\omega_\nu - \omega_p)/\omega_p$ equivalent to $\omega_\nu = (y + 1)\omega_p/2$. L plasmons have the fixed energy ω_p , yet neutrinos from decay occupy the full interval $0 < \omega_\nu < \omega_p$ owing to the peculiar L dispersion relation. The neutrino distribution is symmetric relative to $\omega_\nu = \omega_p/2$. In Fig. 5.5 I show the dimensionless ω_ν distribution which is universal for any value of ω_p .

For $\omega_\nu \ll \omega_p$ the dimensionless integral can be expanded and yields $(32/3)(\omega_\nu/\omega_p)^4$, i.e., the spectrum decreases as a power law. Because the T-plasmon spectrum decreases exponentially, the L-plasmon decay provides the dominant neutrino flux at very low ω_ν . This point is illustrated in Fig. 5.6 where I show both spectra in common units of $3\Gamma_p\omega_p T/4\pi^2$ for $\omega_p/T = 0.25$ on a log-log-plot. The central solar temperature is 1.3 keV, so L-plasmon decay takes over for sub-eV neutrinos where the overall rate is extremely small.

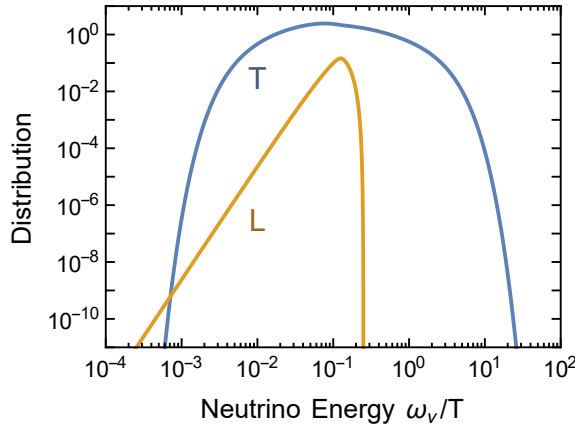


Figure 5.6: Neutrino spectrum from thermal T and L plasmon decay for $\omega_p/T = 0.25$ in units of $3\Gamma_p\omega_p T/4\pi^2$. At very low energies, L-plasmon decay dominates.

5.2.5 Compton pole process?

Thus far we have used kinetic theory in that we treat the excitations of the medium as free particles which propagate until they decay or collide. Plasmons were treated as quasi-stable excitations, distributed as an ideal Bose gas, which occasionally decay

into a neutrino pair. In a previous study of solar thermal neutrino emission [275] another channel was considered in the form $\gamma + e^- \rightarrow e^- + \gamma$ followed by $\gamma \rightarrow \nu\bar{\nu}$, i.e., the decaying plasmon was treated as an intermediate virtual particle in a Compton-like process. In its propagator, an imaginary part (a width) was included, but it was stressed that this width is small and that one needs to integrate over a narrow range of virtual energy-momenta near the on-shell condition. This ‘‘Compton plasmon pole’’ process was found to dominate thermal pair emission, a finding that would change everything about neutrino energy losses from stars.

However, this result is spurious. In a plasma, of course any particle is an intermediate state between collisions and as such a pole in a more complicated process. It is the very basis of the kinetic approach to treat particles as on-shell states coming from far away without memory of their previous history. This assumption need not always be justified, but there is no particular reason why in the present context it should not apply to the plasmon. Its width is very small as stressed in reference [275].

On the other hand, it is not wrong to trace the plasmon one step back in its collision history. In this case one must be consistent, however, as to which processes produce and absorb plasmons and are thus responsible for its width. In reference [275] the plasmon width was taken as a complicated expression from the literature based essentially on inverse bremsstrahlung, whereas the last thing the plasmon did before decaying was taken to be Compton scattering. In this way, their Eq. (11) includes in the numerator essentially the Compton production rate, in the denominator the imaginary part of the propagator based on inverse bremsstrahlung. The emission rate gets spuriously enhanced by a large ratio of plasmon interaction rates based on different processes.

In summary, as long as the plasmon width is small, as everybody agrees it is, the ‘‘pole process’’ is identical with the plasmon decay process, not a new contribution. The only difference is that for a given momentum, the plasmon energy distribution is taken to follow a delta function (plasmon decay) or a narrow resonance distribution (pole process). The overall normalization is the same in both cases.

5.2.6 Solar neutrino flux

We finally integrate the plasmon decay rate over a standard solar model and show the expected neutrino flux at Earth in Fig. 5.7. A solar model from the Saclay group which is described in more detail in appendix C is used. At this stage we do not worry about flavor oscillations and simply give the all-flavor flux at Earth, recalling that plasmon decay produces pure $\nu_e\bar{\nu}_e$ pairs at the source. One finds

$$\Phi_T = 4.12 \times 10^5 \text{ cm}^{-2} \text{ s}^{-1} \quad \text{and} \quad \Phi_L = 4.67 \times 10^3 \text{ cm}^{-2} \text{ s}^{-1} \quad (5.2.16)$$

for the integrated fluxes at Earth.

The T plasmon flux now reaches much smaller energies than in Fig. 5.6 when we considered conditions near the solar center. Very low-energy neutrinos from plasmon decay require the plasmon to be very relativistic because the accessible energy range

is $\omega - |\mathbf{k}| < \omega_\nu < \omega + |\mathbf{k}|$, so the low-energy flux is exponentially suppressed due to the exponential suppression of the density of high-energy plasmons. At larger solar radii T is smaller, but ω_p drops even faster and T plasmons are more relativistic. Therefore, lower-energy neutrinos become kinematically allowed, i.e., lower-energy neutrinos derive from larger solar radii. From Fig. 5.7 we conclude that the L plasmon flux begins to dominate at energies so low that the assumption of massless neutrinos is not necessarily justified.

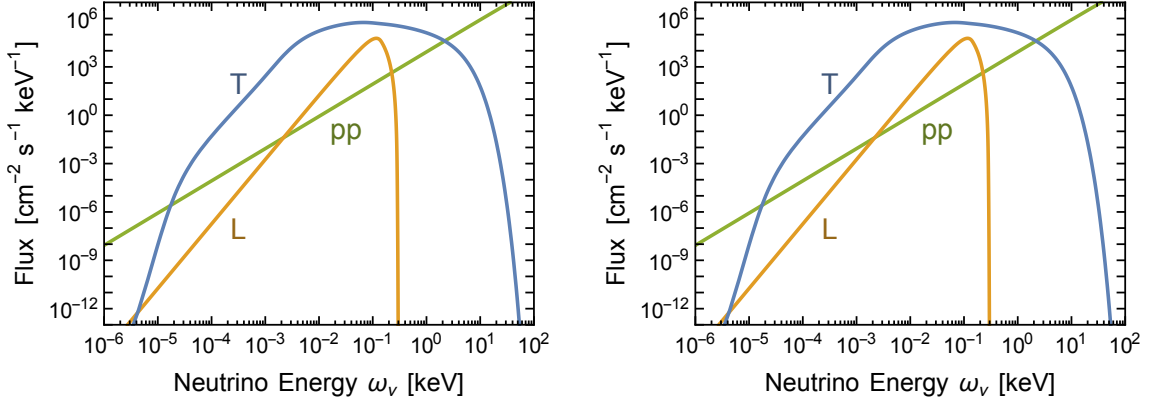


Figure 5.7: Solar neutrino flux at Earth from transverse and longitudinal plasmon decay. This is the total ν flux produced as nearly pure ν_e in the Sun. There is an equal $\bar{\nu}$ flux. It is also shown the low-energy tail of the usual flux from the nuclear pp reaction which are born as ν_e .

For comparison I also show the ν flux from the pp reaction that produces the lowest-energy flux from nuclear reactions. All standard solar models agree on this flux within around 1%, so we may use as a generic number $6.0 \times 10^{10} \text{ cm}^{-2} \text{ s}^{-1}$. The reaction $p + p \rightarrow d + e^+ + \nu_e$ has a neutrino endpoint energy of $Q = 420.22 \text{ keV}$. Including the thermal kinetic energy of the protons in the solar plasma, the overall endpoint of the solar spectrum is $Q = 423.41 \text{ keV}$ [63]. This reference also gives a numerical tabulation of the solar ν_e spectrum from the pp reaction. Ignoring a small e^+ final-state correction, the spectrum follows that of an allowed weak transition of the normalized form

$$\begin{aligned} \frac{dN}{d\omega_\nu} &= \frac{\omega_\nu^2 (Q + m_e - \omega_\nu) \sqrt{(Q + m_e - \omega_\nu)^2 - m_e^2}}{A^5} \\ &= \frac{(Q + m_e) \sqrt{Q(Q + 2m_e)}}{A^5} \omega_\nu^2 + \mathcal{O}(\omega_\nu^3) \end{aligned} \quad (5.2.17)$$

where $A = 350.8 \text{ keV}$ if we use the solar endpoint energy. The analytic form of the normalization factor A is too complicated to be shown here. The low-energy pp flux spectrum at Earth is the power law

$$\frac{d\Phi_{pp}}{d\omega_\nu} = 8150 \text{ cm}^{-2} \text{ s}^{-1} \text{ keV}^{-1} \left(\frac{\omega_\nu}{\text{keV}} \right)^2, \quad (5.2.18)$$

an approximation that is good to about $\pm 1.5\%$ for energies below 10 keV. This shallow power law is simply determined by the low-energy neutrino phase space. It dominates over plasmon decay at very low energies, although, of course, it does not produce antineutrinos. I will show later that both are subdominant compared to the neutrino flux produced in bremsstrahlung transitions.

5.3 Photo production

5.3.1 Matrix element and decay rate

The Compton process (Fig. 5.8), also known as photo production or photoneutrino production, was one of the first processes to be considered as an energy-loss mechanism for stars [294–296]. In these older papers, only the energy-loss rate was calculated, whereas the neutrino spectrum was calculated in the nonrelativistic limit in reference [275] and for general kinematics in reference [297]. We restrict ourselves to the nonrelativistic limit where electron recoils are neglected. The process then amounts to the conversion $\gamma \rightarrow \nu\bar{\nu}$, catalyzed through bystander electrons which take up three-momentum, and as such is somewhat similar to plasmon decay. However, no plasma mass is needed because momentum is taken up by the electrons. Even though we neglect recoils, the process is not “forward” for the electrons. We can interpret plasmon decay as the coherent version of photo production.

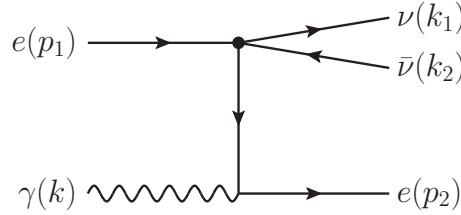


Figure 5.8: Photo production of neutrino pairs (Compton process). A second diagram with vertices interchanged is not shown.

In the nonrelativistic limit one finds for the squared matrix element, averaged over initial spins and polarizations and summed over final ones,

$$\overline{|\mathcal{M}|^2} = \frac{1}{4} \sum_{\epsilon, s_1, s_2} |\mathcal{M}|^2 = \frac{e^2 G_F^2}{\omega^2} M^{\mu\nu} N_{\mu\nu} \quad (5.3.1)$$

where the neutrino tensor was given in Eq. (5.2.5). The nonrelativistic electron tensor for the Compton process is [275]

$$M^{\mu\nu} = \sum_{\epsilon} \left\{ (C_V^2 + C_A^2) (-\omega\epsilon^\mu + \delta^{\mu 0}\epsilon \cdot q) (-\omega\epsilon^\nu + \delta^{\nu 0}\epsilon \cdot q) + C_A^2 [k^\mu k^\nu - (\epsilon \cdot q)^2 g^{\mu\nu}] \right\}, \quad (5.3.2)$$

where ϵ is the photon polarization vector and $q = k_1 + k_2$ the four momentum carried away by the neutrino pair.

It is noteworthy that both the vector and axial-vector currents contribute on comparable levels, in contrast to plasmon decay. This is heuristically understood if we observe that the vector part amounts to electric dipole emission by the electron being “shaken” by the incoming EM wave. The rate is proportional to $(G_F/m_e)^2$ because the outgoing radiation couples with strength G_F and the mass appears due to its inertia against the acceleration. Axial-current emission amounts to magnetic dipole emission caused by the electron spin. The coupling is through the electron dipole moment $\propto 1/m_e$, so the rate is also proportional to $(G_F/m_e)^2$. In the case of axion emission, $\gamma + e \rightarrow e + a$, enabled by a derivative axial-vector coupling, the rate is suppressed by a factor $(\omega/m_e)^2$ relative to Compton scattering. For neutrinos the coupling structure is the same for both axial and vector coupling. Note however that these considerations require some handwaving and one should always check which terms in the nonrelativistic expansion of the Hamiltonian contribute to a certain order.

We use the symmetry under the exchange $1 \leftrightarrow 2$ and integrate over the phase space of $\bar{\nu}$ and over the angles of ν . With $\omega_p = 0$ one finds for the differential “decay rate” of T plasmons with energy ω of either polarization

$$\frac{d\Gamma_\omega}{d\omega_\nu} = n_e \frac{2}{3} \frac{G_F^2 \alpha}{\pi^2 m_e^2} (C_V^2 + 5C_A^2) \frac{(\omega - \omega_\nu)^2 \omega_\nu^2}{\omega} \left[1 - \frac{2(\omega - \omega_\nu)\omega_\nu}{\omega^2} \right] \quad \text{for } \omega_\nu < \omega. \quad (5.3.3)$$

Integrated over the photon distribution it gives the familiar result [275]

$$\begin{aligned} \frac{dn_\nu}{d\omega_\nu} &= n_e \frac{2}{3} \frac{G_F^2 \alpha}{\pi^4 m_e^2} \int_{\omega_\nu}^{\infty} d\omega \omega_\nu^2 (\omega - \omega_\nu)^2 \frac{1}{e^{\omega/T} - 1} \\ &\quad \times (C_V^2 + 5C_A^2) \omega \left[1 - \frac{2(\omega - \omega_\nu)\omega_\nu}{\omega^2} \right]. \end{aligned} \quad (5.3.4)$$

Including the modified dispersion relation in the plasma with a nonvanishing ω_p leads to a more complicated expression that modifies the result for ω near ω_p and by up to a few percent elsewhere, for us a negligible correction. On the other hand, at energies near ω_p , Compton emission is subdominant relative to plasmon decay. Moreover, one should then also worry about longitudinal plasmons which can be understood as collective electron oscillations. One therefore would need to avoid double counting between $\gamma_L + e \rightarrow e + \nu\bar{\nu}$ and bremsstrahlung $e + e \rightarrow e + e + \nu\bar{\nu}$, see the related discussion in reference [298]. Therefore, we can use the emission rate based on the $\omega_p = 0$ expression of Eq. (5.3.4), but we will include ω_p in the phase space of initial T plasmons, cutting off $\omega < \omega_p$ initial-state photons.

5.3.2 Correlation effects

So far we have assumed that electrons are completely uncorrelated and the overall neutrino emission rate is the incoherent sum from individual scattering events. However, electrons are anticorrelated by the Pauli exclusion principle and by Coulomb

repulsion, both effects meaning that at the location of a given electron it is less likely than average to find another one. These anticorrelations lead to a reduction of the rate, i.e., we need to include a structure factor $S(\mathbf{q}^2)$ where $\mathbf{q} = \mathbf{k} - \mathbf{k}_1 - \mathbf{k}_2$ is the three-momentum transfer. For photon transport, exchange effects produce a 7% correction in the solar center and less elsewhere, whereas Coulomb correlations provide a 20–30% correction [299].

Beginning with the exchange correlation, a simple approach is to include a Pauli blocking factor $(1 - f_{\mathbf{p}})$ for the final state electron in the phase-space integration. For nonrelativistic electron targets that barely recoil, the final-state \mathbf{p} can be taken the same as the initial one, so the overall reduction is the average Pauli blocking factor

$$\begin{aligned} R_\eta &= \frac{2}{n_e} \int \frac{d^3\mathbf{p}}{(2\pi)^3} f_{\mathbf{p}}(1 - f_{\mathbf{p}}) \\ &= \int_0^\infty \frac{dx x^2}{e^{x^2-\eta} + 1} \left(1 - \frac{1}{e^{x^2-\eta} + 1} \right) \bigg/ \int_0^\infty \frac{dx x^2}{e^{x^2-\eta} + 1}, \end{aligned} \quad (5.3.5)$$

where the nonrelativistic degeneracy parameter $\eta = (\mu - m_e)/T$ is given by

$$n_e = 2 \int \frac{d^3\mathbf{p}}{(2\pi)^3} \frac{1}{e^{\frac{\mathbf{p}^2}{2m_e T} - \eta} + 1}. \quad (5.3.6)$$

It has been checked that this expression is indeed the $|\mathbf{q}| = \kappa \rightarrow 0$ limit of $1 + h_x(\kappa)$ given in Eq. (6) of reference [299]. In this paper and the literature on solar opacities, the Pauli blocking effect is interpreted as an anticorrelation of the electrons in analogy to what is caused by a repulsive force. So we can picture Pauli effects either as a blocking of final electron states in collisions or as an anticorrelation of initial-state electron targets.

Next we turn to Coulomb repulsion where for solar conditions the structure function can be reasonably approximated essentially by a Debye-Hückel screening prescription [299]

$$S_e(\mathbf{q}^2) = 1 - \frac{k_e^2}{\mathbf{q}^2 + k_e^2 + k_i^2}. \quad (5.3.7)$$

The screening scales are

$$k_e^2 = R_\eta \frac{4\pi\alpha n_e}{T} \quad \text{and} \quad k_i^2 = \frac{4\pi\alpha}{T} \sum_Z Z^2 n_Z, \quad (5.3.8)$$

where n_Z is the number density of ions with charge Ze . For electrons, the correction factor R_η for partial degeneracy is included.⁹ For conditions of the central Sun

⁹Our R_η defined in Eq. (5.3.5) is the same as R_α defined in reference [299] by a ratio of Fermi integrals. The overall structure factor was written in the form $1 + h_x(\kappa) + h_r(\kappa)$ with $h_r(\kappa) = -R_\eta k_e^2 / (\kappa^2 + k_e^2 + k_i^2)$. However, for the exchange correlations, the $\kappa \rightarrow 0$ limit is justified and $R_\eta = 1 + h_x(0)$ so that $1 + h_x + h_r = R_\eta - R_\eta k_e^2 / (\kappa^2 + k_e^2 + k_i^2) = R_\eta S_e(\kappa)$. In other words, the exchange correlations indeed amount to a global factor R_η for final-state Pauli blocking besides a reduction of the electron screening scale k_e^2 .

we have an electron density of about $n_e = 6.3 \times 10^{25} \text{ cm}^{-3}$ and a temperature $T = 1.3 \text{ keV}$, providing $\eta = -1.425$, leading to $R_\eta = 0.927$. The Debye-Hückel scales are $k_e = 5.4 \text{ keV}$ and $k_i = 7.0 \text{ keV}$. As these scales are comparable to a typical momentum transfer there is no simple limit for Coulomb corrections. In our numerical estimate of the solar emission we use a simple prescription to account for this effect: the largest possible momentum transfer for an initial photon of energy ω is $|\mathbf{q}_{\text{max}}| = 2\omega$. Using $S_e(4\omega^2)$ to multiply Eq. (5.3.3) provides an upper limit to the suppression caused by Coulomb correlations, i.e., the neutrino flux will be slightly overestimated.

Coulomb correlations apply to processes where the electron density is the crucial quantity, i.e., to the vector-current part proportional to C_V^2 . The axial-current contributions, proportional to C_A^2 , depend on the electron spins which are not correlated by Coulomb interactions. If an electron at a given location has a certain spin, the chance of finding one with the same or opposite spin at some distance is the same, i.e., the spins are not correlated. Therefore, the interference of spin-dependent scattering amplitudes from different electrons average to zero and we do not need any Coulomb correlation correction. Only the emission of $\nu_e \bar{\nu}_e$ has any V contribution and in all cases, the A term strongly dominates. Therefore, overall Coulomb corrections are small for photo production.

Treating exchange corrections as an average final-state Pauli blocking factor reveals that it applies for both V and A processes. We can also see this point in terms of initial-state correlations. Electrons of opposite spin are not correlated because they can occupy the same location, whereas those with equal spin “repel” each other. Therefore, the interference effects between initial electrons of equal and opposite spins do not average to zero.

In summary, the photo production rate is reduced by the overall Pauli blocking factor R_η given in Eq. (5.3.5) which in the Sun is a few percent. The terms proportional to C_V^2 , on the other hand, require the additional Coulomb structure factor given in Eq. (5.3.7) which can be a 30% correction. The V channel essentially applies only to $\nu_e \bar{\nu}_e$ emission, where Coulomb correlations provide an overall reduction of perhaps 10%.

5.3.3 Solar neutrino flux

We now integrate the source reaction rate over our solar model and show the neutrino flux in Fig. 5.9 on a linear scale. The blue curve derives from the V channel and includes Coulomb correlations, whereas the orange curve applies to the A channel. To obtain the proper flux the curves need to be multiplied with C_V^2 and $5C_A^2$, respectively.

In Fig. 5.10 I compare the axial-vector Compton flux for a single flavor with the fluxes from T-plasmon decay and with pp neutrinos. While we have not included the plasma frequency in the squared matrix element for the Compton process, we do include it in the phase-space integration. In this way, the lowest-energy Compton flux is suppressed and explains the kink in the low-energy flux. As a consequence, the lowest-energy neutrino flux is dominated by plasmon decay. Notice that T-

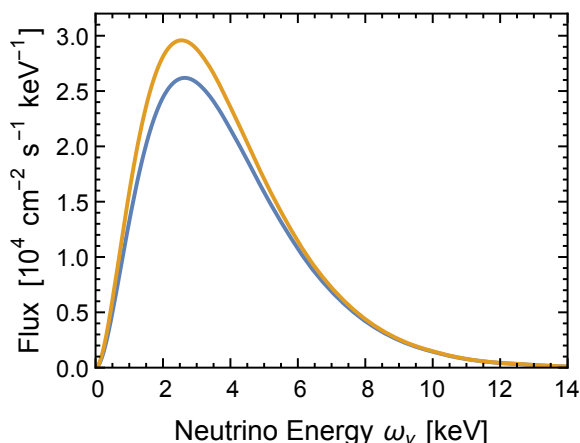


Figure 5.9: Neutrino flux from Compton production for the vector (blue) and axial-vector (orange) interaction. For the proper flux, the V curve is to be multiplied with C_V^2 , the A curve with $5C_A^2$. The difference between the blue and orange curves derives from Coulomb correlations which apply only to the V channel. The Coulomb correlations were treated in an approximate way as described in the text and the suppression could be slightly larger.

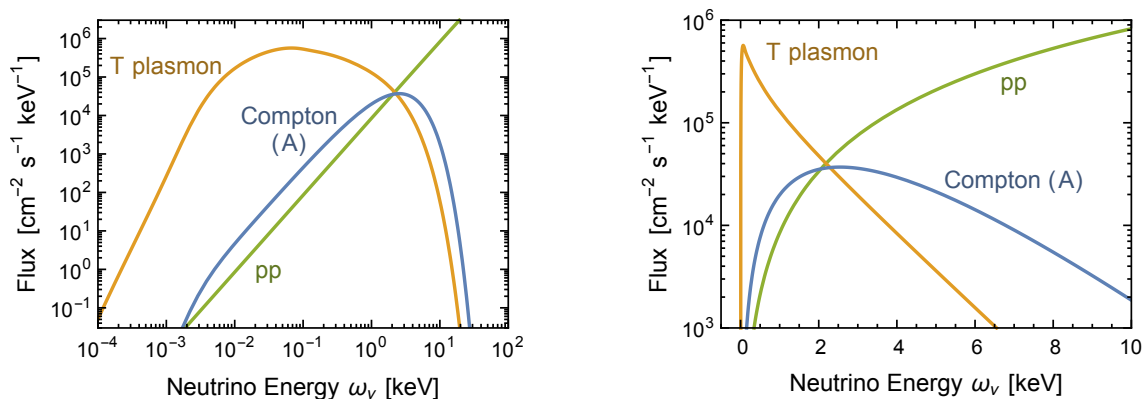


Figure 5.10: Solar neutrino flux at Earth from the Compton process (axial-vector channel and only one flavor) compared with the pp flux (only ν_e) and transverse plasmon decay (ν_e and equal flux $\bar{\nu}_e$). Flavor oscillations are not considered here.

plasmon decay produces almost exclusively $\nu_e\bar{\nu}_e$ pairs, whereas the axial-vector Compton process produces equal fluxes of all flavors. For $\nu_e\bar{\nu}_e$, there is an additional contribution from the V channel. Apart from Coulomb-correlation corrections and overall coefficients, the spectrum is the same as shown in Fig. 5.9. The flavor dependence of fluxes at Earth will be studied later.

5.4 Bremsstrahlung

5.4.1 Matrix element

Next we consider bremsstrahlung production of neutrino pairs (Fig. 5.11), also known as the free-free process, where we consider nuclei or ions with charge Ze to provide a

Coulomb potential without recoil. This process was not included in a previous study of low-energy solar neutrino emission [275]. In general, it is the dominant energy loss mechanism in stars with low temperature and high electron density [300, 301]. The first differential flux evaluation was carried out for our nonrelativistic and nondegenerate conditions a long time ago in reference [302], which has some flaws as described below, and recently also for general conditions [303].

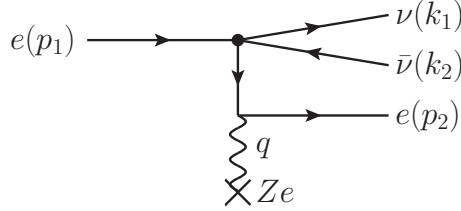


Figure 5.11: Bremsstrahlung production of neutrino pairs. The Coulomb potential is provided by a heavy nucleus or ion with charge Ze taking up the momentum transfer $q = (0, \mathbf{q})$. The outgoing neutrino radiation carries the four-momentum $k = k_1 + k_2 = (\omega, \mathbf{k})$. There is a second diagram with the vertices exchanged.

The scattering targets are taken to be very heavy (no recoil) with charge Ze and number density n_Z and the electrons are taken to be nonrelativistic. The emission rate of neutrino pairs per unit volume and unit time is then

$$\dot{n}_\nu = n_Z \int \frac{d^3 \mathbf{p}_1}{(2\pi)^3} \frac{d^3 \mathbf{p}_2}{(2\pi)^3} \frac{d^3 \mathbf{k}_1}{(2\pi)^3} \frac{d^3 \mathbf{k}_2}{(2\pi)^3} f_1 (1 - f_2) \frac{\sum_{s_1, s_2} |\mathcal{M}|^2}{(2m_e)^2 2\omega_1 2\omega_2} 2\pi \delta(E_1 - E_2 - \omega), \quad (5.4.1)$$

where the sum is taken over the electron spins and f_1 and f_2 are the initial and final-state electron occupation numbers. The final-state neutrino radiation is described by $k = (\omega, \mathbf{k}) = k_1 + k_2 = (\omega_1 + \omega_2, \mathbf{k}_1 + \mathbf{k}_2)$. For the squared matrix element we find

$$\sum_{s_1, s_2} |\mathcal{M}|^2 = \frac{8Z^2 e^4}{|\mathbf{q}|^4 \omega^2} \left(\frac{G_F^2}{2} \right) \left(C_V^2 M_V^{\mu\nu} + C_A^2 M_A^{\mu\nu} \right) N_{\mu\nu}, \quad (5.4.2)$$

where the neutrino tensor was given in Eq. (5.2.5) and \mathbf{q} is the momentum transfer to the nucleus.

For nonrelativistic electrons, as usual we can ignore the transfer of three-momentum to the external radiation so that $\mathbf{q} = \mathbf{p}_1 - \mathbf{p}_2$. In this approximation we find

$$M_V^{\mu\nu} = \begin{pmatrix} \left(\frac{\mathbf{q} \cdot \mathbf{k}}{\omega}\right)^2 & \frac{\mathbf{q} \cdot \mathbf{k}}{\omega} \mathbf{q} \\ \frac{\mathbf{q} \cdot \mathbf{k}}{\omega} \mathbf{q} & \mathbf{q}^i \mathbf{q}^j \end{pmatrix} \quad \text{and} \quad M_A^{\mu\nu} = \begin{pmatrix} \mathbf{q}^2 & \frac{\mathbf{q} \cdot \mathbf{k}}{\omega} \mathbf{q} \\ \frac{\mathbf{q} \cdot \mathbf{k}}{\omega} \mathbf{q} & \left(\frac{\mathbf{q} \cdot \mathbf{k}}{\omega}\right)^2 \delta^{ij} \end{pmatrix}. \quad (5.4.3)$$

With $C_V = C_A = 1$ one should find the bremsstrahlung rates in the old literature before the discovery of neutral currents. However, the terms proportional to $\mathbf{q} \cdot \mathbf{k} / \omega$ are missing (see the steps from Eqs. (5) to (6) in reference [302]). For the V-case, bremsstrahlung arises from the electron velocity abruptly changing in a collision. In the nonrelativistic limit, the 0-component of the electron current remains unchanged.

However, the squared matrix element is quadratic in the velocity change. Therefore, a consistent nonrelativistic expansion requires to go to second order in the small velocity everywhere. If one expands the electron current only to linear order before taking the matrix element one misses some of the terms. A similar issue explains the factor 2/3 difference in the axion bremsstrahlung calculation between reference [304] (Eqs. (38) to (42)) and [305] (Eqs. (1) to (4)).

The electron gas is assumed to be isotropic, so in Eq. (5.4.1) we may first perform an angle average over the electron direction, keeping their relative angle fixed. So we average over the relative angle between \mathbf{q} and \mathbf{k} , leading to $\mathbf{q}^i \mathbf{q}^j \rightarrow \frac{1}{3} \mathbf{q}^2 \delta^{ij}$, $(\mathbf{q} \cdot \mathbf{k}) \mathbf{q} \rightarrow \frac{1}{3} \mathbf{q}^2 \mathbf{k}$, and $(\mathbf{q} \cdot \mathbf{k})^2 \rightarrow \frac{1}{3} \mathbf{q}^2 \mathbf{k}^2$. Therefore, in an isotropic medium we may write

$$\left\langle \sum_{s_1, s_2} |\mathcal{M}|^2 \right\rangle_{\cos(\mathbf{q}, \mathbf{k})} = \frac{8Z^2 e^4}{3\mathbf{q}^2} \left(\frac{G_F^2}{2} \right) \frac{(C_V^2 \bar{M}_V^{\mu\nu} + C_A^2 \bar{M}_A^{\mu\nu}) N_{\mu\nu}}{\omega^4}, \quad (5.4.4)$$

where

$$\bar{M}_V^{\mu\nu} = \begin{pmatrix} \mathbf{k}^2 & \omega \mathbf{k} \\ \omega \mathbf{k} & \omega^2 \delta^{ij} \end{pmatrix} \quad \text{and} \quad \bar{M}_A^{\mu\nu} = \begin{pmatrix} 3\omega^2 & \omega \mathbf{k} \\ \omega \mathbf{k} & \mathbf{k}^2 \delta^{ij} \end{pmatrix}. \quad (5.4.5)$$

Notice that lowering the indices in this matrix changes the sign of the time-space part (the 0j and j0 components), i.e., lowering the indices amounts to $\omega \mathbf{k} \rightarrow -\omega \mathbf{k}$. For the contractions one finds explicitly

$$\begin{aligned} \bar{M}_V^{\mu\nu} N_{\mu\nu} &= 16 [\omega_1 \omega_2 (\omega_1^2 + \omega_2^2 + \omega_1 \omega_2) + (\mathbf{k}_1 \cdot \mathbf{k}_2)^2 - \omega^2 \mathbf{k}_1 \cdot \mathbf{k}_2] \\ &\rightarrow \frac{16}{3} \omega_1 \omega_2 (3\omega_1^2 + 3\omega_2^2 + 4\omega_1 \omega_2), \end{aligned} \quad (5.4.6a)$$

$$\begin{aligned} \bar{M}_A^{\mu\nu} N_{\mu\nu} &= 16 [\omega_1 \omega_2 (2\omega_1^2 + 2\omega_2^2 + \omega_1 \omega_2) - (\mathbf{k}_1 \cdot \mathbf{k}_2)^2 + 4\omega_1 \omega_2 \mathbf{k}_1 \cdot \mathbf{k}_2] \\ &\rightarrow \frac{32}{3} \omega_1 \omega_2 (3\omega_1^2 + 3\omega_2^2 + \omega_1 \omega_2). \end{aligned} \quad (5.4.6b)$$

The second expressions apply after an angle average over the relative directions of \mathbf{k}_1 and \mathbf{k}_2 where $\mathbf{k}_1 \cdot \mathbf{k}_2 \rightarrow 0$ and $(\mathbf{k}_1 \cdot \mathbf{k}_2)^2 \rightarrow \frac{1}{3} \omega_1^2 \omega_2^2$.

5.4.2 Emission rate

We may write the neutrino pair emission rate of Eq. (5.4.1) in a way that separates the properties of the emitted radiation (the neutrino pairs) from the properties of the medium (thermal electrons interacting with nuclei) and find

$$\dot{n}_\nu = n_Z n_e \frac{8Z^2 \alpha^2}{3} \int \frac{d^3 \mathbf{k}_1}{2\omega_1 (2\pi)^3} \frac{d^3 \mathbf{k}_2}{2\omega_2 (2\pi)^3} \left(\frac{G_F}{\sqrt{2}} \right)^2 \frac{(C_V^2 \bar{M}_V^{\mu\nu} + C_A^2 \bar{M}_A^{\mu\nu}) N_{\mu\nu}}{\omega^4} \mathcal{S}(\omega), \quad (5.4.7)$$

where $\omega = \omega_1 + \omega_2$ is the energy carried away by a neutrino pair. Collecting coefficients in a slightly arbitrary way, the relevant response function of the medium is

$$\mathcal{S}(\omega) = \frac{(4\pi)^2}{(2m_e)^2} \frac{1}{n_e} \int \frac{d^3\mathbf{p}_1}{(2\pi)^3} \frac{d^3\mathbf{p}_2}{(2\pi)^3} f_1(1-f_2) \frac{1}{\mathbf{q}} 2\pi\delta(E_1 - E_2 - \omega), \quad (5.4.8)$$

where $\mathbf{q} = \mathbf{p}_1 - \mathbf{p}_2$ is the momentum transfer in the electron-nucleus collision mediated by the Coulomb field. We see that for both vector and axial vector emission it is the same property of the medium causing the emission. We will return to this point later for the free-bound and bound-bound emission processes because we can relate both vector and axial-vector processes to the monochromatic photon opacities, the latter providing us essentially with $\mathcal{S}(\omega)$.

We now integrate over neutrino emission angles and find the neutrino emission spectrum by using $\omega_1 = \omega_\nu$ and $\omega_2 = \omega - \omega_\nu$. Integrating over the anti-neutrino energy we find

$$\begin{aligned} \frac{d\dot{n}_\nu}{d\omega_\nu} &= n_Z n_e \frac{8 Z^2 \alpha^2}{3} \left(\frac{G_F}{\sqrt{2}} \right)^2 \frac{1}{3\pi^4} \int_{\omega_\nu}^{\infty} d\omega \mathcal{S}(\omega) \frac{\omega_\nu^2 (\omega - \omega_\nu)^2}{\omega^4} \\ &\times \left[C_V^2 (3\omega^2 - 2\omega\omega_\nu + 2\omega_\nu^2) + 2C_A^2 (3\omega^2 - 5\omega\omega_\nu + 5\omega_\nu^2) \right], \end{aligned} \quad (5.4.9)$$

which is the rate of neutrino emission per unit volume, unit time, and unit energy interval. The same spectrum applies to antineutrinos because all expressions were symmetric under the exchange $1 \leftrightarrow 2$.

5.4.3 Photon and axion emission

It is useful to compare the bremsstrahlung emission rate of neutrino pairs with that of photons and axions to connect to the previous literature and, more importantly, to relate the bremsstrahlung absorption rate of photons to the neutrino pair emission rate. For photon emission, the neutral-current interaction of Eq. (5.2.1) gets replaced by $ie\bar{\psi}_e\gamma^\mu\psi_e A_\mu$. On the level of the squared matrix element, or rather, on the level of the emission rate, this substitution translates to

$$\dot{n}_\gamma = n_Z n_e \frac{8 Z^2 \alpha^2}{3} \int \frac{d^3\mathbf{k}}{2\omega(2\pi)^3} e^2 \frac{\bar{M}_V^{\mu\nu} \epsilon_\mu \epsilon_\nu}{\omega^4} \mathcal{S}(\omega). \quad (5.4.10)$$

For the contraction we find $\bar{M}_V^{\mu\nu} \epsilon_\mu \epsilon_\nu = \omega^2$. We have used the polarization vector for a transverse photon (not a longitudinal plasmon) so that $\mathbf{k} \cdot \boldsymbol{\epsilon} = 0$, $\epsilon^0 \epsilon^0 = 0$, and $\boldsymbol{\epsilon} \cdot \boldsymbol{\epsilon} = 1$. So the spectral photon production rate per transverse polarization degree of freedom is

$$\frac{d\dot{n}_\gamma}{d\omega} = n_Z n_e \frac{8 Z^2 \alpha^2}{3} \frac{\alpha}{\pi} \frac{\mathcal{S}(\omega)}{\omega}. \quad (5.4.11)$$

This quantity is directly related to the medium response function $\mathcal{S}(\omega)$. Therefore, we can express the neutrino emissivity of Eq. (5.4.9) in terms of the photon emissivity

as

$$\begin{aligned} \frac{d\dot{n}_\nu}{d\omega_\nu} &= \frac{G_F^2}{6\pi^3\alpha} \int_{\omega_\nu}^{\infty} d\omega \left(\frac{d\dot{n}_\gamma}{d\omega} \right) \frac{\omega_\nu^2(\omega - \omega_\nu)^2}{\omega^3} \\ &\times \left[C_V^2 (3\omega^2 - 2\omega\omega_\nu + 2\omega_\nu^2) + 2C_A^2 (3\omega^2 - 5\omega\omega_\nu + 5\omega_\nu^2) \right]. \end{aligned} \quad (5.4.12)$$

Therefore, given the spectral photon emissivity, e.g. taken from the photon opacity calculation, we can directly extract the neutrino emission spectrum. We will return to this point in Sec. 5.5.

Axions couple to the electron axial current with an interaction of the derivative form $(C_e/2f_a)\bar{\psi}_e\gamma^\mu\gamma_5\psi_e\partial_\mu a$, where a is the axion field, f_a the axion decay constant, and C_e a model-dependent numerical coefficient. One often uses a dimensionless axion-electron Yukawa coupling $g_{ae} = C_e m_e/f_a$ so that the interaction is $(g_{ae}/2m_e)\bar{\psi}_e\gamma^\mu\gamma_5\psi_e\partial_\mu a$. The bremsstrahlung emission rate is found to be

$$\dot{n}_a = n_Z n_e \frac{8Z^2\alpha^2}{3} \int \frac{d^3\mathbf{k}}{2\omega(2\pi)^3} \left(\frac{g_{ae}}{2m_e} \right)^2 \frac{\bar{M}_A^{\mu\nu} k_\mu k_\nu}{\omega^4} \mathcal{S}(\omega). \quad (5.4.13)$$

For massless axions with $\omega = |\mathbf{k}|$ we find for the contraction $\bar{M}_A^{\mu\nu} k_\mu k_\nu = 2\omega^4$. Therefore, the spectral emissivity is

$$\frac{d\dot{n}_a}{d\omega} = n_Z n_e \frac{8Z^2\alpha^2}{3} \left(\frac{g_{ae}}{2m_e} \right)^2 \frac{\omega}{2\pi^2} \mathcal{S}(\omega). \quad (5.4.14)$$

Notice that this spectrum is harder than the photon spectrum by a factor ω^2 caused by the derivative structure of the axion interaction. Still, fundamentally it depends on the same medium response function $\mathcal{S}(\omega)$. It has been checked that in the nondegenerate limit this axion emission rate agrees with reference [304].

5.4.4 Medium response function and screening effects

The medium response function defined in Eq. (5.4.8) could be easily evaluated if the nuclei used as scattering centers were uncorrelated. However, their Coulomb interaction leads to anticorrelations encoded in an ion structure factor $S_i(\mathbf{q}^2)$ similar to the case of electron-electron correlations discussed in Sec. 5.3.2. Therefore, under the integral in Eq. (5.4.8) we need to include $S_i(\mathbf{q}^2)$, which we will discuss later. I mention in passing that $\mathcal{S}(\omega)$ given in Eq. (5.4.8), with or without including $S_i(\mathbf{q}^2)$, fulfills the detailed-balancing condition $\mathcal{S}(-\omega) = \mathcal{S}(\omega) e^{\omega/T}$. Here a negative ω means energy absorbed by the medium, whereas a positive ω for us always means energy emitted, although in the literature one usually uses the opposite convention.

To write $\mathcal{S}(\omega)$ in a more compact form we first note that the electron number density is given by Eq. (5.3.6) in terms of the nonrelativistic degeneracy parameter η . We further write the kinetic electron energy in dimensionless form as $u = \mathbf{p}^2/(2m_e T)$ so that the occupation number is $f_u = 1/(e^{u-\eta} + 1)$. Then the structure function is

$$\mathcal{S}(\omega) = \frac{\pi}{m_e \sqrt{2m_e T}} s(\omega/T) \quad (5.4.15)$$

where

$$s(w) = \int_0^\infty du_2 \frac{\sqrt{u_1 u_2}}{e^{u_1 - \eta} + 1} \frac{1}{e^{-(u_2 - \eta)} + 1} \int_{-1}^{+1} dc_\theta \frac{2m_e T}{\mathbf{q}^2} S_i(\mathbf{q}^2) / \int_0^\infty du \frac{\sqrt{u}}{e^{u - \eta} + 1}. \quad (5.4.16)$$

Here $u_1 = u_2 + w$ and $w = \omega/T$. Moreover, $\mathbf{q}^2 = |\mathbf{p}_1 - \mathbf{p}_2|^2 = \mathbf{p}_1^2 + \mathbf{p}_2^2 - 2|\mathbf{p}_1||\mathbf{p}_2|c_\theta$ with $c_\theta = \cos \theta$. Therefore, $\mathbf{q}^2/(2m_e T) = u_1 + u_2 - 2\sqrt{u_1 u_2} c_\theta$.

Besides the original squared matrix element, this function depends on electron degeneracy effects and Coulomb correlation effects encoded in $S_i(\mathbf{q}^2)$. Anticipating that electron degeneracy is not a large correction we first reduce this expression to Maxwell-Boltzmann rather than Fermi-Dirac statistics. Formally this is the $\eta \rightarrow -\infty$ limit, leading to the non-degenerate (ND) structure function

$$s_{\text{ND}}(w) = \int_0^\infty du e^{-u-w} \sqrt{(u+w)u} F_i(u, w) / \int_0^\infty du e^{-u} \sqrt{u}, \quad (5.4.17)$$

where the integral in the denominator is simply $\sqrt{\pi}/2$. The integral kernel is

$$F_i(u, w) = \int_{-1}^{+1} dc_\theta \frac{2m_e T S_i(\mathbf{q}^2)}{\mathbf{q}^2}. \quad (5.4.18)$$

The ion structure function from Coulomb correlation effects will be an expression of the type given in Eq. (5.3.7), but with the role of electrons and ions interchanged. However, in a multi-component plasma, an exact treatment is difficult; because screening will be a relatively small correction, we use

$$S_i(\mathbf{q}^2) = \frac{\mathbf{q}^2}{\mathbf{q}^2 + k_s^2}, \quad (5.4.19)$$

where k_s is a phenomenological screening scale. We use k_i given in Eq. (5.3.8) for the ion correlations. With $\mu = k_s^2/(2m_e T)$ we therefore use

$$\begin{aligned} F_i(u, w) &= \int_{-1}^{+1} dc_\theta \frac{1}{\mu + 2u + w - 2\sqrt{(u+w)u} c_\theta} \\ &= \frac{1}{2\sqrt{(u+w)u}} \log \left(\frac{\mu + 2u + w + 2\sqrt{(u+w)u}}{\mu + 2u + w - 2\sqrt{(u+w)u}} \right). \end{aligned} \quad (5.4.20)$$

Without screening ($\mu = 0$) this expression diverges logarithmically for small w . However, for axion emission and neutrino pair emission, this divergence is moderated by at least one power of ω , so even without correlation effects, the emission of soft radiation does not diverge. Near the solar center one finds $k_i = 7$ keV and with $T = 1.3$ keV one finds $\mu = 0.037 \ll 1$, so screening is not a strong effect. Overall then the ND structure function is

$$\begin{aligned} s_{\text{ND}}(w) &= \frac{e^{-w}}{\sqrt{\pi}} \int_0^\infty du e^{-u} \log \left(\frac{\mu + 2u + w + 2\sqrt{(u+w)u}}{\mu + 2u + w - 2\sqrt{(u+w)u}} \right) \\ &\rightarrow \frac{2e^{-w}}{\sqrt{w}} \quad (\text{large } w) \end{aligned} \quad (5.4.21)$$

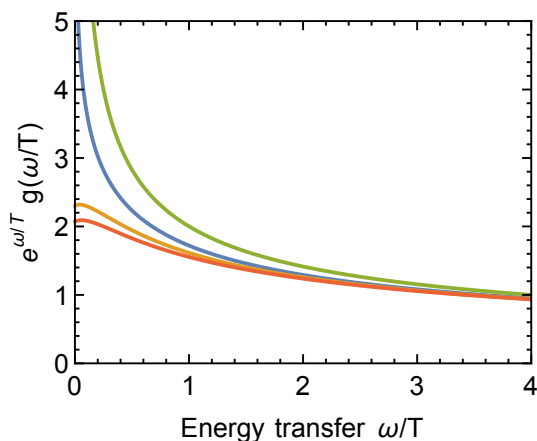


Figure 5.12: Structure function $e^w s(w)$ for bremsstrahlung. *Blue line*: Non-degenerate electrons given in Eq. (5.4.21) without Coulomb correlations ($\mu = 0$). *Orange line*: Coulomb correlations included with $\mu = 0.04$ appropriate for the solar center. *Red line*: Electron degeneracy included with $\eta = -1.4$ appropriate for the solar center. *Green line*: Asymptotic form for large $w = \omega/T$.

In Fig. 5.12 I show $e^w s_{\text{ND}}(w)$ with and without Coulomb correlation effects and the asymptotic form for large w . I also show as a red line $e^w s(w)$ including Fermi-Dirac statistics for the electrons with $\eta = -1.4$, appropriate for the solar center.

While correlation effects strongly modify the structure function at low energy transfer, this effect is much smaller after folding with the neutrino phase space according to Eq. (5.4.9). Even without correlations, the neutrino spectrum does not diverge at low energies. Including Coulomb correlations reduces it at low energies by some 20% and only by very little in the main keV-range of the spectrum. Pauli blocking of final states provides a further 5% suppression effect at very low energies, so overall these are fairly minor effects.

5.4.5 Electron-electron bremsstrahlung

The electron-electron bremsstrahlung process is similar to electron-proton bremsstrahlung with a number of important modifications [304]. The vector-current emission rate is of higher order in velocity—the simple dipole term vanishes in the scattering of equal-mass particles. In the non-degenerate and non-relativistic limit and ignoring Coulomb correlations, the axial-vector rate is $1/\sqrt{2}$ that of the electron-proton rate. In other words, we obtain the ee bremsstrahlung rate from the axial-current part of Eq. (5.4.9) with the substitution $Z^2 n_Z n_e \rightarrow n_e^2/\sqrt{2}$.

Taking degeneracy effects and Coulomb correlations exactly into account would be very hard. Instead we simply add the electron-electron term to the electron-ion one and therefore use the same treatment as for the latter. These corrections are rather small and ee bremsstrahlung is subdominant, so the overall error introduced by this approach is on the level of a few percent.

5.4.6 Solar neutrino flux

As a final step we integrate the bremsstrahlung emission rate over our standard solar model to obtain the neutrino flux at Earth. In Fig. 5.13 I show separately the vector and axial-vector contributions from electron-ion scattering as well as the one from electron-electron scattering which only contributes in the axial channel. These curves need to be multiplied with the flavor-dependent values of C_V^2 and $2C_A^2$ to obtain the proper fluxes. For the electron-ion contributions, I include only hydrogen and helium as targets. The contribution from metals is only a few percent and will be included in the opacity-derived flux in Sec. 5.5.

Finally I show in Fig. 5.14 the axial-channel bremsstrahlung flux for one flavor in comparison with the ν_e flux from the nuclear pp reaction and from T plasmon decay. Similar to the Compton process, the bremsstrahlung flux becomes important in the cross-over region between the T-plasmon and pp fluxes.

Bremsstrahlung is the dominant contribution at very low energies. From Eq. (5.4.9) we see that for very low neutrino energies, the spectrum varies as ω_ν^2 , independently of details of the structure function $\mathcal{S}(\omega)$. This scaling remains true after integrating over the Sun, so the very-low energy thermal emission spectrum scales as ω_ν^2 and thus in the same way as the pp flux given in Eq. (5.2.18).

5.4.7 Beyond the Born approximation

Traditionally the bremsstrahlung emission rate of neutrinos and other particles is calculated in Born approximation starting with the usual Feynman rules. However, the bremsstrahlung emission by a non-relativistic electron scattering on an ion receives a significant modification if one uses appropriately modified electron wave functions instead of plane waves, a point first discussed in the context of x-ray production in free-free transitions a long time ago by Sommerfeld [306]. Such an

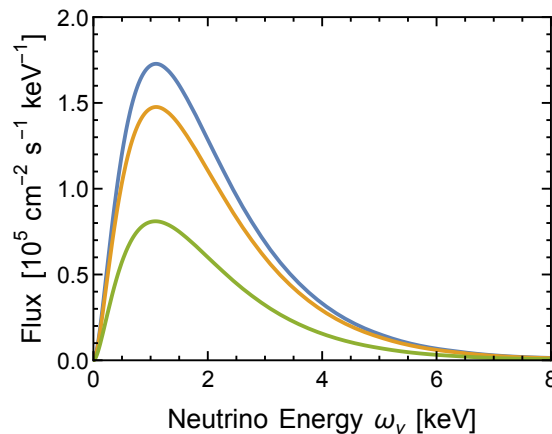


Figure 5.13: Neutrino flux from bremsstrahlung production for the vector (blue) and axial-vector (orange) electron-ion interaction, and from the ee interaction (green) which contributes only in the axial-vector channel. For the proper flux, the blue curve is to be multiplied with C_V^2 , the orange and green curves with $2C_A^2$.

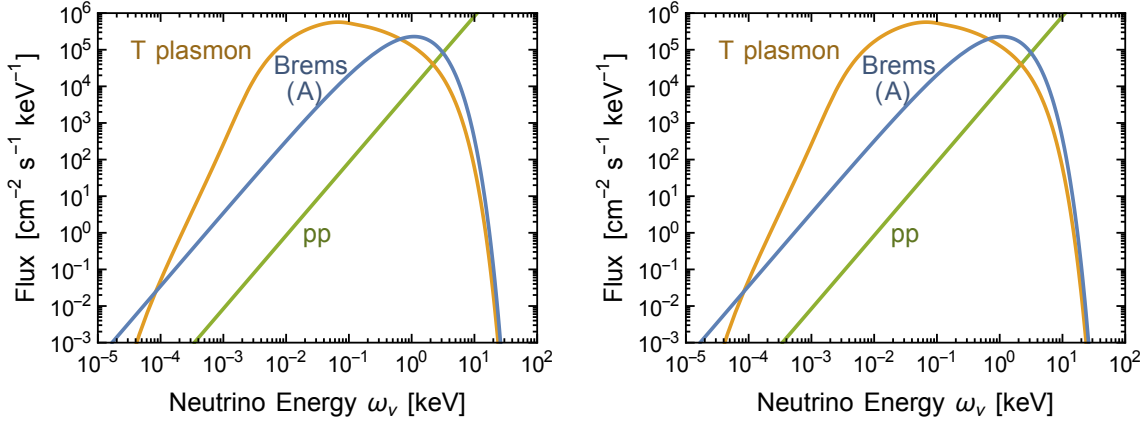


Figure 5.14: Solar neutrino flux at Earth from the axial-channel bremsstrahlung process (eI and ee contributions) for one flavor, compared with the pp flux (only ν_e) and transverse plasmon decay (ν_e and equal flux $\bar{\nu}_e$). Flavor oscillations are not considered here.

enhancement in bremsstrahlung emission arises because of the long-range Coulomb potential. It is the counterpart of what is known as Fermi-Coulomb function in the context of beta decay and of the so-called Sommerfeld enhancement, to be taken into account in dark matter annihilation processes [307]. In these cases, the correction is simply given by $f(v) = |\psi(0)|^2$, i.e., by the normalization of the outgoing (or ingoing) Coulomb distorted wave function

$$\sigma = \sigma_0 f(v) = \sigma_0 \frac{2\pi Z\alpha}{v} \frac{1}{1 - e^{-\frac{2\pi Z\alpha}{v}}}, \quad (5.4.22)$$

where σ_0 is the cross section evaluated with plane waves and v is the velocity of the outgoing (or ingoing) particle.

Such corrections have been extensively studied also for bremsstrahlung (see e.g. reference [308]). Elwert found that a good approximation to correct the Born scattering formula is obtained by simply multiplying Eq. (5.4.8) by the factor [309]

$$f_E = \frac{v_i}{v_f} \frac{1 - e^{-\frac{2\pi Z\alpha}{v_i}}}{1 - e^{-\frac{2\pi Z\alpha}{v_f}}}, \quad (5.4.23)$$

which is the ratio $|\psi_f(0)|^2/|\psi_i(0)|^2$ of the final and initial state electron wave functions. In Fig. 5.15 (green line) I show the effect on the overall solar neutrino flux of including this factor in the bremsstrahlung rate, leading to a typical 20–30% enhancement. I also show as an orange line the effect of including Coulomb correlations which reduce the flux typically by some 5%. At very small energies, the Elwert factor becomes less important and Coulomb correlations more important.

As previously noted in the context of solar axion emission [280], the Sommerfeld correction is included in the photon opacity calculation. On the other hand, using unscreened Coulomb wave functions in a stellar plasma is not fully consistent—the true correction should be considerably smaller, especially for bremsstrahlung on hydrogen and helium. Therefore, as in reference [280] we calculate these rates directly,

not from the opacities, and leave out the Elwert factor, possibly underestimating the true flux by some 10%. On the other hand, we will include the Coulomb correlation factor. At keV-range energies this makes no big difference, but should be a reasonable correction in the far sub-keV range where bremsstrahlung is the dominant flux and the Elwert factor is small.

5.5 Free-bound and bound-bound transitions

The nuclei of the solar plasma are imperfectly ionized, notably the “metals” (elements heavier than helium). Therefore, in addition to bremsstrahlung (free-free electron transitions), free-bound (fb) and bound-bound (bb) transitions are also important for particle emission. In the context of axion emission by electrons, these processes imprint a distinctive line pattern on the expected solar axion flux [280]. Likewise, the photon opacities, as input to solar models, depend strongly on these processes. In reference [275] free-bound processes were included by explicit atomic transition calculations for a number of elements.

However, following the approach taken in an earlier paper for calculating the

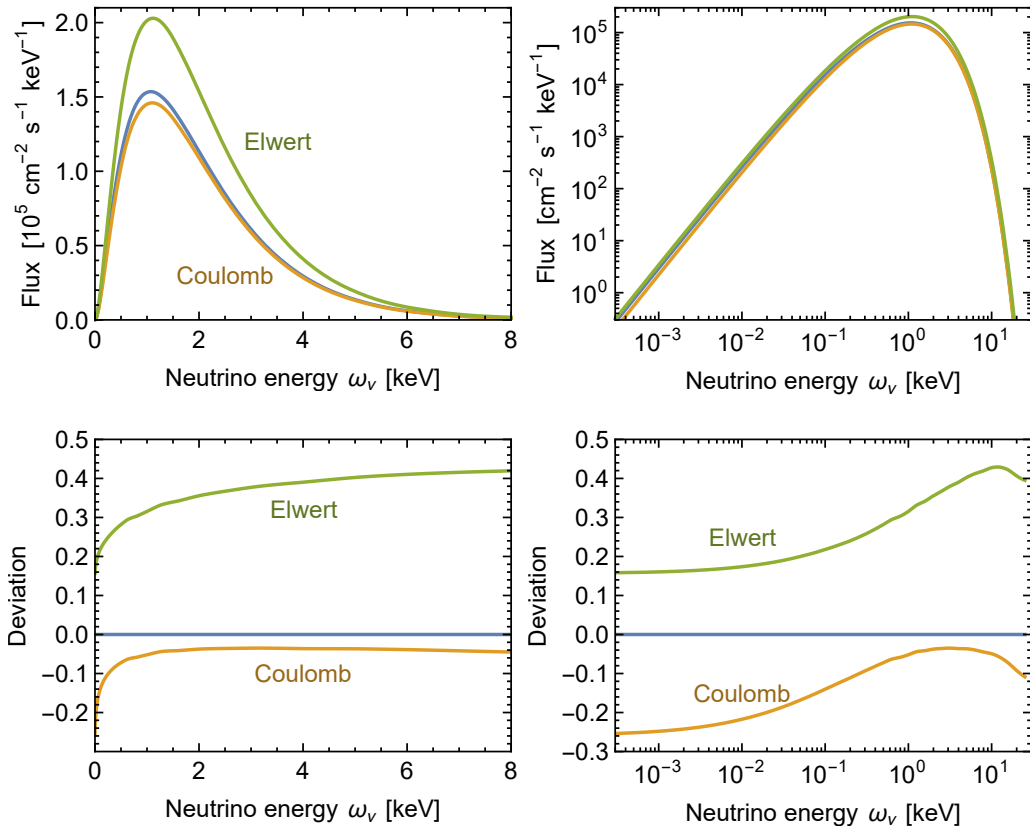


Figure 5.15: Solar neutrino flux from bremsstrahlung production for axial-vector electron-ion interaction, without corrections (blue), and including respectively correlations (orange) and the Elwert factor (green). For the proper flux, the curves in the upper panels are to be multiplied with $2C_A^2$.

solar axion flux [280], the emission rate can be related to the photon opacity by Eq. (5.4.12), i.e., the neutrino emissivity is the same as the phase-space weighted photon emissivity. Therefore, one can use the solar photon opacity from the literature to derive the neutrino emissivity. In Sec. 5.4.3 we have derived the relation between photon and neutrino emissivity explicitly for bremsstrahlung, but it applies in this form to all processes where a nonrelativistic electron makes a transition in the potential of an external scattering center which takes up momentum. In other words, it applies in the long-wavelength approximation with regard to the electron. On the other hand, this relation does not apply to electron-electron bremsstrahlung, the Compton process, or plasmon decay.

While we could have used this relation to extract the bremsstrahlung emissivity from the opacities, we have preferred to treat bremsstrahlung on hydrogen and helium as well as electron-electron bremsstrahlung explicitly in the interest of completeness. For the fb and bb transitions as well as bremsstrahlung on metals we proceed as in reference [280] to extract the neutrino emissivity. In Fig. 5.16 I show the resulting neutrino flux spectrum at Earth in comparison with the bremsstrahlung result on hydrogen and helium derived earlier. I show the vector and axial-vector contributions, each to be multiplied with the flavor-dependent C_V^2 or $2C_A^2$ to arrive at the proper flux. While the fb and bb contributions are subdominant relative to bremsstrahlung, they dominate at higher energies. This behavior was to be expected because they are more relevant than ff processes in the Rosseland opacities at any radius (see e.g. Fig. 15 of reference [78]).

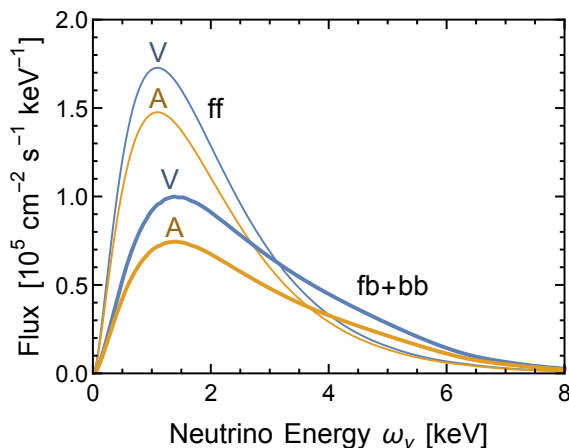


Figure 5.16: Solar neutrino flux at Earth from free-free (ff), free-bound (fb) and bound-bound (bb) electron-ion transitions for the vector (V) and axial-vector (A) contributions. The proper fluxes are found by multiplying the curves with C_V^2 and $2C_A^2$, respectively. The ff curves include bremsstrahlung on hydrogen and helium and are the same as in Fig. 5.13; they exclude electron-electron bremsstrahlung. The fb+bb curves include bremsstrahlung on metals.

5.6 Solar neutrino flux at Earth

5.6.1 Flavor-dependent fluxes

In order to consolidate the solar flux results from different thermal processes I show the spectra at Earth in Fig. 5.17. In the left panel all contributions relevant for the vector coupling are shown, where the true flux is found by multiplication with the flavor-dependent value of C_V^2 . At low energies, plasmon decay dominates, at intermediate ones bremsstrahlung, and at the highest energies Compton process. In the right panel I show the analogous axial-vector result which does not have any significant plasmon-decay contribution.

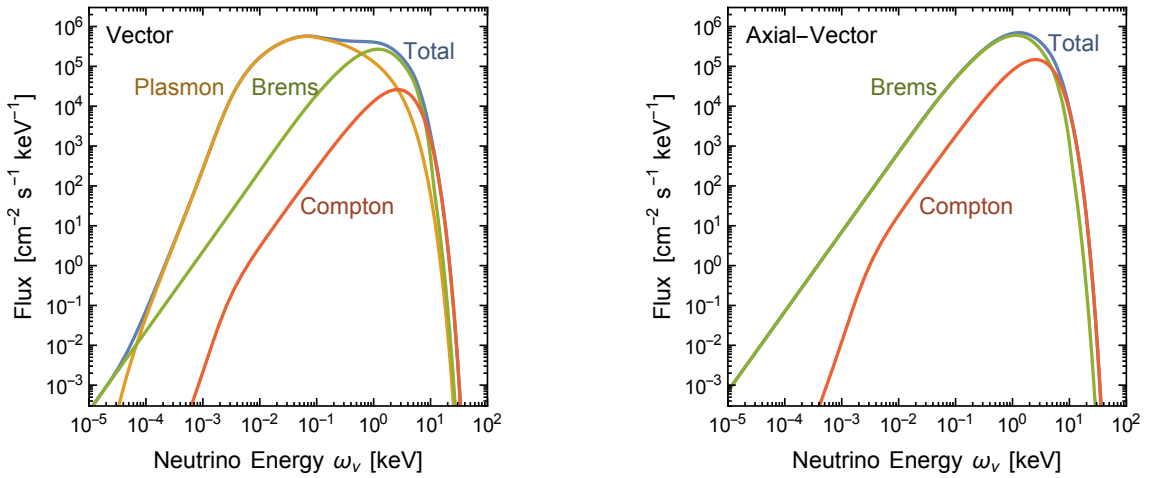


Figure 5.17: Solar neutrino flux at Earth from the indicated processes, where “brems” includes ff, fb and bb. *Left panel:* Vector coupling, for proper flux multiply with C_V^2 . *Right panel:* Axial-vector coupling, for proper flux multiply with C_A^2 .

The intrinsic uncertainties of the various emissivity calculations should not be larger than a few tens of percent concerning various issues of in-medium effects such as correlations or Coulomb wave functions of charged particles. In addition, every process has a different dependence on temperature, density and chemical composition so that different standard solar models will produce somewhat different relative weights of the different processes. We have not studied the variation of the different flux contributions depending on different standard solar models, but the overall uncertainty again should be in the general ten percent range.

One may show the same results in a somewhat different form if we observe that the vector-current processes produce almost exclusively $\nu_e \bar{\nu}_e$ pairs, whereas the axial-vector processes produce all flavors in equal measure. In the upper panels of Fig. 5.18 I show these total fluxes, where now the coupling constants $C_V^2 = 0.9263$ and $C_A^2 = 1/4$ are included. In addition I show the ν_e flux from the nuclear pp reaction. In the bottom panels I add the different source channels for every flavor and show the keV-range fluxes for ν_e , $\bar{\nu}_e$, and each of the other species, still ignoring flavor oscillations.

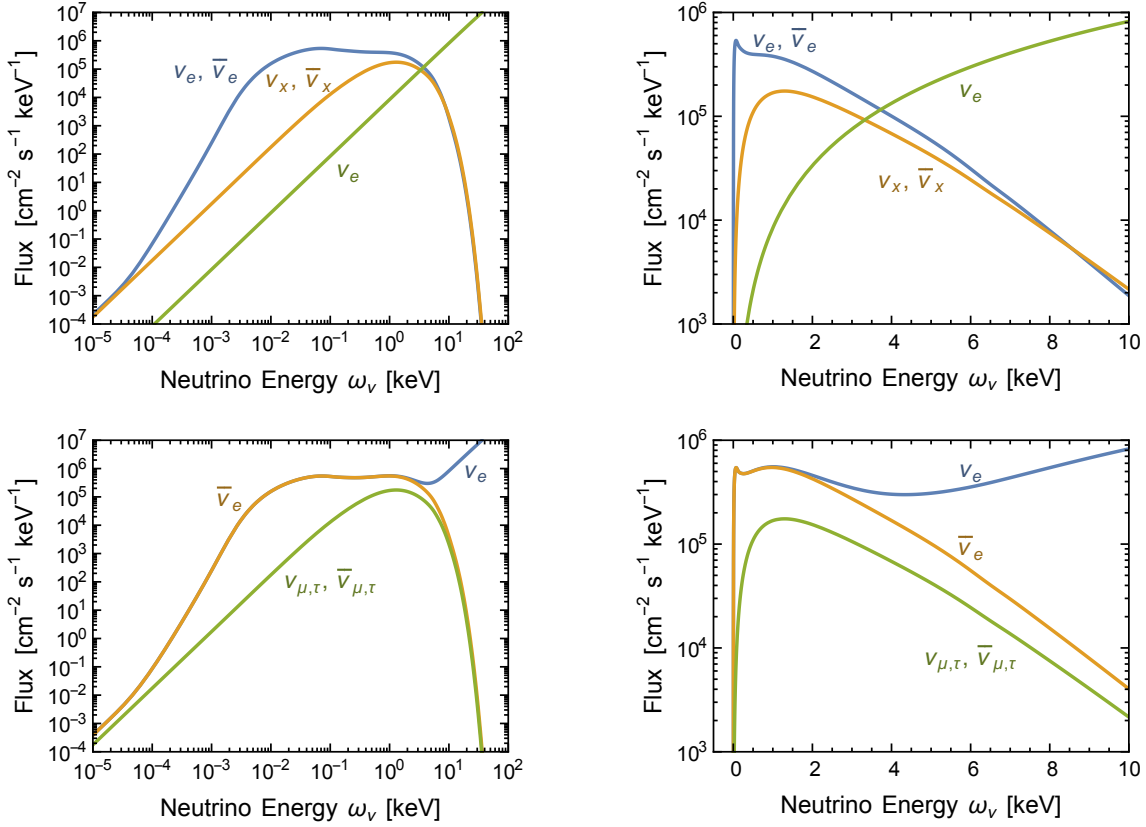


Figure 5.18: Flavor-dependent solar neutrino fluxes at Earth, ignoring flavor mixing. *Top panels:* Thermal flux from vector-current interactions producing only $\nu_e\bar{\nu}_e$ pairs, axial-vector emission, producing equal fluxes of every flavor, where x stands for e , μ or τ , and ν_e from the nuclear pp reaction. *Bottom panels:* ν_e , $\bar{\nu}_e$, and other single-species fluxes after adding the source channels.

5.6.2 Including flavor mixing

Flavor-eigenstate neutrinos are mixtures of three different mass eigenstates. After propagating over a long distance, these mass eigenstates effectively decohere, so the neutrino flux arriving at Earth is best described as an incoherent mixture of mass eigenstates. It depends on the nature of a possible detector if these should be re-projected on interaction eigenstates or if these fluxes can be used directly if the detection channel is flavor blind. As we do not know the nature of such a future detector, the neutrino flux in terms of mass eigenstates is the most natural form of presentation.

The axial-current production channel has amplitude $C_A = +1/2$ for ν_e and $C_A = -1/2$ for the other flavors, yet on the level of the rate (proportional to C_A^2) all flavors are produced in equal measure. Therefore, the density matrix in flavor space is proportional to the 3×3 unit matrix and thus the same in any basis. Without further ado we can think of the axial-current processes as producing mass eigenstates, so in the upper panels of Fig. 5.18, the fluxes marked ν_x and $\bar{\nu}_x$ can be interpreted as x standing for the mass indices 1, 2 and 3.

The vector-current channels, on the other hand, have the peculiar property of

producing almost exclusively e -flavored states as discussed earlier, which is also true of the charged-current pp nuclear reaction. These states oscillate in flavor space after production. The relevant oscillation scale is $\omega_{\text{osc}} = \Delta m^2/2E = 3.8 \times 10^{-8} \text{ eV}/E_{\text{keV}}$ for the solar mass difference of $\Delta m^2 = 7.5 \times 10^{-5} \text{ eV}^2$ and using $E_{\text{keV}} = E/\text{keV}$. For the atmospheric mass difference $\Delta m^2 = 2.5 \times 10^{-3} \text{ eV}^2$ the oscillation scale is $\omega_{\text{osc}} = 1.25 \times 10^{-3} \text{ eV}/E_{\text{keV}}$. These numbers should be compared with the matter-induced energy splitting between ν_e and the other flavors of $\Delta V = \sqrt{2}G_{\text{F}}n_e = 7.6 \times 10^{-12} \text{ eV}$ for the electron density $n_e = 6 \times 10^{25} \text{ cm}^{-3}$ of the solar center. Therefore, for keV-range neutrinos, the matter effect is very small and neutrino oscillations proceed essentially as in vacuum. The source region in the Sun is much larger than the oscillation length and is far away from Earth, so flavor oscillations effectively decohere long before reaching here. Therefore, we may think of the e -flavored channels as producing an incoherent mixture of mass eigenstates. On the probability level, the best-fit mass components of ν_e are

$$p_1 = 67.9\%, \quad p_2 = 29.9\%, \quad p_3 = 2.2\%. \quad (5.6.1)$$

On this level of precision, these probabilities do not depend on the mass ordering. The final fluxes in terms of mass eigenstates were shown in Fig. 5.2 in Sec. 5.1 as our main result.

Distinguishing Dirac and Majorana neutrinos by their gravi-majoron decays¹⁰

The mechanism to generate neutrino mass generation remains a mystery. A completely new approach to explain small Dirac or Majorana neutrino masses [311] relies on new physics at the low-energy frontier of particle physics instead of high-energy extensions of the Standard Model. The key idea is that a hypothetical topological vacuum susceptibility of gravity induces fermion condensation [312, 313], that can give rise to effective fermion masses [311]. If this effect is realized in nature, it is most important for the lightest fermions and could be the unique origin of neutrino masses.

Phenomenologically, neutrino condensation would be accompanied by the appearance of pseudoscalar Nambu-Goldstone bosons ϕ , similar to light mesons in QCD, that can be interpreted as neutrino-antineutrino bound states [311, 313] and that were called gravi-majorons. This suggestive terminology is a bit of a misnomer because majorons [314] were originally invoked to explain Majorana masses, whereas it is a key point of our discussion that ϕ bosons appear for both the Dirac and Majorana option. An important difference to conventional Nambu-Goldstone bosons is that the $\nu\nu\phi$ vertex, due to its low-energy origin, “melts” for high-energy off-shell situations so that constraints based on scattering processes, e.g. majoron production in supernovae, typically do not apply [311, 315]. On the other hand, decays of the type $\nu_i \rightarrow \bar{\nu}_j + \phi$ proceed in the usual way.

While this scenario is somewhat speculative, it may become empirically motivated in the near future. One predicts a neutrinoless Universe after photon decoupling, or at least all neutrinos in the lowest mass state, due to decays and annihilations into gravi-majorons [311]. If near-future cosmological observations [19] fail to detect a hot dark matter component on the minimal level expected from oscillation experiments, we may be forced to contemplate the absence of the usual cosmic neutrino background.

¹⁰This Chapter closely follows the discussion of L. Funcke, G. Raffelt and E. Vitagliano, “Distinguishing Dirac and Majorana neutrinos by their gravi-majoron decays,” [arXiv:1905.01264](https://arxiv.org/abs/1905.01264), submitted to Phys. Rev. D [310].

Similar questions arise if the KATRIN experiment [316] detects a neutrino mass in conflict with cosmological limits.

The gravitational mass model works for both Dirac and Majorana neutrinos. Therefore, one important question remains how we can experimentally distinguish between these two possibilities. In high-energy models, neutrinoless double-beta ($0\nu\beta\beta$) decay [317] is the most promising approach and one that remains viable in our scenario. Moreover, one predicts that the low-energy gravitational mass model offers an additional opportunity through fast $\nu_i \rightarrow \bar{\nu}_j + \phi$ decays.

It is not new that details e.g. of radiative decays $\nu_i \rightarrow \bar{\nu}_j + \gamma$ depend on the Dirac vs. Majorana nature [318, 319]. The γ spectrum in relativistic decays depends on this property, inherited from the angular γ distribution relative to the spin of the mother neutrino in its rest frame. However, radiative decays of light neutrinos are usually too slow to be of any practical interest.

The $\nu_i \rightarrow \bar{\nu}_j + \phi$ decays in the gravitational mass model are fast enough to distinguish between the Majorana and Dirac cases by using the flux and spectrum of the daughter neutrinos. A Dirac neutrino ν_i decays into a neutrino, either active ν_j or sterile N_j , whereas a Majorana neutrino always decays into an active state, which however in a detector appears as either a neutrino ν_j or an antineutrino $\bar{\nu}_j$. This is possible because a Majorana neutrino does not have a defined lepton number, and what one calls antineutrino is simply a state with right-handed helicity.

A detector that can distinguish neutrinos from antineutrinos can identify the Dirac or Majorana nature by looking at neutrino vs. antineutrino appearance, assuming an asymmetry at the source. Moreover, given the source spectrum, the energy spectrum depends on the nature of the mass term independently of an asymmetry at the source. If the mass spectrum is degenerate, Majorana and Dirac particles can be distinguished because spin-flip is not suppressed compared to spin conservation. As a result, Majorana neutrinos would decay to antineutrinos, whereas Dirac neutrinos would decay to sterile states.

6.1 Differences to previous majoron-like models

6.1.1 Dirac or Majorana neutrino nature

In contrast to the original majoron model [314], the gravitational neutrino mass mechanism works for both Dirac and Majorana neutrinos. Therefore we can in principle distinguish three possible scenarios:

- (1) *Pure left-handed Majorana case:* If neutrinos are identical to their antiparticles and no right-handed states exist, neutrinos are massless in the Standard Model. The neutrino condensate then generates small left-handed Majorana masses.
- (2) *Pure Dirac case:* If neutrinos are distinct from their antiparticles, right-handed states exist and the condensate generates small effective Dirac masses.

- (3) *Mixed case*: If neutrinos are identical to their antiparticles and right-handed states exist, the condensate generates Dirac masses as well as left- and right-handed Majorana masses. In this case, the active and sterile Dirac states have masses $m_\nu \sim \text{meV} - \text{eV}$ and are substantially mixed.

For simplicity, I will focus on the minimal cases (1) and (2). In the former case, the effective left-handed Majorana mass terms violate isospin by one unit but are allowed after electroweak symmetry breaking. Here, let me note that only the condensate but not gravity is assumed to violate isospin.

Concerning case (3), the only interesting aspect worth mentioning is that this active-sterile neutrino scenario could be motivated by short-baseline anomalies [320]. While light sterile neutrinos generally conflict with cosmological constraints on neutrino masses and the effective number of neutrino species [321], these tensions disappear in the gravitational mass model, because (i) the mass bounds are weakened [311, 322] and (ii) the active relic neutrino background is massless before photon decoupling and therefore uncoupled to the sterile states.

Note that the presence of light sterile neutrinos would strongly distort the parameter space for $0\nu\beta\beta$ decay [323] and could even make the decay vanish completely [324]. In contrast, gravi-majorons do not affect the $0\nu\beta\beta$ decay rate because their emission is strongly suppressed (Sec. 6.1.3). Finally, there was a debate whether the $0\nu\beta\beta$ decay rate might be altered because the gravitational neutrino masses are not hard masses generated at high-energy scales but effective ones generated at the low-energy condensation scale Λ_G . However, since there is no momentum flow through the masses generated by the condensate, we expect them to be indistinguishable from hard neutrino masses in the $0\nu\beta\beta$ process.

6.1.2 Late neutrinoless Universe

Interactions between neutrinos and Nambu-Goldstone bosons are strongly constrained by cosmological data. For example, almost the entire parameter space of the “neutrinoless Universe” model [325], which evades the cosmological bounds $\sum_i m_{\nu_i} \lesssim 0.2 \text{ eV}$ [326], was ruled out by early-universe neutrino free-streaming constraints [327–331] and precision measurements of the primordial radiation density [15]. In contrast, gravi-majorons are not ruled out because they only arise in the late Universe after photon decoupling.

When the Universe cools down to the low phase transition temperature $T_G \lesssim T_{\text{decoupling}} \sim 0.3 \text{ eV}$, the neutrino condensate forms and the emerging gravi-majorons $\phi \equiv \{\phi_k, \eta_\nu\}$ [311, 313] start to interact with neutrinos through the same nonperturbative gravitational vertex that is responsible for the neutrino masses,

$$\mathcal{L}_{\text{int}} = \sum_{k=1}^{14} \partial_\mu \phi_k \sum_{i,j=1}^3 \frac{g_{ij}}{m_i + m_j} \bar{\nu}_i \gamma^\mu \gamma_5 \nu_j + i\eta_\nu \sum_{i,j=1}^3 y_{ij} \bar{\nu}_i \gamma_5 \nu_j + \text{h.c.} \quad (6.1.1)$$

Here, the ϕ_k are 14 (almost) massless Nambu-Goldstone bosons,¹¹ η_ν is a massive pseudo-Nambu-Goldstone boson with $m_{\eta_\nu} \sim \Lambda_G \sim T_G$, and g_{ij} and y_{ij} are the (off)diagonal couplings normalized to be dimensionless (with $g_{ii} = y_{ii} = m_i/\Lambda_G$). In the following, we neglect the sum over k and assume conservatively that the couplings are to a single Nambu Goldstone boson.

After the cosmological phase transition, the previously massless neutrinos become massive, quickly decay into the lowest mass eigenstate, and (partially) annihilate into gravi-majorons through the process $\nu + \bar{\nu} \rightarrow \phi + \phi$ [311]. Thus, the early-universe massless neutrino “radiation” converts into massless gravi-majoron radiation after photon decoupling. This almost complete annihilation could only be evaded in the hypothetical presence of substantial neutrino asymmetries in the Dirac case, weakening the cosmological neutrino mass bounds to $\sum m_\nu < 4.8$ eV at 95% CL [322].

To conclude, unless there are large primordial neutrino asymmetries, the gravitational neutrino mass model [311] predicts a late neutrinoless Universe and could be falsified by a cosmological neutrino mass detection, e.g. by the upcoming DESI or Euclid surveys [19]. The KATRIN beta-decay experiment [316] could provide a hint towards our predicted neutrinoless Universe if it detects an unexpectedly large neutrino mass scale. One should stress that KATRIN’s measurement of the electron energy spectrum would be unaffected by the gravi-majorons, because their interactions take place on much longer timescales than the beta-decay process.

6.1.3 Stellar and laboratory bounds

One might naively expect that gravi-majorons are ruled out by astrophysical observations, because their couplings are severely constrained by stellar processes. As explained in Ref. [315], the least suppressed two-photon coupling of the gravi-majorons is $g_{\phi\gamma} \sim (\Lambda_G/m_e)^3/\Lambda_G \sim 10^{-10} \text{ GeV}^{-1}$ for $\Lambda_G \sim 0.1$ eV, which at first sight is already ruled out by constraints from solar axion experiments, $g_{\phi\gamma} \lesssim 0.88 \times 10^{-10} \text{ GeV}^{-1}$ at 95% CL for $m_\phi \lesssim 0.02$ eV [332]. However, the gravi-majoron production in astrophysical environments with $E \gg m_\nu$ is additionally suppressed by $(\Lambda_G/E)^n$ due to the high-energy softening of the gravitational vertex, where n is an unknown power-law exponent that has to be fixed by phenomenological requirements (as discussed in [311, 315]). Thus, the common relation between axion-like predictions for laboratory and solar axion experiments does not apply [315]. By similar arguments one also evades other astrophysical bounds on the gravitational $\nu\bar{\nu}\gamma$, $\nu\bar{\nu}\phi$, $\nu\bar{\nu}\nu\bar{\nu}$, $e\bar{e}\phi$, and $e\bar{e}\nu\bar{\nu}$ couplings.

Regarding laboratory experiments, the most important bounds on the emission of conventional majoron-like bosons comes from $0\nu\beta\beta$ decay [333] and leptonic decays of mesons [334]. Following the argumentation above, these bounds do not apply to gravi-majorons because they and their couplings to the virtual intermediate neutrinos dissolve in these high-energy processes. Moreover, just like any pseudoscalar Nambu-Goldstone bosons, our gravi-majorons do not mediate long-range interactions

¹¹Zero hard neutrino masses imply $m_{\phi_k} = 0$, but some ϕ_k get $m_{\phi_k} \sim 10^{-33} \text{ eV}(\Lambda_G/0.1 \text{ eV})^3$ by $SU(2)_W$ effects.

in macroscopic systems due to their spin-dependent coupling. However, short-distance fifth-force experiments can put important bounds on our new gravitational interactions, as discussed in [311, 315].

Note finally that the gravitational vertex suppression is due to the large four-momentum transfer in the processes under consideration, which is why the suppression does not apply to neutrino oscillations or to the neutrino decays considered in Sec. 6.2.

6.2 Neutrino decay rate

As predicted by the gravitational neutrino mass model [311], the presence of gravi-majorons implies neutrino decay through the vertex of Eq. (6.1.1). The crucial new point is that the Dirac and Majorana neutrino cases yield different decay channels, so that the composition of the daughter neutrinos depends on the type of masses generated through the gravitational mechanism.

6.2.1 Matrix element for the neutrino decay

Here I will calculate the matrix element for the decay process $\nu_i \rightarrow \bar{\nu}_j + \phi$ of a Dirac or a Majorana neutrino with fixed initial spin and derivative coupling to a gravi-majoron. In the case of Majorana neutrinos, I will assume that both the final and initial neutrinos are Majorana particles. The interaction term in the Lagrangian is

$$\mathcal{L}_{\text{int}} = \partial_\mu \phi \sum_{ij} \frac{g_{ij}}{m_i + m_j} \bar{\nu}_i \gamma^\mu \gamma_5 \nu_j + \text{h.c.} \quad (6.2.1)$$

For the Dirac neutrino case, fixing the initial spin is equivalent to choosing an active *or* a sterile initial state, whereas for a Majorana neutrino it simply means choosing if it is a neutrino (left-handed) or an antineutrino (right-handed). Using the Feynman rules of Ref. [335], I find

$$\mathcal{M}^{\text{D}} = g_{\phi,ij} \bar{u}_{\nu_j} \gamma^\mu \gamma^5 u_{\nu_i} J_\mu^\phi \quad (\text{Dirac}) \quad (6.2.2a)$$

$$\mathcal{M}^{\text{M}} = g_{\phi,ij} \bar{u}_{\nu_j} \gamma^\mu \gamma^5 u_{\nu_i} J_\mu^\phi \times 2 \quad (\text{Majorana}), \quad (6.2.2b)$$

where I have neglected global phases and $J_\mu^\phi = k_\mu$ is the gravi-majoron current. Note that the matrix element for the Majorana case is twice as large as for the Dirac case because the Hermitian conjugate in the Lagrangian also contributes to the amplitude, so that the rate will be four times larger for a decaying Majorana neutrino. This can be compared e.g. to radiative decays, for which the decay width of Majorana neutrinos is two times larger than the decay width of Dirac neutrinos [336]. The global constant can be reabsorbed in the coupling definition.

Let us consider the case of a decaying Majorana neutrino. Squaring the amplitude

one finds

$$|\mathcal{M}^M|^2 = \frac{g_{ij}^2}{(m_i + m_j)^2} \text{Tr} \left[(\not{p}_i + m_i)(1 + h_i \gamma^5 \not{\not{p}}_i) \gamma^\mu \gamma^5 \right. \\ \left. \times (\not{p}_j + m_j)(1 + h_j \gamma^5 \not{\not{p}}_j) \gamma^\nu \gamma^5 \right] k_\mu k_\nu, \quad (6.2.3)$$

where p_i , p_j and k are the four-momenta of ν_i , ν_j and ϕ respectively and I used [36]

$$u_\nu \bar{u}_\nu = \frac{1}{2} (\not{p} + m_\nu) (1 + h \gamma^5 \not{\not{p}}) \quad (6.2.4)$$

with the spin vector

$$S = \left(\frac{|\mathbf{p}|}{m_\nu}, \frac{E_\nu}{m_\nu} \hat{\mathbf{p}} \right). \quad (6.2.5)$$

The squared amplitude in Eq. (6.2.3) has 16 terms, 8 of which contain an odd number of γ^μ and 4 of which have a γ^5 so that they do not contribute for symmetry reasons. The remaining terms give

$$|\mathcal{M}^M|^2 = 4 g_{ij}^2 [(p_i \cdot p_j - m_i m_j)(1 + h_i h_j S_i \cdot S_j) - h_i h_j (p_i \cdot S_j)(p_j \cdot S_i)] . \quad (6.2.6)$$

Analogously, one can compute the decay through a pseudoscalar coupling

$$\mathcal{L}_{\text{int}} = i\phi \sum_{ij} g_{ij} \bar{\nu}_i \gamma_5 \nu_j + \text{h.c.} \quad (6.2.7)$$

and find explicitly that it has the same squared amplitude as in Ref. [337]. Notice that there are two factors to be taken into account. The coupling in our interaction Lagrangian is twice as large as in Ref. [337]; furthermore, I use a different spinor normalization, so an additional factor $1/(4 m_i m_j)$ has to be included. Our results agree with Ref. [337] but differ from the ones reported in Ref. [338], where the couplings are defined as in our Lagrangian but the rate is quoted directly from Ref. [337]; the results in Ref. [338] would be correct if they considered exclusively Dirac neutrinos. In the following I will consider only the pseudoscalar coupling, as the derivative coupling is equivalent to the latter.

After substituting Eq. (6.2.5) in (6.2.8), one can evaluate the squared amplitude in the ν_i rest frame, where the spin vector $S = (0, \mathbf{S})$, so that $S \cdot p = 0$; the emission of a certain helicity is not isotropic,

$$|\mathcal{M}^M|^2 = 4 g_{ij}^2 \left[(m_i E_j - m_i m_j) \left(1 - h_i h_j E_j \frac{\mathbf{p}_j}{|\mathbf{p}_j|} \cdot \mathbf{S}_i \right) - h_i h_j \left(m_i \frac{|\mathbf{p}_j|}{m_j} \right) (\mathbf{p}_j \cdot \mathbf{S}_i) \right]. \quad (6.2.8)$$

The anisotropy in the emission translates to different differential rates for different helicity final states [319]. We can evaluate the squared amplitudes in the laboratory frame, in which $E_i \gg m_i$, finding for the helicity conserving decay

$$|\mathcal{M}_{\nu_i \rightarrow \nu_j + \phi}^M|^2 = 4 g_{ij}^2 m_i m_j (A - 2) \quad (6.2.9)$$

and for the helicity flipping decay

$$|\mathcal{M}_{\nu_i \rightarrow \bar{\nu}_j + \phi}^{\text{M}}|^2 = 4 g_{ij}^2 m_i m_j \left(\frac{m_i^2 + m_j^2}{m_i m_j} - A \right), \quad (6.2.10)$$

where

$$A \equiv \left(\frac{m_i E_j}{m_j E_i} + \frac{m_j E_i}{m_i E_j} \right). \quad (6.2.11)$$

The decay rates for Dirac neutrinos to a neutrino or a sterile (right-handed) neutrino are found by dividing these expressions by 4 and interpreting $\bar{\nu}_j$ as a sterile state N_j . These are the expressions that are relevant for the decay rate discussed in the main text. As a final remark, the calculation I have carried out in this Section can be repeated by substituting the external current J_μ to obtain the cross section of neutrinos coherently scattering on nuclei. This allows for distinguishing Dirac from Majorana neutrino by looking at the endpoint of the photon emitted by the nuclei, even though the effect is very small [339].

6.2.2 Differential rate

The differential rate Γ for the decay $\nu_i \rightarrow \bar{\nu}_j + \phi$ in a generic reference frame is

$$d\Gamma = \frac{1}{2E_i} (2\pi)^4 \delta^{(4)}(p_i - p_j - k) |\mathcal{M}|^2 \frac{d^3 \mathbf{p}_j}{(2\pi)^3 2E_j} \frac{d^3 \mathbf{k}}{(2\pi)^3 2\omega}, \quad (6.2.12)$$

where the squared amplitudes for both the helicity-preserving and helicity-changing processes have been found previously; here, p_i , p_j and k are the four-momenta of ν_i , ν_j and ϕ respectively. After integration over the gravi-majoron momenta and over the direction of the neutrino, the differential rate is

$$\frac{d\Gamma}{dE_j} = \frac{1}{16\pi E_i |\mathbf{p}_i|} |\mathcal{M}|^2. \quad (6.2.13)$$

In the laboratory frame, where $E_i \gg m_i$, I find for Majorana neutrinos

$$\frac{d\Gamma_{\nu_i \rightarrow \nu_j + \phi}^{\text{M}}}{dE_j} = \frac{g_{ij}^2}{4\pi E_i |\mathbf{p}_i|} m_i m_j (A - 2) \quad (6.2.14a)$$

$$\frac{d\Gamma_{\nu_i \rightarrow \bar{\nu}_j + \phi}^{\text{M}}}{dE_j} = \frac{g_{ij}^2}{4\pi E_i |\mathbf{p}_i|} m_i m_j \left(\frac{m_i^2 + m_j^2}{m_i m_j} - A \right), \quad (6.2.14b)$$

where A was defined in Eq. (6.2.11). Dirac neutrinos decay either into active (left-handed) neutrinos or into sterile (right-handed) neutrinos N_j . The differential decay rates equal 1/4 times the rates for Majorana neutrinos,

$$\frac{d\Gamma_{\nu_i \rightarrow \nu_j + \phi}^{\text{D}}}{dE_j} = \frac{1}{4} \frac{d\Gamma_{\nu_i \rightarrow \nu_j + \phi}^{\text{M}}}{dE_j}, \quad (6.2.15a)$$

$$\frac{d\Gamma_{\nu_i \rightarrow N_j + \phi}^{\text{D}}}{dE_j} = \frac{1}{4} \frac{d\Gamma_{\nu_i \rightarrow \bar{\nu}_j + \phi}^{\text{M}}}{dE_j}. \quad (6.2.15b)$$

To get the total decay rates, the differential rates must be integrated over the allowed energy range for the daughter neutrino ν_j ,

$$\frac{E_i}{2} \left(1 + \frac{1}{x_{ij}^2} \right) - \frac{|\mathbf{p}_i|}{2} \left(1 - \frac{1}{x_{ij}^2} \right) \leq E_j \leq \frac{E_i}{2} \left(1 + \frac{1}{x_{ij}^2} \right) + \frac{|\mathbf{p}_i|}{2} \left(1 - \frac{1}{x_{ij}^2} \right) \quad (6.2.16)$$

where $x_{ij} \equiv m_i/m_j > 1$. In the lab frame with $E_i \gg m_i$, Eq. (6.2.16) reduces to

$$\frac{E_i}{x_{ij}^2} \leq E_j \leq E_i. \quad (6.2.17)$$

The decay rates for Majorana neutrinos are then

$$\Gamma_{\nu_i \rightarrow \nu_j + \phi}^{\text{M}} = \frac{g_{ij}^2 m_i m_j}{4\pi E_i} \left(\frac{x_{ij}}{2} - 2 + \frac{2}{x_{ij}} \log x_{ij} + \frac{2}{x_{ij}^2} - \frac{1}{2x_{ij}^3} \right), \quad (6.2.18a)$$

$$\Gamma_{\nu_i \rightarrow \bar{\nu}_j + \phi}^{\text{M}} = \frac{g_{ij}^2 m_i m_j}{4\pi E_i} \left(\frac{x_{ij}}{2} - \frac{2}{x_{ij}} \log x_{ij} - \frac{1}{2x_{ij}^3} \right). \quad (6.2.18b)$$

These results agree with the literature [337, 340, 341], if one accounts for the different normalization of the couplings.

There are two important limits for these expressions: the case of a large mass hierarchy $m_i \gg m_j$ and the degenerate case $m_i \simeq m_j$. The latter remains allowed in the gravitational mass model, because the cosmological mass bounds are substantially weakened (Sec. 6.1.2). In the limit of a large mass hierarchy, one finds

$$\Gamma_{\nu_i \rightarrow \nu_j + \phi}^{\text{M}} = \Gamma_{\nu_i \rightarrow \bar{\nu}_j + \phi}^{\text{M}} = \frac{\Gamma_{\text{tot}}^{\text{M}}}{2}, \quad (6.2.19)$$

where the total decay rate is

$$\Gamma_{\text{tot}}^{\text{M}} = \frac{g_{ij}^2 m_i m_j}{4\pi E_i}; \quad (6.2.20)$$

here, the first factor is the total decay rate in the rest frame of ν_i and m_i/E_i is the Lorentz factor.

The total decay rate in Eq. (6.2.20) yields the neutrino rest-frame lifetimes $\tau_i = 1/\Gamma_i$ of

$$\frac{\tau_3}{m_3} \simeq \frac{4 \times 10^{-11} \text{ s}}{g_{32}^2 + g_{31}^2 \text{ eV}} \quad , \quad \frac{\tau_2}{m_2} \simeq \frac{1 \times 10^{-9} \text{ s}}{g_{21}^2 \text{ eV}}. \quad (6.2.21)$$

For example, the smallest possible, normal-ordered neutrino masses of $m_1 = 0$ meV, $m_2 = 9$ meV, and $m_3 = 50$ meV [342] give

$$\tau_3 \simeq \frac{2 \times 10^{-12} \text{ s}}{g_{32}^2 + g_{31}^2} \quad , \quad \tau_2 \simeq \frac{9 \times 10^{-12} \text{ s}}{g_{21}^2}. \quad (6.2.22)$$

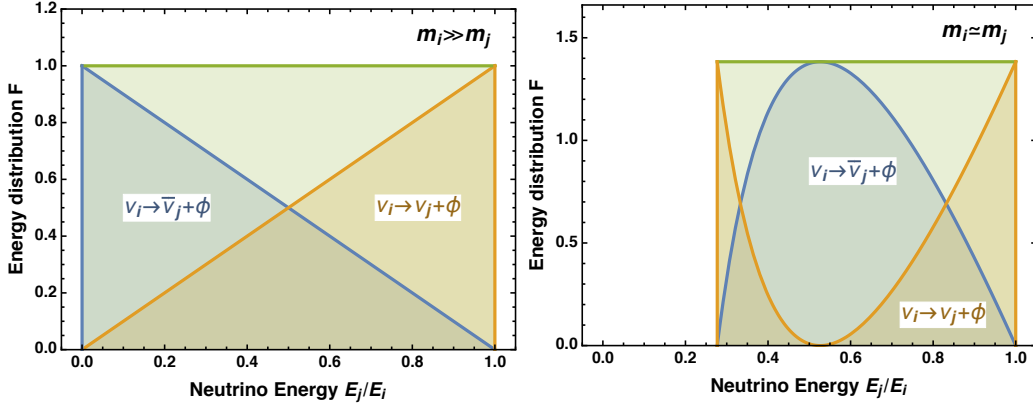


Figure 6.1: Normalized energy distributions $F(E_j/E_i)$ of the daughters ν_j and $\bar{\nu}_j$ produced in the decay of Majorana neutrinos $\nu_i \rightarrow \nu_j + \phi$ (orange), $\nu_i \rightarrow \bar{\nu}_j + \phi$ (blue), and their sum (green), for hierarchical (left panel) and degenerate (right panel) neutrino masses. For the Dirac case, the blue curve instead refers to the decay to undetectable sterile states N_j .

The degenerate limit, $m_i \simeq m_j$, gives

$$\Gamma_{\nu_i \rightarrow \bar{\nu}_j + \phi}^{\text{M}} = 2\Gamma_{\nu_i \rightarrow \nu_j + \phi}^{\text{M}} = \frac{g_{ij}^2 (m_i - m_j)^3 m_i}{3\pi m_i^2 E_i}. \quad (6.2.23a)$$

This is the main difference with neutrino decays into scalars in a degenerate mass scenario, where helicity flipping processes are strongly suppressed [338].¹² Given that the spin-flip processes are not suppressed (but their rate is different from the spin-conserving ones), we can identify several different observables to distinguish Majorana and Dirac neutrinos, as I will discuss in Sec. 6.3.

To show how the cases for Majorana and Dirac neutrinos are different, in Fig. 6.1 I plot the energy distributions $F(E_j/E_i)$ of the daughter neutrinos produced in the decay of the parent neutrinos ν_i , which is proportional to the differential rate and normalized to the total decay rate. Let us begin with the decay of Majorana neutrinos with energy E_i . In the upper panel of Fig. 6.1, I show the hierarchical case, $m_i \gg m_j$. The spectrum of neutrinos and antineutrinos is a box given by the sum of two triangles, one corresponding to outgoing ν_j and one to outgoing $\bar{\nu}_j$. In the degenerate case $m_i \simeq m_j$ shown in the lower panel of Fig. 6.1, the two triangles are distorted, but the sum of the ν_j and $\bar{\nu}_j$ distributions is still a box, as the sum of Eqs. (6.2.14a) and (6.2.14b) is independent of energy. In the Dirac case, the spectrum of active daughter neutrinos is only the orange triangle because

¹²Notice that the scalar decay rate of Majorana (M) and Dirac (D) neutrinos in Eq. (2.6) of Ref. [338] needs to be corrected to

$$\Gamma_{\text{scalar}}^{\text{M(D)}}(\nu_i \rightarrow \nu_j + \phi_{\text{scalar}}) = \frac{g_{\text{scalar}}^2 (m_i^2 - m_j^2)}{\zeta^{\text{M(D)}} \pi E_i} \quad (6.2.24)$$

where $\zeta^{\text{M}} = 1$ and $\zeta^{\text{D}} = 4$. This corrects for an inconsistency between the coupling definition in their Lagrangian and their rate (if neutrinos are Majorana particles), as well as an incorrect expansion of their Eq. (2.2). The author thanks Nicole Bell for communications on this point.

the complement to the box, the blue triangle, corresponds to undetectable sterile daughter neutrinos.

6.3 Constraints and detection opportunities

One of the possibilities to distinguish Majorana from Dirac neutrinos relies on the observation of the differential energy spectrum from a source whose flux is known. In this case, there is no need for an asymmetry between the initial neutrino and antineutrino fluxes, because the differential energy spectrum is differently affected by the decay depending on the nature of the neutrino mass.

A second possibility is given by the appearance or disappearance of neutrinos or antineutrinos from a source whose flux is asymmetric between ν and $\bar{\nu}$. For example, the Sun emits only neutrinos [129], besides a tiny contribution of antineutrinos coming from heavy-element decay, which is much smaller than the geoneutrino background [343, 344]. The detection of antineutrinos could point towards the decay of Majorana neutrinos. Notice, however, that other explanations for such a detection would be possible, e.g. a spin precession due to the existence of a neutrino magnetic dipole moment [345].

Finally, the observation of a change in the flavor pattern in the neutrino flux from a known source could in principle distinguish Majorana and Dirac neutrinos, if it is possible to distinguish neutrinos from antineutrinos in the detector. Otherwise, it is only possible to observe the decay, as the latter changes the neutrino composition in terms of mass eigenstates of the flux.

6.3.1 Solar, atmospheric, and long-baseline neutrinos

The current constraints on neutrino decay for a normal nondegenerate mass ordering are at 99% C.L.

$$\frac{\tau_3}{m_3} > 9.3 \times 10^{-11} \frac{\text{s}}{\text{eV}} \quad \text{and} \quad \frac{\tau_2}{m_2} > 1.0 \times 10^{-3} \frac{\text{s}}{\text{eV}} . \quad (6.3.1)$$

The bound on τ_3 is obtained through an analysis of atmospheric and long-baseline neutrinos [346], while the bound on τ_2 has been recently obtained with updated solar neutrino measurements [347], which have improved the previous estimate [348]. It is important to notice that these bounds only apply to invisible neutrino decays, i.e., the decay products are assumed not to cause significant signals in the detectors [346, 348]. Moreover, I should stress again that these limits on the lifetimes assume a hierarchical ordering [338, 349]. The constraints in Eq. (6.3.1) require the off-diagonal couplings to be

$$\sqrt{g_{32}^2 + g_{31}^2} < 2 \times 10^{-1} \quad \text{and} \quad g_{21} < 3 \times 10^{-4} . \quad (6.3.2)$$

These bounds on the couplings are valid both for Majorana neutrinos and, once multiplied by a factor of 2, also for Dirac neutrinos. In the Majorana case, additional

strong bounds can be obtained, because solar neutrinos would decay to antineutrinos showing up at experiments like SNO [350] and KamLAND [351].

The analysis of KamLAND data gives bounds on the lifetime of ν_2 Majorana neutrinos of [351]

$$\frac{\tau_2}{m_2} > 6.7 \times 10^{-2} \frac{\text{s}}{\text{eV}} \quad (\text{degenerate}) \quad (6.3.3a)$$

$$\frac{\tau_2}{m_2} > 1.1 \times 10^{-3} \frac{\text{s}}{\text{eV}} \quad (\text{hierarchical}) \quad (6.3.3b)$$

at 90% CL, which translate to bounds on the coupling

$$g_{21} < 4 \times 10^{-5} \quad (\text{degenerate}) \quad (6.3.4a)$$

$$g_{21} < 3 \times 10^{-4} \quad (\text{hierarchical}) . \quad (6.3.4b)$$

Concerning ν_3 decay, there is as yet no dedicated analysis in the context of majoron models [342], presumably because it was not known until recently that there is a small component of ν_3 in electron neutrinos. To estimate the flux of ν_3 from the Sun, we see that this mass eigenstate is not affected by matter effects, so its component is simply $|U_{e3}|^2 = 0.02$ [352]. In conclusion, approximately 2% of the neutrinos coming from the Sun are ν_3 . The bounds on the lifetime of ν_3 Majorana neutrinos are then

$$\frac{\tau_3}{m_3} > 1.3 \times 10^{-4} \frac{\text{s}}{\text{eV}} \quad (\text{degenerate}) \quad (6.3.5a)$$

$$\frac{\tau_3}{m_3} > 2.2 \times 10^{-5} \frac{\text{s}}{\text{eV}} \quad (\text{hierarchical}) \quad (6.3.5b)$$

at 90% CL, and the bounds on the coupling are finally

$$\sqrt{g_{32}^2 + g_{31}^2} < 3 \times 10^{-4} \quad (\text{degenerate}) \quad (6.3.6)$$

$$\sqrt{g_{32}^2 + g_{31}^2} < 2 \times 10^{-3} \quad (\text{hierarchical}). \quad (6.3.7)$$

These bounds apply to any model where neutrinos can decay to a light pseudoscalar. A final remark concerns the possibility of using Borexino [82] to put competitive bounds on the lifetime of solar neutrinos. The analysis in [82] only yields bounds on the conversion of ν to $\bar{\nu}$ assuming either equal shapes for the solar ν and the converted $\bar{\nu}$ or a unknown shape for the $\bar{\nu}$ spectrum, while no dedicated analysis is carried out for neutrino decay. An analysis of Borexino data is promising, because of the large exposure time (10 years) and the low background. I will leave such an analysis to future work.¹³

¹³This will be discussed in S. Appel, L. Oberauer, G. Raffelt and E. Vitagliano (for the Borexino collaboration), ‘‘Solar antineutrino fluxes with Borexino at LNGS and neutrino decay,’’ work in progress [353].

6.3.2 IceCube and supernova neutrinos

Neutrino decays imply a distinct flavor composition of long-traveling astrophysical neutrinos, because all neutrinos arrive in the lightest mass state. Observable decay effects require $\Gamma_i(m_i/E) \gtrsim D^{-1}$ and therefore [354]

$$g_{ij} \gtrsim 5 \times 10^{-8} \left(\frac{50 \text{ meV}}{m_i} \right) \left(\frac{E}{10 \text{ TeV}} \right)^{1/2} \left(\frac{100 \text{ Mpc}}{D} \right)^{1/2}. \quad (6.3.8)$$

As mentioned in Ref. [311], the relatively weak constraints in Eq. (6.3.2) from atmospheric, long-baseline, and solar neutrinos therefore imply that a deviation from an equal neutrino flavor ratio $(\nu_e : \nu_\mu : \nu_\tau) = (1 : 1 : 1)$ could be measured at experiments such as IceCube. The latest IceCube data gives a best-fit ratio of $(0 : 0.2 : 0.8)$ but is consistent with ratios like $(1 : 1 : 1)$ and $(1 : 0 : 0)$ [355]. While normal mass ordering would imply a dominance of ν_e due to $\nu_1 = (0.68 : 0.11 : 0.21)$, inverted ordering would yield a dominance of ν_μ and ν_τ due to $\nu_3 = (0.02 : 0.54 : 0.44)$ [352]. An equal flavor ratio is not allowed, because only the intermediate eigenstate ν_2 has an almost equal flavor content. Thus, the predicted neutrino decays are one possibility to test the gravitational neutrino mass model in future.

An additional question is whether one can distinguish Majorana from Dirac neutrinos at IceCube. At low energies, the detector cannot distinguish neutrinos from antineutrinos. Nevertheless, for neutrinos with energies around 6.3 PeV in the laboratory frame, the Glashow resonance makes IceCube more efficient for $\bar{\nu}_e$ detection [356]. Such a resonance is the s-channel of the process $\bar{\nu}_e + e^- \rightarrow W^- \rightarrow \bar{\nu}_\alpha + l_\alpha^-$ and allows the detector to distinguish neutrinos from antineutrinos. However, the main problem here is the unknown asymmetry of the neutrino and antineutrino fluxes. For analyzing IceCube data, it is customary to assume equal fluxes for ν_α and $\bar{\nu}_\alpha$, both in energy and flavor [357]. In this case, it would be impossible to distinguish Majorana from Dirac neutrinos. However, in general, these fluxes are expected to be different. Neutrinos are produced by the decay of charged pions. If there is an asymmetry in charged-pion production, there will be an asymmetry in neutrino fluxes. For example, the production mechanism $p + \gamma \rightarrow \Delta^+ \rightarrow n + \pi^+$ involving proton collisions on photons of the environment ($p\gamma$ sources) produces no π^- and thus no $\bar{\nu}_e$ [356]. In the far future, a better understanding of neutrino production in astrophysical sources would give us tools to distinguish the Majorana from the Dirac scenario.

The same might be true for supernova neutrinos, which are expected to decay into the lightest mass eigenstate while traveling to Earth. While this decay scenario requires modified analyses of SN1987A neutrino spectra [311], it could also be probed through the future detection of the supernova relic neutrino flux, i.e., the redshifted neutrino background from all past supernovae. In Ref. [358] it was argued that a complete decay scenario can potentially enhance the supernova relic neutrino background density up to the current experimental detection bound, so that its measurement might be feasible with near-future experiments.

Axionlike particle detection with multi-messenger astronomy¹⁴

High-energy multi-messenger astronomy can be used to search for signals of physics beyond the Standard Model. In this Chapter we will explore the possibility that the apparent excess in the extragalactic background light (EBL) spectrum detected by the CIBER collaboration could be due to the decay of an axionlike particle with mass around an electronvolt. Taking into account multi-messenger, multi-wavelength observations, I will show that a warm dark matter component, produced either thermally or non-thermally, can explain the enhanced EBL. The increased level of EBL alleviates the tension between the neutrino flux detected at IceCube and the gamma-ray flux measured by Fermi, assuming sources with $p\gamma$ production, e.g. blazars.

7.1 Introduction

Recently, the Cosmic Infrared Background Experiment (CIBER) collaboration has claimed the detection of an unexpectedly large diffuse flux compared to theoretical expectations in the 0.8–1.7 μm range of wavelengths [360]. This measurement is complementary to other observations in the infrared band like the ones carried out by AKARI [361] and IRTS [362]. Even if an astrophysical explanation of the detected excess or systematic errors are not ruled out, it is worthwhile to speculate about a possible flux due to big bang relics, such as an axionlike particles (ALP) with mass around 1 eV. ALPs generalize the concept of the axion, introduced to solve the so-called strong CP problem, which has a multifaceted phenomenology [363]. However, ALPs could couple to particles other than photon, e.g. involving a hidden photon. The contribution of such ALP decays to the cosmic infrared background (CIB) was examined in Ref. [364]. In this Chapter we will revisit the hypothesis, taking into

¹⁴This Chapter closely follows the discussion of O. Kalashev, A. Kusenko and E. Vitagliano, “Cosmic infrared background excess from axionlike particles and implications for multi-messenger observations of blazars,” *Phys. Rev. D* **99** (2019) 023002, [arXiv:1808.05613](#) [359].

account the detector energy resolution, the possibility of warm dark matter, and the implications of increased EBL for blazar multi-messenger observations.

While a solid lower bound to the CIB radiation can be obtained through deep sky galaxy counts [365], the precise shape and intensity of the diffuse, unresolved spectrum in the near-infrared wavelength range is still unknown. Direct measurements [361, 366, 367] are difficult because of the large uncertainties caused by zodiacal light. Theoretical models are also subject to uncertainties, which result in different predictions [368–370]. The uncertainties make it difficult to identify any additional contribution to the extragalactic background light (EBL) besides the standard flux due to galaxy emission. Possible enhancements could come from ultraviolet redshifted photons produced by bottom-up astrophysical accelerators, ranging from high redshift galaxies [371] to black holes [372].

The EBL can also be measured indirectly. Very high-energy gamma rays from blazars have been used to set an upper limits on infrared background radiation [373], by similar arguments to the ones discussed in Chapter 4. An indirect measurement has been recently carried out using 739 active galaxies and one gamma-ray burst [374]. However, while such kinds of measurements could in principle strongly constrain substantial contributions not resolved by deep galaxy surveys, the possibility of secondary gamma rays produced by cosmic rays along the line of sight [375–379] undermine these upper bounds.

In the last few years, searches for indirect probes of portals connecting the Standard Model of particle physics with the dark matter sector have been pursued [380]. ALPs as a DM candidate have recently received great attention due to the non-detection of weakly interactive massive particles [381]. It is, therefore, important to examine the CIB data in light of the ALP hypothesis.

Apart from the increase of the EBL, this hypothesis has an observable impact on the propagation of TeV photons because it implies an enhanced opaqueness through $\gamma\gamma \rightarrow e^+e^-$ processes. A higher level of EBL would help alleviate the tension between the observed neutrino spectrum and the gamma-ray spectrum of blazars, as discussed below. This is a case study in which multi-messenger, multi-wavelength observations can be exploited to obtain new tools to indirectly probe fundamental physics beyond the Standard Model, making use of data from neutrino telescopes (IceCube), gamma-ray satellites (Fermi-LAT) and sounding rockets equipped with infrared cameras (CIBER), extending the already flourishing multi-messenger astronomy tools [234].

7.2 Flux from axionlike particle decay

We are interested in the redshift evolution of the diffuse infrared radiation produced by the decay of a relic axionlike particle to a photon and a hidden photon, $a \rightarrow \gamma + \chi$ [364, 383]. The possibility of having axions with suppressed two-photon coupling has received some attention recently due to the peculiar phenomenology of photophobic axions [384]. The decay is due to the Chern-Simons [385] interaction Lagrangian

$$\mathcal{L} = \frac{g_{a\chi\gamma}}{4} a F^{\mu\nu} \tilde{F}_{\mu\nu}^{\chi}, \quad (7.2.1)$$

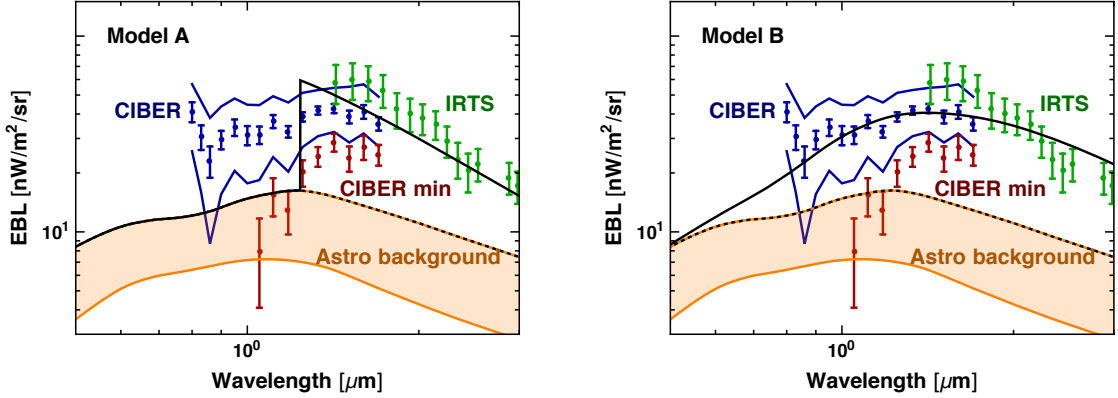


Figure 7.1: Photon intensity flux from a decaying cold dark matter ALP. Experimental data include CIBER data with Kelsall ZL model (blue, continuous lines are systematic error), CIBER with minimum EBL model (red), IRTS (green) [360, 362]. The total flux (solid black) include the flux from ALP decay and the astrophysical diffuse (dotted black), which we assume to be the upper bound of the band reported in [382], shown in orange. *Left, model A:* $\omega_{\max} = 1 \text{ eV}$, $\tau = 2 \times 10^{22} \text{ s}$, $R = 2/3$. *Right, model B:* $\omega_{\max} = 8 \text{ eV}$, $\tau = 1 \times 10^{16} \text{ s}$, $R = 2 \times 10^{-4}$.

where $\tilde{F}^{\mu\nu} = \epsilon_{\mu\nu\rho\sigma} F^{\rho\sigma}/2$. While such a coupling between dark matter and photons is not directly motivated by other phenomena (like the QCD axion), experimental signatures would be quite different from the ones of the QCD axion, motivating us to explore this class of parametric models. The non-relativistic decay rate for the ALP is found to be

$$\Gamma = \frac{1}{16\pi} \overline{|\mathcal{M}|^2} \frac{m_a^2 - m_\chi^2}{m_a^3} = \frac{g_{a\chi\gamma}^2}{128\pi} \frac{(m_a^2 - m_\chi^2)^3}{m_a^3} \quad (7.2.2)$$

where the squared amplitude averaged over final polarization states is $\overline{|\mathcal{M}|^2} = g_{a\chi\gamma}^2 (m_a^2 - m_\chi^2)/8$. This correctly reduces to the usual axion decay rate [386] when $m_\chi = 0$ and one includes a factor of 2 due to the final state involving identical photons, because we have to divide by 2 (identical particles in the final state) and multiply by 4 the squared amplitude. Interestingly, the decay rate depends just on one kinematic quantity in the non-relativistic approximation, namely, the maximum available energy for the outgoing photon

$$\omega_{\max} = \frac{m_a^2 - m_\chi^2}{2m_a}. \quad (7.2.3)$$

The degeneracy would be broken if the ALP were non-negligibly relativistic.

The energy intensity (energy flux per unit of energy, time, surface per steradians)

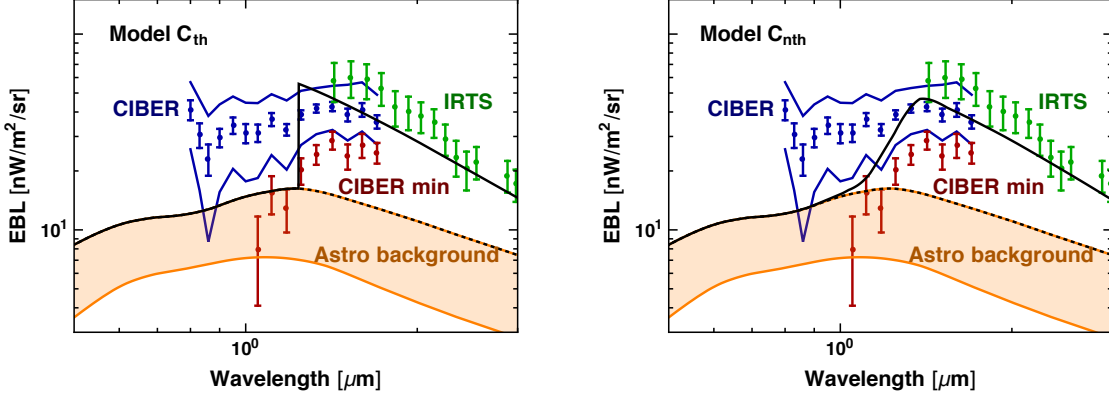


Figure 7.2: Same as Fig. 7.1, but assuming a decaying warm dark matter ALP. *Left, model C_{th}*: $T_{\text{th}} = 0.37 T_{\gamma}^{(0)} = 0.086 \text{ meV}$, $\omega_{\text{max}} = 1 \text{ eV}$, $\tau = 9 \times 10^{21} \text{ s}$, $R_{\text{th}} = 7 \times 10^{-3}$. *Right, model C_{nth}*: $T_{\text{nth}} = 16.7 \text{ meV}$, $\omega_{\text{max}} = 1 \text{ eV}$, $\tau = 3 \times 10^{21} \text{ s}$, $R_{\text{nth}} = 2/3 \times 10^{-3}$.

is computed from a window function $W(z', \omega')$,

$$\begin{aligned}
 I(\omega) &= \frac{\omega^2}{4\pi} \frac{dN}{dS d\omega dt} = \omega^2 \int_z^\infty dz' W(z', \omega') \\
 &= \frac{\omega^2}{4\pi} \int_z^\infty \frac{dz'}{H(z')} \frac{(1+z)^2}{(1+z')^3} e^{-\Gamma t(z')} \\
 &\times \int \frac{d^3 \mathbf{p}'_a}{(2\pi)^3 2E'_a} \frac{d^3 \mathbf{p}'_x}{(2\pi)^3 2E'_x} \frac{\omega'}{4\pi^2} \times (2\pi)^4 \delta^{(4)}(p'_x + k' - p'_a) \overline{|\mathcal{M}|^2} f_a(\mathbf{p}'_a), \quad (7.2.4)
 \end{aligned}$$

where $H(z) = H^0 \sqrt{\Omega_\Lambda + \Omega_M(1+z)^3}$ is the Hubble function, z is the redshift at which the flux is “observed”, z' is the redshift at which a decays with a squared amplitude $|\mathcal{M}|^2$, the frequency at the production point is $\omega' = \omega(1+z')/(1+z) = \omega^{(0)}(1+z')$ (as well as $\mathbf{p}' = \mathbf{p}(1+z')/(1+z)$), $f_a(\mathbf{p}_a)$ is the momentum distribution of the ALPs, so that the number density (when there is no decay) is $n_a = \int d^3 \mathbf{p}_a / (2\pi)^3 f_a(\mathbf{p}_a)$. In the following the superscript (0) will indicate comoving quantities. We here include the reduction in the number density due to decay with rate Γ over the age of the universe

$$t(z') = \frac{1}{3H^0 \sqrt{\Omega_\Lambda}} \log \left[\frac{\sqrt{\Omega_\Lambda + \Omega_M(1+z')^3} + \sqrt{\Omega_\Lambda}}{\sqrt{\Omega_\Lambda + \Omega_M(1+z')^3} - \sqrt{\Omega_\Lambda}} \right], \quad (7.2.5)$$

whereas we do not need to account for absorption; the latter is negligible in the wavelength range under study. The only relevant process reducing the flux of a single source is due to Thomson scattering [387]. However, Thomson scattering preserves the energy of the scattering photon. As such, it is irrelevant in the case of diffuse production with no significant fluctuations in the electron spatial distribution, which we can consider in first approximation to be homogeneous. We will now explore two main scenarios, involving cold dark matter or warm dark matter.

7.2.1 ALP cold dark matter

Eq. (7.2.4) correctly reduces to Eq. (50) of [388], when one takes a cold dark matter (CDM) distribution for the ALP population

$$f_a(\mathbf{p}_a) = n_a^{(0)} (2\pi)^3 \delta^{(3)}(\mathbf{p}_a) \left(|\mathbf{p}_a| / |\mathbf{p}_a^{(0)}| \right)^3 \quad (7.2.6)$$

and gets rid of Dirac deltas. Integration over z' yields

$$\begin{aligned} I(\omega) &= \frac{1}{4\pi} \omega^2 (1+z)^2 n_a^{(0)} \Gamma \int_z^\infty dz' e^{-\Gamma t(z')} \frac{\delta[\omega' - \omega_{\max}]}{H(z')} \\ &= \frac{1}{4\pi} \omega (1+z)^3 n_a^{(0)} \Gamma e^{-\Gamma t(\tilde{z})} \frac{\theta[\tilde{z} - z]}{H(\tilde{z})}; \end{aligned} \quad (7.2.7)$$

here, $1 + \tilde{z} = (1+z)\omega_{\max}/\omega$ and $\theta[\tilde{z} - z]$ is the Heaviside function. As expected, the comoving intensity is simply found by multiplying with $(1+z)^{-4}$ (one power coming from ω). For $z = 0$ this agrees with Eq. (3) of [364]. In the same paper, the three-fold parameter space to explain the CIBER excess was explored. The maximum available energy must be $\omega_{\max} \lesssim 10.2 \text{ eV}$ to avoid constraints due to reionization and more stringently to the Lyman-alpha forest absorption spectrum. The lifetime Γ^{-1} should be roughly of the order of the age of the Universe, and cannot be too small because ALPs can be produced in astrophysical systems, modifying stellar evolution [364].

On the one hand, ALP decay to a photon plus a hidden photon avoids the direct detection bounds on the coupling $g_{a\chi\gamma}$, which instead constrains the $g_{a\gamma\gamma}$ of standard ALPs (decaying to two photons),¹⁵ as well as astrophysical bounds due to horizontal branch stars and SN1987A [149]; however, ALPs could still contribute to stellar cooling via plasmon decay $\gamma \rightarrow a + \chi$, which is possible in a medium as the photon dispersion relation allows for such a decay (just like as discussed for neutrinos in Sec. 5.2). We will explore these bounds in Sec. 7.4. Notice that these bounds can be avoided if a and χ are heavy and almost degenerate in mass. Finally, there is another parameter which can be varied to fit CIBER data, the ALP number density $n_a^{(0)} = R \rho_{\text{DM}}/m_a$, where R is a numerical factor and ρ_{DM} is the total DM energy density.

7.2.2 ALP warm dark matter

In the following we will also consider the scenario in which the ALP population represents a small warm dark matter (WDM) contribution to the DM energy density. This implies an additional fourth tunable parameter, namely the effective temperature. WDM can be produced both thermally or non-thermally [389, 390]. In the first case, we suppose that the abundance is given by $f_a(\mathbf{p}_a) = 1/[\exp(|\mathbf{p}_a|/T_{\text{th}}(z')) - 1]$.

¹⁵In principle there should also be the operator $\frac{g_{a\gamma\gamma}}{4} a F^{\mu\nu} \tilde{F}_{\mu\nu}$, but it can be technically natural to set $g_{a\gamma\gamma} = 0$ assuming a Z_2 symmetry of which a and γ are different representations. This also sets to zero the kinetic mixing $g_{\text{kin}} F^{\mu\nu} F_{\mu\nu}^{\chi}$, which would also contribute to stellar cooling.

The distribution could arise, for example, if the ALP and the hidden photon were in thermal equilibrium with the primordial plasma; their population would be the result of relativistic decoupling, similar to what happens to neutrinos. The processes which contribute most to equilibrium are pair annihilations $e^+ + e^- \leftrightarrow a + \chi$ and to a lesser extent plasmon decay $\gamma \leftrightarrow a + \chi$, which is possible in the early universe just as in stars. While plasmon decay is negligible in the early-universe production of ALPs, it is very relevant for star cooling, as previously stressed and as I will show in Sec. 7.4. Other processes like $a + e^- \leftrightarrow \chi + e^-$ could slightly affect the dark sector effective temperature after decoupling, without changing the number density.

The cross section for pair annihilation is

$$\sigma(e^+ + e^- \rightarrow a + \chi) = \frac{\alpha g_{a\chi\gamma}^2}{96}; \quad (7.2.8)$$

the process drives a and χ out of equilibrium when the thermal width is roughly comparable to the Hubble function, viz. $\langle \Gamma_{e^+e^-} \rangle \simeq H$. By noting that in a radiation dominated universe $H = 1.66\sqrt{g^*}T^2/m_{\text{Pl}}$, where g^* is the effective number of relativistic degrees of freedom at the decoupling and $m_{\text{Pl}} = 1.22 \times 10^{19}$ GeV is the Planck scale [391], this happens when

$$3\frac{\zeta(3)}{\pi^2}T^3\frac{\alpha g_{a\chi\gamma}^2}{96} \simeq 1.66\sqrt{g^*}\frac{T^2}{m_{\text{Pl}}} \quad (7.2.9)$$

which is

$$T_{\text{dec}} \simeq 4.8 \times 10^3 \text{ GeV} \left(\frac{10^{-9} \text{ GeV}^{-1}}{g_{a\chi\gamma}} \right)^2. \quad (7.2.10)$$

Suppose that there is no new physics between the electroweak phase transition and the decoupling scale. If ALPs decouple at T_{dec} , their number density at late times is governed by g_{*s} , the effective number of thermal degrees characterizing the entropy at the decoupling epoch. The number density of ALPs at low redshift is therefore

$$n_a^{(0)} = \frac{g_{*s}(T^{(0)})}{g_{*s}(T_{\text{dec}})} \frac{n_\gamma^{(0)}}{2} \quad (7.2.11)$$

where the sum is over all the particle content of the Standard Model plus a and χ . Assuming $g_{a\chi\gamma} \simeq 6 \times 10^{-9} \text{ GeV}^{-1}$ (i.e. $\tau \simeq 9 \times 10^{20}$ s), one approximately finds $n_a^{(0)} \simeq 20 \text{ cm}^{-3}$.

The most important consequence of a high decoupling temperature is that big bang nucleosynthesis constraints are relaxed. The energy density of the ALPs (one degree of freedom) and of the hidden photons (two or three degrees of freedom depending on the mass) is suppressed compared to the energy density of additional sterile neutrinos or axions which decouple later. To compare, suppose we had introduced a sterile neutrino, which would have implied at least 2 new degrees of freedom. If the decoupling is after the QCD phase transition its contribution to the effective number of neutrinos $\Delta N_{\text{eff}} \simeq 0.57$ would have been at least three times

larger than $\Delta N_{\text{eff}} \lesssim 0.2$ due to a and χ [15]. This conclusion remains approximately valid as far as the decoupling takes place before the QCD phase transition.

To recap, there are cosmological constraints coming from measurements of the temperature and polarization power spectra of the CMB anisotropies, the large-scale matter power spectrum, and the Hubble expansion rate [392,393], which usually apply to a lately decoupled axion. However, these bounds can be relaxed depending on the decoupling temperature of the ALP. Interestingly, better cosmological measurements could exclude also this class of ALP models.

Alternatively, a non-thermally produced DM can have a momentum distribution with a strongly model dependent functional dependence, typical of freeze-in scenarios, where the distribution is set by the thermal distribution of the parent particle, the masses and the couplings [394–399]. An out-of-equilibrium decay of heavy particles can also alter the clustering properties of dark matter [400]. In the case of very low reheating scenarios, cosmological upper bounds on the mass of hot dark matter can be relaxed [401]. One can assume a benchmark distribution

$$f_a(\mathbf{p}_a) = \frac{R_{\text{nth}}}{e^{|\mathbf{p}_a|/T_{\text{nth}}(z')} - 1}, \quad (7.2.12)$$

where R_{nth} is again a numerical factor and $T_{\text{nth}}^{(0)}$ can be in principle higher than the CMB temperature. Eq. (7.2.4) can be expressed in terms of special functions with these distribution. The Dirac delta function can be used to get rid of the angular part of the \mathbf{p}_a , and this would introduce a minimum absolute value of the momentum $|\mathbf{p}_a^{(0),\text{min}}|$:

$$\begin{aligned} W(z', \omega') &= \frac{R_{\text{nth}}}{(2\pi)^3} \frac{(1+z)^2}{1+z'} e^{-\Gamma t(z')} \frac{\Gamma}{H(z')} \frac{m_a}{2\omega_{\text{max}}} \\ &\times \frac{1}{6} \left[3|\mathbf{p}_a^{(0),\text{min}}|^2 - 6T^2 \text{Li}_2 \left(e^{|\mathbf{p}_a^{(0),\text{min}}|/T} \right) \right. \\ &\quad - 6i\pi |\mathbf{p}_a^{(0),\text{min}}| T \\ &\quad \left. - 6|\mathbf{p}_a^{(0),\text{min}}| T \log \left(e^{|\mathbf{p}_a^{(0),\text{min}}|/T} - 1 \right) + 2\pi^2 T^2 \right]; \end{aligned} \quad (7.2.13)$$

where Li_2 is the polylogarithm of order 2, $T = T_{\text{th}}^{(0)}$ (or $T = T_{\text{nth}}^{(0)}$) and

$$|\mathbf{p}_a^{(0),\text{min}}| = \pm \frac{(m_a^2 - m_\chi^2)^2 - 4m_a^2 \omega'^2}{4(1+z')\omega'^2 (m_a^2 - m_\chi^2)} \quad (7.2.14)$$

depending on whether ω' is smaller or bigger than ω_{max} .

The photon intensity spectrum due to astrophysical diffuse sources, assumed to be the one reported in Ref. [382], plus the ALP decay contribution is shown in Figs. 7.1 and 7.2 for different choices of the parameters. I plot two CDM scenarios with small and large ω_{max} (model A and B) in Fig. 7.1. In Fig. 7.2 I show two WDM scenario, assuming for one a thermally produced ALP (model C_{th}), and for the other

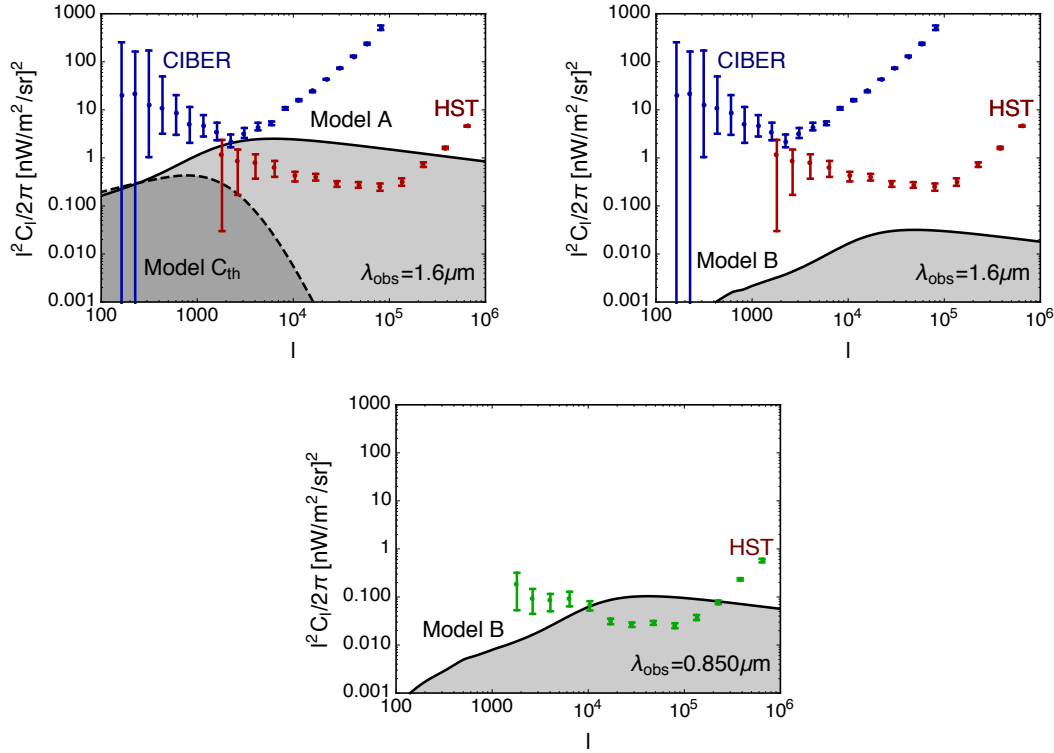


Figure 7.3: Angular power spectrum due to the decay of an ALP. The data shown are the anisotropies detected by CIBER at observational wavelength $\lambda_{\text{obs}} = 1.6 \mu\text{m}$ (dark blue), and by HST at observational wavelength $\lambda_{\text{obs}} = 1.6 \mu\text{m}$ (dark red) and $\lambda_{\text{obs}} = 0.85 \mu\text{m}$ (dark green). *Top left*: anisotropies in the $1.6 \mu\text{m}$ band for models A (solid line) and C_{th} (dashed line); *top right*: anisotropies in the $1.6 \mu\text{m}$ band for model B; *bottom*: anisotropies in the $0.85 \mu\text{m}$ band for model B.

an extremely large T_{nth} , to make more evident the ALP kinetic energy effect on the photon spectrum (model C_{nth}). Considering a thermally produced ALP population (in the following named model C_{th}), the intensity spectrum is indistinguishable from the model A CDM spectrum. Model A and C_{th} however differ strongly for what concerns the intensity anisotropies, as we will see below.

7.3 Anisotropy constraints

The gravitational clustering of dark matter makes the photon flux produced by the decaying ALP anisotropic. In this Section we revisit the calculations as done in [364, 402]. We take into account the energy resolution of the detector, following [403]. To the best of our knowledge, this is the first time such a procedure is carried out in the context of infrared photons produced by dark matter decay. Our main goal in this Section is then to revisit the bounds on CDM scenarios from anisotropies, and to extend the analysis to a WDM scenario.

The average intensity of the flux detected in an energy band centered in ω with

width $\Delta\omega$ is

$$I(\omega, \Delta\omega) = \frac{1}{\Delta\omega} \int_{\Delta\omega} d\omega \omega^2 \int_z^\infty dz' W(z', \omega') \quad (7.3.1)$$

assuming a $\Delta\omega = \omega$ flat passband filter for the detector [404]. Fluctuations toward a direction of the sky $\hat{\mathbf{n}}$ can be expanded as spherical harmonics

$$\delta I(\omega, \Delta\omega, \hat{\mathbf{n}}) = I(\omega, \Delta\omega, \hat{\mathbf{n}}) - I(\omega, \Delta\omega) = \sum_{l,m} a_{l,m}(\omega, \Delta\omega) Y_{l,m}(\hat{\mathbf{n}}). \quad (7.3.2)$$

Anisotropies are often conveniently described in terms of the angular power spectrum (suppressing the ω dependence from the notation)

$$C_l(\Delta\omega) = \langle |a_{l,m}(\Delta\omega)|^2 \rangle = \frac{1}{2l+1} \sum_{m=-l,+l} |a_{l,m}(\Delta\omega)|^2 \quad (7.3.3)$$

which written in terms of the window function is

$$\begin{aligned} C_l(\Delta\omega) &= \frac{1}{\Delta\omega} \int_{\Delta\omega} d\omega_1 \omega_1^2 \int_z^\infty dz'_1 W(z'_1, \omega'_1) \\ &\times \frac{1}{\Delta\omega} \int_{\Delta\omega} d\omega_2 \omega_2^2 \int_z^\infty dz'_2 W(z'_2, \omega'_2) \\ &\times \frac{2}{\pi} \int dk k^2 P_\delta [k, r(z'_1), r(z'_2)] j_l(kr(z'_1)) j_l(kr(z'_2)) \end{aligned} \quad (7.3.4)$$

where $r(z) = \int_0^z dz'/H(z')$ is the comoving distance, $j_l(kr(z))$ is the spherical Bessel function and the power spectrum (i.e., the density contrast) is defined as $\langle \delta_{\mathbf{k}_1}(r(z_1)) \delta_{\mathbf{k}_2}(r(z_2)) \rangle = (2\pi)^3 \delta^{(3)}(k_1 - k_2) P_\delta(k_1, r(z_1), r(z_2))$. If the power spectrum varies slowly as a function of k we can use the Limber approximation [405], which is correct up to $\mathcal{O}(l^{-2})$ [406]

$$\begin{aligned} &\frac{2}{\pi} \int dk k^2 P_\delta [k, r(z'_1), r(z'_2)] j_l(kr(z'_1)) j_l(kr(z'_2)) \\ &\simeq \frac{1}{r(z'_1)^2} P_\delta \left(k = \frac{l}{r(z'_1)}, r(z'_1) \right) \delta^{(1)}(r(z'_1) - r(z'_2)). \end{aligned} \quad (7.3.5)$$

Notice that we do not have to worry about the sharpness of the differential flux caused by the delta function in the window function for CDM, because this is cured by averaging over the energy bandwidth of the detector. This procedure has been used for similar analyses with gamma rays [407, 408]. Defining $z_M = \omega^{\max}/(\omega - \Delta\omega/2) - 1$ and $z_m = \omega^{\max}/(\omega + \Delta\omega/2) - 1$ as the maximum and minimum redshift observed in the anisotropy measurement, we have

$$\begin{aligned} C_l(\Delta\omega) &= \int_{z_m}^{z_M} dz \left[\frac{1}{4\pi} \frac{e^{-\Gamma t(z)}}{H(z)(1+z)^3} \omega_{\max}^2 \Gamma n_a^{(0)} \frac{1}{\Delta\omega} \right]^2 \\ &\times \frac{1}{r(z)^2} P_\delta \left(k = \frac{l}{r(z)}, r(z) \right) H(z). \end{aligned} \quad (7.3.6)$$

Our redshift dependence agrees with the one of Eq. (A10) of [403], because we are considering the angular power spectrum of the energy flux (units are energy *squared* per time, per surface, per steradians and per energy); to compare the results of [403] and ours, Eq. (A1) of the same reference shall be multiplied times ν , which gives an additional $(1+z)^{-2}$ in the final expression.

The anisotropy power spectra for lighter ($\omega_{\max} = 1$ eV) and heavier ($\omega_{\max} = 8$ eV) dark matter are shown in Fig. 7.3, where they are compared with data of CIBER [409] and of the Hubble Space Telescope (HST) [410]. The matter power spectrum was calculated with the CLASS code [411], publicly available at [412]. In the first case, we explored both the CDM and the WDM cases (assuming $m_a = 2$ eV for the latter). The WDM power spectrum has been computed in the adiabatic approximation [413], $P_{\delta, \text{WDM}} = (\mathcal{T}_{\text{WDM}}/\mathcal{T}_{\text{CDM}})^2 P_{\delta, \text{CDM}}$, where \mathcal{T} is the transfer function.¹⁶ The latter relates the primordial and the present-day power spectra [414], and is another CLASS output [415]. In all cases, given that we needed to integrate over the redshift, we assumed conservatively a linear evolution for the matter power spectrum, using the non-linear matter power spectrum P_{δ} obtained with CLASS, calculated at redshift $z = 0$ and evolved backwards

$$P_{\delta} \left(k = \frac{l}{r(z)}, r(z) \right) = P_{\delta} \left(k = \frac{l}{r(z)}, r = 0 \right) D(z)^2. \quad (7.3.7)$$

Here, $D(z) \propto H(z) \int_z^{\infty} dz' (1+z') H(z')^{-3}$ is the linear growth factor, to be normalized with $D(0) = 1$ [407].

As heuristically expected, WDM evades quite easily the constraints due to anisotropy measurements, as understood by showing the model C_{th} anisotropy spectrum (dashed line in top-left panel of Fig. 7.3). These become unrestrictive when considering a non-thermally produced hot dark matter with high effective temperature, like in model C_{nth} , as their free-streaming length is even larger. Light CDM (model A) can be considered excluded by our analysis.

For what concerns heavier dark matter (model B), our results are shown in the central and right panels of Fig. 7.3, where the anisotropy power spectrum is computed both for the $1.6 \mu\text{m}$ wavelength band (light red) and for the $0.85 \mu\text{m}$ band. The $0.85 \mu\text{m}$ band slightly overshoots the observed data in the relevant wavelength; however, the exclusion is much weaker than what has been found in previous analysis [364], due to averaging over the detector bandwidth.

A final comment is required about the anisotropy measurements. While our goal in this Section has been to revisit previous analyses accounting for the detector bandwidth, a cold dark matter origin for the CIBER excess is still excluded, even if less strongly than previously thought. On the other hand, a thermal ALP population origin is not falsified by anisotropy measurements. Nevertheless, anisotropies hint either to the possible presence of an additional astrophysical class of sources to the EBL, which would possibly explain the angular power spectra of difference wave-

¹⁶The transfer function \mathcal{T}_{WDM} must be evaluated including the dominant dark matter component, which is assumed here cold and different from the decaying ALP.

lengths complementing the dominant contributions of shot power at low multipoles and galaxies at high multipoles [402], or to a different modelling of the latter.

7.4 Star cooling constraints

The processes by which the populations of ALPs a and hidden photons χ are mostly produced in a plasma depend on the temperature and density conditions of the stars considered. Let us consider plasmon decay $\gamma \rightarrow a + \chi$, analogous to the plasmon decay to neutrinos discussed in Sec. 5.2. Other processes like photo-production, pair annihilation of photons or bremsstrahlung are suppressed by a higher order in the coupling $g_{a\chi\gamma}$ or $e = \sqrt{4\pi\alpha}$. While these processes can be relevant for other kind of particles and interactions, we anticipate that the strongest constraints come from stars which would mostly emit a and χ through plasmon decay.

Given that we are interested in an order of magnitude estimate, we will not take into account the L-plasmon decay, as it would be a negligible correction, keeping only the T-plasmon decay into account [149]. The longitudinal plasmon decay in fact contributes negligibly to the cooling, because there is no resonant conversion from L-plasmon to pseudoscalars [281]. The decay of a strongly non-relativistic plasmon is due to the coupling of Eq. (7.2.1). The usual Feynman diagram rules then gives

$$\Gamma_\gamma = \frac{1}{3} \frac{g_{a\chi\gamma}^2}{128\pi} \omega_{\text{pl}}^3 \frac{\omega_{\text{pl}}}{\omega} \quad (7.4.1)$$

in the non-relativistic, non-degenerate limit of the plasma. This is the formula to be used in most of stellar plasma cases, where

$$\omega_{\text{pl}}^2 = \frac{4\pi\alpha n_e}{m_e}, \quad (7.4.2)$$

with n_e electron number density and m_e electron mass [149].

The production of ALPs and hidden photons in horizontal branch stars through plasmon decay (when their mass is smaller than the plasma frequency) puts bounds on the coupling $g_{a\chi\gamma}$. The energy loss per unit mass due to plasmon decay is given by

$$\epsilon = \frac{1}{\rho_s \pi^2} \int dk k^2 \frac{\omega}{e^{\omega/T} - 1} \Gamma_\gamma \quad (7.4.3)$$

where ρ_s is the mass density of the star. So one obtains

$$\begin{aligned} \epsilon &= \frac{\zeta(3)}{192\pi^3} \frac{\omega_{\text{pl}}^4 T^3 g_{a\chi\gamma}^2}{\rho_s} \\ &\simeq 0.6 \text{ erg/g/s} \times \left(\frac{\omega_{\text{pl}}}{1 \text{ keV}} \right)^4 \left(\frac{T}{10 \text{ keV}} \right)^3 \left(\frac{10^4 \text{ g/cm}^3}{\rho_s} \right) \left(\frac{g_{a\chi\gamma}}{10^{-8} \text{ GeV}^{-1}} \right)^2 \end{aligned} \quad (7.4.4)$$

with canonical parameters of horizontal branch star cores; the star cooling bound implies that $\epsilon \lesssim 10 \text{ erg/g/s}$. A more stringent bound is given by the required

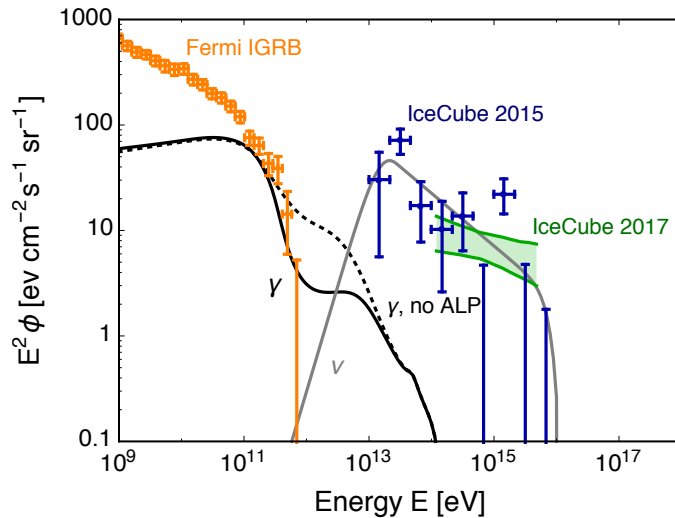


Figure 7.4: The gamma-ray and neutrino fluxes expected in a minimal $p\gamma$ production scenario of Ref. [216] (see details in text). Also shown is the per-flavor IceCube neutrino flux according to [245] (blue data points) and a more recent estimate [246] (green band). The gamma-ray flux in the absence of ALP decays (dotted line) is decreased in the presence of an additional EBL component (solid line), which alleviates the tension with Fermi LAT IGRB measurements [420].

agreement between the predicted and observationally inferred core mass at the helium flash of red giants. This is to be expected, because the bounds on the coupling $g_{a\chi\gamma}$ can be directly read from the existing constraints on a putative neutrino magnetic dipole moment μ_ν . The plasmon decay rate is the same for both channels [149], after substituting

$$g_{a\chi\gamma} \rightarrow 4\mu_\nu ; \quad (7.4.5)$$

non-standard neutrino losses would delay the ignition of helium in low-mass red giants [416]. With a 95% confidence level $\mu_\nu \lesssim 1.4 \times 10^{-9} \text{GeV}^{-1}$ [417], which translates to the bound $g_{a\chi\gamma} \lesssim 6 \times 10^{-9} \text{GeV}^{-1}$. Interestingly, a cooling excess has been claimed for this class of stars [418], and the plasmon decay to an ALP and a hidden photon with a coupling of this size would contribute as an additional cooling channel. It shall be noted however that plasmon decay cannot account for some of the cooling hints [418, 419].

7.5 Gamma-ray attenuation

The increased EBL flux has observable impact on the propagation of very high-energy $E > 0.1 \text{ TeV}$ photons due to enhanced rate of e^+e^- pair production. This effect may relax the tension between the predicted gamma-ray flux and the Fermi LAT measurement of isotropic gamma-ray background (IGRB) [420] in traditional multi-messenger scenarios of high-energy neutrino origin [243, 244, 247, 421–423] and eliminates the need of hidden cosmic-ray accelerators [216]. In Fig. 7.4 I illustrate

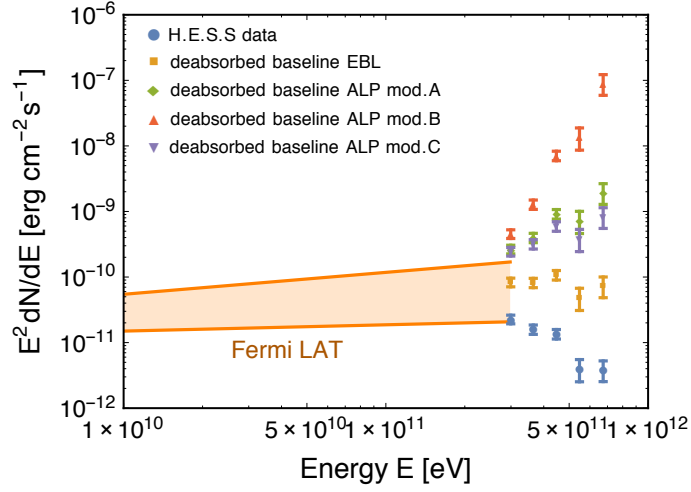


Figure 7.5: Observed spectral energy distribution of PG 1553+113 measured during the flare observed by Fermi LAT (power law approximation) and H.E.S.S. (as shown in Fig.3 of Ref. [426]) together with the deabsorbed spectra calculated using EBL model of Ref. [369] with or without extra contribution from ALP.

the effect. We calculate the neutrino and the accompanying gamma-ray flux in the minimal $p\gamma$ production scenario of Ref. [216] with $\epsilon_\nu^b = 25$ TeV, assuming the low X-ray luminosity AGN evolution of Ref. [424] for the sources and the minimal EBL model [382] with or without the contribution from ALPs, for which we use model A.¹⁷ The spectra shown were obtained by solving transport equations for neutrinos and electron-photon cascades with a public numerical code [425]. The effect of the increased EBL is clearly seen on the gamma-ray flux above 100 TeV. In principle, the enhanced Universe opaqueness for gamma rays predicted in the above scenario will only sharpen the well known problem of unexpectedly hard gamma-ray spectra detected from remote blazars. In Appendix 7.6 a consistency check is carried out to verify the compatibility of our scenario with blazar observations. We found that the only parameter range excluded by analysis of the deabsorbed spectra is the one of model B, which is already excluded by the observed angular power spectrum, whereas models A and $C_{\text{th(nth)}}$ are viable.

7.6 A check: consistency with blazar observations

The enhanced Universe opaqueness for gamma rays predicted in the ALP decay scenario sharpens the well-known problem of unexpectedly hard gamma-ray spectra detected from remote blazars. A possible solution proposed in Refs. [375–379, 427–431] is based on the natural assumption that the blazars also emit ultrahigh energy cosmic rays which contribute to the observed gamma-ray flux through secondary

¹⁷I remark again that model A and C_{th} are indistinguishable at the level of the intensity spectrum.

electromagnetic cascades produced in line-of-sight cosmic-ray interactions. The above scenario allows us to avoid exponential gamma-ray flux suppression with distance from the source.

A straightforward way to find if an extra component is needed to fit the observations is to construct the so called deabsorbed spectrum, i.e. the primary spectrum recovered from the observations assuming no extra components. The negative break in the deabsorbed spectrum can be considered as a good indication of the presence of an extra component. By definition the deabsorbed spectrum

$$F_{\text{deabsorbed}} = e^{\tau(z,E)} F_{\text{observed}} \quad (7.6.1)$$

depends not only on source redshift but also on the EBL model assumed through optical depth τ . We will illustrate this point on the high-frequency peaked BL Lac object PG 1553+113, one of the most variable remote sub-TeV gamma-ray sources known today. Its gamma-ray flaring activity has been detected by H.E.S.S. telescopes during the nights of 26th and 27th of April 2012, when the source flux above 0.3 TeV increased by a factor of 3 with evident signs of variability on the scale of hours [426]. In Fig. 7.5 (left) I show the average spectrum of the object measured during the flare by Fermi LAT and H.E.S.S. (as shown in Fig. 3 of Ref. [426]) together with the deabsorbed spectra calculated using the EBL model of Ref. [369] with or without extra contribution from the ALP decay models A, B and C_{th(nth)}. We use the lower limit $z > 0.43$ [432] as a conservative source redshift estimate. It is now clear from the figure that increased EBL may lead to a negative break in the deabsorbed spectrum, which indicates the presence of an extra component.

Let us assume now that the extra component is not as highly variable as we would expect in the case of secondary γ from cosmic rays. Would it contradict observations? To answer this question in a conservative manner, we calculate the maximally expected integral flux of primary γ above 0.3 TeV during the flare phase $F_{\text{max}}^{\text{var}}$ and the minimal required integral flux of the constant extra component $F_{\text{min}}^{\text{ext}}$. We calculate $F_{\text{max}}^{\text{var}}$ assuming power law injection and maximal initial γ flux consistent with Fermi LAT observations below 30 GeV. $F_{\text{min}}^{\text{ext}}$ is then calculated simply by subtracting of the primary component from the average observed flux at flare phase. For ALP models A, B and C we get $F_{\text{max}}^{\text{var}}/F_{\text{min}}^{\text{ext}}$ integral flux ratios equal to 2.3, 0.36 and 7.6 respectively. From the observation that the average integral flare flux above 0.3 TeV is 3 times higher than pre-flare flux we infer

$$3 = \frac{F^{\text{var}} + F^{\text{ext}}}{F^{\text{const}} + F^{\text{ext}}} < \frac{F^{\text{var}} + F^{\text{ext}}}{F^{\text{ext}}} = \frac{F^{\text{var}}}{F^{\text{ext}}} + 1, \quad (7.6.2)$$

where F^{const} is the possible contribution of primary photons in pre-flare flux. Now it is obvious that the condition $F^{\text{var}}/F^{\text{ext}} < 0.36$ which we have in case of model B contradicts Eq. (7.6.2), while other models are still in line with this inequality.

Conclusions

Before the advent of accelerators, the study of messengers from the sky (back then, cosmic rays) was the main source of information for fundamental particle physics; nowadays, the rapid development of neutrino and multi-messenger astronomy has established once more astrophysical observations as a major tool to search for physics beyond the Standard Model.

The main theme of this thesis was to search for signals of new physics by using astrophysical neutrinos. Such a task is possible only if we know what is the flux we expect from different sources at all the possible energy ranges. This is why the thesis included both a first part summarizing the contributions to the grand unified neutrino spectrum (GUNS), and a second part providing possible applications of neutrino astronomy to explore beyond the Standard Model physics.

After presenting the main idea of the GUNS in the Introduction, we have analyzed the neutrino spectrum collecting the contributions to the flux according to the neutrino production mechanisms. In Chapter 2, we collect the results regarding the neutrinos produced in the early universe. These neutrinos would be the product of decoupling (cosmic neutrino background) and of the decay of light elements during the Big Bang nucleosynthesis. Chapter 3 is devoted to the study of neutrinos from nuclear reactions (fission, fusion, and decay). These neutrinos have typical energies in the MeV range and are produced in the Sun, in reactors, in the Earth, and in stellar explosions. The latter produce transient signals (from supernovae) and a background given by the sum of all supernovae, the so-called diffuse supernova neutrino background. In Chapter 4, neutrinos produced by interaction of the cosmic rays with hadrons and photons are analyzed. These include neutrinos with energies ranging from around 20 MeV to 10^{20} eV, which are produced in the Earth and Sun atmospheres, by interactions of the cosmic rays in the environment surrounding cosmic accelerators (e.g. pp sources such as star-forming galaxies and $p\gamma$ sources like active galactic nuclei and blazars), and by interactions of the cosmic rays during propagation (cosmogenic neutrinos).

In Chapter 5 we have calculated the previously overlooked solar neutrino flux produced by various thermal processes that produce pairs with keV-range energies. There are several reasons to analyze this flux. A proposed dark matter detector

for keV-mass sterile neutrinos might find this flux to be a limiting background and conversely, conceivably it could measure this solar flux, thus providing nontrivial information on the solar metal content. Even though these are somewhat futuristic ideas, it is well motivated to provide a benchmark calculation of the thermal solar neutrino flux. One complication is that there is not a single dominant production channel, but all the ABCD processes (atomic, bremsstrahlung, Compton, plasmon decay) are relevant in different ranges of energy. Each of them has its own idiosyncratic issues concerning in-medium many-body effects, yet the flux calculations should be correct on the general 10% level of precision.

The second part of the thesis is devoted to probing fundamental particle physics with neutrinos, exploiting both MeV neutrinos from the Sun and high-energy neutrinos produced in cosmic accelerators.

In Chapter 6, we have explored the possibility of distinguishing Majorana from Dirac neutrinos by their gravi-majoron decays, assuming a gravitational origin of neutrino masses. Interactions between neutrinos and conventional Nambu-Goldstone bosons are strongly constrained by cosmology, astrophysics, and laboratory experiments. In contrast, the gravi-majorons considered here are not ruled out because they only arise in the very late Universe and effectively decouple from high-energy processes. The detection of an unexpectedly large absolute neutrino mass scale in beta-decay experiments could provide a hint towards the gravitational mass mechanism, because it evades all cosmological mass bounds. Such large absolute neutrino mass scale implies a degenerate mass hierarchy, allowing us to distinguish Majorana from Dirac neutrinos through their decay. In the Majorana case, we have put strong bounds on the decay of the heaviest neutrino at 90% CL, using data from experiments searching for antineutrino appearance from the Sun. Such bounds are interesting *per se*, because they generally apply to any model in which neutrinos decay to light pseudoscalars. We also explored the possibility of distinguishing Dirac from Majorana neutrinos with future IceCube data; however, this possibility requires a better understanding of neutrino production in astrophysical sources.

Finally, Chapter 7 is devoted to the tension between the gamma-ray flux measured by Fermi and the larger than expected neutrino flux detected by IceCube. One assumes the existence of axionlike particles with mass around an electronvolt which produce photons through decay. If one assumes a $p\gamma$ scenario, the tension between Fermi and IceCube is alleviated, because gamma rays would produce electron-positron pairs by scattering on the enhanced extragalactic background light (EBL). This is also consistent with the excess in the EBL spectrum detected by the CIBER collaboration. This is an example of how multi-messenger, multi-wavelength observations can be used for dark matter indirect detection.

There are different possible future directions for the research tackled in this thesis. Astrophysical observations are increasingly used to search for new physics. The production of neutrinos in stars via the ABCD processes analyzed in Chapter 5 is the dominant cooling channel for many classes of stars. When introducing weakly interactive slim particles like axions or minicharged particles, one modifies stellar evolution. As mentioned in Chapter 7, there are several astrophysical observations

that point to an additional cooling channel in white dwarfs, horizontal branch stars and red giants, for example through axion production. It would be interesting to revisit the neutrino production in these stars and check whether there is some ingredients missing in our understanding of star cooling through Standard Model particles.

On the other hand, the observed hints for excessive cooling may be true, proving the existence of beyond the Standard Model particles, e.g. the axion. Generally, there is an interaction between the axion, the magnetic field, and the electric field. Interestingly, this interaction is at the core of axion direct detection experiments. I have recently contributed to this research topic by coauthoring a paper in which we proposed the “tunable plasma haloscope” experiment [433]. The latter consists of a wire metamaterial in which dark matter axions are converted to plasmons through their interactions with an external magnetic field. This line of research can be further expanded to find new experimental concepts or possible indirect signals in astrophysical systems.

The bounds on neutrino decays to light pseudoscalars of Chapter 6 were obtained using the data from SNO and KamLAND, but a similar analysis can be carried out with Borexino data. These will be the strongest bounds of this kind on the decay of the heaviest neutrino mass eigenstates. This analysis is currently ongoing [353].

Finally, high-energy multi-messenger astronomy will be crucial to further deepen our understanding of astrophysical processes and fundamental particle physics. The future will bring more data in neutrino astronomy, and perhaps even a galactic supernova. Perhaps, long-standing mysteries such as the production location of most energetic particles in the universe, the properties of neutrinos, and the nature of dark matter, will be solved soon thanks to astrophysical neutrinos.

Neutrino Mass Matrix

Neutrino fluxes from practically any source depend on flavor so that what arrives at a detector depends on flavor oscillations driven by neutrino masses and mixing. We restrict ourselves to a minimal scenario that includes only the three known species.

The weak-interaction neutrino fields ν_α with $\alpha = e, \mu$ or τ are given in terms of fields with definite masses ν_i by a unitary transformation $\nu_\alpha = \sum_{i=1}^3 U_{\alpha i} \nu_i$, implying

$$|\nu_\alpha\rangle = \sum_{i=1}^3 U_{\alpha i}^* |\nu_i\rangle \quad \text{and} \quad |\bar{\nu}_\alpha\rangle = \sum_{i=1}^3 U_{\alpha i} |\bar{\nu}_i\rangle \quad (\text{A.1})$$

for neutrino and antineutrino single-particle states [129]. The mixing matrix is conventionally expressed in terms of three two-flavor mixing angles $0 \leq \theta_{ij} < \pi/2$ and a CP-violating phase $0 \leq \delta < 2\pi$ in the form

$$\begin{aligned} \mathbf{U} &= \begin{pmatrix} 1 & 0 & 0 \\ 0 & c_{23} & s_{23} \\ 0 & -s_{23} & c_{23} \end{pmatrix} \begin{pmatrix} c_{13} & 0 & s_{13}e^{-i\delta} \\ 0 & 1 & 0 \\ -s_{13}e^{i\delta} & 0 & c_{12} \end{pmatrix} \begin{pmatrix} c_{12} & s_{12} & 0 \\ -s_{12} & c_{12} & 0 \\ 0 & 0 & 1 \end{pmatrix} \\ &= \begin{pmatrix} c_{12}c_{13} & s_{12}c_{13} & s_{13}e^{-i\delta} \\ -s_{12}c_{23} - c_{12}s_{23}s_{13}e^{i\delta} & c_{12}c_{23} - s_{12}s_{23}s_{13}e^{i\delta} & s_{23}c_{13} \\ s_{12}s_{23} - c_{12}c_{23}s_{13}e^{i\delta} & -c_{12}s_{23} - s_{12}c_{23}s_{13}e^{i\delta} & c_{23}c_{13} \end{pmatrix}, \end{aligned} \quad (\text{A.2})$$

where $c_{ij} = \cos \theta_{ij}$ and $s_{ij} = \sin \theta_{ij}$. We have left out a factor $\text{diag}(1, e^{i\alpha_{21}/2}, e^{i\alpha_{31}/2})$ of Majorana phases that are important, for example, in neutrinoless double-beta decay, but not for flavor oscillations.

The best-fit mixing angles determined from global fits of all flavor oscillation data are given in Table A.1. Within uncertainties, the octant of θ_{23} remains unknown, i.e., if $\sin^2 \theta_{23}$ is larger or smaller than 1/2. CP violation is favored, but the range of allowed δ remains large.

With the results of Table A.1 for normal mass ordering one finds the matrix of

Table A.1: Neutrino mixing angles according to Cappozzi et al. [352], very similar to those of Refs. [434, 435].

	Normal Ordering		Inverted Ordering	
	Best fit	1σ range	Best fit	1σ range
$\sin^2 \theta_{12}$	0.304	0.291–0.318	0.303	0.290–0.317
$\sin^2 \theta_{13}$	0.0214	0.0207–0.0223	0.0218	0.0211–0.0226
$\sin^2 \theta_{23}$	0.551	0.481–0.570	0.557	0.533–0.574
δ/π	1.32	1.14–1.55	1.52	1.37–1.66

mixing probabilities, which is the same for ν and $\bar{\nu}$,

$$(|U_{\alpha i}|^2) = \begin{pmatrix} 0.681_{-0.014}^{+0.013} & 0.297_{-0.013}^{+0.014} & 0.0214_{-0.0007}^{+0.0009} \\ 0.109_{-0.035}^{+0.074} & 0.352_{-0.065}^{+0.080} & 0.539_{-0.069}^{+0.019} \\ 0.210_{-0.073}^{+0.040} & 0.351_{-0.082}^{+0.067} & 0.439_{-0.019}^{+0.069} \end{pmatrix}. \quad (\text{A.3})$$

The uncertainties correspond to the maximal and minimal values within the 1σ ranges shown in Table A.1. Of course, the rows and columns of this matrix of probabilities always have to add up to 1. The first row, for example, means that a produced ν_e has a 68% chance to be a ν_1 , 30% to be ν_2 , and 2% to be ν_3 . The mass eigenstates are conventionally numbered such that the probabilities in the first row appear in declining order, i.e., according to the ν_i admixtures to ν_e .

The matrix \mathbf{U} being unitary, its inverse \mathbf{U}^{-1} , which allows us to express mass states in terms of flavor states, is identical with its conjugate transpose \mathbf{U}^\dagger . Therefore, the probabilities for finding a given mass eigenstates in any of the flavors correspond to the columns of Eq. (A.3). For example, the last column tells us that a ν_3 , for example in the cosmic neutrino background, has a 2% chance of being ν_e , a 54% chance of being ν_μ , and 44% of being ν_τ , and analogous for the other columns.

The numbering convention of mass states leaves open the ordering of the mass values. The matter effect on flavor conversion in the Sun implies $m_1 < m_2$. The atmospheric ordering may be normal with $m_1 < m_2 < m_3$ or inverted with $m_3 < m_1 < m_2$. Global fits somewhat prefer normal ordering. The probability matrix for inverted ordering is similar to Eq. (A.3) within the shown uncertainties.

Flavor oscillations of relativistic neutrinos are driven by the squared-mass differences. We express the mass spectrum in terms of the parameters [352]

$$\delta m^2 = m_2^2 - m_1^2 = 73.4 \text{ meV}^2, \quad (\text{A.4a})$$

$$\Delta m^2 = m_3^2 - \frac{m_1^2 + m_2^2}{2} = \pm 2.45 \times 10^3 \text{ meV}^2, \quad (\text{A.4b})$$

where normal ordering corresponds to $\Delta m^2 > 0$, inverted ordering to $\Delta m^2 < 0$. The nominal 1σ range of the measured values is 1.4 and 2.2%, respectively. The small mass splitting δm^2 is also called the solar mass difference because it drives solar neutrino conversion, whereas Δm^2 is the atmospheric one. Often the atmospheric

splitting is instead identified with either $m_3^2 - m_2^2$ or $m_1^2 - m_3^2$, depending on the mass ordering, which however is a less practical convention.

Direct laboratory limits on the unknown overall mass scale of approximately 2 eV derive from the electron endpoint spectrum in tritium β decay [47]. The KATRIN experiment is expected to improve the sensitivity to approximately 0.2 eV in the near future [20].

Cosmological data constrain the fraction of hot dark matter, implying 95% C.L. limits $\sum m_\nu < 0.11\text{--}0.68$ eV, depending on the used data and cosmological model [6, 14, 15]. Near-future surveys should be able to set a lower limit, i.e., provide a neutrino-mass detection [6]. Of course, these results have to be interpreted with the usual caveats concerning cosmological assumptions and possible unrecognized systematics.

The neutrino signal from the next nearby supernova can provide a 95% C.L. time-of-flight limit of 0.14 eV if the emission shows few-millisecond time variations caused by hydrodynamic instabilities as suggested by 2D and 3D simulations [436].

Searches for neutrinoless double beta decay are only sensitive to Majorana masses, and specifically to the combination $\langle m_\nu \rangle = |\sum_{i=1}^3 U_{ei}^2 m_i|$. Current limits are on the level of 0.11–0.52 eV, depending on isotope and on uncertainties of the nuclear matrix elements [47].

Appendix B

Neutrino Mixing in Matter

When they propagate in matter, neutrinos experience a flavor-dependent potential caused by the electroweak interaction. In a normal medium, consisting of nuclei and electrons, it is

$$V_{\text{weak}} = \pm\sqrt{2}G_{\text{F}}n_B \times \begin{cases} Y_e - Y_n/2, & \text{for } \nu_e, \\ -Y_n/2, & \text{for } \nu_{\mu,\tau}, \end{cases} \quad (\text{B.1})$$

where n_B is the baryon density, $Y_e = n_e/n_B$ the net electron fraction per baryon (electrons minus positrons), and $Y_n = n_n/n_B$ the neutron fraction. The upper sign is for ν , the lower sign for $\bar{\nu}$. Equivalently, we can use a nominally negative baryon density to denote the $\bar{\nu}$ potential. Radiative corrections actually provide a small difference between the ν_μ and ν_τ potentials [437, 438], as does the possible presence of muons in a supernova core [439]. We also ignore background neutrinos which complicate neutrino propagation in the form of collective flavor evolution [440].

The flavor of a neutrino of fixed energy E evolves as a function of distance z as $i\partial_z\Psi = (\mathbf{H}_0 + \mathbf{V})\Psi$, where Ψ is a three-vector of flavor amplitudes, whereas antineutrinos evolve as $i\partial_z\bar{\Psi} = (\mathbf{H}_0^* - \mathbf{V})\bar{\Psi}$. In the ultrarelativistic limit, the mass contribution in the flavor basis is

$$\mathbf{H}_0 = \frac{1}{2E}\mathbf{U} \begin{pmatrix} m_1^2 & 0 & 0 \\ 0 & m_2^2 & 0 \\ 0 & 0 & m_3^2 \end{pmatrix} \mathbf{U}^\dagger \quad (\text{B.2})$$

and the matrix of potential energies is

$$\mathbf{V} = \sqrt{2}G_{\text{F}} \begin{pmatrix} n_e - n_n/2 & 0 & 0 \\ 0 & -n_n/2 & 0 \\ 0 & 0 & -n_n/2 \end{pmatrix}. \quad (\text{B.3})$$

Without flavor mixing, the in-medium dispersion relation in the relativistic limit is given by the effective masses $m_{\text{eff}}^2 = m^2 + V_{\text{weak}}2E$, shown as thin grey lines in Fig. B.1 for a schematic choice of mass and mixing parameters. A nominally negative density is used to show the energy levels for antineutrinos. The background medium

is taken to have equal densities of electrons and neutrons as would be the case for ${}^4\text{He}$ or ${}^{12}\text{C}$. For a different composition, the lines acquire a different slope caused by the common neutral-current potential for all flavors.

For nonvanishing mixing angles, the effective masses are obtained by diagonalizing $\mathbf{H}_0 + \mathbf{V}$, which is achieved by a unitary matrix \mathbf{U}_M such that

$$\begin{aligned} \mathbf{M}_{\text{eff}}^2 &= \begin{pmatrix} m_{1,\text{eff}}^2 & 0 & 0 \\ 0 & m_{2,\text{eff}}^2 & 0 \\ 0 & 0 & m_{3,\text{eff}}^2 \end{pmatrix} \\ &= \mathbf{U}_M^\dagger (\mathbf{U} \mathbf{M}^2 \mathbf{U}^\dagger + 2E \mathbf{V}) \mathbf{U}_M. \end{aligned} \quad (\text{B.4})$$

For antineutrinos, one substitutes $\mathbf{V} \rightarrow -\mathbf{V}$ and $\delta \rightarrow -\delta$, the latter equivalent to $\mathbf{U} \rightarrow \mathbf{U}^*$. Notice that $m_{i,\text{eff}}^2$ can be negative because it is just a formal way for writing the in-medium energy levels. In Fig. B.1, the $m_{i,\text{eff}}^2$ are shown as thick colored lines. Notice that θ_{23} and δ do not enter if the ν_μ and ν_τ potentials are equal — otherwise there will be a third level crossing. Notice also that asymptotically the colored lines have a nonvanishing offset relative to the grey lines.¹⁸

Of particular interest is the case of neutrinos produced at high density in the interior of a star which then propagate all the way to the surface. If the propagation is adiabatic (and this is the case for solar and supernova neutrinos), a state originally in a propagation eigenstate emerges as such. So we should decompose the flavor states at the point of production into local propagation states which then connect to vacuum mass states at the stellar surface (MSW effect). In sufficiently dense matter, the propagation eigenstates coincide with interaction eigenstates. In Fig. B.1 (normal ordering), a ν_e produced at very high density corresponds to the largest m_{eff}^2 , i.e., the thick green line. Following this line to zero density (vacuum), we see that a produced ν_e will emerge as the mass eigenstate ν_3 . Conversely, a $\bar{\nu}_e$ (large negative density) is on the blue line and thus emerges as ν_1 . A detailed discussion of all such cases, relevant in the supernova context, was provided by Dighe and Smirnov [170].

Often the flavor-diagonal contribution to \mathbf{V} provided by neutrons is not included because it drops out of the oscillation equation. In this case, and using the best-fit mixing parameters in normal ordering from Table A.1, the same plot of $m_{i,\text{eff}}^2$ is shown in Fig. B.2 (top). In the Sun, the central density is 150 g cm^{-3} with $Y_e = 0.681$, corresponding to $n_e = 6.14 \times 10^{25} \text{ cm}^{-3} = 4.72 \times 10^{11} \text{ eV}^3$ and thus to $V_e = 7.8 \times 10^{-12} \text{ eV}$, where

$$V_e = \sqrt{2} G_F n_e. \quad (\text{B.5})$$

With $E = 18.8 \text{ MeV}$, near the highest solar ν_e energy, one finds $V_e 2E < 233 \text{ meV}^2 = 4.0 \delta m^2$, indicated by a vertical dashed line in Fig. B.2.

The probability for a ν_e that was produced in the medium to be found in any of the propagation eigenstates i is $P_{ei}^M = |\mathbf{U}_{ei}^M|^2$, shown in Fig. B.2 (middle) from a

¹⁸Similar plots in the context of supernova neutrinos [170] show in-medium curves asymptotically approaching the zero-mixing lines. This behavior is caused by the transition from their Eq. (43) to (44) where one should expand consistently to lowest order in all m^2 .

numerical solution for \mathbf{U}_M using the best-fit mixing parameters. At zero density, the P_{ei} correspond to the top row in the matrix of Eq. (A.3). At very high density, ν_e essentially coincides with ν_3 , so after adiabatic propagation it would emerge in the third mass eigenstate as mentioned earlier.

Neutrinos propagating from a distant source decohere into mass eigenstates, so for example the ν_e produced in the Sun arrive with probabilities P_{ei} in the different mass eigenstates, depending on the exact point of production and depending on their energy. A detector which is only sensitive to ν_e projects from each of the ν_i fluxes the ν_e component, corresponding to the probability $|\mathbf{U}_{ei}|^2$, so the ν_e survival probability is

$$P_{ee} = \sum_{i=1}^3 |\mathbf{U}_{ei}^M|^2 |\mathbf{U}_{ei}|^2, \quad (\text{B.6})$$

shown as a red line in Fig. B.2 (bottom). For neutrinos produced at very low density and/or with very low energies, this is, using Eq. (A.2)

$$P_{ee}^{\text{vac}} = (c_{12}^4 + s_{12}^4)c_{13}^4 + s_{13}^4 = 0.553, \quad (\text{B.7})$$

where the numerical value is for the best-fit mixing angles in normal mass ordering.

The mass differences are hierarchical, $\delta m^2 \ll \Delta m^2$, allowing for an approximate determination of \mathbf{U}_M [441]. Writing it in the form of Eq. (A.2), one finds for the in-medium mixing angles $\theta_{23}^M = \theta_{23}$, $\delta^M = \delta$, and

$$2\theta_{12}^M = \text{ArcTan}(\cos 2\theta_{12} - \epsilon_{\odot}, \cos \theta'_{13} \sin 2\theta_{12}), \quad (\text{B.8a})$$

$$2\theta_{13}^M = \text{ArcTan}(\cos 2\theta_{13} - \epsilon_a, \sin 2\theta_{13}), \quad (\text{B.8b})$$

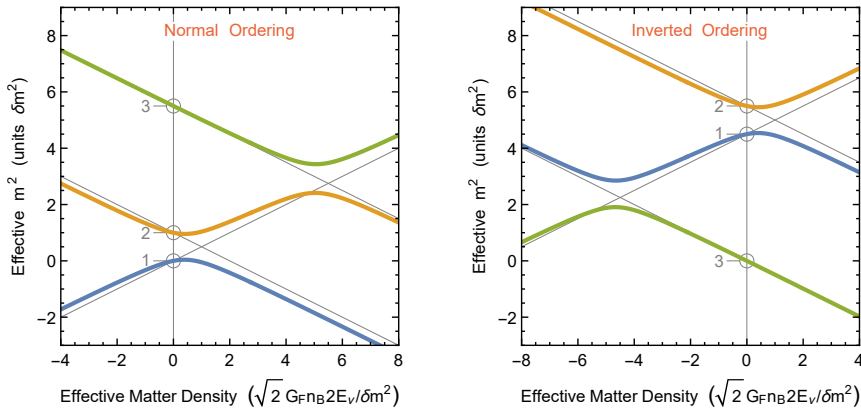


Figure B.1: Effective neutrino masses in a medium in units of the solar mass difference δm . For this schematic plot, $m_1 = 0$, the atmospheric mass difference was chosen as $\Delta m^2 = 5 \delta m^2$, and the mixing angles as $\sin^2 \theta_{12} = 0.30$ and $\sin^2 \theta_{13} = 0.01$. The electron and neutron densities were taken to be equal ($n_e = n_n = n_B/2$) appropriate for a medium consisting of ${}^4\text{He}$ or ${}^{12}\text{C}$. A negative density is to be interpreted as a positive density for the energy levels of antineutrinos. At zero density the levels are the squared vacuum masses. The thin grey lines are the energy levels for vanishing mixing angles.

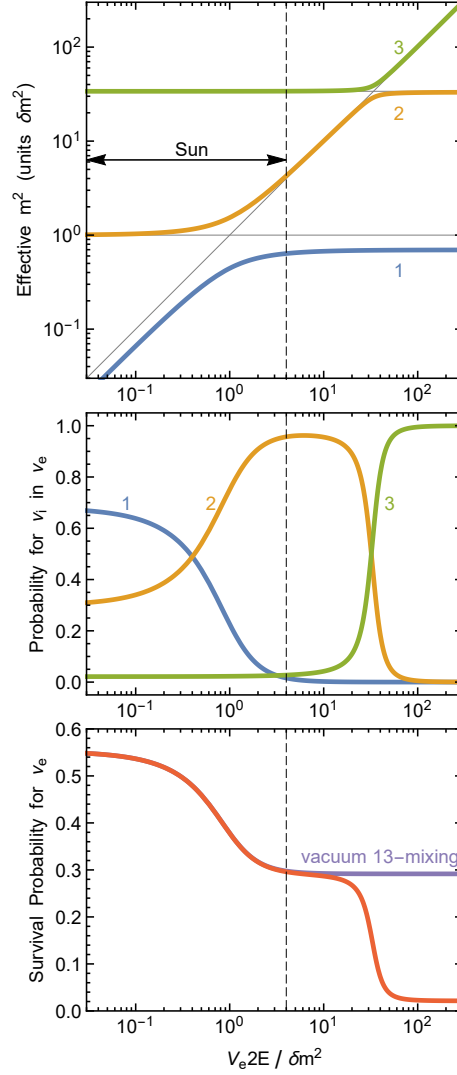


Figure B.2: *Top:* Effective in-medium neutrino masses-squared, $m_{i,\text{eff}}^2$ with $i = 1, 2$ or 3 , in units of the solar value δm^2 . The neutron contribution, which is flavor diagonal, has been ignored. The mixing parameters are the best-fit values in normal ordering from Table A.1. In the Sun, the maximum on the horizontal axis is 4.0 (vertical dashed line), corresponding to $n_e = 6.14 \times 10^{25} \text{ cm}^{-3}$ at the solar center and the largest ν_e energy of $E = 18.8 \text{ MeV}$. *Middle:* Probability of a produced ν_e to be in the propagation eigenstates 1, 2 or 3, corresponding to $|U_{ei}^M|^2$. *Bottom:* Probability of a produced ν_e , after adiabatic propagation, to be measured as a ν_e according to Eq. (B.6). For solar conditions (left of the dashed line), ignoring the matter effect on 13-mixing yields an excellent approximation.

where $\theta'_{13} = \theta_{13}^M - \theta_{13}$. Here, $\alpha = \text{ArcTan}(x, y)$ is an angle such that $\sin \alpha = y/\sqrt{x^2 + y^2}$ and $\cos \alpha = x/\sqrt{x^2 + y^2}$. Further,

$$\epsilon_{\odot} = \frac{2EV_e}{\delta m^2} \left(\cos^2 \theta_{13}^M + \frac{\sin^2 \theta'_{13}}{\epsilon_a} \right), \quad (\text{B.9a})$$

$$\epsilon_a = \frac{2EV_e}{m_3^2 - m_1^2 - \delta m^2 \sin^2 \theta_{12}}, \quad (\text{B.9b})$$

where $\epsilon_a < 0$ for inverted mass ordering ($m_3^2 < m_1^2$). The approximate analytic probabilities $|U_{ei}^M|^2$ agree very well with the numerical values shown in the middle panel of Fig. B.2. The agreement is better than 10^{-3} except for $|U_{e1}^M|^2$ where above 10 on the horizontal axis the analytic probability falls off faster than the numerical one. The differences between analytic and numerical solutions are essentially irrelevant on a level of precision where we have ignored radiative corrections to the weak potential.

The maximum value of $2EV_e$ in the Sun is small compared with $m_3^2 - m_1^2$, so for solar conditions we may neglect the matter effect on θ_{13} . In this case \mathbf{U}_M is given in terms of the vacuum mixing angles except for

$$2\theta_{12}^M = \text{ArcTan}(\cos 2\theta_{12} - \epsilon_{\odot}, \sin 2\theta_{12}) \quad (\text{B.10})$$

with

$$\epsilon_{\odot} = \frac{2EV_e}{\delta m^2} \cos^2 \theta_{13}. \quad (\text{B.11})$$

In this case, the probability for a produced ν_e to be found in any of the three propagation eigenstates is

$$P_{e1} = \cos^2 \theta_{13} \cos^2 \theta_{12}^M, \quad (\text{B.12a})$$

$$P_{e2} = \cos^2 \theta_{13} \sin^2 \theta_{12}^M, \quad (\text{B.12b})$$

$$P_{e3} = \sin^2 \theta_{13}. \quad (\text{B.12c})$$

The ν_e survival probability is

$$P_{ee} = \frac{1 + \cos 2\theta_{12} \cos 2\theta_{12}^M}{2} \cos^4 \theta_{13} + \sin^4 \theta_{13} \quad (\text{B.13})$$

marked as “vacuum 13–mixing” in Fig. B.2 (bottom). The best-fit value $\sin^2 \theta_{13} = 0.0214$ implies that we can safely neglect $\sin^4 \theta_{13}$, whereas $\cos^4 \theta_{13} = 0.958$ deviates significantly from 1.

Standard solar model

In Chapter 5 the neutrino fluxes produced from integration over the solar volume are shown. The neutrino production rates are nontrivial functions of several parameters (temperature, density, mass-fraction of each species) which depend on the radial position in the Sun and determine the local plasma properties. These radial profiles of temperature, density, etc. are not directly measured; rather, they are obtained from a solar model. The latter is a theoretical description of the Sun, obtained by evolving certain initial conditions (mass, helium and metal abundances) through a stellar evolution code, which in turn depends on radiative opacities, the treatment of convection, and so forth, to fit the present-day radius, luminosity, and photospheric composition. The latter is the one present-day boundary condition about which estimations vary the most.

In principle, consistency would require us to use a specific solar model for all processes; this should be a solar model obtained using the opacity code and the abundances exploited for the neutrino bremsstrahlung emission calculation. However, the differences between different solar models for thermally emitted neutrinos are small, introducing uncertainties in the neutrino emissivity on the order of 10% perhaps, so we can use more practical criteria for our calculations. First, we want to use a solar model that not only covers in detail the central core but also the external layers because they rule the low energy flux from T-plasmon decay.¹⁹ The Saclay solar model [442, 443] is, in this regard, the most complete one known to us. This model has the additional interest that it was built to reproduce the sound-speed profile (to a large extent due to the temperature profile) measured by helioseismology by adjusting some parameters (like initial metallicity, opacities) which are not directly measurable. The model used was built when the surface chemical composition GS98 [67] was suitable to reproduce the helioseismology data with very minor adjustments.

The recent revision of the surface chemical composition AGSS09 [68] led to a downward adjustment of abundances, mostly CNO, Ne and refractories, providing a lower opacity and thus some tension between solar models and helioseismology. This

¹⁹Note however that the latter is subdominant to the bremsstrahlung neutrinos, which are mostly produced in the core.

tension has led to a large number of publications but is largely irrelevant for the level of precision that we must assume in our calculations. The difference between GS98 and AGSS09 abundances is 20–40% in CNO and $\sim 12\%$ in refractories; both are obtained from spectroscopic observations together with hydrodynamical simulations. One should emphasize that the first one agrees with the helioseismic measurements, whereas the second one (which is a more accurate 3D simulation) does not, see reference [62] for a recent discussion. This situation constitutes the so-called solar abundance problem. Differences in sound speed profiles (temperatures) are however only around 1%.

The GS98 surface composition was preferred as it fits better the solar internal structure. The radial profile of the abundance of several chemical elements is not specified in the Saclay model, so the abundance profiles of the GS98 model of reference [444] was used. The profiles of temperature, electron density, plasma frequency, degeneracy parameter η , Pauli blocking factor, and screening scales for our solar model choice are displayed in the following figures.

On the other hand, by far the most detailed monochromatic opacities publicly available are those of the [Opacity Project](#) [75], which are tabulated for different metals and can thus be combined for different solar compositions. For this reason, they were used in reference [280] to compute the axion emission in free-bound and bound-bound transitions. In the same study, three different opacity codes were compared with excellent agreement. Therefore the OP opacities for the calculations in this thesis were used.

In figures C.1–C.4 I show the radial variation of various characteristic parameters of our standard solar model. In figure C.5 I show the region of origin of the thermal solar neutrinos calculated in the main text. The left panel shows that most of the flux originates within $0.2 R_{\odot}$ with a maximum around $0.1 R_{\odot}$. Notice that emission near the solar center is suppressed by the small volume of this region, i.e., by the geometric r^2 factor. In the right panel, I show the same information, but for each neutrino energy, the flux is normalized to 1. For smaller neutrino energies, the production site is somewhat shifted to larger solar radii.

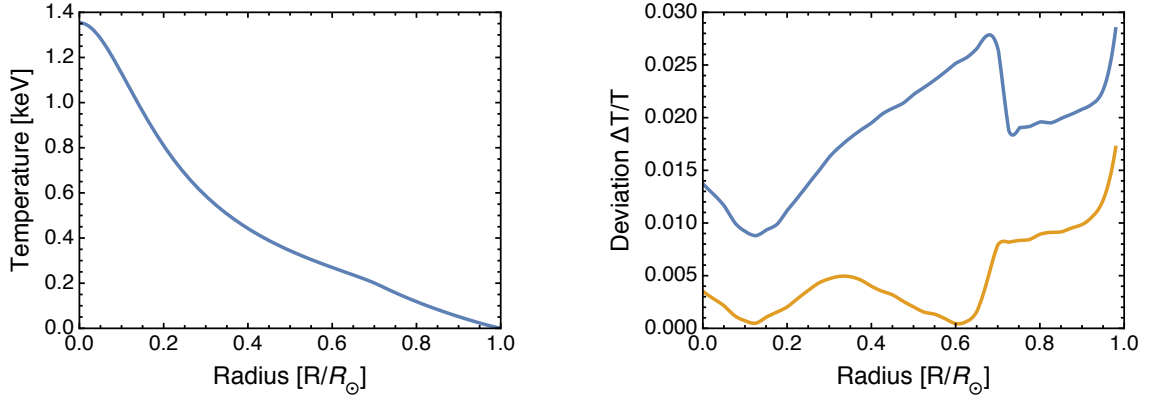


Figure C.1: Temperature profile. *Left panel:* Saclay model [442, 443], our standard case. *Right panel:* Relative deviations between solar models. *Blue line:* Saclay model vs. model [444] with AGSS09 abundances. *Orange line:* Saclay model vs. model [444] with GS98 abundances.

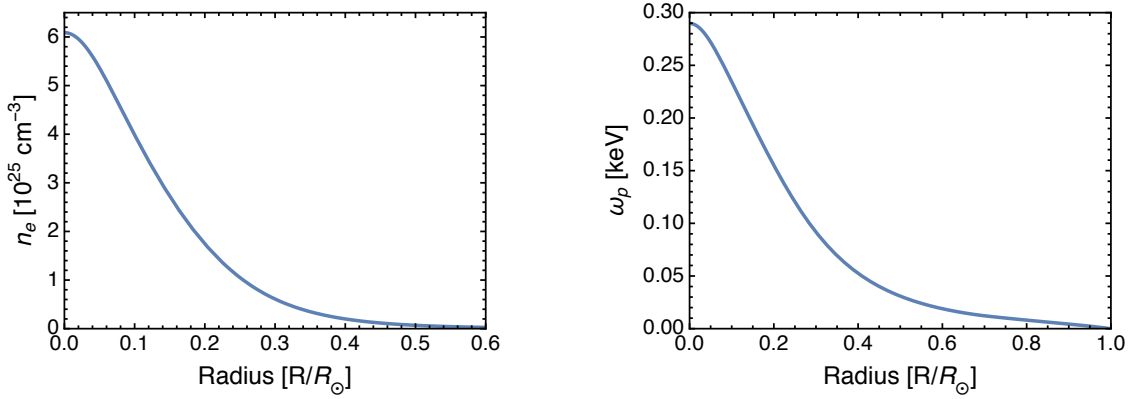


Figure C.2: *Left panel:* Electron number density. *Right panel:* Plasma frequency.

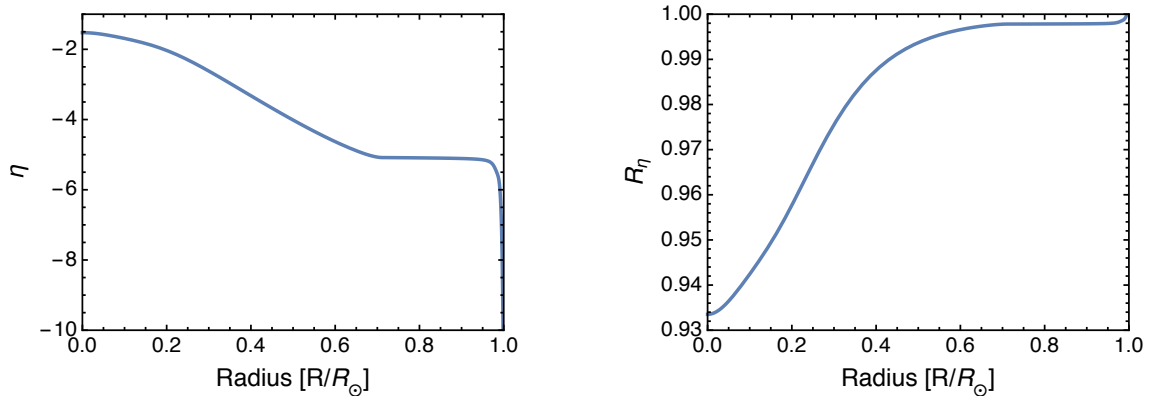


Figure C.3: *Left panel:* Nonrelativistic degeneracy parameter η , where $\eta \rightarrow -\infty$ corresponds to a Maxwell-Boltzmann distribution. *Right panel:* Average Pauli blocking factor when electron recoils are small.

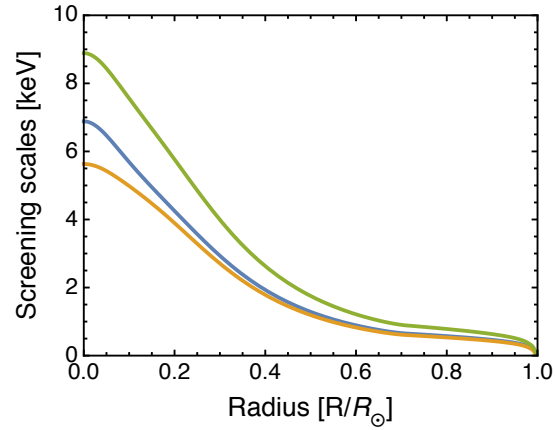


Figure C.4: Phenomenological screening scales. *Orange line*: Electron screening k_e . *Blue line*: Ion screening k_i . *Green line*: Total Debye scale k_s .

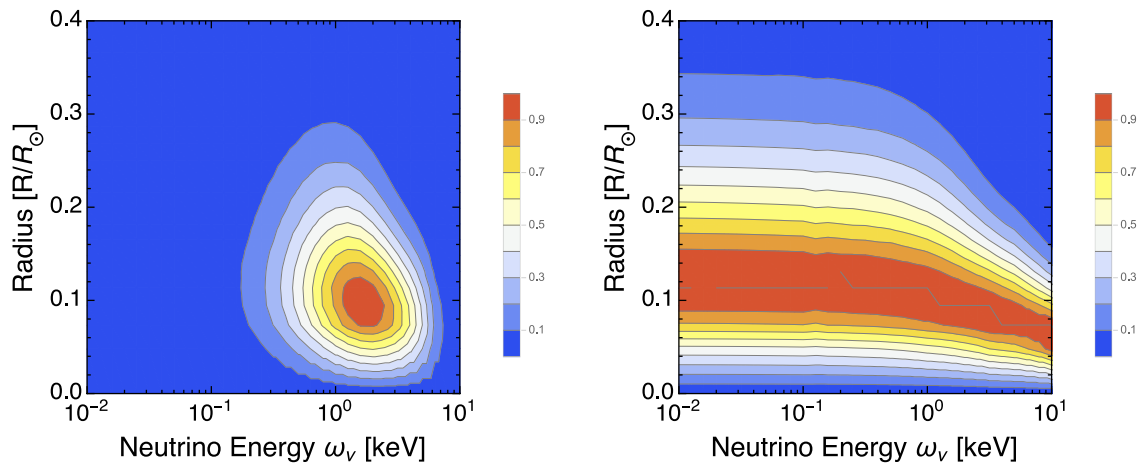


Figure C.5: Isocontours of thermal neutrino emission. *Left panel*: The total flux (including the geometrical r^2 factor) is normalized to 1. *Right panel*: For each neutrino energy, the flux is normalized to 1. The production site of very low energy neutrinos is displaced towards the solar surface, but only slightly.

Bibliography

- [1] M. T. Ressel and M. S. Turner, *The Grand Unified Photon Spectrum: A coherent view of the diffuse extragalactic background radiation*, *Comments Astrophys.* **14** (1990) 323. For full text see [ADS](#).
- [2] E. Vitagliano, I. Tamborra and G. Raffelt, *Grand unified neutrino spectrum at Earth*, work in progress.
- [3] A. D. Dolgov, *Neutrinos in cosmology*, *Phys. Rept.* **370** (2002) 333 [[hep-ph/0202122](#)].
- [4] S. Hannestad, *Primordial neutrinos*, *Ann. Rev. Nucl. Part. Sci.* **56** (2006) 137 [[hep-ph/0602058](#)].
- [5] J. Lesgourgues, G. Mangano, G. Miele and S. Pastor, *Neutrino cosmology*. Cambridge University Press, 2013.
- [6] J. Lesgourgues and L. Verde, *Neutrinos in cosmology*, in *Review of Particle Physics* [47].
- [7] M. Fukugita and T. Yanagida, *Baryogenesis without grand unification*, *Phys. Lett. B* **174** (1986) 45.
- [8] W. Buchmüller, R. D. Peccei and T. Yanagida, *Leptogenesis as the origin of matter*, *Ann. Rev. Nucl. Part. Sci.* **55** (2005) 311 [[hep-ph/0502169](#)].
- [9] S. Davidson, E. Nardi and Y. Nir, *Leptogenesis*, *Phys. Rept.* **466** (2008) 105 [[0802.2962](#)].
- [10] P. F. de Salas and S. Pastor, *Relic neutrino decoupling with flavour oscillations revisited*, *JCAP* **1607** (2016) 051 [[1606.06986](#)].
- [11] J. Birrell, C.-T. Yang and J. Rafelski, *Relic neutrino freeze-out: Dependence on natural constants*, *Nucl. Phys. B* **890** (2014) 481 [[1406.1759](#)].
- [12] E. Grohs, G. M. Fuller, C. T. Kishimoto, M. W. Paris and A. Vlasenko, *Neutrino energy transport in weak decoupling and big bang nucleosynthesis*, *Phys. Rev. D* **93** (2016) 083522 [[1512.02205](#)].

- [13] R. H. Cyburt, B. D. Fields, K. A. Olive and T.-H. Yeh, *Big bang nucleosynthesis: Present status*, *Rev. Mod. Phys.* **88** (2016) 015004 [[1505.01076](#)].
- [14] PLANCK Collaboration, P. A. R. Ade et al., *Planck 2015 results. XIII. Cosmological parameters*, *Astron. Astrophys.* **594** (2016) A13 [[1502.01589](#)].
- [15] PLANCK Collaboration, N. Aghanim et al., *Planck 2018 results. VI. Cosmological parameters*, [1807.06209](#).
- [16] A. D. Dolgov, S. H. Hansen, S. Pastor, S. T. Petcov, G. G. Raffelt and D. V. Semikoz, *Cosmological bounds on neutrino degeneracy improved by flavor oscillations*, *Nucl. Phys. B* **632** (2002) 363 [[hep-ph/0201287](#)].
- [17] E. Castorina, U. Franca, M. Lattanzi, J. Lesgourgues, G. Mangano, A. Melchiorri and S. Pastor, *Cosmological lepton asymmetry with a nonzero mixing angle θ_{13}* , *Phys. Rev. D* **86** (2012) 023517 [[1204.2510](#)].
- [18] I. M. Oldengott and D. J. Schwarz, *Improved constraints on lepton asymmetry from the cosmic microwave background*, *EPL* **119** (2017) 29001 [[1706.01705](#)].
- [19] T. Brinckmann, D. C. Hooper, M. Archidiacono, J. Lesgourgues and T. Sprenger, *The promising future of a robust cosmological neutrino mass measurement*, *JCAP* **1901** (2019) 059 [[1808.05955](#)].
- [20] KATRIN Collaboration, M. Arenz et al., *First transmission of electrons and ions through the KATRIN beamline*, *JINST* **13** (2018) P04020 [[1802.04167](#)]. For the latest status see the [KATRIN homepage](#).
- [21] J. K. Becker, *High-energy neutrinos in the context of multimessenger physics*, *Phys. Rept.* **458** (2008) 173 [[0710.1557](#)].
- [22] C. Spiering, *Towards High-Energy Neutrino Astronomy. A Historical Review*, *Eur. Phys. J.* **H37** (2012) 515 [[1207.4952](#)].
- [23] A. Ringwald and Y. Y. Y. Wong, *Gravitational clustering of relic neutrinos and implications for their detection*, *JCAP* **0412** (2004) 005 [[hep-ph/0408241](#)].
- [24] P. F. de Salas, S. Gariazzo, J. Lesgourgues and S. Pastor, *Calculation of the local density of relic neutrinos*, *JCAP* **1709** (2017) 034 [[1706.09850](#)].
- [25] A. Ringwald, *Prospects for the direct detection of the cosmic neutrino background*, *Nucl. Phys. A* **827** (2009) 501C [[0901.1529](#)].
- [26] P. Vogel, *How difficult it would be to detect cosmic neutrino background?*, *AIP Conf. Proc.* **1666** (2015) 140003.

- [27] Y.-F. Li, *Prospectives on direct detection of the cosmic neutrino background*, *J. Phys. Conf. Ser.* **888** (2017) 012146.
- [28] L. Stodolsky, *Speculations on detection of the “neutrino sea”*, *Phys. Rev. Lett.* **34** (1975) 110. [Erratum: *Phys. Rev. Lett.* **34** (1975) 508].
- [29] G. Duda, G. Gelmini and S. Nussinov, *Expected signals in relic neutrino detectors*, *Phys. Rev. D* **64** (2001) 122001 [[hep-ph/0107027](#)].
- [30] C. Hagmann, *Cosmic neutrinos and their detection*, [astro-ph/9905258](#).
- [31] V. Domcke and M. Spinrath, *Detection prospects for the Cosmic Neutrino Background using laser interferometers*, *JCAP* **1706** (2017) 055 [[1703.08629](#)].
- [32] M. Yoshimura, N. Sasao and M. Tanaka, *Experimental method of detecting relic neutrino by atomic de-excitation*, *Phys. Rev. D* **91** (2015) 063516 [[1409.3648](#)].
- [33] T. J. Weiler, *Resonant absorption of cosmic-ray neutrinos by the relic-neutrino background*, *Phys. Rev. Lett.* **49** (1982) 234.
- [34] S. Weinberg, *Universal neutrino degeneracy*, *Phys. Rev.* **128** (1962) 1457.
- [35] A. G. Cocco, G. Mangano and M. Messina, *Probing low energy neutrino backgrounds with neutrino capture on beta decaying nuclei*, *JCAP* **0706** (2007) 015 [[hep-ph/0703075](#)].
- [36] A. J. Long, C. Lunardini and E. Sabancilar, *Detecting non-relativistic cosmic neutrinos by capture on tritium: phenomenology and physics potential*, *JCAP* **1408** (2014) 038 [[1405.7654](#)].
- [37] M. Arteaga, E. Bertuzzo, Y. F. Perez-Gonzalez and R. Zukanovich Funchal, *Impact of beyond the standard model physics in the detection of the cosmic neutrino background*, *JHEP* **09** (2017) 124 [[1708.07841](#)].
- [38] M. Lisanti, B. R. Safdi and C. G. Tully, *Measuring anisotropies in the cosmic neutrino background*, *Phys. Rev. D* **90** (2014) 073006 [[1407.0393](#)].
- [39] S. Betts et al., *Development of a relic neutrino detection experiment at PTOLEMY: Princeton Tritium Observatory for Light, Early-Universe, Massive-Neutrino Yield*, [1307.4738](#).
- [40] PTOLEMY Collaboration, E. Baracchini et al., *PTOLEMY: A Proposal for thermal relic detection of massive neutrinos and directional detection of MeV dark matter*, [1808.01892](#).
- [41] R. A. Alpher, H. Bethe and G. Gamow, *The origin of chemical elements*, *Phys. Rev.* **73** (1948) 803.

- [42] R. A. Alpher and R. C. Herman, *Theory of the origin and relative abundance distribution of the elements*, *Rev. Mod. Phys.* **22** (1950) 153.
- [43] G. Steigman, *Primordial nucleosynthesis in the precision cosmology era*, *Ann. Rev. Nucl. Part. Sci.* **57** (2007) 463 [0712.1100].
- [44] F. Iocco, G. Mangano, G. Miele, O. Pisanti and P. D. Serpico, *Primordial nucleosynthesis: From precision cosmology to fundamental physics*, *Phys. Rept.* **472** (2009) 1 [0809.0631].
- [45] R. A. Alpher and R. Herman, *Evolution of the universe*, *Nature* **162** (1948) 774.
- [46] R. A. Alpher and R. Herman, *Reflections on early work on big bang cosmology*, *Physics Today* **41N8** (1988) 24.
- [47] PARTICLE DATA GROUP Collaboration, M. Tanabashi et al., *Review of Particle Physics*, *Phys. Rev. D* **98** (2018) 030001. For online version see PDG homepage.
- [48] R. Khatri and R. A. Sunyaev, *Time of primordial ${}^7\text{Be}$ conversion into ${}^7\text{Li}$, energy release and doublet of narrow cosmological neutrino lines*, *Astron. Lett.* **37** (2011) 367 [1009.3932].
- [49] A. V. Ivanchik and V. Yu. Yurchenko, *Relic neutrinos: Antineutrinos of primordial nucleosynthesis*, *Phys. Rev. D* **98** (2018) 081301 [1809.03349].
- [50] D. D. Clayton, *Principles of Stellar Evolution and Nucleosynthesis*. Chicago University Press, 1983.
- [51] R. Kippenhahn, A. Weigert and A. Weiss, *Stellar Structure and Evolution*. Springer, Berlin, 2012, 10.1007/978-3-642-30304-3.
- [52] J. N. Bahcall and R. K. Ulrich, *Solar models, neutrino experiments, and helioseismology*, *Rev. Mod. Phys.* **60** (1988) 297.
- [53] J. N. Bahcall, *Neutrino Astrophysics*. Cambridge University Press, Cambridge (UK), 1989.
- [54] W. C. Haxton, R. G. H. Robertson and A. M. Serenelli, *Solar neutrinos: Status and prospects*, *Ann. Rev. Astron. Astrophys.* **51** (2013) 21 [1208.5723].
- [55] A. Serenelli, *Alive and well: A short review about standard solar models*, *Eur. Phys. J. A* **52** (2016) 78 [1601.07179].
- [56] SUPER-KAMIOKANDE Collaboration, S. Fukuda et al., *Solar ${}^8\text{B}$ and hep neutrino measurements from 1258 days of Super-Kamiokande data*, *Phys. Rev. Lett.* **86** (2001) 5651 [hep-ex/0103032].

- [57] J. N. Bahcall, *Line versus continuum solar neutrinos*, *Phys. Rev. D* **41** (1990) 2964.
- [58] BOREXINO Collaboration, G. Bellini et al., *Final results of Borexino Phase-I on low-energy solar neutrino spectroscopy*, *Phys. Rev. D* **89** (2014) 112007 [[1308.0443](#)].
- [59] BOREXINO Collaboration, M. Agostini et al., *First simultaneous precision spectroscopy of pp , ${}^7\text{Be}$, and pep solar neutrinos with Borexino Phase-II*, [1707.09279](#).
- [60] L. C. Stonehill, J. A. Formaggio and R. G. H. Robertson, *Solar neutrinos from CNO electron capture*, *Phys. Rev. C* **69** (2004) 015801 [[hep-ph/0309266](#)].
- [61] F. L. Villante, *ecCNO solar neutrinos: A challenge for gigantic ultra-pure liquid scintillator detectors*, *Phys. Lett. B* **742** (2015) 279 [[1410.2796](#)].
- [62] N. Vinyoles, A. M. Serenelli, F. L. Villante, S. Basu, J. Bergstrom, M. C. Gonzalez-Garcia, M. Maltoni, C. Pena-Garay and N. Song, *A new Generation of Standard Solar Models*, *Astrophys. J.* **835** (2017) 202 [[1611.09867](#)].
- [63] J. N. Bahcall, *Gallium solar neutrino experiments: Absorption cross-sections, neutrino spectra, and predicted event rates*, *Phys. Rev. C* **56** (1997) 3391 [[hep-ph/9710491](#)].
- [64] J. N. Bahcall, *Central temperature of the sun can be measured via the ${}^7\text{Be}$ solar neutrino line*, *Phys. Rev. Lett.* **71** (1993) 2369 [[hep-ph/9309292](#)].
- [65] J. N. Bahcall, E. Lisi, D. E. Alburger, L. De Braekeleer, S. J. Freedman and J. Napolitano, *Standard neutrino spectrum from ${}^8\text{B}$ decay*, *Phys. Rev. C* **54** (1996) 411 [[nucl-th/9601044](#)].
- [66] W. T. Winter, S. J. Freedman, K. E. Rehm and J. P. Schiffer, *The ${}^8\text{B}$ neutrino spectrum*, *Phys. Rev. C* **73** (2006) 025503 [[nucl-ex/0406019](#)].
- [67] N. Grevesse and A. J. Sauval, *Standard Solar Composition*, *Space Sci. Rev.* **85** (1998) 161.
- [68] M. Asplund, N. Grevesse, A. J. Sauval and P. Scott, *The chemical composition of the Sun*, *Ann. Rev. Astron. Astrophys.* **47** (2009) 481 [[0909.0948](#)].
- [69] J. Bergström, M. C. Gonzalez-Garcia, M. Maltoni, C. Peña-Garay, A. M. Serenelli and N. Song, *Updated determination of the solar neutrino fluxes from solar neutrino data*, *JHEP* **03** (2016) 132 [[1601.00972](#)].
- [70] J. N. Bahcall and A. Ulmer, *Temperature dependence of solar neutrino fluxes*, *Phys. Rev. D* **53** (1996) 4202 [[astro-ph/9602012](#)].

- [71] P. Scott, N. Grevesse, M. Asplund, A. J. Sauval, K. Lind, Y. Takeda, R. Collet, R. Trampedach and W. Hayek, *The elemental composition of the Sun I. The intermediate mass elements Na to Ca*, *Astron. Astrophys.* **573** (2015) A25 [[1405.0279](#)].
- [72] P. Scott, M. Asplund, N. Grevesse, M. Bergemann and A. J. Sauval, *The elemental composition of the Sun II. The iron group elements Sc to Ni*, *Astron. Astrophys.* **573** (2015) A26 [[1405.0287](#)].
- [73] N. Grevesse, P. Scott, M. Asplund and A. J. Sauval, *The elemental composition of the Sun III. The heavy elements Cu to Th*, *Astron. Astrophys.* **573** (2015) A27 [[1405.0288](#)].
- [74] C. A. Iglesias and F. J. Rogers, *Updated OPAL opacities*, *Astrophys. J.* **464** (1996) 943.
- [75] N. R. Badnell, M. A. Bautista, K. Butler, F. Delahaye, C. Mendoza, P. Palmeri, C. J. Zeippen and M. J. Seaton, *Updated opacities from the Opacity Project*, *Mon. Not. Roy. Astron. Soc.* **360** (2005) 458 [[astro-ph/0410744](#)].
- [76] C. Blancard, P. Cossé and G. Faussurier, *Solar mixture opacity calculations using detailed configuration and level accounting treatments*, *Astrophys. J.* **745** (2012) 10.
- [77] G. Mondet, C. Blancard, P. Cossé and G. Faussurier, *Opacity calculations for solar mixtures*, *Astrophys. J. Suppl.* **220** (2015) 2.
- [78] M. Krief, A. Feigel and D. Gazit, *Solar opacity calculations using the super-transition-array method*, *Astrophys. J.* **821** (2016) 45 [[1601.01930](#)].
- [79] J. Colgan, D. P. Kilcrease, N. H. Magee, M. E. Sherrill, J. Abdallah, Jr., P. Hakel, C. J. Fontes, J. A. Guzik and K. A. Mussack, *A new generation of Los Alamos opacity tables*, *Astrophys. J.* **817** (2016) 116 [[1601.01005](#)].
- [80] S. Basu and H. M. Antia, *Seismic measurement of the depth of the solar convection zone*, *Mon. Not. Roy. Astron. Soc.* **287** (1997) 189.
- [81] S. Basu and H. M. Antia, *Constraining solar abundances using helioseismology*, *Astrophys. J.* **606** (2004) L85 [[astro-ph/0403485](#)].
- [82] BOREXINO Collaboration, G. Bellini et al., *Study of solar and other unknown anti-neutrino fluxes with Borexino at LNGS*, *Phys. Lett. B* **696** (2011) 191 [[1010.0029](#)].
- [83] R. A. Malaney, B. S. Meyer and M. N. Butler, *Solar antineutrinos*, *Astrophys. J.* **352** (1990) 767.

- [84] SUPER-KAMIOKANDE Collaboration, A. Renshaw et al., *First indication of terrestrial matter effects on solar neutrino oscillation*, *Phys. Rev. Lett.* **112** (2014) 091805 [[1312.5176](#)].
- [85] SUPER-KAMIOKANDE Collaboration, K. Abe et al., *Solar neutrino measurements in Super-Kamiokande-IV*, *Phys. Rev. D* **94** (2016) 052010 [[1606.07538](#)].
- [86] R. Davis, Jr., D. S. Harmer and K. C. Hoffman, *Search for neutrinos from the Sun*, *Phys. Rev. Lett.* **20** (1968) 1205.
- [87] B. T. Cleveland, T. Daily, R. Davis, Jr., J. R. Distel, K. Lande, C. K. Lee, P. S. Wildenhain and J. Ullman, *Measurement of the solar electron neutrino flux with the Homestake chlorine detector*, *Astrophys. J.* **496** (1998) 505.
- [88] M. Wurm, *Solar neutrino spectroscopy*, *Phys. Rept.* **685** (2017) 1 [[1704.06331](#)].
- [89] KAMIOKANDE-II Collaboration, K. S. Hirata et al., *Observation of ^8B solar neutrinos in the Kamiokande-II detector*, *Phys. Rev. Lett.* **63** (1989) 16.
- [90] KAMIOKANDE Collaboration, Y. Fukuda et al., *Solar neutrino data covering solar cycle 22*, *Phys. Rev. Lett.* **77** (1996) 1683.
- [91] GALLEX Collaboration, W. Hampel et al., *GALLEX solar neutrino observations: Results for GALLEX IV*, *Phys. Lett. B* **447** (1999) 127.
- [92] F. Kaether, W. Hampel, G. Heusser, J. Kiko and T. Kirsten, *Reanalysis of the GALLEX solar neutrino flux and source experiments*, *Phys. Lett. B* **685** (2010) 47 [[1001.2731](#)].
- [93] GNO Collaboration, M. Altmann et al., *Complete results for five years of GNO solar neutrino observations*, *Phys. Lett. B* **616** (2005) 174 [[hep-ex/0504037](#)].
- [94] SAGE Collaboration, J. N. Abdurashitov et al., *Measurement of the solar neutrino capture rate with gallium metal. III: Results for the 2002–2007 data-taking period*, *Phys. Rev. C* **80** (2009) 015807 [[0901.2200](#)].
- [95] A. A. Shikhin, V. N. Gavrin, V. V. Gorbachev, T. V. Ibragimova, A. V. Kalikhov and V. E. Yants, *Registration of ^{71}Ge rare decays in radiochemical gallium experiments SAGE and BEST*, *J. Phys. Conf. Ser.* **798** (2017) 012201.
- [96] C. Giunti and M. Laveder, *Statistical significance of the gallium anomaly*, *Phys. Rev. C* **83** (2011) 065504 [[1006.3244](#)].
- [97] V. Barinov, B. Cleveland, V. Gavrin, D. Gorbunov and T. Ibragimova, *Revised neutrino-gallium cross section and prospects of BEST in resolving the gallium anomaly*, *Phys. Rev. D* **97** (2018) 073001 [[1710.06326](#)].

- [98] H. H. Chen, *Direct approach to resolve the solar-neutrino problem*, *Phys. Rev. Lett.* **55** (1985) 1534.
- [99] SNO Collaboration, B. Aharmim et al., *Low-energy-threshold analysis of the Phase I and Phase II data sets of the Sudbury Neutrino Observatory*, *Phys. Rev. C* **81** (2010) 055504 [[0910.2984](#)].
- [100] KAMLAND Collaboration, S. Abe et al., *Measurement of the ^8B solar neutrino flux with the KamLAND liquid scintillator detector*, *Phys. Rev. C* **84** (2011) 035804 [[1106.0861](#)].
- [101] KAMLAND Collaboration, A. Gando et al., *^7Be solar neutrino measurement with KamLAND*, *Phys. Rev. C* **92** (2015) 055808 [[1405.6190](#)].
- [102] BOREXINO Collaboration, M. Agostini et al., *Comprehensive measurement of pp -chain solar neutrinos*, *Nature* **562** (2018) 505.
- [103] SNO+ Collaboration, S. Andringa et al., *Current status and future prospects of the SNO+ experiment*, *Adv. High Energy Phys.* **2016** (2016) 6194250 [[1508.05759](#)].
- [104] JUNO Collaboration, F. An et al., *Neutrino physics with JUNO*, *J. Phys. G* **43** (2016) 030401 [[1507.05613](#)].
- [105] JINPING Collaboration, J. F. Beacom et al., *Physics prospects of the Jinping neutrino experiment*, *Chin. Phys. C* **41** (2017) 023002 [[1602.01733](#)].
- [106] SNO+ Collaboration, M. Anderson et al., *Measurement of the ^8B solar neutrino flux in SNO+ with very low backgrounds*, *Phys. Rev. D* **99** (2019) 012012 [[1812.03355](#)].
- [107] HYPER-KAMIOKANDE Collaboration, K. Abe et al., *Hyper-Kamiokande Design Report*, [1805.04163](#).
- [108] J. R. Alonso et al., *Advanced scintillator detector concept (ASDC): A concept paper on the physics potential of water-based liquid scintillator*, [1409.5864](#).
- [109] THEIA INTEREST GROUP Collaboration, G. D. Orebi Gann, *Physics potential of an advanced scintillation detector: Introducing THEIA*, [1504.08284](#).
- [110] F. Capozzi, S. W. Li, G. Zhu and J. F. Beacom, *DUNE as the next-generation solar neutrino experiment*, [1808.08232](#).
- [111] B. Dutta and L. E. Strigari, *Neutrino physics with dark matter detectors*, [1901.08876](#).
- [112] D. G. Cerdeño, J. H. Davis, M. Fairbairn and A. C. Vincent, *CNO neutrino Grand Prix: The race to solve the solar metallicity problem*, *JCAP* **1804** (2018) 037 [[1712.06522](#)].

- [113] G. Fiorentini, M. Lissia and F. Mantovani, *Geo-neutrinos and Earth's interior*, *Phys. Rept.* **453** (2007) 117 [0707.3203].
- [114] L. Ludhova and S. Zavatarelli, *Studying the Earth with Geoneutrinos*, *Adv. High Energy Phys.* **2013** (2013) 425693 [1310.3961].
- [115] G. Bellini, A. Ianni, L. Ludhova, F. Mantovani and W. F. McDonough, *Geo-neutrinos*, *Prog. Part. Nucl. Phys.* **73** (2013) 1 [1310.3732].
- [116] S. Dye, *Geo-neutrinos and the Radioactive Power of the Earth*, *Rev. Geophys.* **50** (2012) 3007 [1111.6099].
- [117] KAMLAND Collaboration, A. Gando et al., *Reactor On-Off Antineutrino Measurement with KamLAND*, *Phys. Rev.* **88** (2013) 033001 [1303.4667].
- [118] A. Caminata, S. Davini, L. Di Noto, M. Pallavicini, G. Testera and S. Zavatarelli, *Search for geo-neutrinos and rare nuclear processes with Borexino*, *Int. J. Mod. Phys. A* **33** (2018) 1843009.
- [119] <https://neutrinos.fnal.gov/sources/geoneutrinos/>.
- [120] S. M. Usman, G. R. Jocher, S. T. Dye, W. F. McDonough and J. G. Learned, *AGM2015: Antineutrino Global Map 2015*, *Sci. Rep.* **5** (2015) 13945 [1509.03898].
- [121] W. McDonough and S. s. Sun, *The composition of the earth*, *Chemical Geology* **120** (1995) 223 . Chemical Evolution of the Mantle.
- [122] G. Eder, *Terrestrial neutrinos*, *Nucl. Phys.* **78** (1966) 657.
- [123] G. Marx, *Geophysics by neutrinos*, *Czechoslovak Journal of Physics B* **19** (1969) 1471.
- [124] T. Araki et al., *Experimental investigation of geologically produced antineutrinos with KamLAND*, *Nature* **436** (2005) 499.
- [125] KAMLAND Collaboration, H. Ozaki and J. Shirai, *Refurbishment of KamLAND Outer Detector*, *PoS ICHEP2016* (2017) 1161.
- [126] I. Shimizu, *Kamland: geo-neutrino measurement in japan*, *Annals of Geophysics* **60** (2017) 0113.
- [127] SNO+ Collaboration, E. Arushanova and A. R. Back, *Physics capabilities of the SNO+ experiment*, *J. Phys. Conf. Ser.* **888** (2017) 012245.
- [128] HANO HANO Collaboration, B. Cicenias and N. Solomey, *The HANO HANO Detector and Ongoing Research and Development*, *Phys. Procedia* **37** (2012) 1324.

- [129] C. Giunti and C. W. Kim, *Fundamentals of Neutrino Physics and Astrophysics*. Oxford University Press, 2007.
- [130] X. Qian and J.-C. Peng, *Physics with Reactor Neutrinos*, *Rept. Prog. Phys.* **82** (2019) 036201 [[1801.05386](#)].
- [131] P. Vogel and J. Engel, *Neutrino Electromagnetic Form-Factors*, *Phys. Rev. D* **39** (1989) 3378.
- [132] P. Huber, *On the determination of anti-neutrino spectra from nuclear reactors*, *Phys. Rev. C* **84** (2011) 024617 [[1106.0687](#)]. [Erratum: *Phys. Rev. C* **85**, 029901 (2012)].
- [133] T. A. Mueller et al., *Improved Predictions of Reactor Antineutrino Spectra*, *Phys. Rev. C* **83** (2011) 054615 [[1101.2663](#)].
- [134] P. Vogel and J. F. Beacom, *Angular distribution of neutron inverse beta decay, anti-neutrino(e) + $p \rightarrow e^+ + n$* , *Phys. Rev. D* **60** (1999) 053003 [[hep-ph/9903554](#)].
- [135] H. Furuta et al., *A Study of Reactor Neutrino Monitoring at Experimental Fast Reactor JOYO*, *Nucl. Instrum. Meth. A* **662** (2012) 90 [[1108.2910](#)].
- [136] SUPER-KAMIOKANDE Collaboration, Y. Fukuda et al., *Evidence for oscillation of atmospheric neutrinos*, *Phys. Rev. Lett.* **81** (1998) 1562 [[hep-ex/9807003](#)].
- [137] CHOOZ Collaboration, M. Apollonio et al., *Limits on neutrino oscillations from the CHOOZ experiment*, *Phys. Lett. B* **466** (1999) 415 [[hep-ex/9907037](#)].
- [138] F. Boehm et al., *Final results from the Palo Verde neutrino oscillation experiment*, *Phys. Rev. D* **64** (2001) 112001 [[hep-ex/0107009](#)].
- [139] DOUBLE CHOOZ Collaboration, Y. Abe et al., *Indication of Reactor $\bar{\nu}_e$ Disappearance in the Double Chooz Experiment*, *Phys. Rev. Lett.* **108** (2012) 131801 [[1112.6353](#)].
- [140] DAYA BAY Collaboration, F. P. An et al., *Observation of electron-antineutrino disappearance at Daya Bay*, *Phys. Rev. Lett.* **108** (2012) 171803 [[1203.1669](#)].
- [141] RENO Collaboration, J. K. Ahn et al., *Observation of Reactor Electron Antineutrino Disappearance in the RENO Experiment*, *Phys. Rev. Lett.* **108** (2012) 191802 [[1204.0626](#)].
- [142] G. Mention, M. Fechner, T. Lasserre, T. A. Mueller, D. Lhuillier, M. Cribier and A. Letourneau, *The Reactor Antineutrino Anomaly*, *Phys. Rev. D* **83** (2011) 073006 [[1101.2755](#)].

- [143] J. M. Conrad and M. H. Shaevitz, *Sterile Neutrinos: An Introduction to Experiments*, *Adv. Ser. Direct. High Energy Phys.* **28** (2018) 391 [[1609.07803](#)].
- [144] C. Giunti and T. Lasserre, *eV-scale Sterile Neutrinos*, [1901.08330](#).
- [145] H.-T. Janka, *Explosion mechanisms of core-collapse supernovae*, *Ann. Rev. Nucl. Part. Sci.* **62** (2012) 407 [[1206.2503](#)].
- [146] K. Scholberg, *Supernova neutrino detection*, *Ann. Rev. Nucl. Part. Sci.* **62** (2012) 81 [[1205.6003](#)].
- [147] A. Mirizzi, I. Tamborra, H.-T. Janka, N. Saviano, K. Scholberg, R. Bollig, L. Hüdepohl and S. Chakraborty, *Supernova neutrinos: Production, oscillations and detection*, *Riv. Nuovo Cim.* **39** (2016) 1 [[1508.00785](#)].
- [148] H.-T. Janka, T. Melson and A. Summa, *Physics of core-collapse supernovae in three dimensions: A sneak preview*, *Ann. Rev. Nucl. Part. Sci.* **66** (2016) 341 [[1602.05576](#)].
- [149] G. G. Raffelt, *Stars as Laboratories for Fundamental Physics*. Chicago University Press, USA, 1996.
- [150] KAMIOKANDE-II Collaboration, K. Hirata et al., *Observation of a neutrino burst from the supernova SN1987A*, *Phys. Rev. Lett.* **58** (1987) 1490.
- [151] R. M. Bionta et al., *Observation of a neutrino burst in coincidence with supernova 1987A in the Large Magellanic Cloud*, *Phys. Rev. Lett.* **58** (1987) 1494.
- [152] E. N. Alekseev, L. N. Alekseeva, I. V. Krivosheina and V. I. Volchenko, *Detection of the neutrino signal from SN1987A in the LMC using the INR Baksan underground scintillation telescope*, *Phys. Lett. B* **205** (1988) 209.
- [153] H. A. Bethe and J. R. Wilson, *Revival of a stalled supernova shock by neutrino heating*, *Astrophys. J.* **295** (1985) 14.
- [154] M. Liebendörfer, A. Mezzacappa, O. E. B. Messer, G. Martinez-Pinedo, W. R. Hix and F.-K. Thielemann, *The neutrino signal in stellar core collapse and postbounce evolution*, *Nucl. Phys. A* **719** (2003) 144 [[astro-ph/0211329](#)].
- [155] M. Kachelrieß, R. Tomàs, R. Buras, H.-T. Janka, A. Marek and M. Rampp, *Exploiting the neutronization burst of a galactic supernova*, *Phys. Rev. D* **71** (2005) 063003 [[astro-ph/0412082](#)].
- [156] M. T. Keil, G. G. Raffelt and H.-T. Janka, *Monte Carlo study of supernova neutrino spectra formation*, *Astrophys. J.* **590** (2003) 971 [[astro-ph/0208035](#)].

- [157] I. Tamborra, B. Müller, L. Hüdepohl, H.-T. Janka and G. Raffelt, *High-resolution supernova neutrino spectra represented by a simple fit*, *Phys. Rev. D* **86** (2012) 125031 [[1211.3920](#)].
- [158] E. O'Connor and C. D. Ott, *Black hole formation in failing core-collapse supernovae*, *Astrophys. J.* **730** (2011) 70 [[1010.5550](#)].
- [159] T. Ertl, H.-T. Janka, S. E. Woosley, T. Sukhbold and M. Ugliano, *A two-parameter criterion for classifying the explodability of massive stars by the neutrino-driven mechanism*, *Astrophys. J.* **818** (2016) 124 [[1503.07522](#)].
- [160] T. Sukhbold, T. Ertl, S. E. Woosley, J. M. Brown and H.-T. Janka, *Core-collapse supernovae from 9 to 120 solar masses based on neutrino-powered explosions*, *Astrophys. J.* **821** (2016) 38 [[1510.04643](#)].
- [161] A. M. Hopkins and J. F. Beacom, *On the normalisation of the cosmic star formation history*, *Astrophys. J.* **651** (2006) 142 [[astro-ph/0601463](#)].
- [162] S. Horiuchi, J. F. Beacom, C. S. Kochanek, J. L. Prieto, K. Z. Stanek and T. A. Thompson, *The cosmic core-collapse supernova rate does not match the massive-star formation rate*, *Astrophys. J.* **738** (2011) 154 [[1102.1977](#)].
- [163] S. J. Smartt, J. J. Eldridge, R. M. Crockett and J. R. Maund, *The death of massive stars — I. Observational constraints on the progenitors of Type II-P supernovae*, *Mon. Not. Roy. Astron. Soc.* **395** (2009) 1409 [[0809.0403](#)].
- [164] Z. G. Jennings, B. F. Williams, J. W. Murphy, J. J. Dalcanton, K. M. Gilbert, A. E. Dolphin, D. R. Weisz and M. Fouesneau, *The supernova progenitor mass distributions of M31 and M33: Further evidence for an upper mass limit*, *Astrophys. J.* **795** (2014) 170 [[1410.0018](#)].
- [165] C. S. Kochanek, *Constraints on core collapse from the black hole mass function*, *Mon. Not. Roy. Astron. Soc.* **446** (2015) 1213 [[1407.5622](#)].
- [166] S. M. Adams, C. S. Kochanek, J. R. Gerke and K. Z. Stanek, *The search for failed supernovae with the Large Binocular Telescope: constraints from 7 yr of data*, *Mon. Not. Roy. Astron. Soc.* **469** (2017) 1445 [[1610.02402](#)].
- [167] S. Chakraborty, R. Hansen, I. Izaguirre and G. Raffelt, *Collective neutrino flavor conversion: Recent developments*, *Nucl. Phys. B* **908** (2016) 366 [[1602.02766](#)].
- [168] R. F. Sawyer, *Neutrino cloud instabilities just above the neutrino sphere of a supernova*, *Phys. Rev. Lett.* **116** (2016) 081101 [[1509.03323](#)].
- [169] I. Izaguirre, G. Raffelt and I. Tamborra, *Fast pairwise conversion of supernova neutrinos: A dispersion-relation approach*, *Phys. Rev. Lett.* **118** (2017) 021101 [[1610.01612](#)].

- [170] A. S. Dighe and A. Yu. Smirnov, *Identifying the neutrino mass spectrum from the neutrino burst from a supernova*, *Phys. Rev. D* **62** (2000) 033007 [[hep-ph/9907423](#)].
- [171] K. Scholberg, *Supernova signatures of neutrino mass ordering*, *J. Phys. G* **45** (2018) 014002 [[1707.06384](#)].
- [172] G. S. Bisnovatyi-Kogan and Z. F. Seidov, *Medium-energy neutrinos in the universe*, *Sov. Astron.* **26** (1982) 132. Translated from: *Astron. Zh.* **59** (1982) 213–223. For online version see [ADS Entry](#).
- [173] L. M. Krauss, S. L. Glashow and D. N. Schramm, *Antineutrino astronomy and geophysics*, *Nature* **310** (1984) 191.
- [174] G. V. Domogatskii, *The isotropic electron antineutrino flux — a clue to the rate of stellar gravitational collapse in the universe*, *Sov. Astron.* **28** (1984) 30. Translated from *Astron. Zh.* **61** (1984) 51–52.
- [175] S. Ando and K. Sato, *Relic neutrino background from cosmological supernovae*, *New J. Phys.* **6** (2004) 170 [[astro-ph/0410061](#)].
- [176] J. F. Beacom, *The diffuse supernova neutrino background*, *Ann. Rev. Nucl. Part. Sci.* **60** (2010) 439 [[1004.3311](#)].
- [177] C. Lunardini, *Diffuse supernova neutrinos at underground laboratories*, *Astropart. Phys.* **79** (2016) 49 [[1007.3252](#)].
- [178] H. Dole, G. Lagache, J.-L. Puget, K. I. Caputi, N. Fernández-Conde, E. Le Floch, C. Papovich, P. G. Pérez-González, G. H. Rieke and M. Blaylock, *The cosmic infrared background resolved by Spitzer. Contributions of mid-infrared galaxies to the far-infrared background*, *Astron. Astrophys.* **451** (2006) 417 [[astro-ph/0603208](#)].
- [179] E. Cappellaro, R. Evans and M. Turatto, *A new determination of supernova rates and a comparison with indicators for galactic star formation*, *Astron. Astrophys.* **351** (1999) 459 [[astro-ph/9904225](#)].
- [180] E. Cappellaro and M. Turatto, *Supernova types and rates*, *Astrophys. Space Sci. Libr.* **264** (2001) 199 [[astro-ph/0012455](#)].
- [181] E. E. Salpeter, *The luminosity function and stellar evolution*, *Astrophys. J.* **121** (1955) 161.
- [182] H. Yüksel, M. D. Kistler, J. F. Beacom and A. M. Hopkins, *Revealing the high-redshift star formation rate with gamma-ray bursts*, *Astrophys. J.* **683** (2008) L5 [[0804.4008](#)].

- [183] G. J. Mathews, J. Hidaka, T. Kajino and J. Suzuki, *Supernova relic neutrinos and the supernova rate problem: Analysis of uncertainties and detectability of ONeMg and failed supernovae*, *Astrophys. J.* **790** (2014) 115 [[1405.0458](#)].
- [184] B. E. Robertson, R. S. Ellis, S. R. Furlanetto and J. S. Dunlop, *Cosmic Reionization and Early Star-forming Galaxies: a Joint Analysis of new Constraints From Planck and the Hubble Space Telescope*, *Astrophys. J.* **802** (2015) L19 [[1502.02024](#)].
- [185] P. Madau and M. Dickinson, *Cosmic star formation history*, *Ann. Rev. Astron. Astrophys.* **52** (2014) 415 [[1403.0007](#)].
- [186] SUPER-KAMIOKANDE Collaboration, K. Bays et al., *Supernova relic neutrino search at Super-Kamiokande*, *Phys. Rev. D* **85** (2012) 052007 [[1111.5031](#)].
- [187] SUPER-KAMIOKANDE Collaboration, H. Zhang et al., *Supernova relic Neutrino search with neutron tagging at Super-Kamiokande-IV*, *Astropart. Phys.* **60** (2015) 41 [[1311.3738](#)].
- [188] KAMLAND Collaboration, A. Gando et al., *A study of extraterrestrial antineutrino sources with the KamLAND detector*, *Astrophys. J.* **745** (2012) 193 [[1105.3516](#)].
- [189] J. F. Beacom and M. R. Vagins, *GADZOOKS! Anti-neutrino spectroscopy with large water Cherenkov detectors*, *Phys. Rev. Lett.* **93** (2004) 171101 [[hep-ph/0309300](#)].
- [190] SUPER-KAMIOKANDE Collaboration, L. Labarga, *The SuperK-gadolinium project*, *PoS EPS-HEP2017* (2018) 118.
- [191] A. G. Cocco, A. Ereditato, G. Fiorillo, G. Mangano and V. Pettorino, *Supernova relic neutrinos in liquid argon detectors*, *JCAP* **0412** (2004) 002 [[hep-ph/0408031](#)].
- [192] DUNE Collaboration, R. Acciarri et al., *Long-Baseline Neutrino Facility (LBNF) and Deep Underground Neutrino Experiment (DUNE). Conceptual Design Report. Volume 4: The DUNE detectors at LBNF*, [1601.02984](#).
- [193] T. Stanev, *High energy cosmic rays*. Springer, 2004.
- [194] C. Grupen, *Astroparticle physics*. Springer, 2005.
- [195] T. K. Gaisser, R. Engel and E. Resconi, *Cosmic Rays and Particle Physics*. Cambridge University Press, 2016.
- [196] E. Vitagliano, *High energy events in IceCube: models and theory*, M.Sc. thesis, University of Naples, 2015.

- [197] K. C. Y. Ng, J. F. Beacom, A. H. G. Peter and C. Rott, *Solar Atmospheric Neutrinos: A New Neutrino Floor for Dark Matter Searches*, *Phys. Rev. D* **96** (2017) 103006 [[1703.10280](#)].
- [198] M. Casse, P. Goret and C. J. Cesarsky, *Atomic Properties of the Elements and Cosmic Ray Composition at the Source*, in *14th International Cosmic Ray Conference (ICRC 1975) Munich, Germany, August 15-29, 1975*, pp. 646–651, 1975.
- [199] R. Enberg, M. H. Reno and I. Sarcevic, *Prompt neutrino fluxes from atmospheric charm*, *Phys. Rev. D* **78** (2008) 043005 [[0806.0418](#)].
- [200] ICECUBE Collaboration, M. G. Aartsen et al., *Atmospheric and astrophysical neutrinos above 1 TeV interacting in IceCube*, *Phys. Rev. D* **91** (2015) 022001 [[1410.1749](#)].
- [201] ICECUBE Collaboration, M. G. Aartsen et al., *Observation and Characterization of a Cosmic Muon Neutrino Flux from the Northern Hemisphere using six years of IceCube data*, *Astrophys. J.* **833** (2016) 3 [[1607.08006](#)].
- [202] A. Bhattacharya, R. Enberg, Y. S. Jeong, C. S. Kim, M. H. Reno, I. Sarcevic and A. Stasto, *Prompt atmospheric neutrino fluxes: perturbative QCD models and nuclear effects*, *JHEP* **11** (2016) 167 [[1607.00193](#)].
- [203] SUPER-KAMIOKANDE Collaboration, E. Richard et al., *Measurements of the atmospheric neutrino flux by Super-Kamiokande: energy spectra, geomagnetic effects, and solar modulation*, *Phys. Rev. D* **94** (2016) 052001 [[1510.08127](#)].
- [204] ICECUBE Collaboration, M. G. Aartsen et al., *Development of a General Analysis and Unfolding Scheme and its Application to Measure the Energy Spectrum of Atmospheric Neutrinos with IceCube*, *Eur. Phys. J. C* **75** (2015) 116 [[1409.4535](#)].
- [205] ICECUBE Collaboration, M. G. Aartsen et al., *Measurement of the Atmospheric ν_e Spectrum with IceCube*, *Phys. Rev. D* **91** (2015) 122004 [[1504.03753](#)].
- [206] M. Honda, M. Sajjad Athar, T. Kajita, K. Kasahara and S. Midorikawa, *Atmospheric neutrino flux calculation using the NRLMSISE-00 atmospheric model*, *Phys. Rev. D* **92** (2015) 023004 [[1502.03916](#)].
- [207] ICECUBE Collaboration, A. Achterberg et al., *First Year Performance of The IceCube Neutrino Telescope*, *Astropart. Phys.* **26** (2006) 155 [[astro-ph/0604450](#)].
- [208] A. Fedynitch, J. Becker Tjus and P. Desiati, *Influence of hadronic interaction models and the cosmic ray spectrum on the high energy atmospheric muon and neutrino flux*, *Phys. Rev. D* **86** (2012) 114024 [[1206.6710](#)].

- [209] J. Edsjo, J. Elevant, R. Enberg and C. Niblaeus, *Neutrinos from cosmic ray interactions in the Sun*, *JCAP* **1706** (2017) 033 [[1704.02892](#)].
- [210] C. A. Argüelles, G. de Wasseige, A. Fedynitch and B. J. P. Jones, *Solar Atmospheric Neutrinos and the Sensitivity Floor for Solar Dark Matter Annihilation Searches*, *JCAP* **1707** (2017) 024 [[1703.07798](#)].
- [211] G. Ingelman and M. Thunman, *High-energy neutrino production by cosmic ray interactions in the sun*, *Phys. Rev. D* **54** (1996) 4385 [[hep-ph/9604288](#)].
- [212] D. Seckel, T. Stanev and T. K. Gaisser, *Signatures of cosmic-ray interactions on the solar surface*, *Astrophys. J.* **382** (1991) 652.
- [213] A. R. Bell, *The Acceleration of cosmic rays in shock fronts. I*, *Mon. Not. Roy. Astron. Soc.* **182** (1978) 147.
- [214] A. Spitkovsky, *Particle acceleration in relativistic collisionless shocks: Fermi process at last?*, *Astrophys. J.* **682** (2008) L5 [[0802.3216](#)].
- [215] F. M. Rieger, V. Bosch-Ramon and P. Duffy, *Fermi acceleration in astrophysical jets*, *Astrophys. Space Sci.* **309** (2007) 119 [[astro-ph/0610141](#)].
- [216] K. Murase, D. Guetta and M. Ahlers, *Hidden Cosmic-Ray Accelerators as an Origin of TeV-PeV Cosmic Neutrinos*, *Phys. Rev. Lett.* **116** (2016) 071101 [[1509.00805](#)].
- [217] Y. Farzan and A. Yu. Smirnov, *Coherence and oscillations of cosmic neutrinos*, *Nucl. Phys. B* **805** (2008) 356 [[0803.0495](#)].
- [218] E. Waxman and J. N. Bahcall, *High-energy neutrinos from astrophysical sources: An Upper bound*, *Phys. Rev. D* **59** (1999) 023002 [[hep-ph/9807282](#)].
- [219] J. N. Bahcall and E. Waxman, *High-energy astrophysical neutrinos: The Upper bound is robust*, *Phys. Rev. D* **64** (2001) 023002 [[hep-ph/9902383](#)].
- [220] ICECUBE Collaboration, M. G. Aartsen et al., *First observation of PeV-energy neutrinos with IceCube*, *Phys. Rev. Lett.* **111** (2013) 021103 [[1304.5356](#)].
- [221] ICECUBE Collaboration, M. G. Aartsen et al., *Evidence for High-Energy Extraterrestrial Neutrinos at the IceCube Detector*, *Science* **342** (2013) 1242856 [[1311.5238](#)].
- [222] P. B. Denton, D. Marfatia and T. J. Weiler, *The Galactic Contribution to IceCube's Astrophysical Neutrino Flux*, *JCAP* **1708** (2017) 033 [[1703.09721](#)].
- [223] M. Fornasa and M. A. Sánchez-Conde, *The nature of the Diffuse Gamma-Ray Background*, *Phys. Rept.* **598** (2015) 1 [[1502.02866](#)].
- [224] I. A. Grenier, J. H. Black and A. W. Strong, *The nine lives of cosmic rays in galaxies*, *Annual Review of Astronomy and Astrophysics* **53** (2015) 199.

- [225] M. Ahlers and F. Halzen, *Opening a New Window onto the Universe with IceCube*, *Prog. Part. Nucl. Phys.* **102** (2018) 73 [[1805.11112](#)].
- [226] ICECUBE Collaboration, M. G. Aartsen et al., *IceCube-Gen2: A Vision for the Future of Neutrino Astronomy in Antarctica*, [1412.5106](#).
- [227] KM3NET Collaboration, S. Adrian-Martinez et al., *Letter of intent for KM3NeT 2.0*, *J. Phys. G* **43** (2016) 084001 [[1601.07459](#)].
- [228] K. Fang et al., *The Giant Radio Array for Neutrino Detection (GRAND): Present and Perspectives*, *PoS ICRC2017* (2018) 996 [[1708.05128](#)].
- [229] ARIANNA Collaboration, S. W. Barwick et al., *A First Search for Cosmogenic Neutrinos with the ARIANNA Hexagonal Radio Array*, *Astropart. Phys.* **70** (2015) 12 [[1410.7352](#)].
- [230] P. Allison et al., *Design and Initial Performance of the Askaryan Radio Array Prototype EeV Neutrino Detector at the South Pole*, *Astropart. Phys.* **35** (2012) 457 [[1105.2854](#)].
- [231] A. V. Olinto et al., *POEMMA: Probe Of Extreme Multi-Messenger Astrophysics*, *PoS ICRC2017* (2018) 542 [[1708.07599](#)].
- [232] FERMI-LAT Collaboration, M. Ackermann et al., *Resolving the Extragalactic γ -Ray Background above 50 GeV with the Fermi Large Area Telescope*, *Phys. Rev. Lett.* **116** (2016) 151105 [[1511.00693](#)].
- [233] ICECUBE Collaboration, M. G. Aartsen et al., *Neutrino emission from the direction of the blazar TXS 0506+056 prior to the IceCube-170922A alert*, *Science* **361** (2018) 147 [[1807.08794](#)].
- [234] LIVERPOOL TELESCOPE, MAGIC, H.E.S.S., AGILE, KISO, VLA/17B-403, INTEGRAL, KAPTEYN, SUBARU, HAWC, FERMI-LAT, ASAS-SN, VERITAS, KANATA, ICECUBE, SWIFT NUSTAR Collaboration, M. G. Aartsen et al., *Multimessenger observations of a flaring blazar coincident with high-energy neutrino IceCube-170922A*, *Science* **361** (2018) eaat1378 [[1807.08816](#)].
- [235] K. Murase and E. Waxman, *Constraining High-Energy Cosmic Neutrino Sources: Implications and Prospects*, *Phys. Rev. D* **94** (2016) 103006 [[1607.01601](#)].
- [236] P. Mertsch, M. Rameez and I. Tamborra, *Detection prospects for high energy neutrino sources from the anisotropic matter distribution in the local universe*, *JCAP* **1703** (2017) 011 [[1612.07311](#)].
- [237] M. Ahlers, K. Helbing and C. Perez de los Heros, *Probing Particle Physics with IceCube*, *Eur. Phys. J. C* **78** (2018) 924 [[1806.05696](#)].

- [238] P. Meszaros, *Gamma Ray Bursts as Neutrino Sources*, in *Neutrino astronomy*, pp. 1–14. 2017.
- [239] E. Waxman, *The Origin of IceCube’s Neutrinos: Cosmic Ray Accelerators Embedded in Star Forming Calorimeters*, in *Neutrino astronomy*, pp. 33–45. 2017.
- [240] K. Murase, *Active Galactic Nuclei as High-Energy Neutrino Sources*, in *Neutrino astronomy*, pp. 15–31. 2017.
- [241] A. Loeb and E. Waxman, *The Cumulative background of high energy neutrinos from starburst galaxies*, *JCAP* **0605** (2006) 003 [[astro-ph/0601695](#)].
- [242] C. Gruppioni et al., *The Herschel PEP/HerMES Luminosity Function. I: Probing the Evolution of PACS selected Galaxies to z 4*, *Mon. Not. Roy. Astron. Soc.* **432** (2013) 23 [[1302.5209](#)].
- [243] I. Tamborra, S. Ando and K. Murase, *Star-forming galaxies as the origin of diffuse high-energy backgrounds: Gamma-ray and neutrino connections, and implications for starburst history*, *JCAP* **1409** (2014) 043 [[1404.1189](#)].
- [244] K. Bechtol, M. Ahlers, M. Di Mauro, M. Ajello and J. Vandenbroucke, *Evidence against star-forming galaxies as the dominant source of IceCube neutrinos*, *Astrophys. J.* **836** (2017) 47 [[1511.00688](#)].
- [245] ICECUBE Collaboration, M. G. Aartsen et al., *A combined maximum-likelihood analysis of the high-energy astrophysical neutrino flux measured with IceCube*, *Astrophys. J.* **809** (2015) 98 [[1507.03991](#)].
- [246] ICECUBE Collaboration, M. G. Aartsen et al., *The IceCube Neutrino Observatory - Contributions to ICRC 2017 Part II: Properties of the Atmospheric and Astrophysical Neutrino Flux*, [1710.01191](#).
- [247] S. Ando, I. Tamborra and F. Zandanel, *Tomographic Constraints on High-Energy Neutrinos of Hadronuclear Origin*, *Phys. Rev. Lett.* **115** (2015) 221101 [[1509.02444](#)].
- [248] M. R. Feyereisen, I. Tamborra and S. Ando, *One-point fluctuation analysis of the high-energy neutrino sky*, *JCAP* **1703** (2017) 057 [[1610.01607](#)].
- [249] P. Meszaros, *Gamma-Ray Bursts*, *Rept. Prog. Phys.* **69** (2006) 2259 [[astro-ph/0605208](#)].
- [250] D. Guetta, D. Hooper, J. Alvarez-Muniz, F. Halzen and E. Reuveni, *Neutrinos from individual gamma-ray bursts in the BATSE catalog*, *Astropart. Phys.* **20** (2004) 429 [[astro-ph/0302524](#)].
- [251] I. Tamborra and S. Ando, *Diffuse emission of high-energy neutrinos from gamma-ray burst fireballs*, *JCAP* **1509** (2015) 036 [[1504.00107](#)].

- [252] P. B. Denton and I. Tamborra, *The Bright and Choked Gamma-Ray Burst Contribution to the IceCube and ANTARES Low-Energy Excess*, *JCAP* **1804** (2018) 058 [[1802.10098](#)].
- [253] P. B. Denton and I. Tamborra, *Exploring the Properties of Choked Gamma-ray Bursts with IceCube's High-energy Neutrinos*, *Astrophys. J.* **855** (2018) 37 [[1711.00470](#)].
- [254] L.-G. Strolger, T. Dahlen, S. A. Rodney, O. Graur, A. G. Riess, C. McCully, S. Ravindranath, B. Mobasher and A. K. Shahady, *The Rate of Core Collapse Supernovae to Redshift 2.5 From The CANDELS and CLASH Supernova Surveys*, *Astrophys. J.* **813** (2015) 93 [[1509.06574](#)].
- [255] K. Fang and B. D. Metzger, *High-Energy Neutrinos from Millisecond Magnetars formed from the Merger of Binary Neutron Stars*, *Astrophys. J.* **849** (2017) 153.
- [256] P. Padovani et al., *Active galactic nuclei: what's in a name?*, *Astron. Astrophys. Rev.* **25** (2017) 2 [[1707.07134](#)].
- [257] M. Petropoulou, S. Dimitrakoudis, P. Padovani, A. Mastichiadis and E. Resconi, *Photohadronic origin of γ -ray BL Lac emission: implications for IceCube neutrinos*, *Mon. Not. Roy. Astron. Soc.* **448** (2015) 2412 [[1501.07115](#)].
- [258] G. Ghisellini, C. Righi, L. Costamante and F. Tavecchio, *The Fermi blazar sequence*, *Mon. Not. Roy. Astron. Soc.* **469** (2017) 255 [[1702.02571](#)].
- [259] M. Ajello et al., *The Cosmic Evolution of Fermi BL Lacertae Objects*, *Astrophys. J.* **780** (2014) 73 [[1310.0006](#)].
- [260] M. Ajello et al., *The Luminosity Function of Fermi-detected Flat-Spectrum Radio Quasars*, *Astrophys. J.* **751** (2012) 108 [[1110.3787](#)].
- [261] A. Palladino, X. Rodrigues, S. Gao and W. Winter, *Interpretation of the diffuse astrophysical neutrino flux in terms of the blazar sequence*, *Astrophys. J.* **871** (2019) 41 [[1806.04769](#)].
- [262] P. Padovani, M. Petropoulou, P. Giommi and E. Resconi, *A simplified view of blazars: the neutrino background*, *Mon. Not. Roy. Astron. Soc.* **452** (2015) 1877 [[1506.09135](#)].
- [263] A. Palladino and W. Winter, *A multi-component model for observed astrophysical neutrinos*, *Astron. Astrophys.* **615** (2018) A168 [[1801.07277](#)].
- [264] L. A. Anchordoqui, *Ultra-High-Energy Cosmic Rays*, *Phys. Rep.* **801** (2019) 1 [[1807.09645](#)].

- [265] PIERRE AUGER Collaboration, A. Aab et al., *Depth of maximum of air-shower profiles at the Pierre Auger Observatory. II. Composition implications*, *Phys. Rev. D* **90** (2014) 122006 [[1409.5083](#)].
- [266] TELESCOPE ARRAY Collaboration, R. U. Abbasi et al., *Mass composition of ultrahigh-energy cosmic rays with the Telescope Array Surface Detector data*, *Phys. Rev. D* **99** (2019) 022002 [[1808.03680](#)].
- [267] R. Aloisio, D. Boncioli, A. di Matteo, A. F. Grillo, S. Petrera and F. Salamida, *Cosmogenic neutrinos and ultra-high energy cosmic ray models*, *JCAP* **1510** (2015) 006 [[1505.04020](#)].
- [268] R. Alves Batista, R. M. de Almeida, B. Lago and K. Kotera, *Cosmogenic photon and neutrino fluxes in the Auger era*, *JCAP* **1901** (2019) 002 [[1806.10879](#)].
- [269] M. Ahlers and F. Halzen, *Minimal Cosmogenic Neutrinos*, *Phys. Rev. D* **86** (2012) 083010 [[1208.4181](#)].
- [270] ICECUBE Collaboration, M. G. Aartsen et al., *Constraints on Ultrahigh-Energy Cosmic-Ray Sources from a Search for Neutrinos above 10 PeV with IceCube*, *Phys. Rev. Lett.* **117** (2016) 241101 [[1607.05886](#)].
[Erratum: *Phys. Rev. Lett.* 119, no.25, 259902 (2017)].
- [271] K. Møller, P. B. Denton and I. Tamborra, *Cosmogenic Neutrinos Through the GRAND Lens Unveil the Nature of Cosmic Accelerators*, *JCAP* **1905** (2019) 047 [[1809.04866](#)].
- [272] M. Ackermann et al., *Astrophysics Uniquely Enabled by Observations of High-Energy Cosmic Neutrinos*, [1903.04334](#).
- [273] E. Vitagliano, J. Redondo and G. Raffelt, *Solar neutrino flux at keV energies*, *JCAP* **1712** (2017) 010 [[1708.02248](#)].
- [274] N. Itoh, H. Hayashi, A. Nishikawa and Y. Kohyama, *Neutrino energy loss in stellar interiors. VII. Pair, photo-, plasma, bremsstrahlung, and recombination neutrino processes*, *Astrophys. J.* **102** (1996) 411.
- [275] W. C. Haxton and W. Lin, *The very low-energy solar flux of electron and heavy flavor neutrinos and antineutrinos*, *Phys. Lett. B* **486** (2000) 263 [[nucl-th/0006055](#)].
- [276] M. Pospelov, A. Ritz and M. B. Voloshin, *Bosonic super-WIMPs as keV-scale dark matter*, *Phys. Rev. D* **78** (2008) 115012 [[0807.3279](#)].
- [277] A. Derevianko, V. A. Dzuba, V. V. Flambaum and M. Pospelov, *Axio-electric effect*, *Phys. Rev. D* **82** (2010) 065006 [[1007.1833](#)].

- [278] H. An, M. Pospelov and J. Pradler, *New stellar constraints on dark photons*, *Phys. Lett. B* **725** (2013) 190 [[1302.3884](#)].
- [279] J. Redondo and G. Raffelt, *Solar constraints on hidden photons re-visited*, *JCAP* **1308** (2013) 034 [[1305.2920](#)].
- [280] J. Redondo, *Solar axion flux from the axion-electron coupling*, *JCAP* **1312** (2013) 008 [[1310.0823](#)].
- [281] E. Hardy and R. Lasenby, *Stellar cooling bounds on new light particles: plasma mixing effects*, *JHEP* **02** (2017) 033 [[1611.05852](#)].
- [282] C. J. Horowitz, *Weak magnetism for anti-neutrinos in supernovae*, *Phys. Rev. D* **65** (2002) 043001 [[astro-ph/0109209](#)].
- [283] M. Drewes et al., *A White Paper on keV Sterile Neutrino Dark Matter*, *JCAP* **1701** (2017) 025 [[1602.04816](#)].
- [284] T. Lasserre, K. Altenmueller, M. Cribier, A. Merle, S. Mertens and M. Vivier, *Direct Search for keV Sterile Neutrino Dark Matter with a Stable Dysprosium Target*, [1609.04671](#).
- [285] Y. F. Li and Z.-z. Xing, *Possible Capture of keV Sterile Neutrino Dark Matter on Radioactive β -decaying Nuclei*, *Phys. Lett. B* **695** (2011) 205 [[1009.5870](#)].
- [286] Y. F. Li and Z.-Z. Xing, *Captures of Hot and Warm Sterile Antineutrino Dark Matter on EC-decaying ^{163}Ho Nuclei*, *JCAP* **1108** (2011) 006 [[1104.4000](#)].
- [287] S. Ando and A. Kusenko, *Interactions of keV sterile neutrinos with matter*, *Phys. Rev. D* **81** (2010) 113006 [[1001.5273](#)].
- [288] M. D. Campos and W. Rodejohann, *Testing keV sterile neutrino dark matter in future direct detection experiments*, *Phys. Rev. D* **94** (2016) 095010 [[1605.02918](#)].
- [289] J. B. Adams, M. A. Ruderman and C. H. Woo, *Neutrino Pair Emission by a Stellar Plasma*, *Phys. Rev.* **129** (1963) 1383.
- [290] M. H. Zaidi, *Emission of neutrino-pairs from a stellar plasma*, *Nuovo Cimento A Serie* **40** (1965) 502.
- [291] E. Braaten and D. Segel, *Neutrino energy loss from the plasma process at all temperatures and densities*, *Phys. Rev. D* **48** (1993) 1478 [[hep-ph/9302213](#)].
- [292] M. Haft, G. Raffelt and A. Weiss, *Standard and nonstandard plasma neutrino emission revisited*, *Astrophys. J.* **425** (1994) 222 [[astro-ph/9309014](#)].
[Erratum: *Astrophys. J.* 438, 1017 (1995)].

- [293] S. Ratkovic, S. I. Dutta and M. Prakash, *Differential neutrino rates and emissivities from the plasma process in astrophysical systems*, *Phys. Rev. C* **67** (2003) 123002 [[astro-ph/0303501](#)].
- [294] H.-Y. Chiu and R. C. Stabler, *Emission of Photoneutrinos and Pair Annihilation Neutrinos from Stars*, *Phys. Rev.* **122** (1961) 1317.
- [295] V. Petrosian, G. Beaudet and E. E. Salpeter, *Photoneutrino Energy Loss Rates*, *Phys. Rev.* **154** (1967) 1445.
- [296] V. I. Ritus, *Photoproduction of neutrinos of electrons and the neutrino radiation from stars*, *Sov. Phys. JETP* **14** (1961) 915.
- [297] S. I. Dutta, S. Ratkovic and M. Prakash, *The photo - neutrino process in astrophysical systems*, *Phys. Rev. D* **69** (2004) 023005 [[astro-ph/0309564](#)].
- [298] G. G. Raffelt, *Plasmon Decay Into Low Mass Bosons in Stars*, *Phys. Rev. D* **37** (1988) 1356.
- [299] D. B. Boercker, *Collective effects on Thomson scattering in the solar interior*, *Astrophys. J.* **316** (1987) L95.
- [300] P. Cazzola, G. De Zotti and A. Saggion, *Electron-nucleus neutrino bremsstrahlung*, *Phys. Rev. D* **3** (1971) 1722.
- [301] D. A. Dicus, E. W. Kolb, D. N. Schramm and D. L. Tubbs, *Neutrino Pair Bremsstrahlung Including Neutral Current Effects*, *Astrophys. J.* **210** (1976) 481.
- [302] G. M. Gandelman and V. S. Pinaev, *Emission of neutrino pairs by electrons and the role played by it in stars*, *Zh. Eksp. Teor. Fiz.* **37** (1960) 1072.
- [303] G. Guo and Y.-Z. Qian, *Spectra and rates of bremsstrahlung neutrino emission in stars*, *Phys. Rev. D* **94** (2016) 043005 [[1608.02852](#)].
- [304] G. G. Raffelt, *Astrophysical axion bounds diminished by screening effects*, *Phys. Rev. D* **33** (1986) 897.
- [305] L. M. Krauss, J. E. Moody and F. Wilczek, *A stellar energy loss mechanism involving axions*, *Phys. Lett. B* **144** (1984) 391.
- [306] A. Sommerfeld, *Über die Beugung und Bremsung der Elektronen*, *Annalen Phys.* **403** (1931) 257.
- [307] N. Arkani-Hamed, D. P. Finkbeiner, T. R. Slatyer and N. Weiner, *A Theory of Dark Matter*, *Phys. Rev. D* **79** (2009) 015014 [[0810.0713](#)].
- [308] W. J. Karzas and R. Latter, *Electron Radiative Transitions in a Coulomb Field.*, *Astrophys. J. Suppl.* **6** (1961) 167.

- [309] G. Elwert, *Verschärfte Berechnung von Intensität und Polarisierung im kontinuierlichen Röntgenspektrum*, *Annalen Phys.* **426** (1939) 178.
- [310] L. Funcke, G. Raffelt and E. Vitagliano, *Distinguishing Dirac and Majorana neutrinos by their gravi-majoron decays*, [1905.01264](#).
- [311] G. Dvali and L. Funcke, *Small neutrino masses from gravitational θ -term*, *Phys. Rev. D* **93** (2016) 113002 [[1602.03191](#)].
- [312] G. Dvali, *Three-form gauging of axion symmetries and gravity*, [hep-th/0507215](#).
- [313] G. Dvali, S. Folkerts and A. Franca, *How neutrino protects the axion*, *Phys. Rev. D* **89** (2014) 105025 [[1312.7273](#)].
- [314] Y. Chikashige, R. Mohapatra and R. Peccei, *Are there real goldstone bosons associated with broken lepton number?*, *Phys. Lett. B* **98** (1981) 265.
- [315] G. Dvali and L. Funcke, *Domestic Axion*, [1608.08969](#).
- [316] G. Drexlin, V. Hannen, S. Mertens and C. Weinheimer, *Current direct neutrino mass experiments*, *Adv. High Energy Phys.* **2013** (2013) 1 [[1307.0101](#)].
- [317] M. J. Dolinski, A. W. P. Poon and W. Rodejohann, *Neutrinoless Double-Beta Decay: Status and Prospects*, Submitted to: *Ann. Rev. Nucl. Part. Phys.* (2019) [[1902.04097](#)].
- [318] A. B. Balantekin and B. Kayser, *On the properties of neutrinos*, *Ann. Rev. Nucl. Part. Sci.* **68** (2018) 313 [[1805.00922](#)].
- [319] A. B. Balantekin, A. de Gouvêa and B. Kayser, *Addressing the Majorana vs. Dirac question with neutrino decays*, *Phys. Lett. B* **789** (2019) 488 [[1808.10518](#)].
- [320] S. Gariazzo, C. Giunti, M. Laveder, Y. F. Li and E. M. Zavanin, *Light sterile neutrinos*, *J. Phys. G* **43** (2016) 033001 [[1507.08204](#)].
- [321] M. Drewes et al., *A White Paper on keV sterile neutrino dark matter*, *JCAP* **1701** (2017) 025 [[1602.04816](#)].
- [322] C. S. Lorenz, L. Funcke, E. Calabrese and S. Hannestad, *Time-varying neutrino mass from a supercooled phase transition: current cosmological constraints and impact on the Ω_m - σ_8 plane*, *Phys. Rev. D* **99** (2019) 023501 [[1811.01991](#)].
- [323] I. Girardi, A. Meroni and S. T. Petcov, *Neutrinoless double beta decay in the presence of light sterile neutrinos*, *JHEP* **1311** (2013) 146 [[1308.5802](#)].

- [324] A. de Gouvêa, *See-saw energy scale and the LSND anomaly*, *Phys. Rev. D* **72** (2005) 033005 [[hep-ph/0501039](#)].
- [325] J. F. Beacom, N. F. Bell and S. Dodelson, *Neutrinoless universe*, *Phys. Rev. Lett.* **93** (2004) 121302 [[astro-ph/0404585](#)].
- [326] A. J. Cuesta, V. Niro and L. Verde, *Neutrino mass limits: robust information from the power spectrum of galaxy surveys*, *Phys. Dark Univ.* **13** (2016) 77 [[1511.05983](#)].
- [327] S. Hannestad, *Structure formation with strongly interacting neutrinos — Implications for the cosmological neutrino mass bound*, *JCAP* **0502** (2005) 11 [[astro-ph/0411475](#)].
- [328] B. Follin, L. Knox, M. Millea and Z. Pan, *First detection of the acoustic oscillation phase shift expected from the cosmic neutrino background*, *Phys. Rev. Lett.* **115** (2015) 091301 [[1503.07863](#)].
- [329] L. Lancaster, F.-Y. Cyr-Racine, L. Knox and Z. Pan, *A tale of two modes: neutrino free-streaming in the early universe*, *JCAP* **1707** (2017) 033 [[1704.06657](#)].
- [330] I. M. Oldengott, T. Tram, C. Rampf and Y. Y. Y. Wong, *Interacting neutrinos in cosmology: exact description and constraints*, *JCAP* **1711** (2017) 027 [[1706.02123](#)].
- [331] C. D. Kreisch, F.-Y. Cyr-Racine and O. Doré, *The neutrino puzzle: anomalies, interactions, and cosmological tensions*, [1902.00534](#).
- [332] CAST Collaboration, V. Anastassopoulos et al., *New CAST limit on the axion-photon interaction*, *Nature Phys.* **13** (2017) 584 [[1705.02290](#)].
- [333] NEMO-3 Collaboration, R. Arnold et al., *Measurement of the $2\nu\beta\beta$ decay half-life of ^{150}Nd and a search for $0\nu\beta\beta$ decay processes with the full exposure from the NEMO-3 detector*, *Phys. Rev. D* **94** (2016) 072003 [[1606.08494](#)].
- [334] P. S. Pasquini and O. L. G. Peres, *Bounds on neutrino-scalar Yukawa coupling*, *Phys. Rev. D* **93** (2016) 053007 [[1511.01811](#)]. Erratum: *Phys. Rev. D* **93** (2016) 079902.
- [335] J. Gluza and M. Zralek, *Feynman rules for Majorana neutrino interactions*, *Phys. Rev. D* **45** (1992) 1693.
- [336] D. Gorbunov and M. Shaposhnikov, *How to find neutral leptons of the νMSM ?*, *JHEP* **0710** (2007) 015 [[0705.1729](#)]. Erratum: *JHEP* **1311** (2013) 101.
- [337] C. W. Kim and W. P. Lam, *Some remarks on neutrino decay via a Nambu-Goldstone boson*, *Mod. Phys. Lett. A* **5** (1990) 297.

- [338] J. F. Beacom and N. F. Bell, *Do solar neutrinos decay?*, *Phys. Rev. D* **65** (2002) 113009 [[hep-ph/0204111](#)].
- [339] A. Millar, G. Raffelt, L. Stodolsky and E. Vitagliano, *Neutrino mass from bremsstrahlung endpoint in coherent scattering on nuclei*, *Phys. Rev. D* **98** (2018) 123006 [[1810.06584](#)].
- [340] M. Lindner, T. Ohlsson and W. Winter, *A combined treatment of neutrino decay and neutrino oscillations*, *Nucl. Phys. B* **607** (2001) 326 [[hep-ph/0103170](#)].
- [341] Z. Moss, M. H. Moulai, C. A. Argüelles and J. M. Conrad, *Exploring a nonminimal sterile neutrino model involving decay at IceCube*, *Phys. Rev. D* **97** (2018) 055017 [[1711.05921](#)].
- [342] PARTICLE DATA GROUP Collaboration, M. Tanabashi et al., *Review of Particle Physics*, *Phys. Rev. D* **98** (2018) 030001.
- [343] R. A. Malaney, B. S. Meyer and M. N. Butler, *Solar antineutrinos*, *Astrophys. J.* **352** (1990) 767.
- [344] F. Mantovani, L. Carmignani, G. Fiorentini and M. Lissia, *Anti-neutrinos from the Earth: The Reference model and its uncertainties*, *Phys. Rev. D* **69** (2004) 013001 [[hep-ph/0309013](#)].
- [345] E. K. Akhmedov and J. Pulido, *Solar neutrino oscillations and bounds on neutrino magnetic moment and solar magnetic field*, *Phys. Lett. B* **553** (2003) 7 [[hep-ph/0209192](#)].
- [346] M. C. Gonzalez-Garcia and M. Maltoni, *Status of oscillation plus decay of atmospheric and long-baseline neutrinos*, *Phys. Lett. B* **663** (2008) 405 [[0802.3699](#)].
- [347] SNO Collaboration, B. Aharmim et al., *Constraints on Neutrino Lifetime from the Sudbury Neutrino Observatory*, *Phys. Rev. D* **99** (2019) 032013 [[1812.01088](#)].
- [348] R. Picoreti, M. M. Guzzo, P. C. de Holanda and O. L. G. Peres, *Neutrino decay and solar neutrino seasonal effect*, *Phys. Lett. B* **761** (2016) 70 [[1506.08158](#)].
- [349] J. M. Berryman, A. de Gouvêa and D. Hernández, *Solar neutrinos and the decaying neutrino hypothesis*, *Phys. Rev. D* **92** (2015) 073003 [[1411.0308](#)].
- [350] SNO Collaboration, B. Aharmim et al., *Electron antineutrino search at the Sudbury Neutrino Observatory*, *Phys. Rev. D* **70** (2004) 093014 [[hep-ex/0407029](#)].

- [351] KAMLAND Collaboration, K. Eguchi et al., *High sensitivity search for $\bar{\nu}_e$'s from the Sun and other sources at KamLAND*, *Phys. Rev. Lett.* **92** (2004) 071301 [[hep-ex/0310047](#)].
- [352] F. Capozzi, E. Lisi, A. Marrone and A. Palazzo, *Current unknowns in the three neutrino framework*, *Prog. Part. Nucl. Phys.* **102** (2018) 48 [[1804.09678](#)].
- [353] S. Appel, L. Oberauer, G. Raffelt, E. Vitagliano and the Borexino collaboration, *Solar antineutrino fluxes with Borexino at LNGS and neutrino decay*, work in progress.
- [354] S. Hannestad and G. G. Raffelt, *Constraining invisible neutrino decays with the cosmic microwave background*, *Phys. Rev. D* **72** (2005) 103514 [[hep-ph/0509278](#)].
- [355] ICECUBE Collaboration, M. G. Aartsen et al., *Measurements using the inelasticity distribution of multi-TeV neutrino interactions in IceCube*, *Phys. Rev. D* **99** (2019) 032004 [[1808.07629](#)].
- [356] H. Nunokawa, B. Panes and R. Zukanovich Funchal, *How unequal fluxes of high energy astrophysical neutrinos and antineutrinos can fake new physics*, *JCAP* **1610** (2016) 036 [[1604.08595](#)].
- [357] ICECUBE Collaboration, M. G. Aartsen et al., *Observation of high-energy astrophysical neutrinos in three years of IceCube data*, *Phys. Rev. Lett.* **113** (2014) 101101 [[1405.5303](#)].
- [358] G. L. Fogli, E. Lisi, A. Mirizzi and D. Montanino, *Three generation flavor transitions and decays of supernova relic neutrinos*, *Phys. Rev. D* **70** (2004) 013001 [[hep-ph/0401227](#)].
- [359] O. E. Kalashev, A. Kusenko and E. Vitagliano, *Cosmic infrared background excess from axionlike particles and implications for multimessenger observations of blazars*, *Phys. Rev. D* **99** (2019) 023002 [[1808.05613](#)].
- [360] S. Matsuura et al., *New Spectral Evidence of an Unaccounted Component of the Near-infrared Extragalactic Background Light from the CIBER*, *Astrophys. J.* **839** (2017) 7 [[1704.07166](#)].
- [361] H. J. Seo, H. M. Lee, T. Matsumoto, W. S. Jeong, M. G. Lee and J. Pyo, *AKARI Observation of the Sub-degree Scale Fluctuation of the Near-infrared Background*, *Astrophys. J.* **807** (2015) 140 [[1504.05681](#)].
- [362] T. Matsumoto, M. G. Kim, J. Pyo and K. Tsumura, *Reanalysis of the near-infrared extragalactic background light based on the IRTS Observations*, *Astrophys. J.* **807** (2015) 57 [[1501.01359](#)].
- [363] D. J. E. Marsh, *Axion Cosmology*, *Phys. Rept.* **643** (2016) 1 [[1510.07633](#)].

- [364] K. Kohri, T. Moroi and K. Nakayama, *Can decaying particle explain cosmic infrared background excess?*, *Phys. Lett. B* **772** (2017) 628 [[1706.04921](#)].
- [365] R. C. Keenan, A. J. Barger, L. L. Cowie and W.-H. Wang, *The Resolved Near-Infrared Extragalactic Background*, *Astrophys. J.* **723** (2010) 40 [[1008.4216](#)].
- [366] J. Bock et al., *The cosmic infrared background experiment*, *New Astron. Rev.* **50** (2006) 215 [[astro-ph/0510587](#)].
- [367] K. Tsumura, T. Matsumoto, S. Matsuura, I. Sakon and T. Wada, *Low-Resolution Spectrum of the Extragalactic Background Light with AKARI InfraRed Camera*, *Publ. Astron. Soc. Jap.* **65** (2013) 121 [[1307.6740](#)].
- [368] R. C. Gilmore, R. S. Somerville, J. R. Primack and A. Dominguez, *Semi-analytic modeling of the EBL and consequences for extragalactic gamma-ray spectra*, *Mon. Not. Roy. Astron. Soc.* **422** (2012) 3189 [[1104.0671](#)].
- [369] Y. Inoue, S. Inoue, M. A. R. Kobayashi, R. Makiya, Y. Niino and T. Totani, *Extragalactic Background Light from Hierarchical Galaxy Formation: Gamma-ray Attenuation up to the Epoch of Cosmic Reionization and the First Stars*, *Astrophys. J.* **768** (2013) 197 [[1212.1683](#)].
- [370] S. T. Scully, M. A. Malkan and F. W. Stecker, *An Empirical Determination of the Intergalactic Background Light Using Near-infrared Deep Galaxy Survey Data out to $5\mu\text{m}$ and the Gamma-Ray Opacity of the Universe*, *Astrophys. J.* **784** (2014) 138 [[1401.4435](#)].
- [371] B. Yue, A. Ferrara, R. Salvaterra and X. Chen, *The Contribution of High Redshift Galaxies to the Near-Infrared Background*, *Mon. Not. Roy. Astron. Soc.* **431** (2013) 383 [[1208.6234](#)].
- [372] B. Yue, A. Ferrara, R. Salvaterra, Y. Xu and X. Chen, *Infrared background signatures of the first black holes*, *Mon. Not. Roy. Astron. Soc.* **433** (2013) 1556 [[1305.5177](#)].
- [373] L. Costamante, *Gamma-rays from Blazars and the Extragalactic Background Light*, *Int. J. Mod. Phys. D* **22** (2013) 1330025 [[1309.0612](#)].
- [374] FERMI-LAT Collaboration, S. Abdollahi et al., *A gamma-ray determination of the Universe's star formation history*, *Science* **362** (2018) 1031 [[1812.01031](#)].
- [375] W. Essey, O. E. Kalashev, A. Kusenko and J. F. Beacom, *Secondary photons and neutrinos from cosmic rays produced by distant blazars*, *Phys. Rev. Lett.* **104** (2010) 141102 [[0912.3976](#)].

- [376] W. Essey and A. Kusenko, *A new interpretation of the gamma-ray observations of active galactic nuclei*, *Astropart. Phys.* **33** (2010) 81 [0905.1162].
- [377] W. Essey, O. Kalashev, A. Kusenko and J. F. Beacom, *Role of line-of-sight cosmic ray interactions in forming the spectra of distant blazars in TeV gamma rays and high-energy neutrinos*, *Astrophys. J.* **731** (2011) 51 [1011.6340].
- [378] K. Murase, C. D. Dermer, H. Takami and G. Migliori, *Blazars as Ultra-High-Energy Cosmic-Ray Sources: Implications for TeV Gamma-Ray Observations*, *Astrophys. J.* **749** (2012) 63 [1107.5576].
- [379] F. Aharonian, W. Essey, A. Kusenko and A. Prosekin, *TeV gamma rays from blazars beyond $z=1$?*, *Phys. Rev. D* **87** (2013) 063002 [1206.6715].
- [380] J. M. Gaskins, *A review of indirect searches for particle dark matter*, *Contemp. Phys.* **57** (2016) 496 [1604.00014].
- [381] I. G. Irastorza and J. Redondo, *New experimental approaches in the search for axion-like particles*, 1801.08127.
- [382] F. W. Stecker, S. T. Scully and M. A. Malkan, *An Empirical Determination of the Intergalactic Background Light from UV to FIR Wavelengths Using FIR Deep Galaxy Surveys and the Gamma-ray Opacity of the Universe*, *Astrophys. J.* **827** (2016) 6 [1605.01382].
- [383] R. Daido, F. Takahashi and N. Yokozaki, *Enhanced axion-photon coupling in GUT with hidden photon*, *Phys. Lett. B* **780** (2018) 538 [1801.10344].
- [384] N. Craig, A. Hook and S. Kasko, *The Photophobic ALP*, *JHEP* **09** (2018) 028 [1805.06538].
- [385] S.-S. Chern and J. Simons, *Characteristic forms and geometric invariants*, *Annals Math.* **99** (1974) 48.
- [386] D. Cadamuro, S. Hannestad, G. Raffelt and J. Redondo, *Cosmological bounds on sub-MeV mass axions*, *JCAP* **1102** (2011) 003 [1011.3694].
- [387] A. A. Zdziarski and R. Svensson, *Absorption of X-rays and gamma rays at cosmological distances*, *Astrophys. J.* **344** (1989) 551.
- [388] M. Cirelli, G. Corcella, A. Hektor, G. Hutsi, M. Kadastik, P. Panci, M. Raidal, F. Sala and A. Strumia, *PPPC 4 DM ID: A Poor Particle Physicist Cookbook for Dark Matter Indirect Detection*, *JCAP* **1103** (2011) 051 [1012.4515]. [Erratum: JCAP 1210, E01 (2012)].
- [389] A. Mazumdar, S. Qutub and K. Saikawa, *Nonthermal axion dark radiation and constraints*, *Phys. Rev. D* **94** (2016) 065030 [1607.06958].

- [390] X.-D. Shi and G. M. Fuller, *New dark matter candidate: nonthermal sterile neutrinos*, *Phys. Rev. Lett.* **82** (1999) 2832 [[astro-ph/9810076](#)].
- [391] E. W. Kolb and M. S. Turner, *The Early Universe*, vol. 69. Front. Phys., 1990.
- [392] S. Hannestad and G. Raffelt, *Cosmological mass limits on neutrinos, axions, and other light particles*, *JCAP* **0404** (2004) 008 [[hep-ph/0312154](#)].
- [393] M. Archidiacono, S. Hannestad, A. Mirizzi, G. Raffelt and Y. Y. Y. Wong, *Axion hot dark matter bounds after Planck*, *JCAP* **1310** (2013) 020 [[1307.0615](#)].
- [394] M. Shaposhnikov and I. Tkachev, *The nuMSM, inflation, and dark matter*, *Phys. Lett. B* **639** (2006) 414 [[hep-ph/0604236](#)].
- [395] A. Kusenko, *Sterile neutrinos, dark matter, and the pulsar velocities in models with a Higgs singlet*, *Phys. Rev. Lett.* **97** (2006) 241301 [[hep-ph/0609081](#)].
- [396] K. Petraki and A. Kusenko, *Dark-matter sterile neutrinos in models with a gauge singlet in the Higgs sector*, *Phys. Rev. D* **77** (2008) 065014 [[0711.4646](#)].
- [397] L. J. Hall, K. Jedamzik, J. March-Russell and S. M. West, *Freeze-In Production of FIMP Dark Matter*, *JHEP* **03** (2010) 080 [[0911.1120](#)].
- [398] H. Baer, K.-Y. Choi, J. E. Kim and L. Roszkowski, *Dark matter production in the early Universe: beyond the thermal WIMP paradigm*, *Phys. Rept.* **555** (2015) 1 [[1407.0017](#)].
- [399] A. Merle, *keV sterile neutrino Dark Matter*, *PoS NOW2016* (2017) 082 [[1702.08430](#)].
- [400] A. V. Patwardhan, G. M. Fuller, C. T. Kishimoto and A. Kusenko, *Diluted equilibrium sterile neutrino dark matter*, *Phys. Rev. D* **92** (2015) 103509 [[1507.01977](#)].
- [401] P. F. de Salas, M. Lattanzi, G. Mangano, G. Miele, S. Pastor and O. Pisanti, *Bounds on very low reheating scenarios after Planck*, *Phys. Rev. D* **92** (2015) 123534 [[1511.00672](#)].
- [402] Y. Gong, A. Cooray, K. Mitchell-Wynne, X. Chen, M. Zemcov and J. Smidt, *Axion decay and anisotropy of near-IR extragalactic background light*, *Astrophys. J.* **825** (2016) 104 [[1511.01577](#)].
- [403] E. R. Fernandez, E. Komatsu, I. T. Iliev and P. R. Shapiro, *The Cosmic Near Infrared Background II: Fluctuations*, *Astrophys. J.* **710** (2010) 1089 [[0906.4552](#)].
- [404] J. Bock et al., *The Cosmic Infrared Background Experiment (CIBER): The Wide-Field Imagers*, *Astrophys. J. Suppl.* **207** (2013) 32 [[1206.4702](#)].

- [405] S. Ando and E. Komatsu, *Anisotropy of the cosmic gamma-ray background from dark matter annihilation*, *Phys. Rev. D* **73** (2006) 023521 [[astro-ph/0512217](#)].
- [406] M. LoVerde and N. Afshordi, *Extended Limber Approximation*, *Phys. Rev. D* **78** (2008) 123506 [[0809.5112](#)].
- [407] A. Ibarra, D. Tran and C. Weniger, *Detecting Gamma-Ray Anisotropies from Decaying Dark Matter: Prospects for Fermi LAT*, *Phys. Rev. D* **81** (2010) 023529 [[0909.3514](#)].
- [408] S. Ando and E. Komatsu, *Constraints on the annihilation cross section of dark matter particles from anisotropies in the diffuse gamma-ray background measured with Fermi-LAT*, *Phys. Rev. D* **87** (2013) 123539 [[1301.5901](#)].
- [409] M. Zemcov et al., *On the Origin of Near-Infrared Extragalactic Background Light Anisotropy*, *Science* **346** (2014) 732 [[1411.1411](#)].
- [410] K. Mitchell-Wynne et al., *Ultraviolet Luminosity Density of the Universe During the Epoch of Reionization*, *Nature Commun.* **6** (2015) 7945 [[1509.02935](#)].
- [411] D. Blas, J. Lesgourgues and T. Tram, *The Cosmic Linear Anisotropy Solving System (CLASS) II: Approximation schemes*, *JCAP* **1107** (2011) 034 [[1104.2933](#)].
- [412] <http://class-code.net/>.
- [413] D. Inman and U.-L. Pen, *Cosmic neutrinos: A dispersive and nonlinear fluid*, *Phys. Rev. D* **95** (2017) 063535 [[1609.09469](#)].
- [414] D. J. Eisenstein and W. Hu, *Power spectra for cold dark matter and its variants*, *Astrophys. J.* **511** (1997) 5 [[astro-ph/9710252](#)].
- [415] J. Lesgourgues and T. Tram, *The Cosmic Linear Anisotropy Solving System (CLASS) IV: efficient implementation of non-cold relics*, *JCAP* **1109** (2011) 032 [[1104.2935](#)].
- [416] G. G. Raffelt, *Limits on neutrino electromagnetic properties: An update*, *Phys. Rept.* **320** (1999) 319.
- [417] N. Viaux, M. Catelan, P. B. Stetson, G. Raffelt, J. Redondo, A. A. R. Valcarce and A. Weiss, *Neutrino and axion bounds from the globular cluster M5 (NGC 5904)*, *Phys. Rev. Lett.* **111** (2013) 231301 [[1311.1669](#)].
- [418] M. Giannotti, I. Irastorza, J. Redondo and A. Ringwald, *Cool WISPs for stellar cooling excesses*, *JCAP* **1605** (2016) 057 [[1512.08108](#)].

- [419] M. Giannotti, I. G. Irastorza, J. Redondo, A. Ringwald and K. Saikawa, *Stellar Recipes for Axion Hunters*, *JCAP* **1710** (2017) 010 [[1708.02111](#)].
- [420] FERMI-LAT Collaboration, M. Ackermann et al., *The spectrum of isotropic diffuse gamma-ray emission between 100 MeV and 820 GeV*, *Astrophys. J.* **799** (2015) 86 [[1410.3696](#)].
- [421] K. Murase, M. Ahlers and B. C. Lacki, *Testing the Hadronuclear Origin of PeV Neutrinos Observed with IceCube*, *Phys. Rev. D* **88** (2013) 121301 [[1306.3417](#)].
- [422] G. Giacinti, M. Kachelrieß, O. Kalashev, A. Neronov and D. V. Semikoz, *Unified model for cosmic rays above 10^{17} eV and the diffuse gamma-ray and neutrino backgrounds*, *Phys. Rev. D* **92** (2015) 083016 [[1507.07534](#)].
- [423] S. Gao, M. Pohl and W. Winter, *On the direct correlation between gamma-rays and PeV neutrinos from blazars*, *Astrophys. J.* **843** (2017) 109 [[1610.05306](#)].
- [424] G. Hasinger, T. Miyaji and M. Schmidt, *Luminosity-dependent evolution of soft x-ray selected AGN: New Chandra and XMM-Newton surveys*, *Astron. Astrophys.* **441** (2005) 417 [[astro-ph/0506118](#)].
- [425] O. E. Kalashev and E. Kido, *Simulations of Ultra High Energy Cosmic Rays propagation*, *J. Exp. Theor. Phys.* **120** (2015) 790 [[1406.0735](#)].
- [426] H.E.S.S. Collaboration, A. Abramowski et al., *The 2012 flare of PG 1553+113 seen with H.E.S.S. and Fermi-LAT*, *Astrophys. J.* **802** (2015) 65 [[1501.05087](#)].
- [427] W. Essey and A. Kusenko, *On weak redshift dependence of gamma-ray spectra of distant blazars*, *Astrophys. J.* **751** (2012) L11 [[1111.0815](#)].
- [428] A. Prosekin, W. Essey, A. Kusenko and F. Aharonian, *Time structure of gamma-ray signals generated in line-of-sight interactions of cosmic rays from distant blazars*, *Astrophys. J.* **757** (2012) 183 [[1203.3787](#)].
- [429] O. E. Kalashev, A. Kusenko and W. Essey, *PeV neutrinos from intergalactic interactions of cosmic rays emitted by active galactic nuclei*, *Phys. Rev. Lett.* **111** (2013) 041103 [[1303.0300](#)].
- [430] Y. Inoue, O. E. Kalashev and A. Kusenko, *Prospects for future very high-energy gamma-ray sky survey: impact of secondary gamma rays*, *Astropart. Phys.* **54** (2014) 118 [[1308.5710](#)].
- [431] A. De Franco, Y. Inoue, M. A. Sanchez-Conde and G. Cotter, *Cherenkov telescope array extragalactic survey discovery potential and the impact of axion-like particles and secondary gamma rays*, *Astropart. Phys.* **93** (2017) 8 [[1707.00250](#)].

- [432] C. W. Danforth, B. A. Keeney, J. T. Stocke, J. M. Shull and Y. Yao, *HST/COS Observations of the Ly alpha Forest toward the BL Lac Object 1ES1553+113*, *Astrophys. J.* **720** (2010) 976 [[1005.2191](#)].
- [433] M. Lawson, A. J. Millar, M. Pancaldi, E. Vitagliano and F. Wilczek, *Tunable axion plasma haloscopes*, [1904.11872](#).
- [434] P. F. de Salas, D. V. Forero, C. A. Ternes, M. Tórtola and J. W. F. Valle, *Status of neutrino oscillations 2018: 3σ hint for normal mass ordering and improved CP sensitivity*, *Phys. Lett. B* **782** (2018) 633 [[1708.01186](#)].
- [435] I. Esteban, M. C. Gonzalez-Garcia, M. Maltoni, I. Martinez-Soler and T. Schwetz, *Updated fit to three neutrino mixing: exploring the accelerator-reactor complementarity*, *JHEP* **01** (2017) 087 [[1611.01514](#)]. For the latest results see the [NuFIT homepage](#).
- [436] J. Ellis, H.-T. Janka, N. E. Mavromatos, A. S. Sakharov and E. K. G. Sarkisyan, *Prospective constraints on neutrino masses from a core-collapse supernova*, *Phys. Rev. D* **85** (2012) 105028 [[1202.0248](#)].
- [437] F. J. Botella, C. S. Lim and W. J. Marciano, *Radiative corrections to neutrino indices of refraction*, *Phys. Rev. D* **35** (1987) 896.
- [438] A. Mirizzi, S. Pozzorini, G. G. Raffelt and P. D. Serpico, *Flavour-dependent radiative correction to neutrino-neutrino refraction*, *JHEP* **10** (2009) 020 [[0907.3674](#)].
- [439] R. Bollig, H.-T. Janka, A. Lohs, G. Martínez-Pinedo, C. J. Horowitz and T. Melson, *Muon creation in supernova matter facilitates neutrino-driven explosions*, *Phys. Rev. Lett.* **119** (2017) 242702 [[1706.04630](#)].
- [440] H. Duan, G. M. Fuller and Y.-Z. Qian, *Collective neutrino oscillations*, *Ann. Rev. Nucl. Part. Sci.* **60** (2010) 569 [[1001.2799](#)].
- [441] A. Ioannisian and S. Pokorski, *Three neutrino oscillations in matter*, *Phys. Lett. B* **782** (2018) 641 [[1801.10488](#)].
- [442] S. Turck-Chieze et al., *Solar neutrino emission deduced from a seismic model*, *Astrophys. J.* **555** (2001) L69.
- [443] S. Couvidat, S. Turck-Chieze and A. G. Kosovichev, *Solar seismic models and the neutrino predictions*, *Astrophys. J.* **599** (2003) 1434 [[astro-ph/0203107](#)].
- [444] A. Serenelli, S. Basu, J. W. Ferguson and M. Asplund, *New Solar Composition: The Problem With Solar Models Revisited*, *Astrophys. J.* **705** (2009) L123 [[0909.2668](#)].